UNIVERSITY OF SOUTHAMPTON

FACULTY OF ENGINEERING AND PHYSICAL SCIENCE

Electronics and Computer Science

User-Centric Visible Light Networking

by

Simeng Feng

Thesis for the degree of Doctor of Philosophy

Supervisors:

Prof. Lajos Hanzo

and Dr. Rong Zhang

January 22, 2019

Dedicated to my parents

UNIVERSITY OF SOUTHAMPTON

ABSTRACT

FACULTY OF ENGINEERING AND PHYSICAL SCIENCE
Electronics and Computer Science

Doctor of Philosophy

USER-CENTRIC VISIBLE LIGHT NETWORKING

by Simeng Feng

In this thesis, we propose a suite of schemes for indoor visible light communications (VLC), where multiple light emitting diode (LED) based access points (APs) serve multiple photo diode (PD) aided user equipment (UE). A novel user-centric (UC) VLC network is conceived, relying on user-clustering, resource allocation and sophisticated multiple access (MA) design. Our objective is to improve both the throughput and outage probability of the proposed UC-VLC network under practical indoor positioning and backhaul network design.

Specifically, instead of relying on the conventional network-centric (NC) design, we conceive the novel concept of UC-VLC supported by amorphous cells exhibiting extra benefits. By beneficially clustering multiple attocells based on the location information of UEs, a centre-shifting UC-clustering strategy is proposed, leading to a multi-AP-multi-UE scenario within each cluster. Upon employing the potent transmit pre-coding (TPC) concept, the multi-user interference (MUI) within each cluster can be completely eliminated, where multiple APs simultaneously serve the clustered UEs. Since the construction of the UC-clusters relies on the knowledge of the UEs' positions, the intrinsic amalgamation of indoor positioning with the VLC network becomes important. Upon combining the benefits of triangulation and fingerprinting based positioning techniques, we propose a novel hybrid solution exhibiting a high accuracy, robustness and scalability. This is achieved by beneficially combining the low-complexity triangulation based positioning with high-accuracy fingerprinting, in order to efficiently support UC-clustering.

Since the improvement of the UC-VLC over NC-VLC has in the past been quantified based on a number of idealized simplifying assumptions, such as operating exactly at the Shannon capacity, our motivation is to quantify the performance of the UC-VLC under more practical considerations. Therefore, adaptive modulation is invoked, which allows the individual UEs to be assigned various modulation-modes. Since the different modulation-modes require different power, the transmit power allocated to each AP is therefore dependent and dynamic. Furthermore, instead of greedily supporting all the

UEs in the network, a dynamic scheduling scheme is advocated. To obtain the maximum throughput of the constructed UC-VLC under practical constraints, an efficient resource allocation strategy is required for dealing with the modulation-mode assignment, power allocation and the scheduling. To solve this complex maximization problem, a heuristic RA algorithm based on dynamic-programming is proposed. Aided by it, we will show under a range of scenarios that the achievable throughput and the outage probability of the proposed UC-VLC system are better than that of the conventional NC-VLC system.

Then, we study the MA of VLC, when the APs are densely deployed, leading to a ultra-dense VLC network, where the inter-cell interference (ICI) amongst the densely-deployed APs is severe. To handle this challenge, both orthogonal MA (OMA) and non-orthogonal MA (NOMA) are considered. In order to cope with the grave ICI of our UC-VLC network, a hybrid NOMA and OMA scheme is proposed for enhancing the performance, where the frequency reuse (FR) technique and the TDMA-based scheduling may be dynamically invoked, which are further amalgamated with the spectrum-efficient NOMA scheme. We will show that the proposed MA scheme is more robust against the ICI, keeping the outage probability as low as possible, at a price of modestly degrading the achievable throughput.

Finally, we consider the realistic backhaul issue of our VLC network. Since the ubiquitous mains power line constitutes a natural backbone feed for VLC, a combined power line communication (PLC) and VLC (PLC-VLC) network is conceived. More specifically, the source data arriving from the Ethernet is fed by a power line into the VLC network through the alternating current (AC) power supply, hence combining the power supply and data communication relying on PLC. In this PLC-VLC network, the power line connects the LEDs without requiring a duplicated fibre-backbone, which is implementationally convenient. To cope with the harsh impulse noise of the PLC channel, broadband OFDM PLC is used. The information gleaned from PLC is then forwarded to multiple UEs via visible light. To increase the downlink bit rate, the NOMA principle is invoked in our VLC network. For the sake of maximizing the sum-throughput of the PLC-VLC network, we conceive an optimal joint power allocation (JPA) strategy for each subcarrier in PLC and for each UE in VLC, which will be demonstrated to outperform the benchmarkers.

Contents

List of Figures

List of Tables

List of Symbols

General notation

- The superscript * represents complex conjugate.
- The superscript ^{T} represents matrix transpose operation.
- The superscript ^{H} represents complex conjugate transpose operation.
- The operator $|\bullet|$ represents the cardinality of a set.
- The operator $Q(\bullet)$ represents the Gaussian Q-function.
- The operator $\boldsymbol{A}_{(i,j)}$ represents the $[i,j]$th entry of $\boldsymbol{A}$.
- The operator $\text{diag}\{\boldsymbol{a}\}$ represents a diagonal matrix whose entries on the main diagonal are given by the elements of $\boldsymbol{a}$.
- The operator $\mathbb{E}(\bullet)$ denotes the expectation .
- The operator $\mathbb{D}(\bullet)$ represents the variance.
- The operator $\binom{a}{b}$ denotes a combination of b items taken from a items.

Special Symbols

Chapter 2

I. Environment-Related Symbols

k	UE index
n	AP index
c	Cluster index
$\mathcal{K}$	UE set
$\mathcal{N}$	AP set

$\mathcal{C}$	Cluster set
$\mathcal{S}_I$	Interference set
H_t	Height of AP Plane
H_r	Height of UE Plane
II. VLC-Channel-Related Symbols	
$h_{k,n}^{(0)}$	Channel gain of LoS path between UE k and AP n
$h_{k,n}^{(1)}$	Channel gain of the first reflected path between UE k and AP n
$h_{k,n}$	Aggregated channel gain between UE k and AP n
$\boldsymbol{H}$	Full channel matrix
$\boldsymbol{H}_c$	VLC Channel matrix of the cluster $\mathcal{C}_c$
$\boldsymbol{G}_c$	ZF pre-coding matrix in cluster $\mathcal{C}_c$
α	Order of Lambertian Emission
ϱ	Refractive index at the UE-end
ρ	Reflection coefficient
$\phi_{1/2}$	Semi-angle at half power
A_s	Physical area of a receiver at the UE-end
dA_{wall}	Reflective area
$D_{k,n}$	Distance between UE k and AP n
$D_{k,r}$	Distance between UE k and the reflection point
$D_{r,n}$	Distance between the reflection point and the AP n
ϕ_0	Angle of irradiance in LoS path
ϕ_1	Angle of irradiance in the first reflected path
ψ_0	Angle of incidence in LoS path
ψ_1	Angle of incidence in the first reflected path
ω_1	Angle of irradiance with respect to the reflection point
ω_2	Angle of irradiance with respect to the UE
$g_{of}(\bullet)$	Gain of the optical filter
$g_{oc}(\bullet)$	Gain of the optical concentrator
ψ_{FoV}	FoV at the UE-end
III. Link-Level-Related Symbols	
I_L	Turn-on current of LED
I_H	Maximum tolerable current of LED
P_L	Lower power bound of LED's dynamic range
P_H	Upper power bound of LED's dynamic range
P_{bias}	DC bias
$P_{\text{Tx,LED}}$	Electronic power of a single LED
$P_{\text{Tx,elec}}$	Transmit electronic power
$\varepsilon_{\text{bottom}}^{\text{ACO}}$	Bottom clipping level of ACO-OFDM
$\varepsilon_{\text{top}}^{\text{ACO}}$	Top clipping level of ACO-OFDM
$\varepsilon_{\text{bottom}}^{\text{DCO}}$	Bottom clipping level of DCO-OFDM

$\varepsilon_{\text{top}}^{\text{DCO}}$	Top clipping level of DCO-OFDM
$\sigma^2_{\text{clip,ACO}}$	Variance of clipping distortion of ACO-OFDM
$\sigma^2_{\text{clip,DCO}}$	Variance of clipping distortion of DCO-OFDM
$\Upsilon_{c,k}$	SINR of the kth UE in cluster $\mathcal{C}_c$
$\Upsilon_{c,k}^{\text{clip}}$	SINR of the kth UE in cluster $\mathcal{C}_c$ considering the clipping-distortion
γ	O/E conversion efficiency
σ^2_{awgn}	Variance of AWGN
N_0	Power spectral density
N	Number of subcarriers
B	Bandwidth
G_{B}	Bandwidth utilization factor
$G_{\text{DC}}^{\text{aco}}$	Attenuation factor of the useful electrical signal power due to DC bias in ACO-OFDM
$G_{\text{DC}}^{\text{dco}}$	Attenuation factor of the useful electrical signal power due to DC bias in DCO-OFDM

IV. Cluster-Related Symbols

τ	FR factor
ζ	Number of pre-defined clusters
r	Pre-defined maximum radius for the radius-based UC-clustering
$q_c^{[i]}$	The ith tentative cluster centre of the cth UE set
d_u	Pre-defined distance threshold for constructing UE set
d_a	Pre-defined distance threshold for constructing AP set
$\mathcal{K}^r$	Rejected UE set
$\mathcal{K}^\circ$	Idle UE set
$\mathcal{K}_c^{[i]}$	The cth expanded UE set during the ith iteration
$\mathcal{N}^\circ$	Idle AP set
$\mathcal{N}_c^\dagger$	Corresponding AP anchoring set for the cth clsuter
$\mathcal{N}_c^\ddagger$	Expanded AP set for the cth cluster

Chapter 3

t_i	Propagation time between UE and the ith AP
v	Propagation speed
s_i	The distance between the UE and the ith AP
θ_i	The angle of arrival between the signal and the ith AP
P_T	Transmission power of AP
p_{k,n_i}	RSS value between the UE k and the AP n_i
$\bar{\boldsymbol{p}}_i$	RSS vector of the ith tile L_i
$\boldsymbol{p}_k$	RSS vector obtained for the estimation point k
r_{k,n_i}	Horizontal distance between the UE k and the projection of AP n_i

d_{k,n_i}	Estimated distance between the UE k and AP n_i
$\mathbb{P}_{\text{bl}}$	LoS blocking probability
Q	Number of small tiles in the fingerprinting database
Υ	Quality threshold in *Evaluation* stage of hybrid positioning
ι	Positioning error tolerance

Chapter 4

I. Link-Level-Related Symbols

$\boldsymbol{x}_c$	Transmit signal vector
$\boldsymbol{y}_c$	MUI-free received signal
$\boldsymbol{P}_c$	Allocated power matrix
$\boldsymbol{\tau}_c$	Noise and interference vector
N^{awgn}	AWGN having a variance of σ^2_{awgn}
$N^{\text{clip}}_{c,k}$	Clipping-distortion having a variance of $\sigma_{\text{clip},c,k}$ of UE k in the cth cluster
$I_{c,k}$	ICI of UE k in the cth cluster
γ_m	minimum SINR of the mth modulation-mode by given a target BER

II. Resource-Allocation-Related Symbols

$P^{\text{tx}}_{\max}$	Maximum transmit power allowance
R^{BH}	Maximum backhaul rate allowance
p^{tx}_j	The jth tightened power constraint
$p_{c,k,m}$	Required power by UE k in the cth cluster, assigned by the mth modulation-mode
$\mathcal{P}_c$	Candidate power allocation set for the cth cluster after solving $\boldsymbol{S1}$
$r_{c,k,m}$	Achievable rate of UE k in the cth cluster, relying on modulation-mode m
$T_{c,n,K}(p^{\text{tx}}_j)$	Achievable maximum sum-throughput upon supporting K UEs, when the transmit power of AP n in the cluster c is restricted by p^{tx}_j
$\mathcal{T}_{c,n}$	AP-n-power-limited sum-throughput set for the cth cluster
$\mathcal{T}_c$	Obtained sum-throughput set for the cth cluster after solving $\boldsymbol{S1}$
$\mathcal{M}$	Modulation-mode set
$\mathcal{M}_c$	Candidate modulation-mode assignment set for the cth cluster after solving $\boldsymbol{S1}$
$\mathcal{M}^*_c$	Feasible modulation-mode assignment set for the cth cluster
$\overline{\text{TP}}$	Normalized throughput
$\overline{\text{OP}}$	Normalized outage probability

Chapter 5

I. Link-Level-Related Symbols

L	Number of layers for LACO-OFDM
β_l	coefficient of the lth layer
p_l	The power of the lth layer of LACO-OFDM
P_L	The power of a total of L layers of LACO-OFDM
$\gamma_{n,k}$	SINR of the kth UE, when supported by AP n
$\gamma_{n,k,l}^{[m]}$	SINR of the lth layer of UE k in cluster $\mathcal{C}_n$, employing modulation-mode m
$\boldsymbol{I}_{n,k}$	ICI vector imposed on the kth UE, excluding the AP n
$I_{n,k}^{[f]}$	ICI arriving from cluster $\mathcal{C}_f$ to the kth UE in cluster $\mathcal{C}_n$

II. Networking-Related Symbols

H_{thr}	Pre-defined quality threshold for the *channel-gain-guaranteed matching*
D_{thr}	Pre-defined distance threshold for *transmission-distance-restricted matching*
I_{thr}	Pre-defined ICI threshold for constructing $\mathcal{G}_{\text{color}}$
$K_{n,g}$	Number of the UEs in cluster $\mathcal{C}_n$ aimed to be supported during the gth iteration
t_g	Time resource allocated to the gth group
$\deg(v_n)$	Degree of the vertex n
$\overline{\deg}(v_n)$	Weighted degree of vertex n
$\mathcal{G}_{\text{asso}}$	A directed bipartite graph for network association
$\mathcal{G}_{\text{color}}$	A coloring graph used for FRB allocation
$\mathcal{V}_{\text{asso}}$	Vertex set for graph $\mathcal{G}_{\text{asso}}$
$\mathcal{V}_{\text{color}}$	Vertex set for graph $\mathcal{G}_{\text{color}}$
$\mathcal{E}_{\text{asso}}$	Edge set for graph $\mathcal{G}_{\text{asso}}$
$\mathcal{E}_{\text{asso}}^{\text{ue}\rightarrow\text{ap}}$	Edge set holding edges spanning from the UE-end to AP-end
$\mathcal{E}_{\text{asso}}^{\text{ue}\leftarrow\text{ap}}$	Edge set holding edges emerging from the AP-end to UE-end
$\mathcal{E}_{\text{color}}$	Edge set for graph $\mathcal{G}_{\text{color}}$
$\mathcal{K}_n^{\text{Ⓢ}}$	Served UE set of cluster $\mathcal{C}_n$
$\mathcal{K}_{n,g}^{\text{Ⓢ}}$	Served UE set of cluster $\mathcal{C}_n$ during the gth iteration
$\mathcal{K}_n^{\varnothing}$	Unsupported UE set of cluster $\mathcal{C}_n$

III. Resource-Allocation-Related Symbols

Λ	Maximum UE-load for each AP
$P_{\max}$	Maximum transmit power
$R_{\max}$	Backhaul allowance
R_j	The jth tightened backhaul constraint

$R_{k,\min}$	Minimum transmission rate required by UE k
$p_{n,k,l}^{[m]}$	Transmit power required by the lth layer for modulation-mode m of UE k in cluster $\mathcal{C}_n$
$P_{n,k}$	Allocated power for the kth UE, supported by AP n
$\boldsymbol{P}_{n,k}^{[i]}$	Required power vector for a total of k UEs under power constraint p_i
$\boldsymbol{P}_{n,k}$	Power allocation matrix during the kth UE-recursion
$\mathcal{P}_n^*$	Feasible power allocation set for cluster $\mathcal{C}_n$
$r_{k,l}^{[m]}$	Achievable rate of the lth layer for UE k using modulation-mode m
$T_{k,l}(R_j)$	Maximum achievable sum-throughput of UE k during the lth layer-recursion under rate constraint R_j
$S_{n,k}(p_i)$	Maximum achievable sum-throughput of all k UEs under power constraint p_i
$\mathcal{T}_{n,k}$	Candidate sum-throughput set at the 1st-tier
$\mathcal{T}_{n,k}^{\mathrm{r}}$	Rate constraint satisfied candidate sum-throughput set for UE k at the 1st-tier
$\mathcal{S}_n$	Candidate sum-throughput set for cluster $\mathcal{C}_n$
$\mathcal{S}_n^{r\&p}$	Ultimate candidate sum-throughput set for cluster $\mathcal{C}_n$
$m_{k,l}^{[j]}$	Modulation-mode decided for the lth layer for UE k under rate constraint R_j
$\boldsymbol{m}_{k,l}^{1\mathrm{st},[j]}$	Modulation-mode assignment vector for layer 1 to layer l of UE k at the 1st-tier, under rate constraint R_j
$\boldsymbol{m}_{n,k}^{2\mathrm{nd},[i]}$	Modulation-mode assignment vector for UE 1 to UE k at the 2nd-tier, under power constraint p_i
$\boldsymbol{M}_{k,l}^{1\mathrm{st}}$	Modulation-mode assignment decision at the lth layer-recursion at the 1st-tier
$\boldsymbol{M}_{n,k}^{2\mathrm{nd}}$	Modulation-mode assignment decision at the kth UE-recursion at the 2nd-tier
$\mathcal{M}_{n,k}$	Modulation-mode assignment set for UE k at the 1st-tier
$\mathcal{M}_{n,k}^{\mathrm{r}}$	Rate constraint satisfied modulation-mode assignment set for UE k at the 1st-tier
$\mathcal{M}_n^*$	Feasible modulation-mode assignment set for cluster $\mathcal{C}_n$

Chapter 6

I. PLC-Related Symbols

$g(f)$	Transfer function of PLC channel
g_n	Channel gain at the nth subcarrier
w_i	Weighting factor of the ith path
a_0, a_1	Attenuation parameters of PLC channel
κ	Exponent of the attenuation factor of PLC channel

d_i	Length of the ith path
v_p	Propagation velocity
$\sigma^2_{\mathrm{p},n}$	Variance of the colored background noise at the nth subcarrier
N_0^{p}	Noise power spectral in PLC
N	Number of subcarriers
B_{p}	Available bandwidth in PLC
B	Available bandwidth of each subcarrier in PLC
ϱ	Probability of the PLC channel being free from impulsive noise
R_{plc}	Achievable throughput of the OFDM-based PLC
$p_{\mathrm{plc},n}$	Allocated power to the nth subcarrier

II. VLC-Related Symbols

$h_{\mathrm{LoS},m}$	Channel gain of UE m based on LoS ray
$h_{\mathrm{Ref},m}$	Channel gain of UE m based on the first reflected ray
h_m	Aggregated channel gain of UE m
s_m	Transmitted signal intended for UE m
n_m	AWGN noise imposed on UE m
B_{v}	Available bandwidth in VLC
σ^2_{v}	Variance of the AWGN noise in VLC
$R_{\mathrm{vlc},m}$	Achievable throughput of UE m in VLC
$p_{\mathrm{vlc},m}$	Allocated power to UE m in VLC

III. JPA-Related Symbols

P_T	Total transmit power constraint
r_m	Minimum rate requirement for UE m
$\boldsymbol{p}_{\mathrm{plc}}$	Power allocation vector for each subcarrier in PLC
$\boldsymbol{p}_{\mathrm{vlc}}$	Power allocation vector for each UE in VLC

List of Publications

1. **S. Feng**, X. Li, R. Zhang, M. Jiang and L. Hanzo, "Hybrid Positioning Aided Amorphous-Cell Assisted User-Centric Visible Light Downlink Techniques", *IEEE Access*, vol. 4, pp. 2705-2713, June 2016.

2. **S. Feng**, R. Zhang, X. Li, Q. Wang, and L. Hanzo, "Dynamic Throughput Maximization for the User-Centric Visible Light Downlink in the Face of Practical Considerations", *IEEE Transactions on Wireless Communications*, vol. 17, no. 8, pp. 5001-5015, August 2018.

3. **S. Feng**, R. Zhang, W. Xu and L. Hanzo, "Multiple Access Design for Ultra-Dense VLC Networks: Orthogonal v.s. Non-Orthogonal", *IEEE Transactions on Communications* (accepted).

4. **S. Feng**, B. Tong and L. Hanzo, " Joint Power Allocation for the Multi-User NOMA-Downlink in a Power-Line-Fed VLC Network", *IEEE Transactions on Vehicular Technology* (under review).

5. P. Botsinis, D. Alanis, **S. Feng**, Z. Babar, H. V. Nguyen, D. Chandra, S. X. Ng, R. Zhang and L. Hanzo, "Quantum-Assisted Indoor Localization for Uplink mm-Wave and Downlink Visible Light Communication Systems", *IEEE Access*, vol. 5, pp. 23327-23351, July 2017.

Declaration of Authorship

I, **Simeng Feng** , declare that the thesis entitled **User-Centric Visible Light Networking** and the work presented in the thesis are both my own, and have been generated by me as the result of my own original research. I confirm that:

- this work was done wholly or mainly while in candidature for a research degree at this University;
- where any part of this thesis has previously been submitted for a degree or any other qualification at this University or any other institution, this has been clearly stated;
- where I have consulted the published work of others, this is always clearly attributed;
- where I have quoted from the work of others, the source is always given. With the exception of such quotations, this thesis is entirely my own work;
- I have acknowledged all main sources of help;
- where the thesis is based on work done by myself jointly with others, I have made clear exactly what was done by others and what I have contributed myself;
- parts of this work have been published as shown in the list of publications:

Signed:.....

Date:.....

Acknowledgements

I would like to express my sincere gratitude to my supervisor Prof. Lajos Hanzo for his professional supervision, his great support and great patience with me throughout my research. His passion towards research, diligence and positive altitudes towards life inspired me and would constantly encourage me after my graduation.

I would also like to thank my supervisor Dr. Rong Zhang for his guidance. At the earlier stage of my PhD research, he introduced me the field of visible light communications and helped me to discover my potential at research with constructive discussions and encouragements. I cannot complete this thesis without him and I am very grateful.

Many thanks also to my host supervisor Prof. Ming Jiang and Prof. Wei Xu. During my short visiting at Sun Yat-Sen University, Prof. Ming Jiang offered his warmest welcome and provided a great opportunity for me to participate in the project of visible light indoor positioning. Furthermore, I am also appreciated that Prof. Wei Xu held my one-month visiting at Southeast University. His altitude of research and insightful advice have greatly benefited me.

I also appreciate the help from my colleagues and all the staffs of the Next Generation Wireless Research Group for their useful discussions and comments throughout my research. Special thanks to Prof. Lie-Liang Yang, Prof. Robert Maunder, Dr. Soon X. Ng, Dr. Mohammed El-Hajjar, Dr. Panagiotis Botsinis, Dr. Dimitrios Alanis, Dr. Xuan Li, Dr. Qi Wang, Mr. Xiaoyu Zhang and Mr. Tong Bai for their technical support and collaborative work.

I would like to express my warmest gratitude to my parents for the lifelong understanding and support. Finally, I would like to greatly thank my boyfriend, Dr. Baolong Li, for his insightful advice, encouragement and company.

Chapter 1

Introduction

The number of connected devices is envisioned to be about 8.6 Billion by 2020, which results in the escalation of tele-traffic [3]. Given this challenge, both academia and the industry have invested substantial efforts into exploring the hitherto barely exploited higher-frequency spectrum, such as the visible light spectrum [4, 5]. The concept of employing visible light to achieve both communication and illumination simultaneously is first proposed by [6], spawning the field of visible light communciation (VLC). As a benefit of its inherent advantages, such as its license-free spectrum, strong immunity to electromagnetic interference, secure communication environment, the light emitting diode (LED) based VLC has been considered as an appealing complementary technology to radio-frequency (RF) communications. Furthermore, it has been shown in [7] that most of the data-traffic is generated in indoor scenarios. Due to its abandant spectral resources at THz-level, VLC constitutes a natural candidate for short-distance indoor communication [8].

According to Friis free space equation, higher frequencies however suffer from a higher propagation path loss [9]. Hence, the number of the access points (APs), constituted by LED arrays, tends to be much higher than that of the base stations (BSs) in outdoor RF scenarios [10]. By densely deploying the APs having a lower power and coverage, VLC is expected to increase the capacity by enabling line-of-sight (LoS) transmissions. However, due to the short distances between the APs, serious inter-cell interference (ICI) is encountered by the user equipment (UE). Therefore, this thesis investigates multi-AP-multi-UE indoor VLC networks, with a specific focus on system-level aspects, such as network association, scheduling, resource allocation, multiple access (MA) etc to mitigate the ICI and thus to achieve improved system performance under practical considerations such as indoor positioning and backhauling.

1.1 Link-Level VLC Issues

Since the transmitted information is modulated onto the light intensity, VLC constitutes an intensity modulation/direct detection (IM/DD) system, which requires the transmitted signal to be real-valued and non-negative [11]. Hence, the conventional RF modulation techniques cannot be directly invoked in VLC without modification. Furthermore, to resist the ICI, multi-user transmission techniques may be employed, leading to a multi-AP-multi-UE transmission link. Hence, in this section, both single-link and multiple-link VLC scenarios are reviewed.

1.1.1 Single-User Transmission

Point-to-point transmission has been widely investigated in VLC, including traditional schemes such as on-off keying (OOK) [12], pulse position modulation (PPM) [13], pulse width modulation (PWM) [14], etc. Thanks to its ability of supporting higher rates and mitigating inter-symbol interference (ISI), orthogonal frequency division multiplexing (OFDM) based modulation has been widely explored in the context of VLC. To be specific, there are two classic optical OFDM schemes, namely DC-biased optical OFDM (DCO-OFDM) and asymmetrically clipped optical OFDM (ACO-OFDM) [15, 16]. More specifically, the Hermitian symmetry is exploited in both of them to obtain real-valued time-domain signals. For DCO-OFDM, a direct current (DC) bias is added to the bipolar signals for guaranteeing the positivity of the signals, leading to a low power-efficiency. In ACO-OFDM, only the odd-indexed subcarriers are modulated and then the resultant antisymmetric signal is directly clipped at zero-level to obtain positive signals. However, this solution suffers from a low spectrum-efficiency.

To enhance the link-level transmission, more advanced modulation schemes have also been proposed. To elaborate, asymmetrically clipped DC biased OFDM (ADO-OFDM) applies ACO-OFDM to the odd-indexed subcarriers, whilst the even-indexed subcarriers transmit DCO-OFDM [17], albeit this solution still requires DC bias. In the hybrid ACO-OFDM (HACO-OFDM), ACO-OFDM is transmitted on the odd-indexed subcarriers, further combined with pulse-amplitude-modulated discrete multitone (PAM-DMT) on the even-indexed subcarriers with only the imaginary part being modulated [18], leaving the real part of the even-indexed subcarriers untapped. By contrast, layered ACO-OFDM (LACO-OFDM) [19] improves ACO-OFDM by actively employing more subcarriers in a layer-based manner, hence attaining a higher rate than ACO-OFDM, despite requiring a lower power than DCO-OFDM. A receiver design was proposed in [20] for LACO-OFDM. The authors demonstrated that their receiver is capable of reducing the effect of noise and inter-layer interference (ILI), hence yielding an improved performance. To reduce the peak-to-average power ratio (PAPR) of LACO-OFDM, a tone-injection

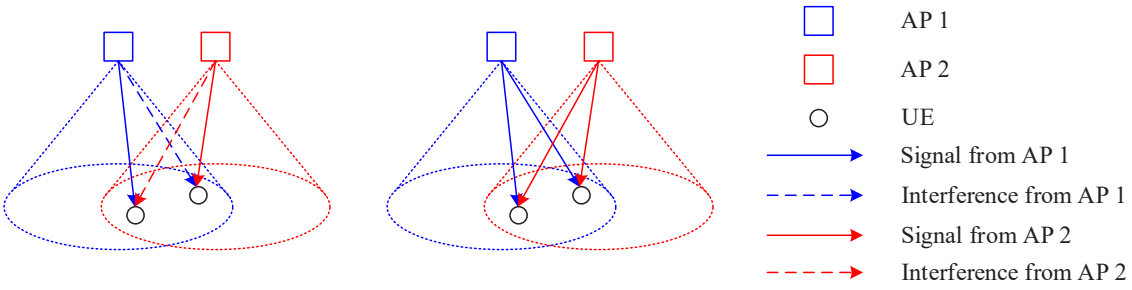

Figure 1.1: Illustration of the superiority by invoking multi-user transmission scheme. The left is based on single-user transmission, while the right demonstrates the multi-user transmission.

aided PAPR reduction design was proposed in [21] and an interleaved discrete-Fourier-transform-spread L/e-ACO-OFDM (IDFTS-L/e-ACO) arrangement was proposed in [22]. To improve the performance of LACO-OFDM, a two-stage receiver design was conceived in [23], where soft successive interference cancellation (SIC) was invoked at the first stage for suppressing the ILI, while the clipping noised was handled by the second stage for suppressing the additive noise. Furthermore, a multi-class coding scheme was proposed for LACO-OFDM in [24], where a signal-to-noise ratio (SNR) gain of 3.6 dB was attained.

1.1.2 Multi-User Transmission

The VLC system tends to rely on densely distributed APs [25], hence purely relying on single-link is unsuitable for multi-user scenarios in the face of grave interference. As shown in the left subplot of Fig. 1.1, the UEs suffer from interference imposed by the neighboring AP. By contrast, as observed in the right subplot of Fig. 1.1, if the two APs can serve the UEs simultaneously with the aid of transmit pre-coding (TPC), the interference can be mitigated, thus the achievable rate of both UEs is improved. Therefore, TPC aided VLC multi-user transmission has been widely studied [26–31]. To elaborate a little further, for the sake of turning the interference into an advantage, a TPC aided coordinated VLC broadcasting architecture was proposed in [26], which improves the signal-to-interference-plus-noise ratio (SINR) at the receiver-side. In [27], an optimal TPC based on zero-forcing (ZF) was proposed, where the optical power constraints were considered for each AP. Upon considering the phase differences in the frequency-domain, both a ZF and a minimum mean-squared error (MMSE) criterion based TPC technique was proposed [28]. To maximize the achievable rate, a ZF based beamforming was designed for the multi-user multiple-input-single-output (MISO) VLC downlink in [29]. Furthermore, the authors of [30] proposed a multi-user TPC aided

multiple-input-multiple-output (MIMO) OFDM indoor VLC system invoking spatial modulation (SM) and spatial pulse position modulation (SPPM). Furthermore, upon taking into account both realistic imperfect channel state information (CSI) and fairness, a linear TPC was developed in [31] to maximize the minimum SINR of UEs.

1.2 System-Level VLC Issues

These link-level research advances have allowed VLC networks to boost the achievable data rates. Since multi-AP-multi-UE transmission is capable of mitigating the interference and hence improving the transmission rate, it is vital to carefully design the association between APs and UEs. Furthermore, to improve the performance, having efficient resource allocation and MA designs is also important. Therefore, in this section, we provide a literature review in terms of network association, resource allocation and MA in VLC systems.

1.2.1 Network Association

In a typical VLC downlink, each AP illuminates only a small confined cell, which is referred to as an optical attocell [9]. The coverage area of a specific attocell depends on the half-power semiangle at the transmitter-end and on the field-of-view (FoV) at the receiver-end [32]. To improve the quality-of-service (QoS), typically a dense distribution of the LED based APs (LED-APs) is relied upon [33]. However, due to the overlap of multiple attocells, the UEs may suffer from interference from neighbouring APs. In conventional networks, the UE-AP association is generally implemented based on the highest SINR, but this *one-to-one* association is deemed to be inefficient. Given the large number of APs, Kamel *et al.* proposed a *one-to-many* association, where the UE is capable of connecting to more than one APs [34]. When supporting multiple UEs, the most straightforward way is based on the network-centric (NC) perspective, which relies on the classic fixed-cell strategy for specifying the UE-AP association [35, 36]. In this manner, more than one UEs may be located in a specific attocell, leading to a potential overloading. Furthermore, the ICI constitutes a bottleneck of this design.

To tackle this, the concept of amorphous-boundary-based user-centric (UC) cluster aided UC-VLC networking considered the UEs' positions, which was first advocated in [10], yielding the *many-to-many* UE-AP association concept. Based on the UE distribution, this philosophy enables multiple APs to simultaneously serve multiple grouped UEs, by clustering a group of neighboring attocells to form cluster, which may rely on TPC techniques. Following this association concept, the energy efficiency of UC-VLC was optimized relying on amorphous cells, which outperformed the conventional fixed

cells [37]. In [38], a UC-cluster formation was jointly constructed with the multi-user scheduling for interference-mitigation. In a hybrid VLC/WiFi system, the throughput achieved upon relying on UC-clusters was demonstrated to be higher than that of the conventional structure after performing load balancing. Furthermore, in the application of scalable video streaming, the authors of [39] demonstrated the superior performance of the UC-clusters over conventional cell in terms of throughput, energy efficiency and video quality. Moreover, instead of simply focusing on static environments, an anticipatory user-association has been put forward by considering both the UE's mobility and the dynamically fluctuating wireless traffic [40].

1.2.2 Multiple Access

In indoor multi-AP-multi-UE VLC network, the employment of efficient MA techniques is capable of facilitating increased data rates [41]. Generally speaking, the MA techniques can be classified into two categories: orthogonal MA (OMA) and non-orthogonal MA (NOMA). Similar to classic RF communications, OMA-based VLC can be further classified as time division MA (TDMA), frequency division MA (FDMA), code division MA (CDMA) and the space division MA (SDMA). To increase the attainable system throughput and to support ubiquitous connectivity, the concept of sharing the time and frequency resources amongst multiple UEs while distinguishing them in the power-domain, has drawn substantial research interests [42]. In this section, both the family of OMA and NOMA techniques are reviewed in the context of VLC systems.

1.2.2.1 Orthogonal Multiple Access

For multi-user access, the most straightforward arrangement is TDMA, where an AP offers access to its associated UEs in orthogonal time-slots. A high-speed VLC local area network (LAN) relying on TDMA was invoked for bidirectional full-duplex VLC transmission in [43] to provide a data rate upto to 8 Gbits/s. However, relying on TDMA imposes a hard limit on the number of UEs, which is given by the number of time-slots. FDMA enables UEs to be multiplexed in the frequency-domain, but each UE requires a different-frequency transceiver, whilst TDMA supports a multiplicity of UEs by a single optical downlink transceiver. Kashef *et al.* [44] investigated the performance of single-carrier (SC) FDMA in a multi-user VLC system, which had a relatively low PAPR. When the aforementioned multi-carrier (MC) modulation schemes were invoked, orthogonal frequency division multiple access (OFDMA) exhibited beneficial flexibility, where each UE is allocated a group of subcarriers in each time-slot. However, the authors of [41] pointed out that the high PAPR and limited dynamic range were the disadvantages of OFDMA-based VLC systems.

As for CDMA in VLC, also referred to as optical CDMA (OCDMA), each UE is assigned an orthogonal optical code (OOC) so that they can be supported simultaneously within the same frequency band. In the context of VLC, a CDMA-based VLC system was conceived in [35], which relied on low-complexity hardware. By defining a circular access area for each AP, which is usually smaller than its actual coverage area, multiple APs were installed to cover the entire indoor area, where OCDMA was employed to serve multiple UEs [45]. It was demonstrated that the proposed MIMO VLC system assisted by CDMA was robust against shadowing, dimming, background radiation and LED non-linearity. In [46], an experimental VLC system relying on CDMA was developed relying on random optical codes. By utilizing red-green-blue (RGB) LEDs, a novel color-shift keying (CSK) based VLC system was advocated in [47], where CDMA was invoked to support multi-user transmission. A 3-dB SNR gain was obtained by the proposed system, compared to conventional OOK modulation. To increase transmission robustness, CDMA and OFDMA can be amalgamated, yielding MC-CDMA. The authors of [48] studied MC-CDMA in VLC based on frequency-domain spreading, which demonstrated that the required transmit power was reduced. Closed-form bit-error-rate (BER) vs SINR equations were derived for a MC-CDMA based VLC system [49], where dimming control was also considered.

In RF-SDMA systems, unique antenna-specific impulse responses are used for distinguishing a number of parallel streams, so that multiple UEs can be supported simultaneously within the same frequency band [50]. However, due to the IM/DD nature of VLC, the RF-SDMA principle cannot be directly invoked in VLC. To elaborate a little further, the authors of [36] proposed an optical beamforming aided VLC system, which was demonstrated to outperform the TDMA benchmarker considered. The authors of [51] proposed a low-complexity coordinated multi-point (CoMP) VLC system, where a TPC tailored for VLC was conceived for eliminating the multi-user interference (MUI). The proposed algorithm was demonstrated to be robust to various UE loadings. To efficiently exploit the limited available bandwidth, an SDMA-OFDM scheme was conceived in [52], where a Walsh-Hadamard transform based spreading scheme was invoked for increasing the multi-user capability.

1.2.2.2 Non-Orthogonal Multiple Access

The mobile tele-traffic is expected to substaintially increase during the 2020s [53]. The NOMA concept was proposed in [42] for the sake of enhancing the bandwidth efficiency attained. In contrast to OMA techniques, NOMA allows multiple UEs to access the network by multiplexing them in the power-domain, where SIC can be applied at the receiver-side to separate the information of each individual UE [54]. Since different UEs are allocated different power levels, depending on their corresponding channel conditions,

multiple UEs are capable of simultaneously utilizing the same time- and spectral-slots [3]. In a nutshell, the NOMA concept has drawn substantial attention thanks to the following benefits:

- Since VLC is a natural member of the small-cell family, the number of UEs within each attocell is limited, which is beneficial for SIC-aided detection [41].
- As the channel of VLC can be viewed as a single-tap channel [26], the CSI required by power allocation at transmitter-side and by SIC at receiver-side is simply given by the channel gain.
- According to [54], NOMA performs better in high SNR scenarios. Since the transmission link in VLC is dominated by the LoS path, the energy of emission is focused within the FoV at the receiver-side, resulting in an inherently high-SNR scenario.

Furthermore, since the low modulation bandwidth of LED is the main challenge of VLC systems [8], as a remedy, the optical-NOMA (O-NOMA) concept is beneficial for enhancing the achievable throughput in the downlink of VLC systems [55]. Therefore, a range of contributions can be found in NOMA-aided VLC systems [56–66]. Specifically, Marshoud *et al.* [56] analysed the BER performance of VLC systems relying on NOMA both with and without perfect CSI, where a performance degradation was imposed by the imperfect outdated CSI. In a single-AP deployment, Yin *et al.* [57] demonstrated that both the coverage probability and ergodic sum rate of the NOMA-VLC system were better than that of OMA, where the performance gain can be further improved by pairing UEs associated with the most conducive channel conditions. Inspired by it, the authors of [58] proposed a user-grouping algorithm for NOMA-VLC systems, where a QoS-guaranteed NOMA power-allocation scheme was invesigated within each cell. To improve the sum rate of MIMO-based multi-user VLC-NOMA systems, a normalized gain difference based power allocation (NGDPA) arrangement was proposed, which was demonstrated to improve the sum rate by upto 29%, compared to NOMA relying on the gain ratio power allocation (GRPA) of [59]. For the sake of achieving fairness, Yang *et al.* [60] proposed an optimal power allocation solution for maximizing the sum rate in a multi-user scenario. By invoking NOMA in an OFDM-based VLC system, both UE-level and subcarrier-level power optimization were considered in [61], in order to maximize the sum rate, regardless of the number of multiplexed UEs. The physical-layer security of a multi-user NOMA-VLC system was investigated in [62], where the secrecy outage probability was derived both for single eavesdropper and multi-eavesdropper scenarios. Furthermore, to compensate for the LED's non-linearity, pre-distortion was invoked in a MIMO NOMA-VLC system, where the analytical BER upper bounds were derived [63]. In addition, the effect of clipping distortion on the sum-rate of two-user

NOMA was investigated in a DCO-OFDM aided VLC system [64], where the clipping was much more gentle than that of a typical OMA situation. Moreover, a bidirectional experimental NOMA-OFDMA VLC system was demonstrated in [65], which indicated that accurate channel estimation is capable of improving the BER performance more efficiently. We can see that the majority of the literature focussed on the NOMA-VLC developments in a single-AP scenario, where the issue of ICI is ignored. However, since VLC environments are typically characterized by strong ICI from the emissions of adjacent APs, the ICI is detrimental in the context of NOMA-VLC [66].

1.2.3 Resource Allocation

Without any doubt, an efficient resource allocation strategy is capable of significantly boosting the system performance. In VLC systems, the non-linearity of LEDs and the illumination constraints make the resource allocation different from that of RF systems. In this section, we provide a literature review of the resource allocation in VLC, where both ICI-agnostic and ICI-aware scenarios are considered.

1.2.3.1 Single-Cell Scenario

The optimal bit-and-power allocation (BPA) algorithm was conceived for VLC-OFDM systems in [67] without considering the ICI in a single-cell scenario. In contrast to the conventional BPA algorithm that assumes the noise power of each subcarrier to be independent of the signal power, the proposed optimal BPA strategy takes the quasi-linear relationship between the noise power and the received signal power into account, where an approximately 16% data rate improvement was achieved. An adaptive modulation scheme was investigated in [68], for each subcarrier of ACO-OFDM and DCO-OFDM under clipping-distortion consideration. It was shown that in a low-SNR scenario, the performance of the ACO-OFDM based adaptive modulation scheme is better than that of the DCO-OFDM based one. In [69], an impressive rate of 2 Gb/s was experimentally demonstrated for a VLC-OFDM system with the aid of an adaptive bit allocation strategy. Additionally, a relay-assisted VLC-OFDM system was studied in [70] under illumination constraints, where an optimal alternating current (AC)/DC power allocation was proposed for minimizing the BER performance. Note that the DC power allocation is determined by simultaneously satisfying a desired luminance ratio, while the AC power allocation deals with the specific fraction of the information signal power to minimize the BER. Instead of relying on white LEDs, a color-division VLC system was conceived in [71], under the additional consideration of human perception and lighting constraints, where the transmission rate was maximized by invoking standard convex optimization solutions. It was demonstrated that the optimal symbol modulation power

allocation scheme significantly outperforms the equal-power allocation scheme. Furthermore, upon considering the channel conditions of multiple UEs, a novel GRPA was proposed for VLC-NOMA systems, where the total transmit power was fixed [55]. To increase the achievable rate, an improved NGDPA method was proposed for a MIMO-NOMA VLC system along with adaptive power allocation, which was demonstrated to outperform the GRPA strategy [59].

1.2.3.2 Multiple-Cell Scenario

The resource allocation of multiple-cell scenarios is usually amalgamated with interference management and other advanced network design solutions. In detail, since frequency reuse (FR) constitutes an efficient technique of reducing the interference, it was investigated in indoor VLC scenario [72]. In order to satisfy the specific statistical delay constraints, an optimal resource allocation was conceived, where the effective capacity (EC) was employed to quantify the system performance. The results suggested that the FR-based transmission performs well in the face of tight delay requirements. The FR technique associated with a sophisticated user-grouping strategy was studied in [58], where the optimized power was allocated to improve the achievable rate under the UE's QoS constraint. As a further advance, a proportional fairness scheduling strategy based on the interference graph concept was proposed in [73], which was capable of achieving an increased sum-rate and fairness. In [74], a scheduling strategy was conceived for multi-color VLC systems to mitigate the ICI. Relying on unequal power allocation between the cell-edge and cell-centre UEs, a static scheduler was proposed, where a dynamic scheduler was also invoked for coordinating the color assignment in order to mitigate the ICI. The results demonstrated that the cell-edge UEs' throughput can be significantly improved at the modest price of a small overall throughput penalty. Furthermore, given a set of densely deployed APs, the cell-free VLC network concept was conceived in [75], where the UEs can be dynamically associated with their candidate APs anywhere within the FoV. To attain an enhanced system performance, the problem of association and power allocation was jointly solved, considering the fairness, load balancing and power control. To solve this non-convex problem, it was divided into two subproblems: namely the UE association subproblem subject to a fixed allocated power for each AP and the power allocation subproblem under a fixed time fraction.

Moreover, to improve the system performance, some authors have focussed their attention on the resource allocation issue of advanced VLC systems. To be specific, an OFDM based NOMA-VLC system was investigated in [61], where multiple APs simultaneously transmit the same OFDM based message to UEs, which are multiplexed on each subcarrier by NOMA. By exploiting both UE-level and the subcarrier-level power allocation, an enhanced power allocation strategy was proposed, which exhibited beneficial

	Power	**Cost**	**Accuracy**	**Multipath Effects**
RF	high	high	meter-level	affected seriously
VLC	low	low	centimetre-level	less serious

Table 1.1: Comparison of RF and VLC based IPS.

performance improvements compared to the conventional fixed power allocation (FPA) and GRPA schemes. To explore the spatial multiple-transmitter diversity, a multiple access discrete multi-tone (MA-DMT) scheme was proposed for VLC in [76], where the interference-constrained max-min throughput problem was formulated. To solve this, a heuristic resource allocation was proposed relying on splitting the problem into two sequential steps: transmitter allocation and subcarrier allocation, based on the assumption that the power was equally distributed between different active subcarriers. To increase the degree of freedom, a multi-chip LED based MISO VLC system was investigated in [77] and a power allocation scheme was designed by considering the luminance, chromaticity, amplitude and BER for maximizing the multi-user sum-rate. The results have shown that increased data rates can be expected upon increasing the blue light component in the mixed light. Furthermore, a power allocation method was analysed theoretically in [78] for an arbitrary number of transmit and receive antennas invoked by a MIMO-VLC system, where the non-negativity of the IM signal, the aggregate optical power budget and the BER requirements were all taken into account. Additionally, to improve the spectral efficiency, a cognitive multi-cell VLC system was conceived in [79] by dividing the UEs into two groups, referred to as the primary UEs and secondary UEs, based on their service requirements. For interference management, a flexible hybrid underlay/overlay resource allocation was proposed in order to maximize the sum rate, under optical constraints and minimum rate requirements. The simulation results provided have shown that the proposed cognitive VLC system associated with the proposed RA strategy achieve a higher sum-rate than that of the conventional non-cognitive VLC system, or the cognitive VLC only relying on the underlay or the overlay mode.

1.3 Practical Considerations for VLC

In this section, let us take into account some practical issues of the VLC system. As we mentioned before, the VLC system based on the UC-clusters conceived is capable of attaining an increased throughput. As a key point of UC-clustering, the UEs' locations play a significant role in determining its performance. As our scenario is focussed on indoor environments, it raises the issue of how to efficiently establish accurate indoor positioning. Although the global positioning system (GPS) is widely used by aircraft, cars and other vehicles as well as by portable devices, the real-time positioning performance is typically degraded by multipath propagation and blocking impairments in

indoor scenarios [80, 81]. Therefore, indoor positioning system (IPS) relying on indoor wireless signals, such as WiFi [82–84], Bluetooth [85–87] and radio frequency identification (RFID) tags [88–90], have been widely investigated for improving the performance of indoor positioning. Unfortunately, these RF-based indoor positioning techniques are gravely affected by multipath interference and their cost becomes excessive, when aiming for high positioning accuracy [80, 91]. Therefore, recently, the VLC-aided indoor positioning has drawn substantial research interests [11]. Since most of the energy is focussed on its LoS path, the multipath effects remain moderate, compared to RF-based IPS. The comparison of the VLC-aided indoor positioning and the RF-based indoor positioning is summarized in Table 1.1.

Furthermore, our VLC system design takes into account the associated backhaul issues. Generally speaking, a backbone network has to offer a high data rate and be readily coupled with the LED-APs [92]. The conventional network access solution for VLC connects the LED-APs to the backbone network via separate network cables [93]. It is however not cost-efficient since modifications of the existing indoor layout are required. Furthermore, since optical fiber has been widely used as backhaul for RF networks [94–96], the research of employing optical fiber based backhaul was extended to VLC [43], where it was experimentally demonstrated that the system was capable of providing a rate of upto 8 Gb/s over 25 km standard single mode fiber. However, it may be impractical to supply an optical fiber link for each of the APs in VLC, since the number of APs is expected to be high to compensate for the path loss [97]. By contrast, the ubiquitous mains power line constitutes a natural backbone feed for VLC without layout modifications, since the APs have already been connected to the power line for power supply. Therefore, extensive studies have been reported on the integration of power line communication (PLC) and VLC (PLC-VLC) [98–111, 97, 92], where the source data is fed by PLC into the VLC network without requiring a duplicated fibre-backbone.

Therefore, in the following, the literature review of both the visible light positioning and the PLC-VLC network is provided.

1.3.1 Visible Light Positioning

Although the multipath effect imposed on visible light positioning is not as serious as in RF-based IPS, the reflections due to walls, the floor and ceiling cannot be practically avoided in visible light positioning. Therefore, the impact of multipath reflections imposed on the performance of visible light positioning was investigated in [112], where the proposed system was constituted by a single LED-AP as the transmitter and a photo diode (PD) based receiver to detect its received signal strength (RSS). The simulation results have shown that without reflections, the positioning errors were within 0.05 cm, which can be viewed as the best-case scenario. By contrast, when the reflections were

taken into account, the positioning errors were increased to about 8 cm, when using powerful non-linear estimation. As the authors of [112] suggested, a visible light positioning framework relies on a large number of LED-APs, which simultaneously transmit their positional information, hence achieving higher positioning accuracy. The positioning technique of [113] relied on casting the LED-AP signal separation problem into a compressed sensing framework, where the UE can detect the set of nearby LEDs using sparse signal recovery algorithms. The positioning accuracy can be as high as a few centimeters, depending on the specific scenarios, such as the SNR, the number of transmitted bits and the number of LED-APs. However, in some VLC applications, there may exist only a single LED-AP, which has to locate multiple receivers, even though no other fixed reference nodes exist with known coordinates. To handle this challenging scenario, a visible light positioning framework was proposed in [114], where the target receivers were equipped with multiple PDs. By exploring the relative positions as well as the RSS indications of the multiple PDs, the positioning accuracy was improved to be on the order of millimeters in the presence of LoS VLC channels. But again, this accuracy was slightly degraded to the order of centimeters in realistic VLC applications, as demonstrated in [114].

Furthermore, to reduce the implementation complexity, a practical visible light positioning system, relying on commercial off-the-shelf luminaires and electronic components was investigated in [115], where the square chord distance metric [116] was invoked for the weighted k-nearest neighbor (WKNN) aided fingerprinting technique. Furthermore, since the positioning accuracy of fingerprinting is based on the site survey[1], it needs frequent recalibration, since the environment may change, such as moved furniture, changed lighting fixture, etc. To overcome this challenge, a simple but efficient regeneration of the fingerprint database relying on the Lambertian propagation model was proposed, where only a few number of off-line measurements was required. The experimental results have shown that a mean error as low as 2.2 cm was achieved within a 3.3 m $\times$ 2.1 m room, whilst a mean error of 2.7 cm was attained relying on the regenerated fingerprint database. Moreover, instead of relying on the PD-based UEs, the scenario of the UEs equipped with camera may have a potential of commercializing the visible light positioning. To this end, an indoor visible light positioning system based on optical camera communications (OCC) was conceived in [117], where the position was estimated by analysing the geometrical relationships of the LED images captured by the camera without any angular measurement. Upon relying on under-sampled phase shift keying (PSK), a mean positioning error of 5 cm can be attained for $h = 120$ cm, where h represents the distance between the center of the lens and its projection on

[1]In general, fingerprinting based indoor positioning consists of two stages: the off-line stage and the on-line stage. A location-related database is required to be constructed during off-line stage, so that the classifying algorithm employed at on-line stage can determine the estimate of the object position based on the off-line database. Hence the site survey during off-line stage is vital for the fingerprinting based indoor positioning.

the camera's sensor. Indoor positioning may be readily invoked by a smartphone as the receiver in visible light positioning [118]. However, it may be impractical in terms of either positioning accuracy or speed, since the information carried by visible light has to be extracted with the aid of image processing, which may exceed the computational complexity of the embedded processors used in smartphones [119]. Therefore, to deliver satisfactory positioning performance in terms of positioning speed and accuracy, a novel visible light positioning based on the off-the-shelf smartphone was conceived in [120], where an elaborate flicker-free line coding scheme and a lightweight image processing algorithm were proposed. According to the associated experimental results, the proposed system is capable of supporting real-time indoor navigation, when the moving speed of UEs is upto 5 m/s, associated with an average positioning accuracy of 7.5 cm.

1.3.2 Backhaul Networking for VLC

The idea of integrating PLC and VLC for indoor networking was pioneered by Komine *et al.* [98], which was based on a narrowband PLC channel and a SC binary phase shift keying (BPSK) modulation scheme [98]. They proposed a low-complexity PLC and VLC composition, where the PLC signal was directly transmitted by VLC without demodulation. However, the PLC constitutes a hostile medium, which is affected by various noise types, including the colored background noise and impulsive noise [99]. To deal with harsh transmission environments, using SC modulation may be deemed unsuitable. The ubiquitous OFDM scheme was then employed in PLC to overcome both the impulse noise and multipath effects. The performance of an integrated system relying on narrowband OFDM power line was first analysed in [100]. It was shown that the signal of the integrated system based on OFDM does not affect the illumination, but the BER of the proposed PLC-VLC system is dominated by the performance of the PLC, when the SNR of VLC is sufficiently high. It hence can be concluded that the PLC-VLC system constitutes an attractive indoor communication system. Apart from OFDM modulation, other MC modulation schemes, such as discrete multi-tone (DMT) techniques were also considered in PLC networks, where low-complexity OOK modulation was employed for VLC in the PLC-VLC system conceived [101]. The simulations have shown that the reflections caused by the mismatches throughout the system degraded the performance of PLC-VLC system. The authors have also provided the detailed block diagram of the PLC transmitter, PLC receiver, VLC transmitter and VLC receiver design. Due to the ever-increasing thirst for more data, the narrowband PLC link may become the bottleneck of achieving a higher transmission rate in PLC-VLC networks. Therefore, in [102], a broadband PLC system based on OFDM was proposed, where a transmission rate approaching to 1 Gbits/s was attained.

To further increase the spectral efficiency and QoS, several novel PLC-VLC systems were proposed in [103]. Notably, the authors stated that the latency requirements and synchronization of the LED-APs constituted the main challenges. Furthermore, a novel form of integration was proposed for maximizing system's throughput, relying on the employment of either amplify-and-forward (AF) or decode-and-forward (DF) relays. To be specific, a PLC-VLC system can be viewed as a relay-assisted two-hop communication system without a direct link between the source and the destination, where the LED-APs act as relay nodes. Correspondingly, a hybrid VLC-PLC system was considered in [104] as a relay-assisted two-hop communication system, where the LED-APs retransmit the received PLC signal to the UE via VLC based on DF or AF relaying. To reduce the computational complexity, a chunk-based subcarrier allocation scheme was proposed for this system, where spatial-optical OFDM (SO-OFDM) was invoked. Although the performance of DF is typically better at sufficiently high SNRs, the required signal processing complexity is higher, hence degrading the energy efficiency. Therefore, a novel and cost-effective indoor broadband broadcast system based on the integration of PLC and VLC was proposed in [105]. In order to reduce the complexity of the system, AF was invoked in [105] so that the PLC signal was amplified and forwarded to the LED-APs without decoding, where only a PLC-to-VLC-module was required at each LED-AP for adding the DC bias of optical transmission. According to the experimental results, the channel of the proposed system can be modelled as a multi-path medium, where channel estimation and equalization techniques can be invoked for improving the performance. Furthermore, a simple energy-efficient all-analog PLC-VLC AF system was conceived in [106], where an analog frequency shifter was invoked in the luminary for translating the PLC spectrum to make it compatible with the VLC channel. This was the first time that the SO-OFDM was employed in VLC, where the LED-APs can be divided into groups, where each group can be modulated by a different filtered OFDM signal so that the PAPR was reduced.

Given the attractive characteristics of PLC-VLC networks, such as its inexpensive, flexible and implementation, numberous researchers have focussed their attention on its applications or considered the system in more practical scenarios. To be specific, the PLC-VLC network relying on broadband PLC was also investigated in aircraft scenarios [107], where the LED-APs were uniformly distributed so that no blind spot existed in the entire cabin area. The simulation results have shown that the overall capacity of the integrated system was bounded by the performance of PLC, where better cables and accurate impedance matching may allow higher bit rates. Since hospitals try to avoid RF radiation, the PLC-VLC system constitutes an attractive candidate access network in this scenario, which was considered in [108], where a 48 Mbs data rate was supported within a bandwidth of 8 MHz in the laboratory. Moreover, in an indoor scenario, the data transmission is often combined with navigation services. The authors of [109] proposed a PLC-VLC system, which can simultaneously support multiple services relying on bit

division multiplexing. The results have shown that the overall transmission rate of the PLC-VLC system was higher than that of conventional time division multiplexing under the same condition. Instead of relying on white LEDs, multi-color LEDs were considered in a PLC-VLC network for increasing the transmission rate [110]. To be specific, quadrature phase shift keying (QPSK) combined with OFDM was utilized over the PLC channel, while CSK was employed for transmission over the VLC channel, where the matching of the OFDM constellation used for the PLC channel to the CSK constellation of the VLC channel was solved.

Additionally, the research of resource allocation designed for PLC-VLC networks is also important. Specifically, the power allocation of the PLC-VLC system was investigated in [111], where the power allocation problem was formulated for a communication scenario in which data is transferred through a cascaded PLC/VLC channel in parallel to an RF channel. The achievable rate of a single UE was maximized by the proposed algorithm, which jointly decided the power allocation of each subcarrier in PLC, VLC and RF. The authors quantified the achievable rate improvement thanks to the optimal power levels compared to an equal power allocation strategy. As an extension, the effect of PLC backhauling in multi-user VLC/RF networks was studied in [97], where the optimal power and subcarrier allocation strategy were obtained by the proposed algorithm. In particular, the benefits of PLC backhauling were observed, where the authors found that 1) if the PLC acts as the backhaul of VLC, the performance of the PLC network tends to limit the overall network performance; 2) the maximum available transmit power of the PLC source plays a significant role in improving the VLC network performance; 3) the PLC network's performance and the maximum achievable rates of VLC are tightly correlated and leave to be jointly improved for meeting the required QoS. However, the transmit power constraints were only considered for the VLC network. Furthermore, in the proposed hybrid system composed of a cascaded PLC/VLC link in parallel to an RF wireless link, the transmission power minimization problem was investigated in [92] under a pre-defined QoS constraint, with the aid of the proposed power allocation strategy. The simulation results demonstrated the superiority of the achievable rate of the proposed hybrid system compared to the RF system. However, only a single-UE scenario was investigated and the power constraint of both PLC and VLC were separately considered.

1.4 Thesis Outline and Novel Contributions

1.4.1 Outline of the Thesis

In this thesis, the focus is on the UC-VLC network design of multi-user scenarios, including the network association, resource allocation and MA design. Furthermore, to

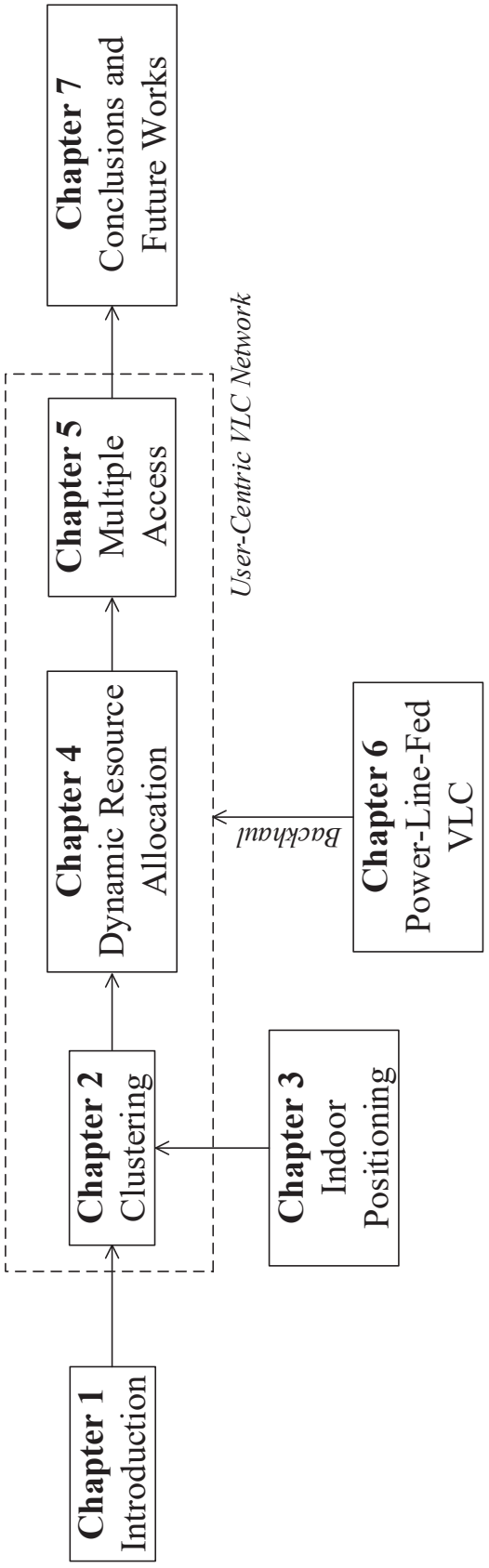

Figure 1.2: Organization of the thesis.

conceive a practical system, VLC-aided positioning and the PLC backhauling are also considered. To begin with, let us now highlight the outline of this thesis, which is portrayed in Fig. 1.2.

▷ **Chapter 2:** User-Centric Clustering

In Chapter 2, motivated by the concept of UC-VLC, we propose a novel UE-AP association based on a centre-shifting UC-clustering strategy. To begin with, the VLC propagation channel is introduced in Section 2.2, where both the LoS and the non-line-of-sight (NLoS) rays are considered. Additionally, the family of MC modulation schemes and their clipping-distortion are investigated, including a rudimentary introduction to multi-user transmission. Section 2.3 presents the review of classic UE-AP association strategies, which we divide into two categories, namely the NC-clustering and the UC-clustering. Upon analysing the pros and cons of these clustering strategies, a novel UC-clustering strategy is proposed in Section 2.4, where the clusters constructed are iteratively updated according to the UEs' location information. We refer to this as the centre-shifting UC-clustering. The superiority of our proposed clustering strategy is characterized in Section 2.5, considering both the idealized no-clipping-distortion and the clipping-distortion scenarios.

▷ **Chapter 3:** VLC-Aided Indoor Positioning

Since the UC-clustering strategy proposed in Chapter 2 requires the knowledge of the UEs' location, a hybrid indoor positioning algorithm relying on visible light is proposed in Chapter 3, striking a trade-off between the positioning accuracy attained and the complexity imposed. Section 3.2 reviews the classic indoor positioning techniques, such as proximity, triangulation and scene analysis. In Section 3.3, we analyse the feasibility of the indoor positioning relying on VLC, which provides an attractive solution for indoor positioning. Upon analysing the visible light positioning assisted by triangulation and fingerprinting, respectively, hybrid positioning is proposed for visible light positioning in Section 3.4. We quantify the performance of the hybrid positioning in terms of its positioning performance and the achievable throughput, where the metrics of accuracy, robustness and scalability are invoked for evaluating the positioning performance.

▷ **Chapter 4:** Dynamic Resource Allocation

After accomplishing the UE-AP association based on the UC-clustering strategy proposed in Chapter 2, we further study the resource allocation in our UC-VLC system for the sake of increasing the throughput. This is achieved by the proposed dynamic resource allocation algorithm, taking into account a range of practical constraints. To be specific, Section 4.2 analyses four practical considerations in the UC-VLC system, namely the LED's imperfections, backhauling, adaptive

modulation-mode assignment and finally, the flexibility of the system. Then the constrained resource allocation problem is formulated in Section 4.3, where the modulation-mode-related throughput is invoked as our maximization objective. To solve this non-convex problem, a dynamic resource allocation, based on a dynamic-programming algorithm is conceived in Section 4.4, which facilitates the allocation of various modulation-modes to the different UEs, as well as various transmit power levels allocated to the different APs, yielding a high design flexibility. Compared to the optimal exhaustive search algorithm, the complexity of our proposed resource allocation algorithm is significantly lower, which is only increased polynomially, instead of exponentially with the number of UEs.

▷ **Chapter 5:** Multiple Access Design

In the previous chapters, only the classic ACO-OFDM or DCO-OFDM is considered for our VLC system. By contrast, in Chapter 5, an advanced VLC modulation scheme, namely LACO-OFDM is invoked for further boosting the achievable throughput. Section 5.2 reviews the LACO-OFDM modulation scheme and highlights the problems and limitations when the LACO-OFDM is directly employed in our previously constructed UC-VLC system. Therefore, in Section 5.3, a novel clustering strategy is proposed, where both the channel conditions of the UEs and the transmission coverage of the APs are considered, leading to an overlapped UE-AP association structure. To fully harness this overlapped characteristic, NOMA is considered as the MA solution for the resultant VLC system. In Section 5.4, we find that although the overlapping area of several clusters has the potential of mitigating the ICI aided by NOMA, the interference inflicted by the densely deployed APs and UEs may still remain excessive. Therefore, a hybrid NOMA/OMA scheme is proposed in this section, where the TDMA-based scheduling and graph-coloring based FR may be adaptively invoked. To exploit the flexibility of the LACO-OFDM at system-level, a dynamic resource allocation scheme is proposed in Section 5.5, which aims for allocating different layers to different UEs, where for each active layer different modulation-modes may be employed.

▷ **Chapter 6:** Power-Line-Fed VLC Network

In this chapter, we proposed a power-line-fed VLC network, where the source data arriving from the Ethernet is fed into the PLC, which is then forwarded to UEs via VLC. The PLC-VLC system model is detailed in Section 6.2, where OFDM is employed by the broadband PLC link to operate in its hostile communication environment, while NOMA is invoked in the VLC to simultaneously support multiple UEs. In order to optimize the throughput of the PLC-VLC network, a maximization problem is formulated in Section 6.3, considering the practical constraints of both PLC on VLC. Then in Section 6.4, an optimal joint power allocation (JPA)

strategy is conceived for attaining the maximum throughput of the PLC-VLC network, where the power allocation of each PLC subcarrier and that of each UE in VLC can be jointly decided by our proposed algorithm.

▷ **Chapter 7:** Conclusions and Future Research

Chapter 7 summarizes the main findings of the thesis and outlines a range of suggestions for further research.

1.4.2 Novel Contributions of the Thesis

The thesis is based on three published journal paper [121–123] and one submitted journal paper [124]. The novel contributions of this theses are listed as follows.

- By exploiting the position information of UEs, a novel UC-VLC framework relying on our centre-shifting UC-clustering strategy is proposed, which is capable of providing a beneficial UE clustering and UE-AP association. A much higher throughput can be expected when the proposed UC-clustering is employed, compared to the conventional NC-clustering strategies.
- A hybrid positioning technique is conceived for beneficially combining the low-complexity of triangulation based positioning and the high accuracy of fingerprinting. The positioning scheme relying on the proposed technique outperforms both the triangulation and the fingerprinting in terms of its accuracy, robustness and scalability, where a low positioning error at the centimeter-level can be achieved by the hybrid positioning technique operating in a room having the size of $15 \times 15 \times 3$ m^3.
- A multi-user sum-throughput maximization problem is formulated under the realistic considerations of clipping distortion, transmit power restriction and backhaul rate limitation in the constructed UC-VLC system. Since the sum-throughput is calculated by considering the throughput of the individual modulation modes, the modulation-mode assignment is multi-user-dependent, making the maximization problem challenging to solve. Therefore, we conceive an efficient dynamic resource allocation method by dividing the original problem into two sub-problems, where a heuristic dynamic-programming based algorithm is proposed for solving successively these two sub-problems.
- Upon considering that multi-cell connections commonly exist in VLC systems, a novel overlapped clustering strategy is proposed for our LACO-OFDM aided VLC network by considering both the channel conditions of the UEs and the transmission coverage of the APs, yielding a *many-to-many* association structure. Our

results demonstrate that the proposed *many-to-many* association outperforms the *one-to-many* association both in terms of its throughput and outage probability.

- We found that although the overlapping areas of several clusters have the potential of mitigating the ICI aided by NOMA, the ICI imposed by the densely deployed APs and UEs may still remain excessive. To circumvent this problem, a hybrid NOMA/OMA scheme is proposed, where TDMA-based scheduling and graph-coloring based FR may be adaptively invoked, depending on the specific scenarios encountered. Our simulations indicate that the achievable throughput of LACO-OFDM aided UC-VLC relying on the proposed MA design is higher than that of the ACO/DCO-OFDM relying on the merged-cell construction aided by TPC. Furthermore, by invoking our hybrid NOMA/OMA scheme, no limitation is imposed on the number of simultaneously served UEs, which cannot be realized in the merged-cell construction due to the limitations imposed by the TPC employed.

- To fully exploit the flexibility of LACO-OFDM, we aim for allocating different layers to different UEs, where for each active layer different modulation-modes may be employed. These decisions are made on the basis of the prevalent communication conditions and realistic constraints. Hence, a dynamic resource allocation strategy is conceived for maximizing the sum-throughput of the LACO-OFDM aided VLC network under a range of practical constraints, such as the maximum transmit power, the maximum backhaul-rate and the minimum individual UE rates.

- A novel power-line-fed VLC network is conceived in a multi-user NOMA-downlink scenario. Upon analysing the relationship between the PLC as well as the VLC links, we propose a joint power allocation strategy for the PLC-VLC network, where the power can be dynamically allocated to PLC and VLC, according to the specific rate requirements of multiple UEs.

Chapter 2

User-Centric Clustering

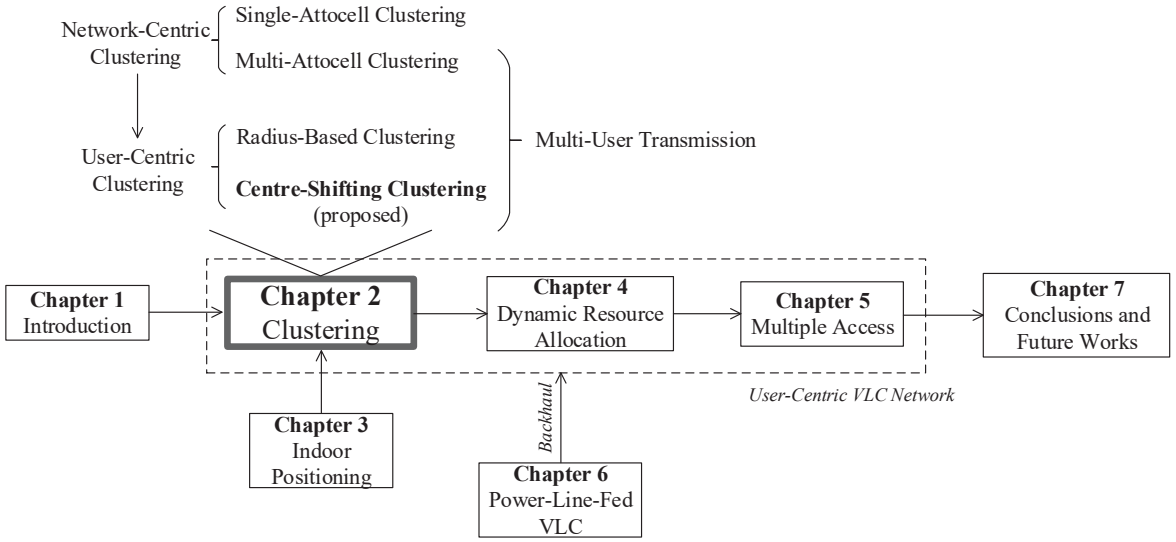

Figure 2.1: Block diagram of Chapter 2.

2.1 Introduction

In VLC, the LED fixtures are employed as APs, which are responsible both for downlink data transmission as well as for illumination. The attocell of VLC is defined as the coverage area of a specific AP. Unlike the cells in RF, the size of attocells is quite small [32]. To guarantee a high downlink transmission quality, the number of APs deployed in VLC networks has to be much higher than that in RF communication, which implies that a given UE may receive multiple rays from various APs. Therefore, simply relying on the *one-to-one* association, where each UE is only associated to a single AP who is capable of providing the strongest RSS, is deemed to be inefficient since it is vulnerable to

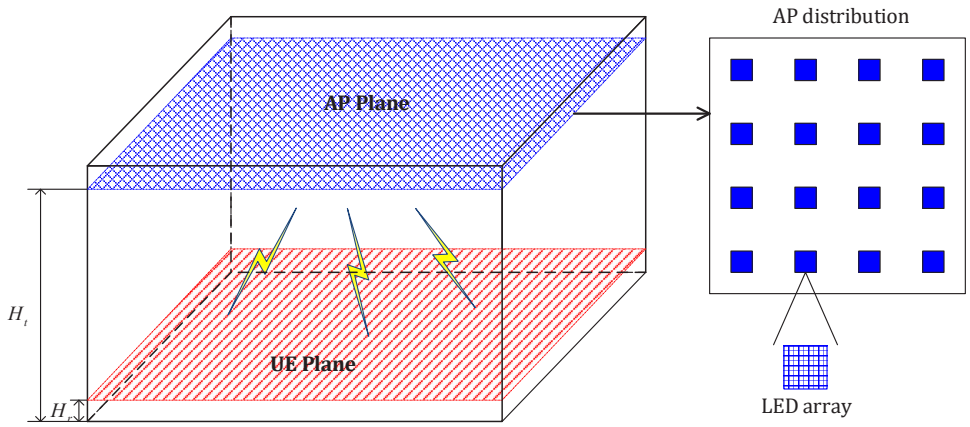

Figure 2.2: An indoor room model for VLC.

severe ICI. Motivated by this, the idea of merging multiple attocells into a larger cluster has been conceived, leading to a multi-AP-multi-UE transmission structure for the VLC network. In this chapter, we depart from the conventional NC-clustering and propose a centre-shifting UC-clustering strategy, which takes into account the UEs' geo-locations, allowing the clusters to have an amorphous boundary. As a benefit, the proposed UC-clustering becomes capable of breathing and reforming when the UEs move, join or leave the system, providing a high-flexibility design.

The remainder of this chapter is organized as follows. Our VLC system model is introduced in Section 2.2, including the VLC propagation channel, our MC modulation scheme as well as the multi-user transmission concept. In Section 2.3, we then review several classic clustering strategies from the perspective of NC and UC clustering. Based on the analysis of those clustering strategies, a centre-shifting UC-clustering is proposed in Section 2.4, which relies on UE set formation and AP set formation. The throughput results of the various clustering strategies are provided in Section 2.5, where both clipping-distortion-free and clipping-contaminated scenarios are considered. Finally, we conclude in Section 2.6.

2.2 System Model

Our VLC system operates in an indoor scenario, where the APs are uniformly installed on the ceiling at a height of H_t, while the UEs are randomly distributed at a height of H_r, resulting in a multi-AP-multi-UE network. As shown in Fig. 2.2, the AP plane and UE plane are parallel, while the single-color-LED arrays based APs and the PD-based UEs face downwards and upwards, respectively. The information is modulated onto the light intensity, so that both illumination and downlink communication is realized simultaneously. Note that a central controller is assumed to monitor the whole room,

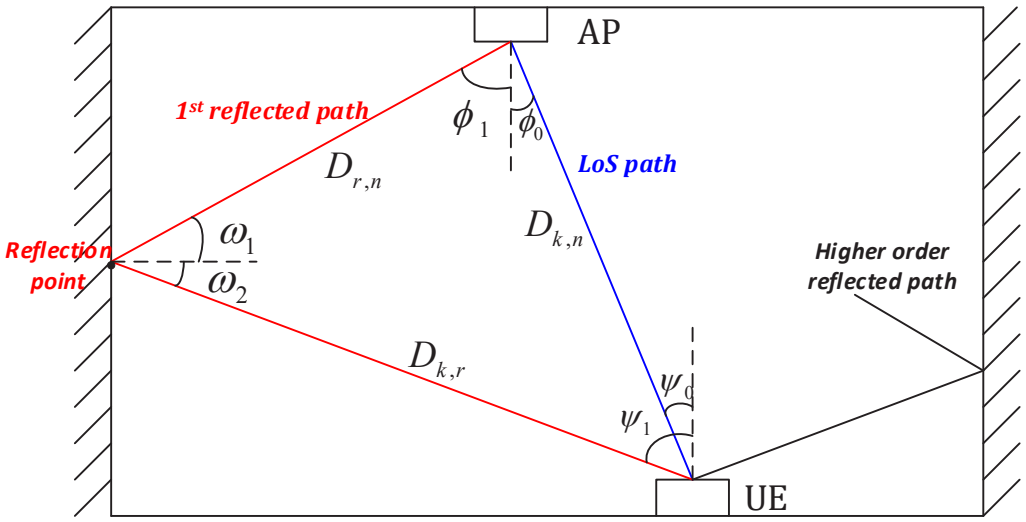

Figure 2.3: A VLC propagation model, including the LoS path, the first reflected path and the higher order reflected path.

which is responsible for information collection, analysis and processing, based on the WiFi uplink feedback.

2.2.1 VLC Propagation

To begin with, the propagation channel in VLC is first introduced in this section. As seen in Fig. 2.3, the VLC channel can be classified into two types: the LoS path and NLoS paths. According to [125], the power received at the UE-end due to the reflected multipath component is demonstrated to be significantly lower than that of the LoS path. To elaborate, the average power received via the first reflected path is only about 10 percent of the average power received via the LoS path, while the power of the higher-order of reflected paths diminishes [6]. Therefore, the contributions of higher-order reflection accompanied by scattering and diffusion may be deemed negligible.

We focus our attention on the propagation based on the LoS path and the first reflected path, where the four walls contribute to the reflections. To elaborate, the LoS channel gain between UE k and AP n is given by [6]:

$$h_{k,n}^{(0)} = \begin{cases} \frac{(\alpha+1)A_s}{2\pi D_{k,n}^2} \cos^{\alpha}(\phi_0) g_{of}(\psi_0) g_{oc}(\psi_0) \cos(\psi_0), & \psi_0 \leq \psi_{FoV}; \\ 0, & \psi_0 > \psi_{FoV}, \end{cases} \tag{2.1}$$

where $\alpha = \ln 2 / \ln[\cos(\phi_{1/2})]$ is the order of Lambertian emission, and $\phi_{1/2}$ denotes the semi-angle at half power. The physical area of a receiver at the UE-end is expressed as A_s, while $D_{k,n}$ denotes the distance between the UE k and AP n. The angle of irradiance

and of incidence in LoS path is represented by ϕ_0 and ψ_0, respectively. Furthermore, $g_{of}(\psi_0)$ and $g_{oc}(\psi_0)$ denote the gain of the optical filter and of the optical concentrator employed. Specifically, $g_{oc}(\psi_0)$ can be written as:

$$g_{oc}(\psi_0) = \begin{cases} \varrho^2/\sin^2(\psi_0), & \psi_0 \leq \psi_{FoV}; \\ 0, & \psi_0 > \psi_{FoV}, \end{cases} \tag{2.2}$$

where ϱ is the refractive index at the UE-end and ψ_{FoV} denotes the FoV at the UE-end.

The channel gain of the first reflected path between UE k and AP n is given by $h_{k,n}^{(1)} = \int_{\text{walls}} dh_{k,n}^{(1)}$, where $dh_{k,n}^{(1)}$ represents the reflection term owing to a small reflection point which is expressed as [6]:

$$dh_{k,n}^{(1)} = \begin{cases} \frac{\rho(\alpha+1)A_s}{2\pi^2 D_{k,r}^2 D_{r,n}^2} dA_{\text{wall}} \cos^{\alpha}(\phi_1) \cos(\omega_1) \cos(\omega_2) g_{of}(\psi_1) g_{oc}(\psi_1) \cos(\psi_1), & \psi_1 \leq \psi_{FoV}; \\ 0, & \psi_1 > \psi_{FoV}, \end{cases} \tag{2.3}$$

where $D_{k,r}$ is the distance between UE k and the reflection point, $D_{r,n}$ is the distance between the reflection point and AP n. The reflective area is denoted by dA_{wall} and ρ is the reflection coefficient. Furthermore, The angle of irradiance and of incidence in the first reflected path is represented by ϕ_1 and ψ_1, respectively, while ω_1 and ω_2 are the angles of irradiance with respect to the reflection point and to the UE.

Finally, in our work, the aggregated optical channel gain between UE k and AP n is calculated by:

$$h_{k,n} = h_{k,n}^{(0)} + h_{k,n}^{(1)}, \tag{2.4}$$

where we assume a single-tap channel response in this thesis since the VLC channel is quasi-static [40]. For simplicity, we assume that the value of $h_{k,n}$ between any UEs and APs can be acquired by the central controller via the Wi-Fi based channel-feedback technique.

2.2.2 VLC Modulation

In VLC, the IM/DD technique is commonly utilized, where only the light intensity is modulated. The IM/DD system requires the modulated signal to be both real and non-negative. To mitigate the undesirable ISI and to attain a high transmission rate, MC based modulation schemes, such as ACO-OFDM [16, 15] and DCO-OFDM [126, 127] have been developed. These two schemes are reviewed in this section, along with the analysis of the LED clipping distortion.

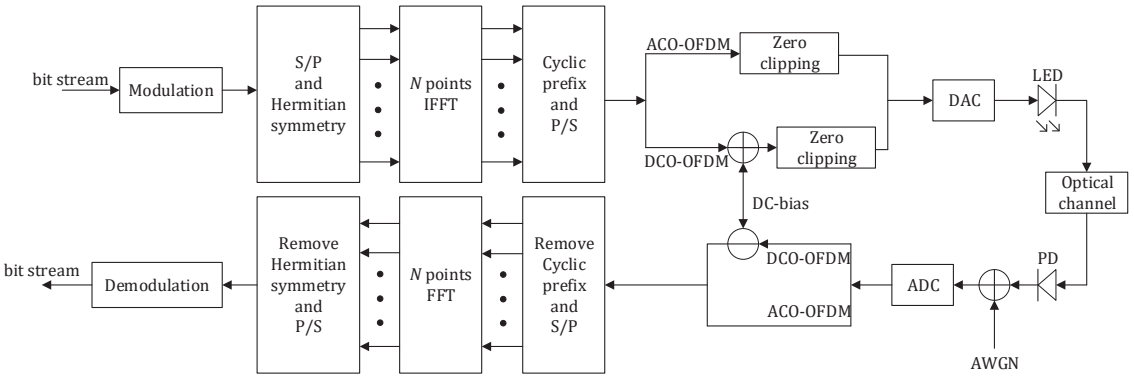

Figure 2.4: A block diagram of the ACO/DCO-OFDM transceiver.

2.2.2.1 Review of ACO/DCO-OFDM Modulation

The classic OFDM signals in RF are complex-valued and bipolar, which are unsuitable for the VLC IM/DD system. Therefore, the Hermitian symmetry is imposed on the subcarriers in the frequency-domain to guarantee having real-valued OFDM signals in VLC [128]. Furthermore, to ensure the positivity of the transmitted signal, a DC-bias is added by the DCO-OFDM scheme. Due to the Hermitian symmetry, the number of data-carrying subcarriers is $N/2$ in DCO-OFDM, where N denotes the total number of subcarreris. As for the ACO-OFDM scheme, the positive transmitted signal is obtained by clipping the real and bipolar signal at zero. The authors of [16] demonstrated that when only the odd-indexed subcarriers are actively invoked for data transmission in ACO-OFDM, the clipping distortion falls on the even-indexed subcarriers, while the data-carrying subcarriers remain free from information loss. However, the number of data-carrying subcarriers is reduced to $N/4$. The schematic of both the ACO-OFDM and DCO-OFDM (ACO/DCO-OFDM) transceiver is depicted in Fig. 2.4. Due to the requirement of DC-bias, the DCO-OFDM has a low power-efficiency, while ACO-OFDM has a low bandwidth-efficiency since only half of the subcarriers are used for payload information transmission.

2.2.2.2 Clipping Distortion of ACO/DCO-OFDM

Given the LED's non-linear characteristic, only a limited linear dynamic range of $[I_L, I_H]$ can be exploited, where I_L and I_H denote the turn-on current and the maximum tolerable AC current, respectively [129]. Due to the linear relationship between current and power, this corresponds to a limited linear power range of $[P_L, P_H]$. Therefore, a carefully designed DC bias P_{bias} has to be added to the modulated signal for the sake of satisfying the LED's forward current requirement, while avoiding overheating of the LEDs. As a result, the signals transmitted by the LEDs will be clipped beyond the dynamic range, leading to undesired clipping distortion and an inevitable BER-degradation.

Explicitly, in the asymmetric structure of the ACO-OFDM signal, the bottom and top clipping level $\varepsilon_{\text{bottom}}$ and ε_{top} are [129]:

$$\varepsilon_{\text{bottom}}^{\text{ACO}} = \max\left(P_L - P_{\text{bias}}, 0\right), \quad \varepsilon_{\text{top}}^{\text{ACO}} = P_H - P_{\text{bias}}, \tag{2.5}$$

while of DCO-OFDM they are [129]:

$$\varepsilon_{\text{bottom}}^{\text{DCO}} = P_L - P_{\text{bias}}, \quad \varepsilon_{\text{top}}^{\text{DCO}} = P_H - P_{\text{bias}}. \tag{2.6}$$

According to the analysis of [130], the clipping distortion variance can be derived by using the statistics of a truncated Gaussian distribution. To be specific, the variance of the clipping distortion engendered by a single LED of the ACO-OFDM signal is expressed as:

$$\begin{aligned}\sigma_{\text{clip,ACO}}^2 =& \frac{P_{\text{Tx,LED}}}{2}\Big\{4\Phi(\lambda_{\text{top}}^{[a]})\lambda_{\text{bottom}}^{[a]} - 2\Phi(\lambda_{\text{top}}^{[a]})\lambda_{\text{top}}^{[a]} - 2\Phi(\lambda_{\text{bottom}}^{[a]})\lambda_{\text{bottom}}^{[a]} \\ &+ 2Q(\lambda_{\text{top}}^{[a]})(\lambda_{\text{top}}^{[a]} - \lambda_{\text{bottom}}^{[a]})^2 + (\lambda_{\text{bottom}}^{[a]2} + 1)\left[1 - 2Q(\lambda_{\text{top}}^{[a]})\right] \\ &- (\lambda_{\text{bottom}}^{[a]2} + 1)\left[1 - 2Q(\lambda_{\text{bottom}}^{[a]})\right] - 4\left[Q(\lambda_{\text{bottom}}^{[a]}) - Q(\lambda_{\text{top}}^{[a]})\right]^2\Big\},\end{aligned} \tag{2.7}$$

where we have:

$$\lambda_{\text{top}}^{[a]} = \frac{\varepsilon_{\text{top}}^{a}}{\sqrt{P_{\text{Tx,LED}}}}, \qquad \lambda_{\text{bottom}}^{[a]} = \frac{\varepsilon_{\text{bottom}}^{a}}{\sqrt{P_{\text{Tx,LED}}}}, \quad \Phi(x) = \frac{\exp(-x^2/2)}{2\pi}. \tag{2.8}$$

Note that the electronic power of a single LED is denoted by $P_{\text{Tx,LED}}$ and $Q(\bullet)$ represents the Gaussian Q-function. Accordingly, the variance of clipping distortion can be expressed in DCO-OFDM as:

$$\begin{aligned}\sigma_{\text{clip,DCO}}^2 =& P_{\text{Tx,LED}}\Big\{\left[Q(\lambda_{\text{bottom}}^{[d]}) - Q(\lambda_{\text{top}}^{[d]})\right]\left[1 - Q(\lambda_{\text{bottom}}^{[d]}) + Q(\lambda_{\text{top}}^{[d]})\right] + \Phi(\lambda_{\text{bottom}}^{[d]})\lambda_{\text{bottom}}^{[d]} \\ &- \left[\Phi(\lambda_{\text{bottom}}^{[d]}) - \Phi(\lambda_{\text{top}}^{[d]}) + \left[1 - Q(\lambda_{\text{bottom}}^{[d]})\right]\lambda_{\text{bottom}}^{[d]} + Q(\lambda_{\text{top}}^{[d]})\lambda_{\text{top}}^{[d]}\right]^2 \\ &- \Phi(\lambda_{\text{top}}^{[d]})\lambda_{\text{top}}^{[d]} + \left[1 - Q(\lambda_{\text{bottom}}^{[d]})\right]\lambda_{\text{bottom}}^{[d]2} + Q(\lambda_{\text{top}}^{[d]})\lambda_{\text{top}}^{[d]2}\Big\},\end{aligned} \tag{2.9}$$

where we have:

$$\lambda_{\text{top}}^{[d]} = \frac{\varepsilon_{\text{top}}^{d}}{\sqrt{P_{\text{Tx,LED}}}}, \qquad \lambda_{\text{bottom}}^{[d]} = \frac{\varepsilon_{\text{bottom}}^{d}}{\sqrt{P_{\text{Tx,LED}}}}. \tag{2.10}$$

The clipping distortion in ACO/DCO-OFDM will further deteriorate the SINR, which inevitably impairs the achievable throughput. Therefore, we will consider this important impairment in our VLC network.

2.2.3 Multi-User Transmission

According to the concept of the UC-VLC relying on clustering, the system may be partitioned into several clusters, where multiple APs are associated with multiple UEs [10]. Within each cluster, the issue of MUI has to be solved, in order to serve the multiple UEs simultaneously. Fortunately, the sophisticated vectorized transmission (VT) philosophy provides an efficient solution by invoking TPC [10], which also reduces the complexity of receivers at the UE-end. By doing so, the multiple APs become capable of simultaneously transmitting MUI-free signals to their associated UEs, without inefficient time/frequency division techniques.

To elaborate, we invoke the ZF based VT at the AP-end for entirely eliminating the MUI. By utilizing the ZF-TPC, the SINR of the kth UE in the cth cluster may be expressed as [121]:

$$\Upsilon_{c,k} = \frac{\gamma^2 \omega_c^2 P_{\text{Tx,elec}}}{\sigma^2_{\text{awgn}} + \gamma^2 P_{\text{Tx,elec}} \sum_{i \in \mathcal{S}_I} h^2_{k,i}}, \tag{2.11}$$

where we have

$$\omega_c = \min_{i=1,\ldots,|\mathcal{C}|} \sqrt{\frac{1}{||\boldsymbol{G}_c(i,:)||^2_F}}, \tag{2.12}$$

where $\boldsymbol{G}_c \in \mathbb{R}^{(|\mathcal{N}_c| \times |\mathcal{K}_c|)} = \boldsymbol{H}_c^H (\boldsymbol{H}_c \boldsymbol{H}_c^H)^{-1}$ is the ZF pre-coding matrix employed in $\mathcal{C}_c$, with $\boldsymbol{H}_c \in \mathbb{R}^{(|\mathcal{K}_c| \times |\mathcal{N}_c|)}$ being the channel matrix for the cluster, where the entry of $\boldsymbol{H}_c$ is based on the aggregated optical channel we introduced in Section 2.2.1. Furthermore, γ is the optical-to-electronic (O/E) conversion efficiency and the variance of additive white gaussian noise (AWGN) is denoted by σ^2_{awgn}, which is dominated by the shot noise and thermal noise at receiver-end. In ACO/DCO-OFDM, the AWGN can be around to $\sigma^2_{\text{awgn}} = N_0 B$, where N_0 is the power spectral density, while B denotes the available bandwidth. Finally, $\mathcal{S}_I$ is the interference set arriving from the APs involved in all clusters, excluding the current cluster $\mathcal{C}_c$.

Taking the influence of clipping distortion into consideration, the SINR of the kth UE in the cluster $\mathcal{C}_c$ is given by:

$$\Upsilon^{\text{clip}}_{c,k} = \frac{\Lambda \omega_c^2 P_{\text{Tx,elec}}}{\sigma^2_{\text{awgn}} + G_{\text{DC}} \omega_c^2 \sigma^2_{\text{clip}} + \Lambda P_{\text{Tx,elec}} \sum_{i \in \mathcal{S}_I} h^2_{k,i}}, \tag{2.13}$$

where we have:

$$\Lambda = \frac{\gamma^2 K^2 G_{\text{DC}}}{G_B^2}. \tag{2.14}$$

	ACO-OFDM	**DCO-OFDM**
no clipping	$\sum_k \frac{B}{4}\log_2(1+\Upsilon_{c,k})$	$\sum_k \frac{B}{2}\log_2(1+\Upsilon_{c,k})$
clipping	$\sum_k \frac{B}{4}\log_2(1+\Upsilon^{\text{clip}}_{c,k})$	$\sum_k \frac{B}{2}\log_2(1+\Upsilon^{\text{clip}}_{c,k})$

Table 2.1: Achievable throughput of ACO/DCO-OFDM.

Note that G_B is the bandwidth utilization factor. Recall from Section 2.2.2.1 that we have $G_B = 1$ for DCO-OFDM, while $G_B = 0.5$ for ACO-OFDM. Furthermore, G_{DC} is the attenuation factor of the useful electrical signal power due to the DC bias, which can be expressed as [129]:

$$G^{\text{aco}}_{\text{DC}} = \frac{\sqrt{2\pi}P_{\text{Tx,elec}}}{\sqrt{2\pi}P_{\text{Tx,elec}} + 4\sqrt{P_{\text{Tx,elec}}}P_{\text{bias}} + 2\sqrt{2\pi}P^2_{\text{bias}}}; \tag{2.15}$$

$$G^{\text{dco}}_{\text{DC}} = \frac{P_{\text{Tx,elec}}}{P_{\text{Tx,elec}} + P^2_{\text{bias}}}. \tag{2.16}$$

Based on Shannon's theorem, the achievable throughput in the cluster $\mathcal{C}_c$ relying on VT in ACO/DCO-OFDM is summarized in Table 2.1.

2.3 Review of Classic Clustering

As a promising member of small-cell based next generation networks, the clustering of multiple APs associated with multiple UEs plays a significant role in VLC, which is reviewed in this section. We consider both regular NC-clustering and sophisticated UC-clustering.

2.3.1 Network-Centric Clustering

The concept of NC-clustering may be readily borrowed from the RF cellular networks. Operating similarly to a BS in RF, each AP in VLC only illuminates a confined cell, which is referred to as an optical attocell. The coverage area of attocells depends not only on the illumination conditions at the AP-end, but also on the FoV at the UE-end. Furthermore, in contrast to the traditional RF cells, the coverage of a single attocell in VLC is restricted to a few metres. An obvious characteristic of NC-clustering is that the shape of the resultant clusters is pre-defined, leading to a network having a fixed cluster-boundary. In multi-AP-multi-UE VLC networks, the issue of ICI cannot be neglected, when using NC-clustering. To elaborate, we can aim either for single-attocell clustering or multi-attocell clustering. More details are provided as follows.

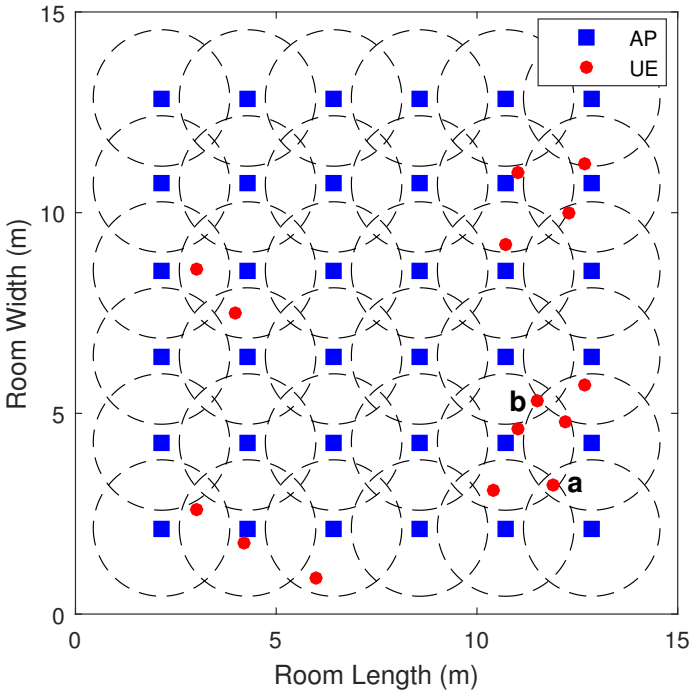

Figure 2.5: Single-attocell NC-clustering relying on unity frequency reuse (UFR), where the cluster boundaries are depicted by dashed lines.

2.3.1.1 Single-Attocell NC-Clustering

The most straightforward method of constructing NC-clusters is to simply consider each attocell as an individual cluster, as seen in Fig. 2.5. However, the ICI imposed on the overlapping areas of attocells, is quite damaging. To elaborate, the UE **a** of Fig. 2.5 is located in an area, which is overlapped by four APs. This situation results in serious ICI impairment. Furthermore, due to the pre-defined cluster boundary, the association of UE **b** is difficult to ascertain, leading to the potential association-blurring issue. Since the UEs are randomly distributed in the room, some clusters may have to serve more than one UE, while some of them have no target UEs, resulting in an unbalanced loading. For the clusters serving multiple UEs, an additional scheduler may be required to deal with the *one-to-many* transmission.

To control the ICI, instead of employing radical the UFR in the NC-VLC constructed above, a higher FR factor τ (FR-τ) may be invoked for alleviating the ICI. Let us consider the four attocells at the south-east corner of Fig. 2.5 as an example, and use the FR-2 scheme. As shown in Fig. 2.6, the attocells **A** and **D** utilize the frequency range f_1 having the bandwidth of $B/2$, while cluster **B** and **C** use the frequency range f_2 with the other half of the bandwidth. In contrast to the UE **a** of the scenario of Fig. 2.5, where three other attocells impose ICI, the ICI imposed on UE **a** in FR-2 of Fig. 2.6 only

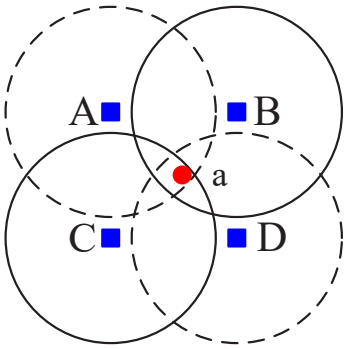

Figure 2.6: A demonstration of ICI reduced by FR-2, where the clusters assigned by frequency range f_1 is indicated by the dashed circles, while the clusters with frequency range f_2 is depicted by the solid circles.

comes from a single attocell, which can be further reduced upon increasing τ. However, we have to bear in mind that a higher factor τ degrades the bandwidth efficiency.

2.3.1.2 Multi-Attocell NC-Clustering

Thanks to the development of multi-user transmission, as introduced in Section 2.2.3, we can now design a cluster based on multi-AP-multi-UE transmission. Therefore, instead of treating a single attocell as a cluster, the multi-attocell NC-clustering (NC-ζ) is conceived by jointly merging several attocells into a larger cluster, so that the grouped multiple UEs can be simultaneously served by multiple APs with the aid of VT transmission. For example, as shown in Fig. 2.7, the network is divided into four clusters by pre-defined boundaries having multi-AP-multi-UE transmission within each of the clusters. We refer to this scheme as NC-4. Although the ICI may be mitigated in this manner compared to the single-attocell NC-clustering, the issue of association-blurring and unbalanced-loading remains unsolved. To elaborate a little further, since the location information of UEs is not considered during the NC-clustering, the association of UE **c** is again unclear. Furthermore, it may be observed that AP **A**, **B** and **C** are much closer to UE **c** and **d**, yet they are not in the same cluster. Instead, those three APs have to use a higher transmit power to serve the UEs in the same cluster, although the distance between them is large, resulting in a strong ICI imposed on UE **c** and **d**. Furthermore, by employing VT, the maximum number of UEs which can be served simultaneously depends on the number of APs in the same cluster. If the clusters have an insufficient number of APs, scheduling has to be employed.

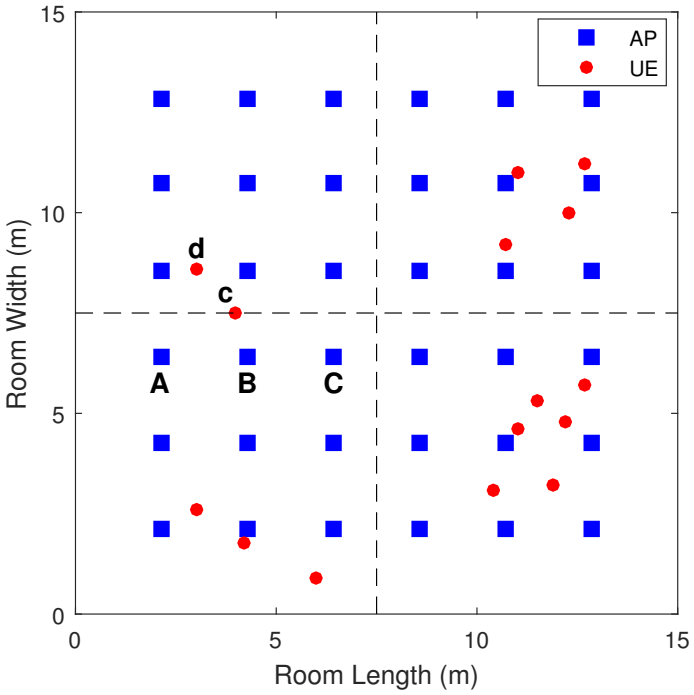

Figure 2.7: NC-4 based on multi-attocell strategy, where the cluster boundaries are depicted by dashed lines.

2.3.2 User-Centric Clustering

By observing the NC-clustering, it can be inferred that purely relying on the AP arrangement, while ignoring the UE's location, when forming clusters is inefficient. Therefore, against the above-mentioned NC-clustering philosophy, the UC-clustering regime has been proposed upon considering the position of UEs[1]. A clear difference with respect to NC-clustering is that the UC-clusters are not pre-defined and fixed, which is adapted according to the specific UE distributions. To elaborate, a classic UC-clustering termed as radius-based UC-clustering is introduced in this section.

As a preliminary, we first introduce some common notations. We let $\mathcal{C}$ be the specific set hosting all clusters, where for the cth cluster $\mathcal{C}_c$, it consists of $|\mathcal{N}_c|$ APs hosted in the set $\mathcal{N}_c$, associated with $|\mathcal{K}_c|$ UEs in the set $\mathcal{K}_c$. To obtain the UC-clusters, a full channel matrix $\boldsymbol{H} \in \mathbb{R}^{(|\mathcal{K}|\times|\mathcal{N}|)}$ is acquired, where the $[k,n]$th entry of $\boldsymbol{H}$ is given by $h_{k,n}$. For guaranteeing the QoS, the central controller assigns each UE to the unique AP before clustering, which provides the globally best link, referring to as its anchoring AP. The AP anchoring process is carried out as follows:

[1]Here we assume that the position of UEs is known by the central controller, where the detailed indoor positioning techniques will be investigated in Chapter 3.

1. A rejected UE set $\mathcal{K}^r$ is defined to hold all the UEs whose association requests have been rejected by APs, which is initialized as $\mathcal{K}^r = \mathcal{K}$.

2. The central controller attempts to associate each UE k in the set $\mathcal{K}^r$ to its candidate anchoring AP n_k, namely to the one which can offer the strongest channel gain to it and has not been rejected before. Note that if a UE has equal channel gains with respect to more than one AP, it is randomly assigned to one of them.

3. If an AP receives more than one association request, the central controller only allows it to become associated with one of the UEs and reject the others. Specifically, the association conflict occurs when $n_k = n_f$. The central controller then searches the matrix $\boldsymbol{H}$ again to find their second preference, n'_k and n'_f. If $[\boldsymbol{H}_{(k,n_k)}] + [\boldsymbol{H}_{(f,n'_f)}]$ is higher than $[\boldsymbol{H}_{(k,n'_k)}] + [\boldsymbol{H}_{(f,n_f)}]$, the AP is allowed to be associated with UE k, while UE f is referred to $\mathcal{K}^r$.

4. The successfully associated UEs are hence removed from $\mathcal{K}^r$. The central controller re-processes the remaining UEs in $\mathcal{K}^r$ by repeating Step 2 and 3, until each UE $k \in \mathcal{K}$ becomes assigned to an anchoring AP, or becomes rejected by all preferred APs.

By doing so, the exclusive UE-AP pairs are obtained, ensuring that all the UEs in $\mathcal{K} \setminus \mathcal{K}^r$ are potentially to be served at least by its own anchoring AP n_k. Note that if we end up with $|\mathcal{K}^r| \neq 0$, a small number of UEs fail to become associated with any APs, which are termed as un-assigned UEs. Those un-assigned UEs can be re-scheduled with high priority in the coming time-slots, which is beyond the scope of this section.

The UC-clustering strategy takes the location of UEs into account. More particularly, the UEs associated with their anchoring APs are jointly grouped into a large cluster based on a pre-defined maximum radius r. The procedure is as follows:

1. Initialise the cth cluster $\mathcal{C}_c = \{\emptyset\}$, where c is initialised to 1.

2. We commence by forming cluster $\mathcal{C}_c$ upon recruiting the first UE k^*, who is selected randomly and has not been included in any clusters, along with its anchoring AP n_{k^*}. Hence, the UE is held in set $\mathcal{K}_c$, where its anchoring AP n_{k^*} is held in set $\mathcal{N}_c$.

3. Recruit another UEs from the set of hitherto un-clustered UEs, who has a distance shorter than r from the UE k^* in the cluster $\mathcal{C}_c$. Then update the cluster $\mathcal{C}_c$, resulting in the expanded set of $\mathcal{K}_c$ and $\mathcal{N}_c$.

4. The clustered UEs will be taken no further considerations. If there are still UEs do not belong to any clusters, we increase c and repeat Step 3 and 4.

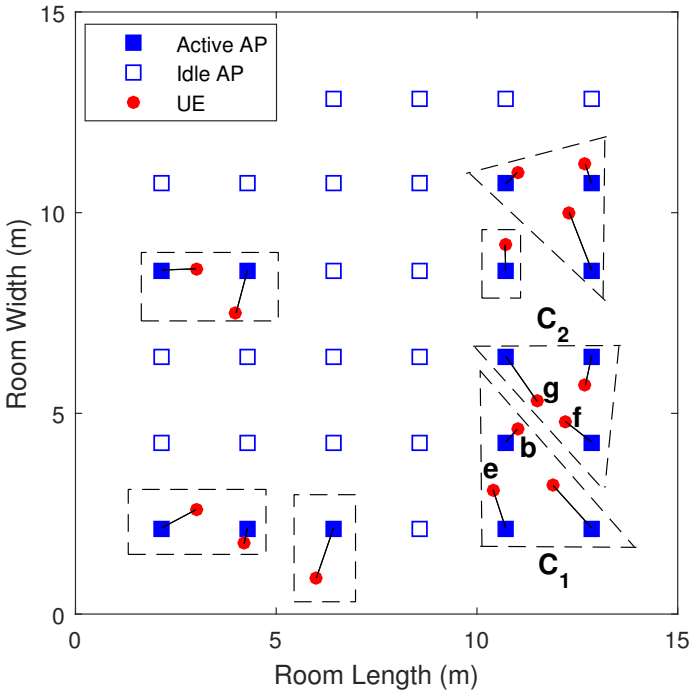

Figure 2.8: Radius-based UC-clustering, where the solid lines represent the association between the UEs and their anchoring APs, while the dashed lines denote the amorphous cluster-boundaries.

As a result, the UC-clusters constructed exhibit amorphous boundaries, which relies on the UE distribution. The corresponding UC-clusters are presented in Fig. 2.8, whilst relying on the same UE distribution as we introduced in the previous sections. As we can see, we have five UC-clusters, where the number of APs equals to the number of UEs. As a benefit, no additional scheduling is required, and the VT concept can be invoked to handle the multi-AP-multi-UE transmission. Since the UC-clusters are constructed by exploiting the knowledge of UE positions, no association-blurring will be imposed. Furthermore, the un-anchored APs can be switched off and set to idle mode. On the one hand, this arrangement is power efficient, since no transmissions are required from them. On the other hand, by switching off some of the APs, the ICI can be significantly reduced. However, the performance of the radius-based UC-clustering strongly depends on the selection of the first UE, when constructing every cluster. For example, the construction of cluster $\mathbf{C}_1$ is implemented by 'recruiting' UE **e** as the starting point. In fact, UE **b** of cluster $\mathbf{C}_1$ is closer to UE **f** and **g**, which are however assigned to cluster $\mathbf{C}_2$. It can be inferred that the ICI between cluster $\mathbf{C}_1$ and $\mathbf{C}_2$ is strong, which may degrade the performance of UC-clustering. Unfortunately, the starting point of each cluster in this strategy is based on random selection, which may be the bottleneck.

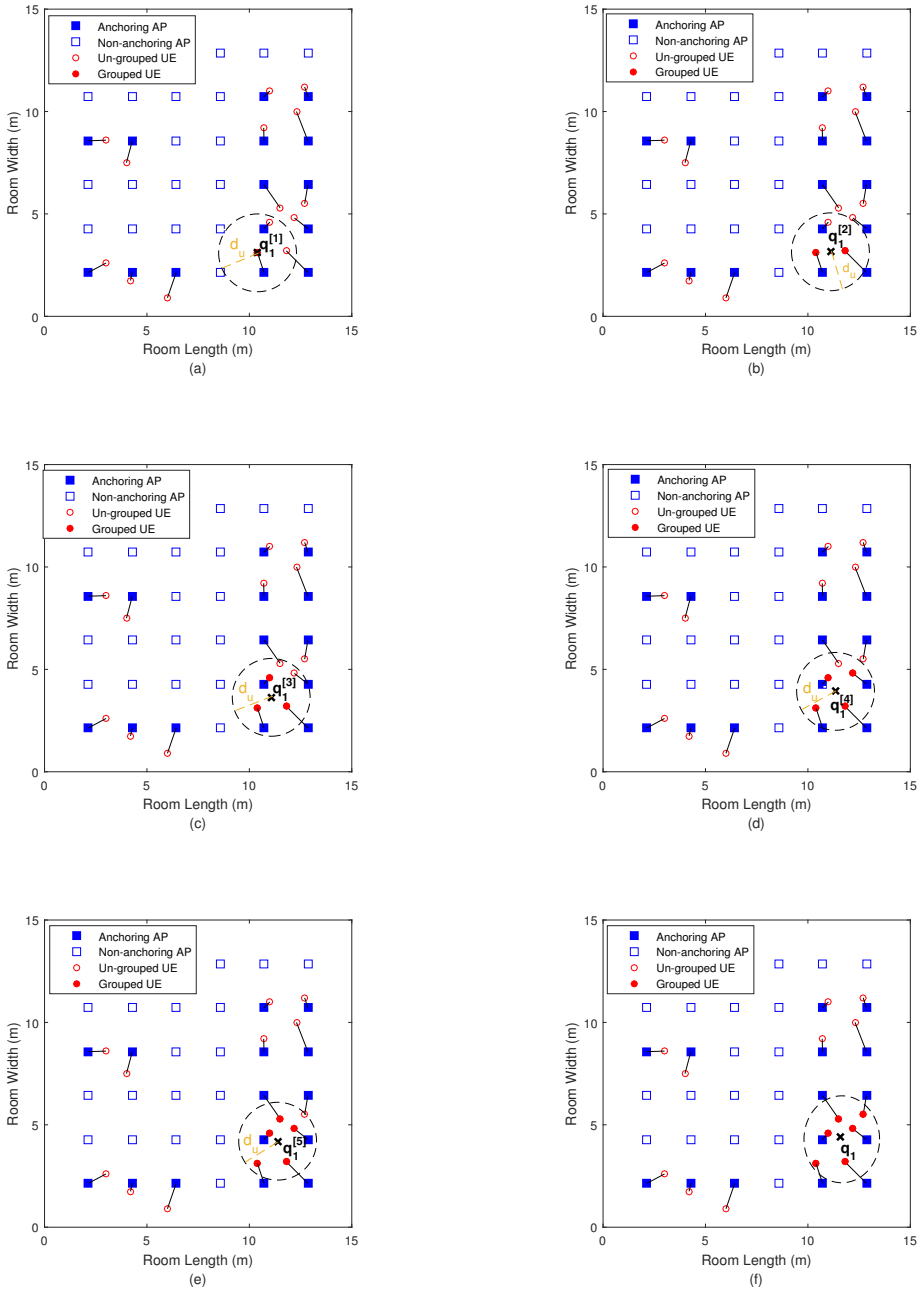

Figure 2.9: A demonstration of UE set construction based on the proposed centre-shifting UC-clustering strategy, where the black cross marker "×" indicates the tentative centre of the current constructed cluster.

2.4 Centre-Shifting UC-Clustering

To further promote the employment of UC-clustering, in this section, an improved UC-clustering strategy is conceived. Recall from Section 2.3.2 that the performance of the radius-based UC-clustering relies on a starting point, which is also the centre of the

cluster. The disadvantage of this is that strong ICI may be imposed. To circumvent this, we propose a dynamic UC-clustering strategy, where the centre of the constructed cluster is not fixed. Specifically, after determining the exclusive UE-AP pairs based on the anchoring process, the proposed UC-clustering is continued by the UE set formation, followed by the AP set formation. We refer to this technique as the centre-shifting UC-clustering.

2.4.1 UE Set Formation

To facilitate the adjustment of the UC-cluster's size, we pre-define a cluster size controller parameter d_u, which represents the maximum distance between the cluster centre and its candidate UEs. Note that all the UEs that do not belong to any of the constructed UE set are by definition part of the idle UE set $\mathcal{K}^\circ$, which is initialised as $\mathcal{K}^\circ := \mathcal{K}$. As shown in Fig. 2.9, the UEs in the idle UE set are represented by hollow circles. To begin with, the first UE $\tilde{k}_1$ considered for constructing the first UE set $\mathcal{K}_1^{[1]}$ is randomly selected from the set $\mathcal{K}^\circ$. As a demonstration, we choose UE **e** as the starting point for constructing $\mathcal{K}_1$, which is also the centre point of cluster $\mathbf{C}_1$ of the radius-based UC-clustering portrayed in Fig. 2.8.

Accordingly, the initial cluster centre of the first set $q_1^{[1]}$ is assigned the coordinate of the UE $\tilde{k}_1$ denoted by $(x_{\tilde{k}_1}, y_{\tilde{k}_1})$, which can be found in Fig. 2.9(a). Note that the centre is tentative and will be updated later according to the position of included UEs at later stages. Next, the set is iteratively expanded by including UE $k^\star \in \mathcal{K}^\circ$, which is located within a distance of d_u from the tentative centre, hence satisfying the distance condition of:

$$k^\star = \arg\min_{k \in \mathcal{U}^\circ} \left\{ \mathbf{d}(k, q_1^{[i]}) \leq d_u \right\}, \quad i = 1, 2, \cdots \tag{2.17}$$

where $\mathbf{d}(k, q_1^{[i]})$ denotes the Euclidean distance between UE k and the tentative centre, which can be calculated as:

$$\mathbf{d}(k, q_1^{[i]}) = \sqrt{(x_k - x_{q_1^{[i]}})^2 + (y_k - y_{q_1^{[i]}})^2}, \tag{2.18}$$

where $x_{q_1^{[i]}}$ and $y_{q_1^{[i]}}$ represent the coordinates of the tentative centre $q_1^{[i]}$. If there are more than one UE satisfying the condition of (2.17) during a specific iteration, only one of them can join this set, which is randomly selected. Note that the newly included UE $k^\star$ has to be removed from the set $\mathcal{K}^\circ$ after each iteration. As a result of the ith iteration, the expanded UE set can be formulated as $\mathcal{K}_1^{[i+1]} = \mathcal{K}_1^{[i]} \cup \{k^\star\}$, where $\mathcal{K}_1^{[i]}$ and $\mathcal{K}_1^{[i+1]}$ represent the current UE set and the set expanded during this iteration. Once we

arrive at $\mathcal{K}_1^{[i+1]} \neq \mathcal{K}_1^{[i]}$, the tentative centre is updated correspondingly as:

$$q_1^{[i+1]} = \left(\frac{x_{q_1^{[i]}} + x_{k^\star}}{2}, \frac{y_{q_1^{[i]}} + y_{k^\star}}{2} \right). \tag{2.19}$$

By repeatedly checking Eq. (2.17) until no more UEs can be included in the current

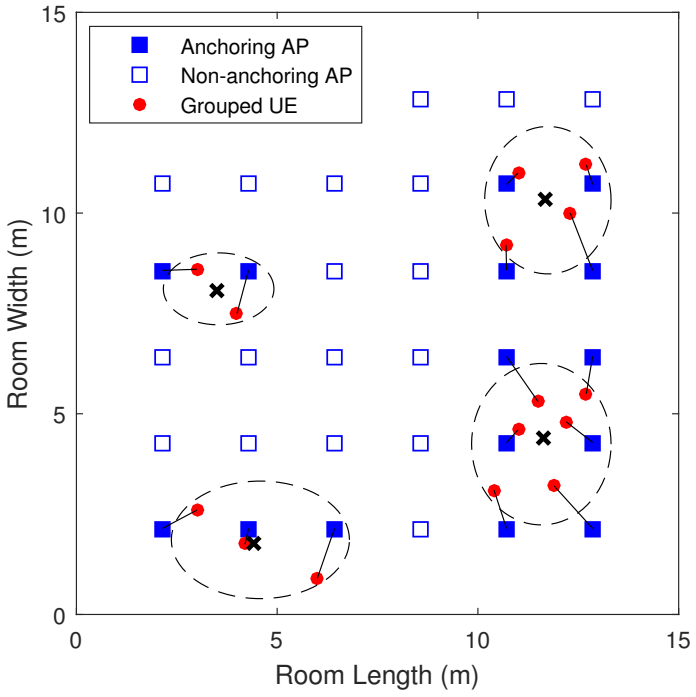

Figure 2.10: Constructed UE set based on the centre-shifting UC-clustering, according to the same UE distribution we utilized before, where the ultimate cluster centres are indicated by the black cross markers.

UE set, it can be concluded that the formation of the set $\mathcal{K}_1$ is completed, where its ultimate centre q_1 can be obtained by averaging the locations of all UEs in the set $\mathcal{K}_1$. This process is demonstrated in Fig. 2.9. For the same UE distribution, all six UEs are clustered into a single set, instead of being split into two separate clusters by using the radius-based UC-clustering of Fig. 2.8. Then, the next UE set formation starts following the same strategy, until we end up with $\mathcal{K}^\circ = \emptyset$. As a result, a total of $|\mathcal{C}|$ UE sets can be obtained. Since the cluster centres are updated during every iteration according to the UEs' positions, we term this strategy as the centre-shifting UC-clustering. The result of the UE sets constructed followed by the centre-shifting UC-clustering is presented in Fig. 2.10, where the same UE distribution is considered as in the previous strategies.

2.4.2 AP Set Formation

To complete the construction of UC-clusters, in this section, we focus our attention on the AP set formation, which is also conducted by central controller. Firstly, for each constructed UE set, the corresponding AP anchoring set $\mathcal{N}_c^{\dagger}$ is given by:

$$\mathcal{N}_c^{\dagger} = \{n_k : k \in \mathcal{K}_c\}. \tag{2.20}$$

The idle AP set $\mathcal{N}^{\circ}$ is defined as the one that holds all the remaining APs, which are exclusive to any of the sets $\mathcal{N}_n^{\dagger}$. In order to enhance the transmission performance attained, the expanded AP set for the cth cluster as $\mathcal{N}_c^{\ddagger}$ tries to include the APs in $\mathcal{N}^{\circ}$ located within a pre-defined AP distance threshold d_a from its ultimate cluster centre q_c. Therefore, the set $\mathcal{N}_c^{\ddagger}$ is obtained as:

$$\mathcal{N}_c^{\ddagger} = \left\{n : \ \arg_{n \in \mathcal{N}^{\circ}} \mathbf{d}(n, q_c) \leq d_a\right\}. \tag{2.21}$$

For a total of $|\mathcal{C}|$ sets, the set $\mathcal{N}^{\ddagger} = \bigcup_{c=1}^{|\mathcal{C}|} \mathcal{N}_c^{\ddagger}$ can be accordingly acquired. Note that only the unique APs in the set $\mathcal{N}^{\ddagger}$ are kept, while those duplicate ones are removed. This is because the duplicate APs are occupied by more than one cluster, leading to transmission conflict. As a result, the cth AP set is constructed by combining its anchoring set and the associated expended set as:

$$\mathcal{N}_c = \mathcal{N}_c^{\dagger} \cup \mathcal{N}_c^{\ddagger}. \tag{2.22}$$

The AP set formation process is demonstrated in Fig. 2.11(a). Note that if an AP in $\mathcal{N}_c$ has no channel links to all the UEs in its corresponding UE set $\mathcal{K}_c$, it has to be removed from $\mathcal{N}_c$. The remaining APs, which do not belong to any AP set $\mathcal{N}_c$ will be switched off in current time-slot for the sake of power saving.

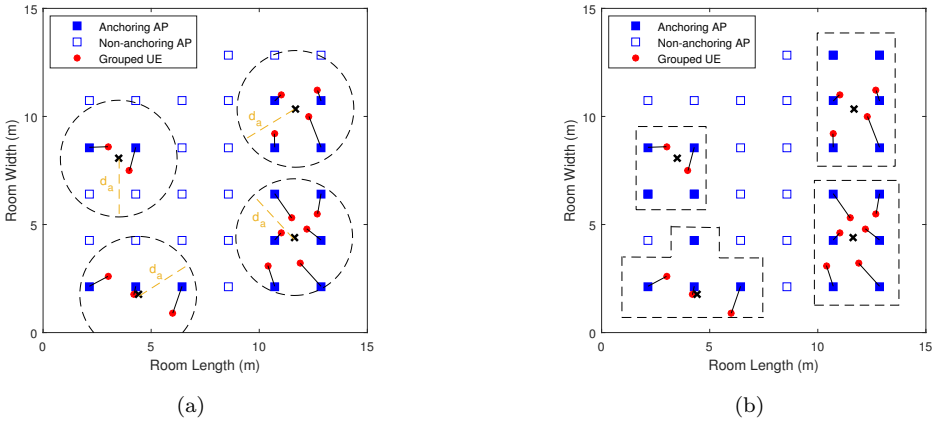

Figure 2.11: (a) presents the AP set formation; (b) demonstrates the resultant centre-shifting UC-clusters.

Algorithm 1 Centre-Shifting UC-Clustering

Input: The location information of all APs and UEs, as well as the association pairs after anchoring.

Require: I: UE Set Formation

Initialisation: $c = 1$, $i = 0$, $\mathcal{K}^{\circ} = \mathcal{K}$.
while $\mathcal{K}^{\circ} \neq \emptyset$ **do**
  $\mathcal{K}_c^{[i]} = \emptyset$,
  $\mathcal{K}_c^{[i+1]} = \{\tilde{k}_n : \text{rand}(k),\ k \in \mathcal{K}^{\circ}\}$,
  $q_c^{[i+1]} = (x_{\tilde{k}_c}, y_{\tilde{k}_c})$;
  while $\mathcal{K}_c^{[i+1]} \neq \mathcal{K}_c^{[i]}$ **do**
    $\mathcal{K}^{\circ} = \mathcal{K} \setminus \mathcal{K}_c^{[i+1]}$,
    $\mathcal{K}_c^{[i]} = \mathcal{K}_c^{[i+1]}$;
    $k^{\star} = \arg\min_{k \in \mathcal{K}^{\circ}} \mathbf{d}(k, q_c^{[i+1]})$;
    if $\mathbf{d}(k^{\star}, q_c^{[i+1]}) \leq d_u$ **then**
      $i = i + 1$;
      $\mathcal{K}_c^{[i+1]} = \mathcal{K}_c^{[i]} \cup \{k^{\star}\}$,
      $q_c^{[i+1]} = \left(\frac{x_{q_c^{[i]}} + x_{k^{\star}}}{2}, \frac{y_{q_c^{[i]}} + y_{k^{\star}}}{2}\right)$;
    end if
  end while
  $\mathcal{K}_c = \mathcal{K}_c^{[i+1]}$, $q_c = q_c^{[i+1]}$, $c = c + 1$;
end while

Require: II: AP Set Formation

Initialisation: $\mathcal{N}^{\circ} = \mathcal{N} \setminus \mathcal{N}^{\dagger}$;
for $c = 1 \to |\mathcal{C}|$ **do**
  $N_c^{\dagger} = \{n_k :\ k \in \mathcal{K}_c\}$,
  $N_c^{\ddagger} = \{n :\ \arg_{n \in \mathcal{N}^{\circ}} \mathbf{d}(n, q_c) \leq d_a\}$;
end for
Remove the duplicated APs in $\mathcal{N}^{\ddagger} = \bigcup_{c=1}^{|\mathcal{C}|} \mathcal{N}_c^{\ddagger}$, and update $\mathcal{N}_c^{\ddagger},\ \forall c$ accordingly;
for $c = 1 \to |\mathcal{C}|$ **do**
  $\mathcal{N}_c = \mathcal{N}_c^{\dagger} \cup \mathcal{N}_c^{\ddagger}$,
  $\mathcal{N}_c = \mathcal{N}_c \setminus \{n \in \mathcal{N}_c :\ \sum_{k \in \mathcal{K}_c} [\boldsymbol{H}_n]_{(k,n)} = 0\}$,
  $\mathcal{C}_c = \{\mathcal{K}_c,\ \mathcal{N}_c\}$;
end for

2.4.3 UC-Clusters

By amalgamating $\mathcal{K}_c$ and its corresponding $\mathcal{N}_c$, the UC-cluster $\mathcal{C}_c$ is deemed to have been successfully constructed. Hence, we have

$$\mathcal{C}_c = \{\mathcal{K}_c, \mathcal{N}_c\},\ \mathcal{K}_c \cap \mathcal{K}_l = \emptyset,\ \mathcal{N}_c \cap \mathcal{N}_l = \emptyset, \quad \Big(c \neq l,\ \forall n, l \in \{1, 2, \cdots, |\mathcal{C}|\}\Big) \tag{2.23}$$

$$\Big\{\mathcal{K}_c : c = 1, 2, \cdots, |\mathcal{C}|\Big\} \subseteq \mathcal{K}, \tag{2.24}$$

$$\Big\{\mathcal{N}_c : c = 1, 2, \cdots, |\mathcal{C}|\Big\} \subseteq \mathcal{N}. \tag{2.25}$$

I-1. Environment-Related Parameters	
room size	$15\times15\times3$ m^3
AP height H_t	2.5 m
number of APs $\lvert\mathcal{N}\rvert$	6×6
LED array per AP	8×8
UE height H_r	0.85 m
number of UEs $\lvert\mathcal{K}\rvert$ (change in Fig. 2.13, 2.14, 2.16)	25
I-2. VLC Channel-Related Parameters	
semi-angle at half-illumination $\phi_{1/2}$	60^o
gain of optical filter $g_{of}(\psi)$	1
gain of optical concentrator $g_{oc}(\psi)$	1
physical area for a PD receiver A_s	1 cm^2
reflection coefficient ρ	0.75
refractive index ϱ	1.5
O/E conversion efficiency γ	0.53 A/W
FoV ψ_{FoV} (change in Fig. 2.12, 2.15)	95^o
I-3. Physical-Link-Related Parameters	
modulation bandwidth B	20 MHz
AWGN power spectral density N_0	10^{-22} A^2/Hz
transmit power $P_{\text{Tx,elec}}$ (change in Fig. 2.14)	1 W
DC bias in DCO-OFDM P_{bias} (change in Fig. 2.17)	10 mW
limited linear power range $[P_L, P_H]$	[1 mW, 30 mW]
I-4. Clustering-Related Parameters	
FR factor τ in single-attocell NC-clustering	2
radius r in radius based UC-clustering	4 m
UE distance threshold d_u in centre-shifting UC-clustering (change in Fig 2.14)	2 m
AP distance threshold d_a in centre-shifting UC-clustering	3 m

Table 2.2: List of Parameters in Chapter 2

This centre-shifting UC-clustering based on the UE set and the AP set formations is summarized in **Algorithm 1**.

The UC-clusters constructed based on this strategy are presented in Fig. 2.11(b). Observe that all clusters are separated by a certain a distance, hence they benefit from a significantly reduced ICI. As a benefit, the association of UEs becomes unambiguous. Besides, in this manner, it can be guaranteed that the number of APs is higher or at least equal to the number of UEs within each cluster. Therefore, the VT technique may be readily invoked for multi-AP-multi-UE transmission. Furthermore, by controlling d_u and d_a, we are capable of achieving a high flexibility in constructing clusters according to the diverse operating scenarios.

2.5 Performance Results

In this section, simulation results are provided for characterizing the performance of the clustering strategy, where the Shannon capacity is employed as our evaluation metric. Specifically, both the no-clipping-distortion scenario and clipping-distortion scenario are considered for the DCO-OFDM based VLC downlink. As for the UC-clustering, both radius-based UC-clustering as well as our proposed centre-shifting UC-clustering are invoked. The conventional NC-clustering strategies, such as UFR, FR-2 and NC-4, are used as our benchmarkers. The VT solution is adopted both for NC-4 and for UC-clustering in the context of multi-user transmission. The simulation parameters are summarized in Table 2.2.

2.5.1 No-Clipping-Distortion Scenario

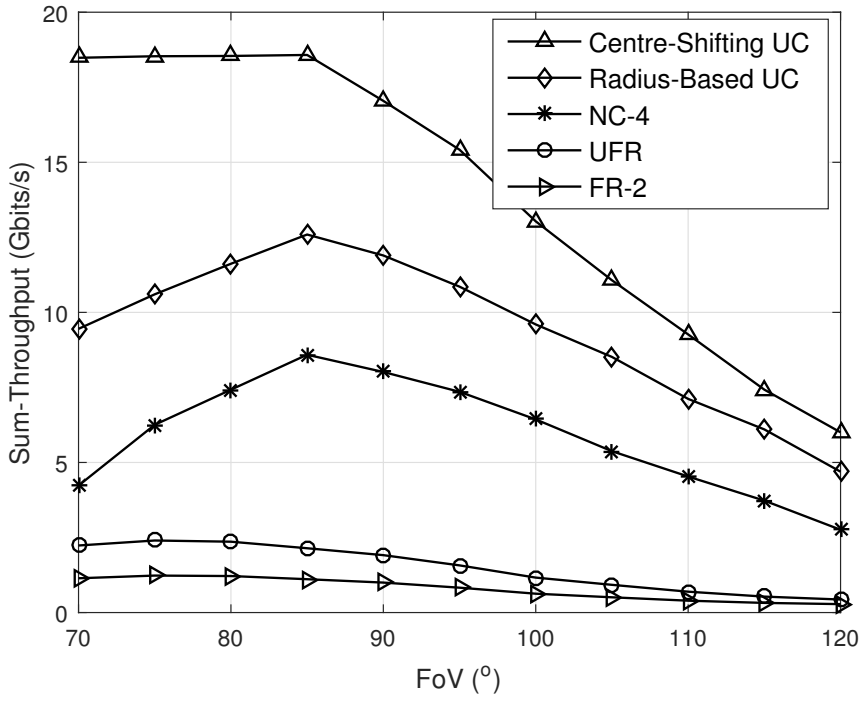

Figure 2.12: Throughput achieved in VLC networks relying on diverse NC/UC-clustering strategies under various FoV values.

The FoV is one of the most important parameters in VLC, since it has a far-reaching impact both on the channel gain and on the interference. Figure 2.12 compares the achievable sum-throughput of the VLC network relying on different clustering strategies under various FoVs, where $|\mathcal{K}| = 25$ UEs are supported in all cases without clipping distortion. We observe that the multi-attocell clustering aided VLC networks exhibit a consistently higher throughput than the single-attocell clustering aided VLC for all

FoVs, which illustrates the superiority of multi-user transmission. Observe in Fig. 2.12 that both UFR and FR-2 almost completely fail in a high FoV scenario due to the grave ICI encountered. By employing the multi-attocell clustering, regardless whether NC or UC is used, part of the ICI becomes MUI, which is then mitigated by our VT technique, hence resulting in a throughput enhancement. As expected, the benefit of centre-shifting UC-clustering is substantial at all FoV values, which is due to the fact that this clustering strategy takes into account the UE positions and as a benefit of having clusters separate by a certain distance.

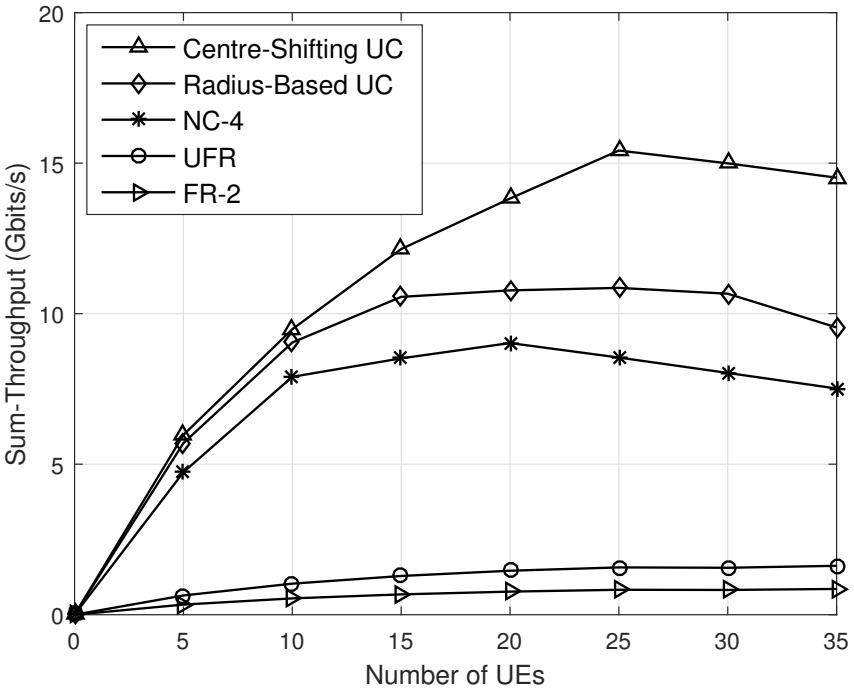

Figure 2.13: Achievable throughput for VLC networks relying on diverse NC/UC-clustering strategies in various UE density scenarios.

Furthermore, we investigate the influence of various UE densities on the throughput achieved by our different clustering strategies, as shown in Fig. 2.13. Again, the multi-attocell clustering aided VLC networks exhibit a consistently higher throughput than the single-attocell clustering scheme, where the proposed centre-shifting UC-clustering achieves the highest throughput, under all UE densities. Upon increasing the number of UEs, the throughput attained by the multi-attocell clustering is first increased and then slightly decreased. Since a total of 36 APs are distributed across the room, the maximum affordable number of UEs in a single time-slot is limited to 36. When the UE density becomes high, it may be difficult to find a unique anchoring AP for each UE, leaving some UEs unsupported. Those unsupported UEs can then be re-considered in the following time slot, which is however not considered in our simulations.

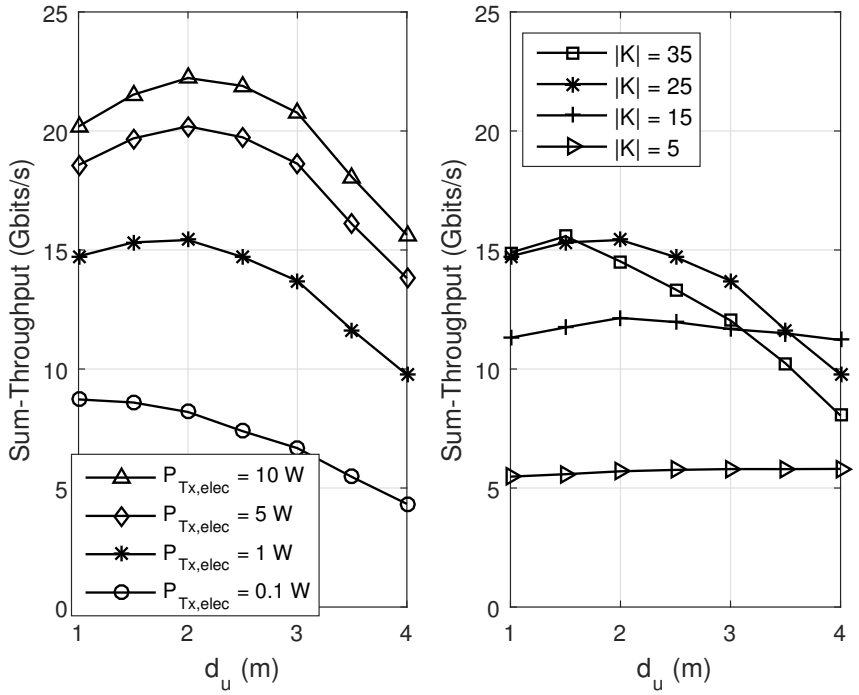

Figure 2.14: **Left**: Influence of the transmit power $P_{\text{Tx,elec}}$ on the sum-throughput attained by the proposed centre-shifting UC-clustering aided VLC network for various clusters sizes; **Right**: Throughput attained by the proposed centre-shifting UC-clustering aided VLC network for various clusters sizes, under various UE densities.

To further explore the performance of the proposed centre-shifting UC-clustering strategy, we investigate the throughput attained by various UE distance thresholds d_u, as seen in Fig. 2.14. By observing the left subfigure of Fig. 2.14, we infer that the best performance of the centre-shifting UC-clustering is around $d_u = 2$ m for supporting $|\mathcal{K}| = 25$ UEs at $\psi_{\text{FoV}} = 95^o$. Furthermore, the higher the transmit power we have, the higher the throughput becomes for the VLC network, but the additional throughput gain is reduced upon increasing the power, since a higher transmit power also imposes an increased ICI. Moreover, we observe that the best performance of the centre-shifting UC-clustering is not achieved with respect to a fixed UE distance threshold d_u, as shown in the right subfigure of Fig. 2.14. When the UE density is fairly low, the larger the clusters we have, the higher the throughput becomes. Due to the sparse UE distribution, the small d_u based UC-clusters may collapse to a single attocell, hence a throughput gain is attained upon increasing d_u. By contrast, the best d_u is gradually reduced upon increasing the number of UEs. This is because by reducing d_u, it is guaranteed that the number of UEs within each constructed cluster remains moderate. Although the more UEs are supported by VT, the higher throughput can be achieved, but the power required is also increased. Therefore, under the constraint of a limited transmit power,

the best choice of d_u depends both on the AP deployment and on the UE density.

2.5.2 Clipping-Distortion Scenario

Let us now investigate the impact of clipping-distortion imposed on VLC systems relying on various clustering strategies. As shown in Fig. 2.15, we compare the throughput achieved both with and without clipping distortion, under various FoV values. Observed from the four subfigures that the clipping-distortion leads to throughput impairments, regardless of the specific clustering strategy and of the FoV values. Furthermore, we observe that the throughput impairment encountered is much lower at large FoVs for the multi-attocell clustering, which implies that the multi-AP-multi-UE transmission is capable of compensating the throughput impairment due to the clipping-distortion at larger FoV.

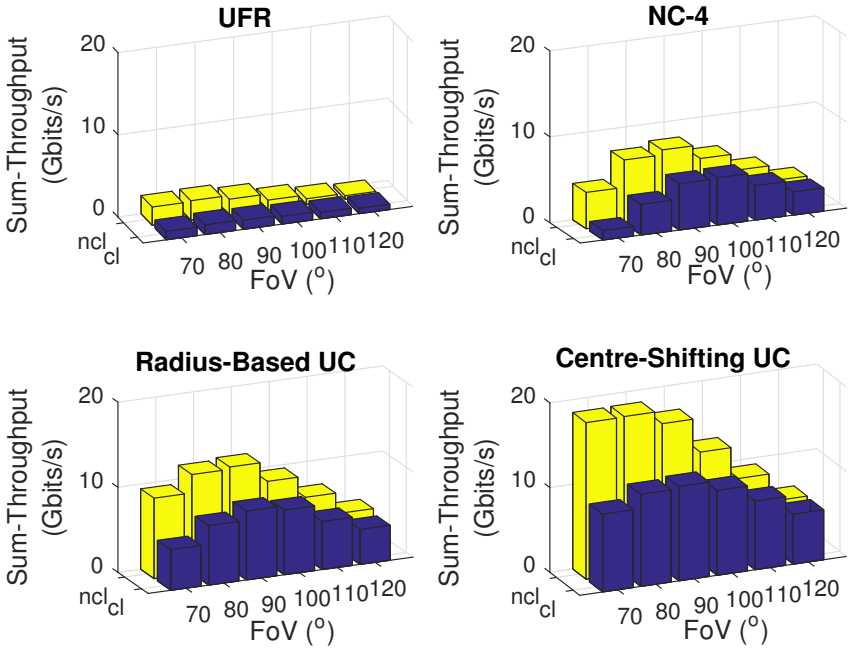

Figure 2.15: Comparison of throughput attained by various clustering strategies between clipping-distortion (cl) and non-clipping-distortion (ncl) scenarios.

The clipping-distortion-contaminated throughput is also quantified as a function of the number of UE, as shown in Fig. 2.16. It can be seen from the figure that the throughput reduced owing to the clipping-distortion has a similar tendency as the clipping-distortion-free throughput for all the clustering strategies, as a function of the number of UEs. Therefore, it can be inferred that the influence of clipping-distortion on the

throughput is less sensitive to the UE density, which implies that, as expected, the effects of clipping-distortion cannot be eliminated by clustering.

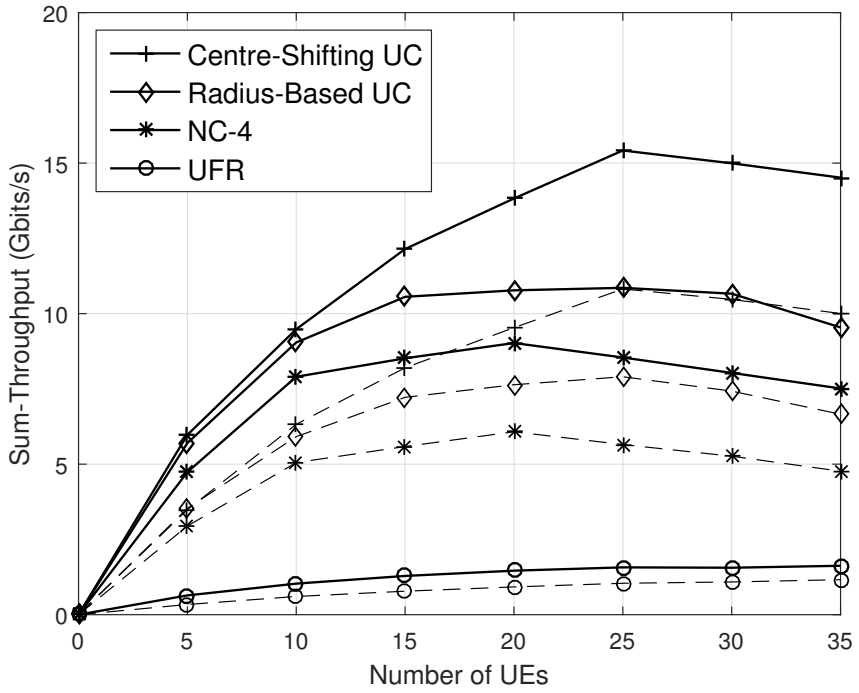

Figure 2.16: Achievable throughput having non-negligible clipping-distortion (dashed lines) as a function of the UE density for different clustering strategies, compared to the throughput associated with no-clipping-distortion (solid lines).

To elaborate, we further investigate the influence of DC-bias on the achievable throughput, for various sizes of clusters constructed by the proposed centre-shifting UC-clustering strategy. As seen in Fig. 2.17, for the DCO-OFDM transmission, the highest throughput is attained, when the DC-bias is around to 15 mW, bearing in mind that the linear dynamic range of LEDs in our simulations is between 1 mW to 30 mW. Recall from Section 2.2.2.1 of the DCO-OFDM characteristic that a DC-bias has to be added to the bipolar signal in order to ensure the positivity of the transmitted signal. When the DC-bias is fairly small, the majority of the signal is still negative, so that it has to be clipped at the lower bound of the LED's linear dynamic range, leading to a substantial throughput loss. Upon increasing the DC-bias from 5 mW to 15 mW, the throughput attained is also increased, but when the DC-bias exceeds 15 mW, the throughput attained starts to reduce, since further increasing the DC-bias introduces clipping the top of the transmitted signal.

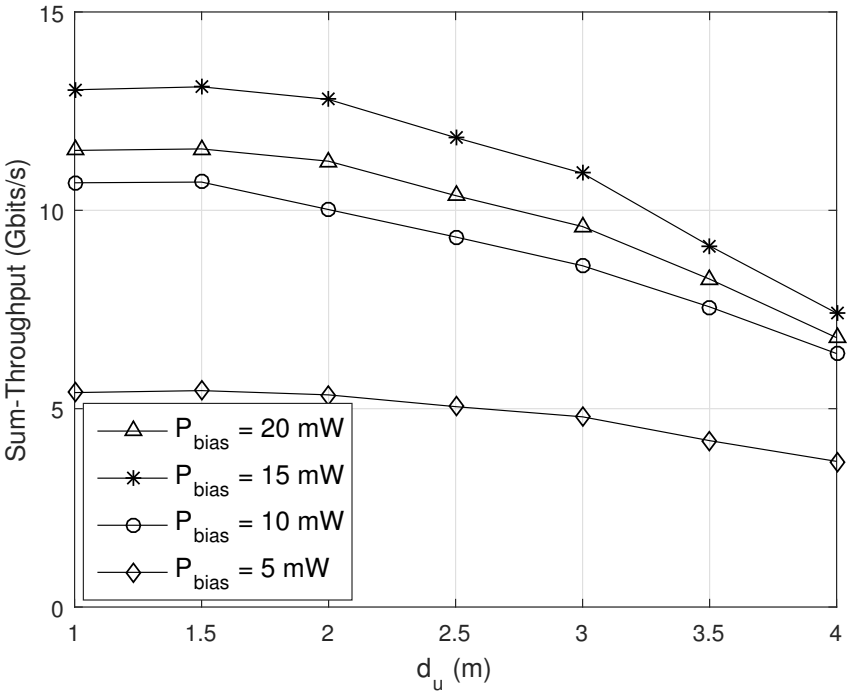

Figure 2.17: Achievable throughput in the centre-shifting UC-clustering aided VLC for various cluster sizes, under different DC-bias clipping scenarios.

2.6 Chapter Conclusions and Summary

In this chapter, clustering strategies were designed for VLC network, based on both the NC and UC perspective. Specifically, our VLC system model was introduced in Section 2.2, where the multi-user transmission developed supported multi-AP-multi-UE transmission in VLC, facilitating the implementation of multi-attocell clustering. In Section 2.3, we first reviewed the family of clustering strategies, namely NC-clustering, such as the UFR, FR-τ and NC-ζ, as well as UC-clustering, such as the radius-based UC-clustering. Note that the constructed clusters relying on both the NC-ζ and the radius-based UC-clustering is beneficial for the multi-AP-multi-UE structure, where the VT has to be invoked for eliminating the MUI. By analysing the defects of each clustering strategy in Section 2.3, the centre-shifting UC-clustering technique was proposed in Section 2.4, where the specific clustering process was presented in Fig. 2.9. To have a fair comparison, the same UE distribution was clustered by both of the existing strategies (Figs. 2.5, 2.7 and 2.8) and by the proposed strategy (Fig. 2.11). It was found that the clusters constructed using our proposed strategy were separated by a safe distance, for efficiently mitigating the ICI. Moreover, by flexibly adjusting the thresholds d_u and d_a, our proposed strategy was capable of supporting diverse scenarios.

The performance of the different clustering strategies quantified in terms of their throughput was characterized in Section 2.5, where the achievable throughput associated both with no clipping-distortion and contaminated by non-negligible clipping-distortion was considered. Figure 2.12 and 2.13 demonstrated that the VLC system relying on our proposed clustering strategy was capable of achieving the highest throughput, while supporting various number of UEs at various FoV values, thanks to its resistance to ICI. This tendency also prevailed, when the clipping-distortion was taken into account, as seen in Figs. 2.15 and 2.16. Additionally, the threshold d_u of our proposed clustering strategy was flexibly adjusted under different simulation environments, such as different transmit power and UE density (Fig. 2.14) and diverse DC-bias values, when considering clipping-distortion (Fig. 2.17). From these results, we infer that the best choice of d_u is strongly dependent on the environment, where the proposed strategy is capable of providing the required flexibility.

This chapter was focussed on the clustering strategies of VLC systems. The simulation results demonstrated that the VLC system relying on the proposed clustering is capable of achieving the best performance in terms of throughput. It is worth mentioning that the position information of UEs is required in order to implement UC-clustering, where the accuracy of positioning is vital for the performance of clustering. Therefore, in the following chapter, VLC-aided indoor positioning will be investigated.

Chapter 3

VLC-Aided Indoor Positioning

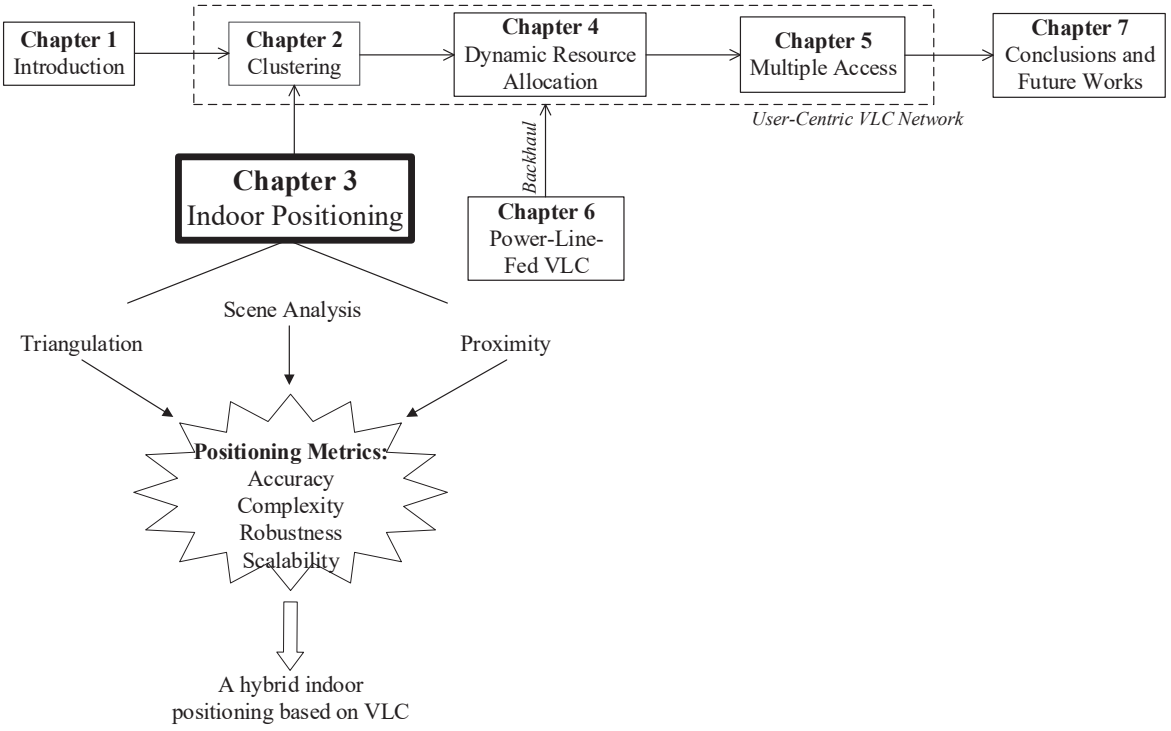

Figure 3.1: Block diagram of Chapter 3.

3.1 Introduction

Recall from Chapter 2 that the UC-clustering strategies are based on the assumption that the central controller has the location knowledge of both the UEs and the APs. Since all APs are installed at fixed positions, the positioning information can indeed be saved by

the central controller. However, as the positions of UEs are dynamically time-varying, it is important to use positioning for tracking their locations. The GPS is widely used to provide a coarse localization capability for outdoor applications. However, more than 80% of the tele-traffic is generated in indoor scenarios, while the indoor performance of GPS is unsatisfactory since the satellite signal has a poor indoor penetration and the multipath reflections are highly complex in indoor environment [91]. Although numerous indoor positioning solutions were proposed based on RF techniques [82–90], the associated cost of high-accuracy positioning is potentially excessive. Therefore, it is necessary to conceive an implementable indoor positioning technique, for supporting our UC-clusters. In this chapter, the VLC-aided indoor positioning is investigated. Aiming for high accuracy and low complexity, a hybrid indoor positioning technique is proposed relying on VLC.

This chapter is organized as follows. We first review several indoor positioning techniques in Section 3.2 and then the feasibility of visible light positioning is analysed in Section 3.3. In Section 3.4, a hybrid indoor positioning technique based on VLC is proposed, which strikes a trade-off between accuracy and complexity. Then, our positioning accuracy results and the resultant performance associated with our UC-clustering are provided in Section 3.5. Finally, the chapter is concluded in Section 3.6, followed by the chapter's summary in Section 3.7.

3.2 Review of Classic Indoor Positioning Techniques

The family of classic indoor positioning techniques are reviewed in this section, which includes the proximity-, triangulation- and scene-analysis- based positioning. The principle of these three algorithms will be described, associated with the unique advantages and disadvantages.

3.2.1 Proximity

As the simplest positioning technique, proximity-based solutions cannot provide absolute positioning results, only relative positioning results [131]. In more detail, let us assume that there is an area covered by a number of APs, whose locations are already known by the central controller. When the target UE is detected by a single AP, it is considered to be collocated with the AP, therefore the estimated position is determined by the whole area covered by this AP. Note that if more than one AP detects its presence, it is considered to be collocated with the one that provides the strongest RSS. Hence the complexity of proximity is quite low. However, the positioning accuracy strongly relies on the density of the APs and no precise positioning results can be obtained.

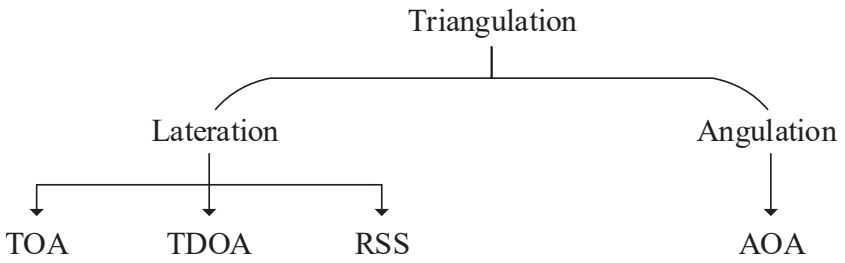

Figure 3.2: Taxonomy of the triangulation-based positioning technique.

3.2.2 Triangulation

Triangulation is one of the classic positioning techniques that exploits the geometric properties of a triangle to estimate the target UE location [132]. It relies on the so-called lateration or angulation method. Specifically, lateration estimates the position of a target UE by measuring its distances from multiple reference points. Note that in our system the LED-APs can be viewed as the reference points, since the central controller has their location information. Instead of directly measuring the distance, other measurements, such as the time of arrival (TOA), time difference of arrival (TDOA) and RSS, etc., can also be employed. Then the distance can be derived mathematically. As for the angulation, it estimates the location of a target UE based on the angles relative to multiple APs, where the metric adopted is the angle of arrival (AOA). The taxonomy of the triangulation is summarized in Fig. 3.2. We will review them in detail subsequently.

(1) *Time of Arrival*

By employing the TOA as the metric, the distance between the target UE and the nearby AP is estimated from the specific time instant which the signal arrives at the AP. In a 2D-plane, the TOA measurement have to be made with respect to at least three non-collinear APs. To elaborate a little further, the one-way propagation time is measured from the target UE to the three APs, respectively. We assume that the propagation time between the UE and the ith AP is t_i, where the propagation speed is v. Therefore, the distance between the UE and the ith AP can be obtained as $s_i = v \times t_i$. Let us assume that the coordinates of the target UE and the ith AP are (x_0, y_0) and (x_i, y_i), respectively. Then the coordinate (x_0, y_0) of the target UE can be derived based on:

$$s_i = \sqrt{(x_i - x_0)^2 + (y_i - y_0)^2},\ i = 1, 2, \cdots, n,\ n \geq 3. \tag{3.1}$$

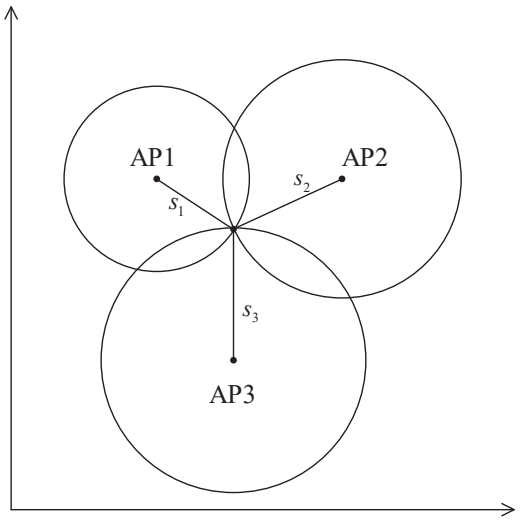

Figure 3.3: Triangulation based on TOA in 2D-plane.

In Fig. 3.3, the case of $n = 3$ is depicted. We can find that the three circles, having a radius of s_1, s_2 and s_3, respectively, intersect at only one point. This point is the estimated position of the target UE.

Although the accuracy of this estimated result is high for pure LoS scenarios, its accuracy is heavily affected by the multipath effects. Furthermore, for employing the TOA metric, it requires that all the transmitters and receivers have to be precisely synchronized, which significantly increases the hardware complexity and cost. To reduce the complexity, instead of requiring the absolute TOA, we may get for measuring the propagation time difference between the UE and APs, where the TDOA metric can be invoked. By doing so, we can attain the UE's location based on the hyperbolic positioning method [131]. In this manner, time synchronization is only required between the specific APs that participated in positioning.

(2) *Received Signal Strength*
The RSS constitutes an alternative technique of estimating the distance of the target UE from some set of APs, relying on the attenuation of the signal strength. It is widely exploited that upon increasing the distance between a receiver and a transmitter, the signal strength is reduced, which means that the distance can be estimated based on the RSS measurement. However, the positioning performance relying on the RSS is also vulnerable to multipath fading. Therefore, the main challenge when applying RSS is to find an appropriate path loss model to estimate the distance.

(3) *Angle of Arrival*

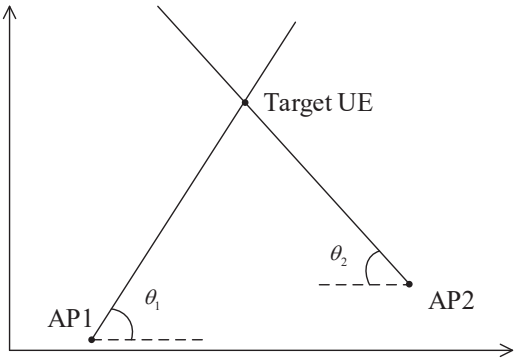

Figure 3.4: Triangulation based on AOA in 2D-plane.

This method estimates the UE's position based on the angles of arrival of signals from multiple APs. As shown in Fig. 3.4, the positioning is estimated according to the intersection of at least two directions from a pair of APs in a 2D-plane. Let us assume that the AOA between the signal and AP1 as well as AP2 are denoted by θ_2 and θ_2, respectively. The coordinates of the target UE and the ith AP are (x_0, y_0) and (x_i, y_i), respectively. Then the positioning of the UE can be derived from:

$$\tan\theta_i = \frac{y_i - y_0}{x_i - x_0},\ i = 1, \cdots, n,\ n \geq 2. \tag{3.2}$$

Although that AOA metric does not require synchronization between APs, it is susceptible to the external environment, where the positioning accuracy decreases upon the target UE moving farther away from the APs. Furthermore, by estimating the AOA requires additional hardware and a PD array has to be employed, which significantly increases both the complexity and the cost.

3.2.3 Scene Analysis

Scene analysis, usually termed as fingerprinting, refers to the positioning technique that first collects the location-related features of a scene and then estimates the location of a target UE by matching the online measured data with the features pre-measured during the first stage [13]. The RSS-based fingerprint is commonly used as the location-related feature in scene analysis [132]. To elaborate a little further, there are two basic fingerprinting stages: namely the off-line stage and the on-line stage. In the off-line stage, the location-related data (i.e. RSS) is collected at each position of the scene. Therefore, the pre-measured location candidates associated with their RSS values are stored in the off-line database. Then the objective of the on-line stage is to estimate the UE's location by comparing its RSS reading to that of the location candidates in

the off-line database. For the matching process, classic pattern recognition techniques such as probabilistic method and the k-nearest-neighbor (kNN) method are commonly employed.

(1) *Probabilistic Methods*

Let us assume that there are N location candidates, denoted as $L_1,\ L_2,\ \cdots,\ L_N$, and $\boldsymbol{s}$ is the RSS vector measured during the on-line stage for a target UE. Hence, the decision rule based on the *a posteriori* probability is given by:

$$\text{Choose } L_i \text{ if } P(L_i|\boldsymbol{s}) > P(L_j|\boldsymbol{s}),\ i,j\ = 1,2,\cdots,N,\ j \neq i. \tag{3.3}$$

Note that $P(L_i|\boldsymbol{s})$ denotes the *a posteriori* probability of the target UE being located at L_i, given the RSS vector $\boldsymbol{s}$. According to Bayes' formula, we have:

$$P(L_i|\boldsymbol{s}) = \frac{P(\boldsymbol{s}|L_i)P(L_i)}{P(\boldsymbol{s})}, \tag{3.4}$$

where the conditional likelihood $P(\boldsymbol{s}|L_i)$ denotes the probability that the RSS vector is $\boldsymbol{s}$, given that the target UE is located at L_i. If we have the measured vector of $\boldsymbol{s} = [s_1, s_2, \cdots, s_M]$ gleaned from M APs, the overall likelihood of each location candidate can be calculated as:

$$P(\boldsymbol{s}|L_i) = P(s_1|L_i) \times P(s_2|L_i) \times \cdots \times P(s_M|L_i),\ \forall i, \tag{3.5}$$

where we assume that the APs are independent from each other. Furthermore, $P(L_i)$ denotes the probability that the UE is located at L_i, regardless of any other information, while $P(\boldsymbol{s})$ denotes the probability that the RSS vector is $\boldsymbol{s}$, which is the same for all L_i. Upon assuming that the values of $P(L_i)$ are the same for all L_i, the decision rule mentioned in Eq. (3.3) can be simplified to the comparison between the likelihood of each location candidate formulated as:

$$\text{Choose } L_i \text{ if } P(\boldsymbol{s}|L_i) > P(\boldsymbol{s}|L_j),\ i,j\ = 1,2,\cdots,N,\ j \neq i. \tag{3.6}$$

(2) *k-Nearest-Neighbor*

Compared to the probabilistic method, the kNN technique is a simple method that can be used for the matching process in fingerprinting. More explicitly, it uses the online RSS to find the k closest location candidates according to the root mean square error metric, so that the estimated location can be obtained by averaging these k locations. To expound further, we assume that the RSS vector for the ith location candidate collected during the off-line stage is $\boldsymbol{S}_i = [S_{1,i}, S_{2,i}, \cdots, S_{j,i}, \cdots, S_{M,i}]$, where $S_{j,i}$ denotes the RSS from the jth AP, measured at the ith location candidate. Additionally, the RSS vector measured

during the on-line stage is obtained as $\boldsymbol{s} = [s_1, s_2, \cdots, s_j, \cdots, s_M]$, where s_j denotes the measured RSS with respect to the jth AP. Therefore, the distance d_i between the off-line vector $\boldsymbol{S}_i$ and the on-line vector $\boldsymbol{s}$ at the ith location candidate is given by:

$$d_i = \sqrt{\sum_{j=1}^{M} (s_j - S_{j,i})^2}, \ i = 1, 2, \cdots, N. \tag{3.7}$$

After calculating the distances for all N location candidates, the k location candidates having the smallest distances are chosen. Therefore, the estimated coordinate (x^*, y^*) can be obtained by averaging over the k location candidates as follows:

$$(x^*, y^*) = \frac{\sum_{i=1}^{k} (x_{L_i}, y_{L_i})}{k}, \tag{3.8}$$

where (x_{L_i}, y_{L_i}) indicates the coordinate of the ith location candidate.

Based on the analysis above, it may be surmised that the positioning accuracy of fingerprinting is high, which can be further improved by increasing the number of location candidates measured during the off-line stage. However, the complexity of fingerprinting strongly relies on the database constructed during the off-line stage, since the matching process is carried out by comparing the RSS value measured during the on-line stage to the database. Furthermore, since the RSS measured during the on-line stage is hosted by a vector having the same number of elements as the number of APs, the distribution and the number of the APs have a substantial influence on the positioning performance and efficiency.

3.3 Feasibility of Visible Light Positioning

The cost of high-accuracy RF-based positioning is often deemed excessive, since complex multi-path cancellation techniques are required [133]. Hence, LED enabled indoor positioning has drawn substantial research attention. Therefore, the feasibility of visible light positioning is analysed in this section.

- Since most of the energy of visible light is concentrated in the LoS ray, by employing VLC-aided indoor positioning is fairly immune to multipath interference [125].
- In most indoor scenarios, the number of positioning targets is high. For example, when indoor positioning is invoked in a supermarket, dozens of products and costumers may rely on positioning. As a benefit of the unexploited and unlicensed visible-light spectrum [10], VLC-aided indoor positioning can afford the vast positioning requirements.

- A higher density of APs benefits from a higher positioning accuracy [125]. As observed in [134], the number of LED-APs is typically an order of magnitude higher than that of WiFi in a building. This implies that the visible light positioning tends to have a higher positioning accuracy due to its densely deployed APs.
- Another advantage of visible light positioning is that the light strength is usually constant. Therefore, site survey and database maintenance can be avoided [13]. Furthermore, recall from Eq. (2.1) that the RSS is a function of distance between the AP and the UE. Therefore, the RSS can be readily employed in visible light positioning since it is closely related to the distance.
- Since there is no interference with RF, visible light positioning can be employed in the RF-sensitive areas, such as hospitals and aircraft [108].
- Upon exploiting the existing lighting fixtures, the implementation of visible light positioning has a low cost.

Inspired by these, we are interested to investigate the VLC-aided indoor positioning relying on the RSS. Instead of invoking a single indoor positioning technique, a hybrid visible light positioning is proposed for our UC-VLC system aiming for achieving high accuracy and low complexity.

3.4 Hybrid Positioning Aided User-Centric VLC Downlink

In this section, we first explore the positioning performance of visible light positioning relying on either triangulation or fingerprinting. After characterizing their performance, we propose a hybrid indoor positioning technique.

3.4.1 Triangulation for VLC-Aided Positioning

In this section, triangulation-based positioning is invoked for VLC-aided indoor positioning based on the RSS metric. As we mentioned before, it exploits the geometric properties of a triangle to estimate locations. To elaborate, triangulation requires three reference APs with their horizontal coordinates denoted as (x_{n_1}, y_{n_1}), (x_{n_2}, y_{n_2}) and (x_{n_3}, y_{n_3}), respectively. Let the coordinate of the target UE be (x_k, y_k). Then the system determines the strongest RSS reading amongst the UE and at least three different

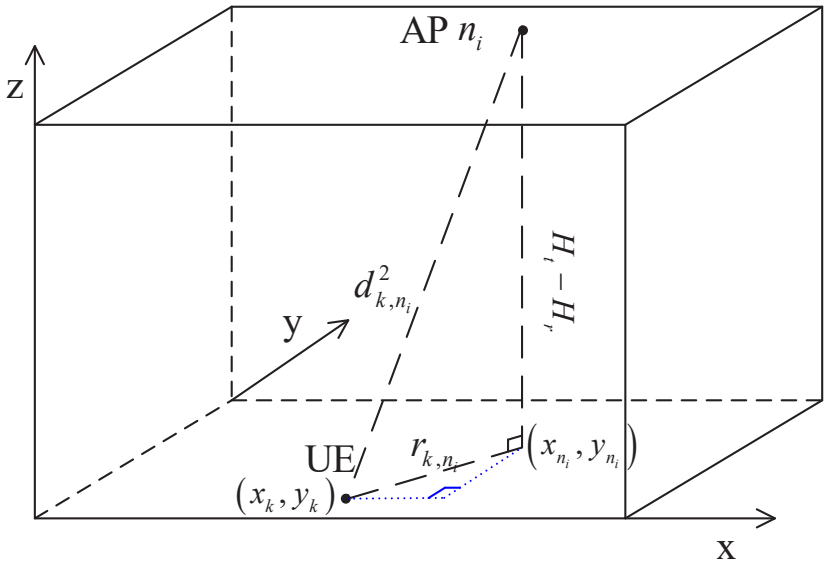

Figure 3.5: Distance estimation based on triangulation in visible light positioning.

APs[1], which is formulated by:

$$p_{k,n_i} = |h_{k,n_i}|^2 P_T, \quad i = 1, 2, 3, \tag{3.9}$$

where h_{k,n_i} represents the channel gain between the UE and the AP n_i, which can rely on only the LoS ray or both the LoS ray and the reflected ray. Furthermore, P_T is the transmit power of the AP, where we assume that each AP has the same transmission power. For simplification, the triangulation is based on the LoS ray, so that the channel gain h_{k,n_i} can be substituted by Eq. (2.1). Therefore, we find that the estimated distance between the UE and the AP n_i is a direct function of the RSS, where the estimated distance may be written as[2]:

$$d^2_{k,n_i} = \sqrt{\frac{A_s g_{of}(\psi) g_{oc}(\psi) P_T (H_t - H_r)^2}{\pi p_{k,n_i}}}. \tag{3.10}$$

[1]This could be integrated into the cell search phase, where the APs transmit their sounding signals in an orthogonal way to the UE. The UE then measures the RSS and feeds it back to the system, which is assumed to be error free.

[2]Note that Eq. (3.10) is based on the order of Lambertian emission $\alpha = 1$, when the semi-angle at half-illumination $\phi_{1/2} = 60^o$, as shown in Table 2.2.

As shown in Fig. 3.5, the horizontal distance $r_{k,ni}$ between the UE and the projection of AP n_i on the UE plane can be calculated as:

$$r_{k,n_i} = \sqrt{d_{k,n_i}^2 - (H_t - H_r)^2}. \tag{3.11}$$

Therefore, the linear system of equations used for estimating the UE's coordinate $(\tilde{x}_k, \tilde{y}_k)$ is:

$$\begin{cases} (\tilde{x}_k - x_{n_1})^2 + (\tilde{y}_k - y_{n_1})^2 = r_{k,n_1}^2 \\ (\tilde{x}_k - x_{n_2})^2 + (\tilde{y}_k - y_{n_2})^2 = r_{k,n_2}^2 \\ (\tilde{x}_k - x_{n_3})^2 + (\tilde{y}_k - y_{n_3})^2 = r_{k,n_3}^2. \end{cases} \tag{3.12}$$

Equation (3.12) can be also streamlined into a matrix form as $\boldsymbol{AC} = \boldsymbol{B}$, where we have:

$$\boldsymbol{A} = \begin{bmatrix} x_{n2} - x_{n1} & y_{n2} - y_{n1} \\ x_{n3} - x_{n1} & y_{n3} - y_{n1} \end{bmatrix}, \tag{3.13}$$

$$\boldsymbol{C} = [\tilde{x}_k, \tilde{y}_k]^T, \tag{3.14}$$

$$\boldsymbol{B} = \frac{1}{2} \begin{bmatrix} \left(r_{k,n_1}^2 - r_{k,n_2}^2\right) + \left(x_{n_2}^2 + y_{n_2}^2\right) - \left(x_{n_1}^2 + y_{n_1}^2\right) \\ \left(r_{k,n_1}^2 - r_{k,n_3}^2\right) + \left(x_{n_3}^2 + y_{n_3}^2\right) - \left(x_{n_1}^2 + y_{n_1}^2\right) \end{bmatrix}. \tag{3.15}$$

Following least square estimation, the coordinate of the UE can be estimated as:

$$\boldsymbol{C} = (\boldsymbol{A}^T \boldsymbol{A})^{-1} \boldsymbol{A}^T \boldsymbol{B}. \tag{3.16}$$

Note that in order to estimate $(\tilde{x}_k, \tilde{y}_k)$, the matrix $\boldsymbol{A}$ should be of full rank, implying that the three reference APs should not be in a single line.

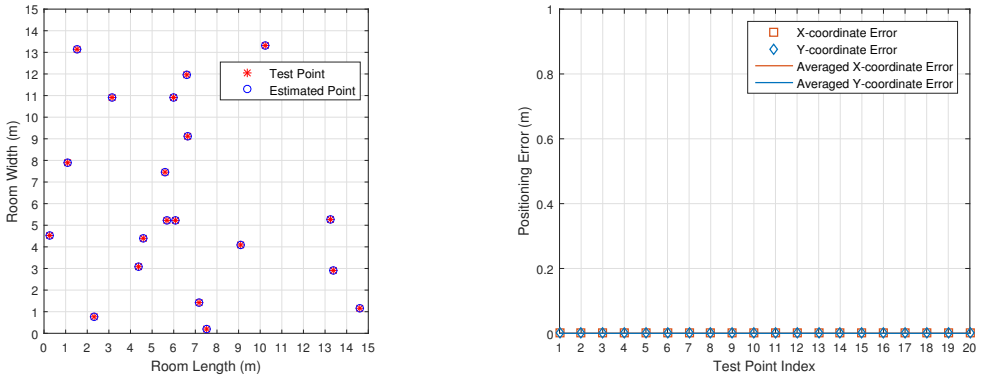

(a) Positioning results

(b) Positioning errors of each test point

Figure 3.6: Visible light positioning based on triangulation for $|\mathcal{K}| = 20$ target points with $\Psi_{\text{FoV}} = 120^o$, using the parameters in Table 2.2.

Since at least three reference APs are required, which can provide visible light rays to the target point for triangulation, the positioning performance is sensitive to the value

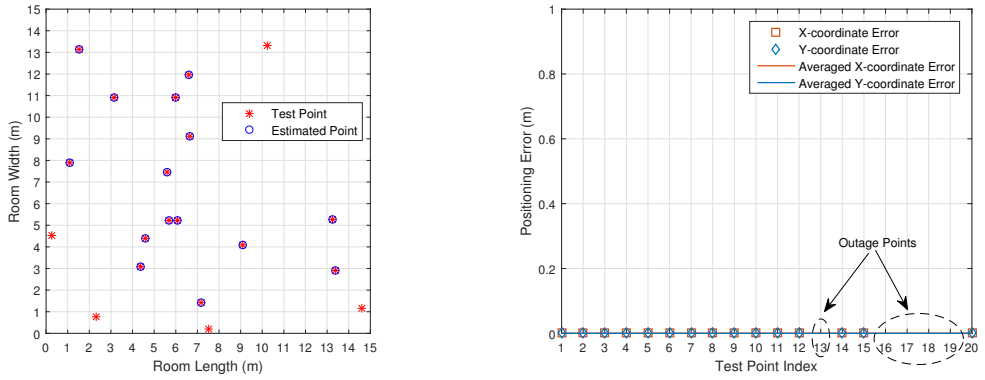

(a) Positioning results

(b) Positioning errors of each test point

Figure 3.7: Visible light positioning based on triangulation with $\Psi_{\text{FoV}} = 100^o$, using the parameters in Table 2.2.

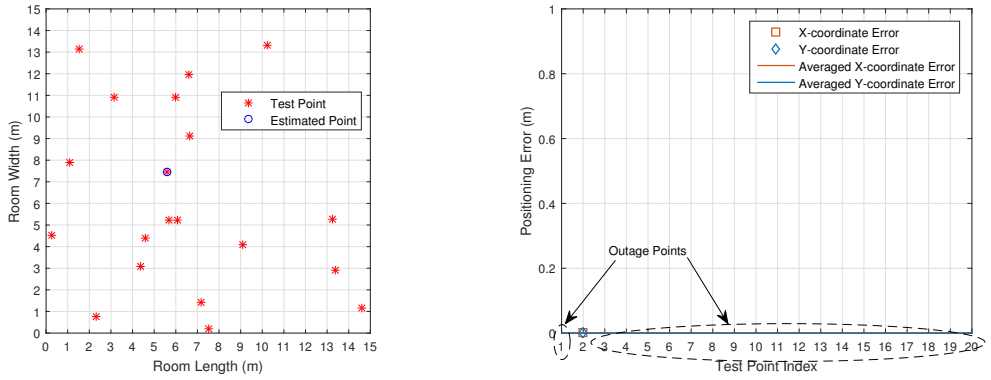

(a) Positioning results

(b) Positioning errors of each test point

Figure 3.8: Visible light positioning based on triangulation with $\Psi_{\text{FoV}} = 80^o$, using the parameters in Table 2.2.

of FoV. Figure 3.6 shows the positioning results and the corresponding errors of a total of 20 test points, which are randomly distributed in a room, under $\Psi_{\text{FoV}} = 120^o$. It can be found that the triangulation performs well in this scenario, where all the position of the test points can be estimated with a near-zero error. This implies that as a benefit of the sufficiently high FoV, each test point has at least three non-collinear APs, hence yielding good positioning accuracy relying on triangulation. When the value of FoV is reduced to $\Psi_{\text{FoV}} = 100^o$, by observing Fig. 3.7, we find that the positioning fails at some points located near the walls of the room, which are therefore termed as outage events. It can be therefore inferred that the areas near the walls are more vulnerable in the face of a low FoV in triangulation-based positioning. Moreover, when the FoV further decreases to, say $\Psi_{\text{FoV}} = 80^o$, the triangulation almost completely fails, since the majority of the test points constitute outage points, as shown in Fig. 3.8. It can be

concluded that when the value of FoV is too small for the target points to be assigned three non-collinear APs, the triangulation fails in VLC-aided positioning.

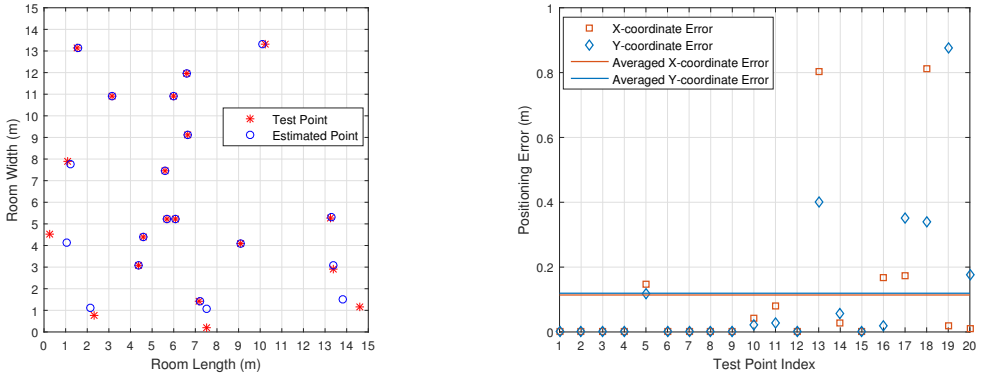

(a) Positioning results (b) Positioning errors of each test point

Figure 3.9: Visible light positioning based on triangulation with $\Psi_{\text{FoV}} = 120^o$, considering both the LoS and the first reflected visible-light rays.

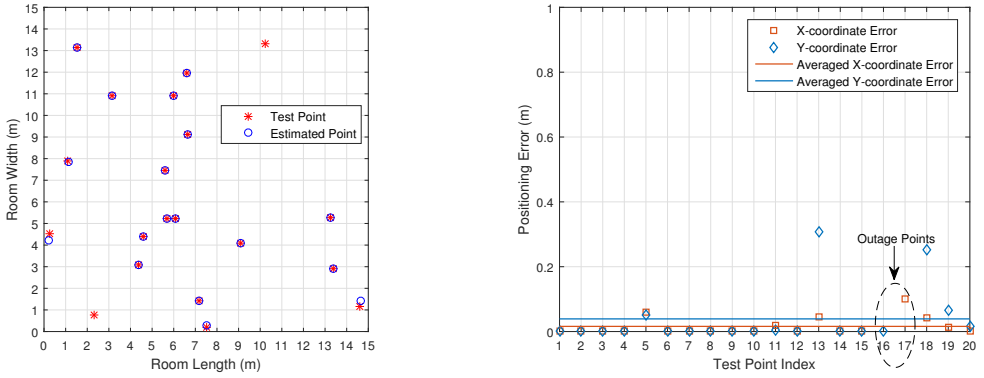

(a) Positioning results (b) Positioning errors of each test point

Figure 3.10: Visible light positioning based on triangulation with $\Psi_{\text{FoV}} = 100^o$, considering both the LoS and the first reflected visible-light rays.

Furthermore, there are also reflected rays in VLC, which may affect the triangulation-based positioning. As seen in Fig. 3.9, although there are no outage points when considering the reflected rays at $\Psi_{\text{FoV}} = 120^o$, the positioning errors of the points located at the edge-area near the walls are higher than that of the scenario having no reflected rays in Fig. 3.6. According to the VLC channel characteristics we introduced in Chapter 2, the edge-area near the walls tends to receive more reflected rays. Therefore, the reference AP may be selected due to the fact that it provides a strong reflected ray to the target point, which degrades the triangulation performance. Upon reducing the FoV, as seen in Figs. 3.10 and 3.11, the positioning results become quite similar to those ignoring the reflected rays. However, by exploiting the reflected rays, we find that

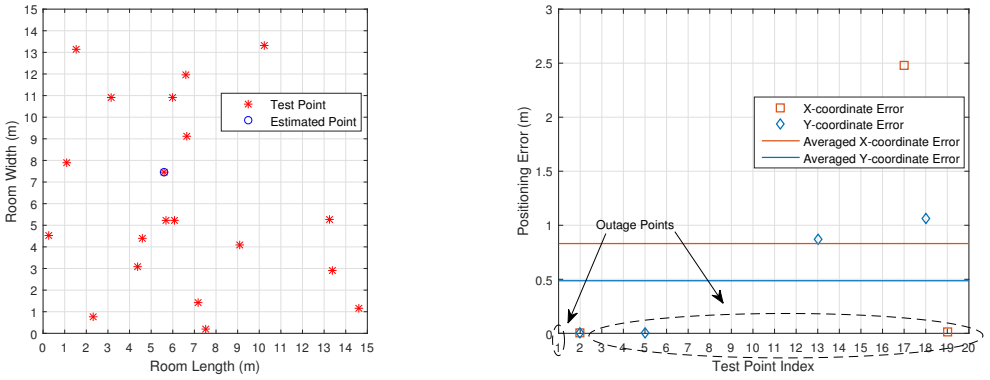

(a) Positioning results

(b) Positioning errors of each test point

Figure 3.11: Visible light positioning based on triangulation with $\Psi_{\text{FoV}} = 80^o$, considering both the LoS and the first reflected visible-light rays.

those outage points seen in Fig. 3.7 are indeed improved in Fig. 3.10, while the average positioning error is higher than in the scenario without considering the reflected rays.

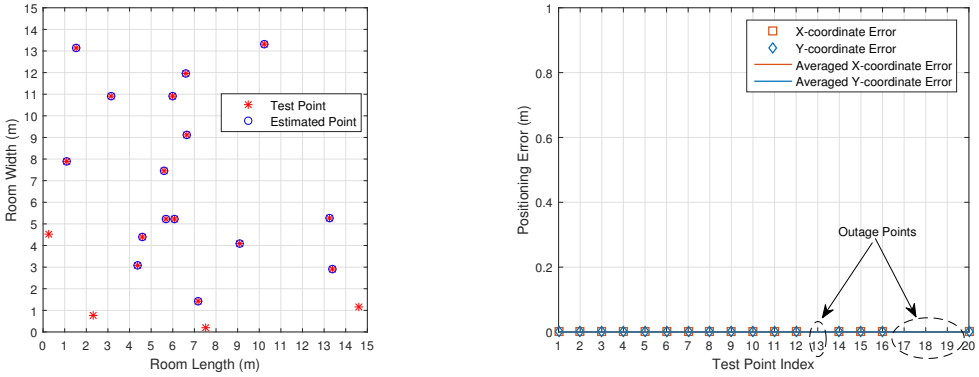

(a) Positioning results

(b) Positioning errors of each test point

Figure 3.12: Visible light positioning based on triangulation with $6 \times 6 = 36$ APs at $\Psi_{\text{FoV}} = 120^o$, considering only the LoS rays.

In order to evaluate the scalability, we investigate the triangulation-based positioning in different AP density scenarios, but all other parameters remain the same as in Fig. 3.6. By observing Figs. 3.12 and 3.13, we find that the probability of the outage points increases upon reducing the number of APs, while for those points which are not in outage, the positioning error is also near-zero, since no reflected rays considered.

Additionally, to quantify the robustness of the triangulation, a blocking probability $\mathbb{P}_{\text{bl}}$ is introduced. Here the blocking probability is defined as the probability of the blocked APs in VLC-aided indoor positioning, where the target points have very low RSS from the blocked APs. Figure 3.14 shows the positioning performance when we

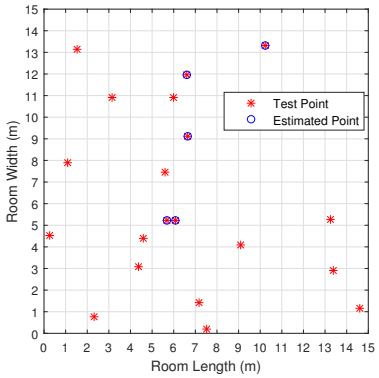

(a) Positioning results

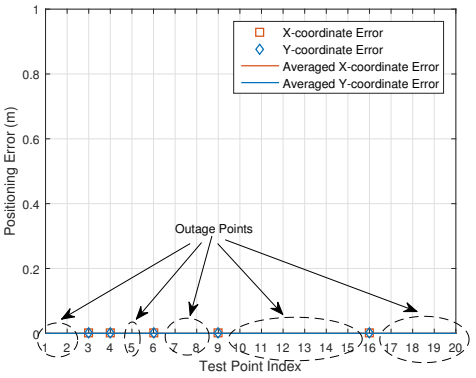

(b) Positioning errors of each test point

Figure 3.13: Visible light positioning based on triangulation with $5 \times 5 = 25$ APs at $\Psi_{\text{FoV}} = 120^o$, considering only the LoS rays.

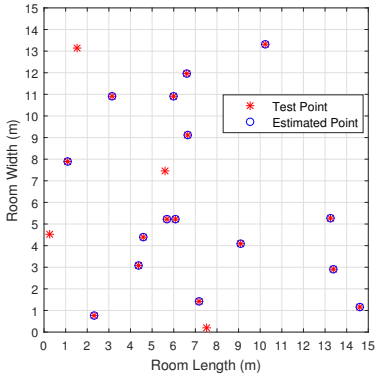

(a) Positioning results

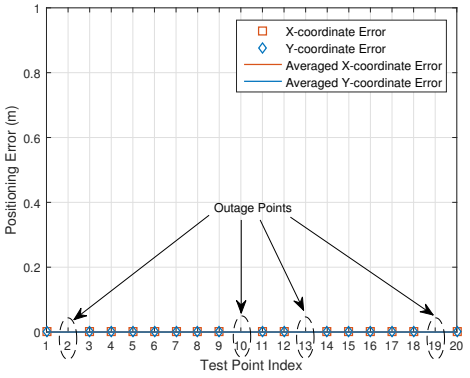

(b) Positioning errors of each test point

Figure 3.14: Visible light positioning based on triangulation with $8 \times 8 = 64$ APs at $\Psi_{\text{FoV}} = 120^o$ under a blocking probability $\mathbb{P}_{\text{bl}}$ of 0.2, considering only the LoS rays.

have $\mathbb{P}_{\text{bl}} = 0.2$. Compared to the results seen in Fig. 3.6, more outage points occur since their preferred reference APs may be blocked.

In a nutshell, the performance of triangulation in VLC-aided indoor positioning is limited. The positioning results of triangulation relying on RSS are accurate in sufficiently high FoV scenarios, in the presence of no reflected rays. By contrast, inadequate performance is achieved, when the FoV is low and there are reflected rays. Furthermore, the scalability and the robustness of the triangulation in visible light positioning is somewhat unsatisfactory. Therefore, purely relying on triangulation in VLC-aided indoor positioning is insufficient.

3.4.2 Fingerprinting for VLC-Aided Positioning

To alleviate the potentially low accuracy of triangulation-based positioning, scene analysis may be invoked, where RSS-based fingerprinting is a commonly used technique. As we mentioned in Section 3.2.3, there are two basic fingerprinting steps: the off-line stage and on-line stage. Let us assume that the specific room considered is divided into a total of Q small tiles, where each tile constitutes a reference position. Therefore, in our VLC system, the off-line stage aims for building a useful reference position database for the scene, where the pre-defined reference position coordinates associated with their RSS values are stored. Then the objective of the on-line stage is to estimate the UE's location by comparing its RSS reading to that of the reference points in the database obtained from the off-line stage.

To elaborate, the RSS vector $\bar{\boldsymbol{p}}_i$ of the ith tile L_i is evaluated at its central location by receiving from all $|\mathcal{N}|$ APs, which can be expressed as:

$$\bar{\boldsymbol{p}}_i = \left[\bar{p}_{i,1}, \bar{p}_{i,2}, \cdots, \bar{p}_{i,|\mathcal{N}|}\right], \tag{3.17}$$

where $\bar{p}_{i,n}$ represents the RSS from the AP n to the ith tile, which can be calculated based on Eq. (3.9). Let us assume that the RSS vector obtained for the target point k is:

$$\boldsymbol{p}_k = \left[p_{k,1}, p_{k,2}, \cdots, p_{k,|\mathcal{N}|}\right]. \tag{3.18}$$

Relying on the probabilistic estimation we introduced in Section 3.2.3, the tile L_i is preferred over L_j, if we have $P(L_i|\boldsymbol{p}_k) > P(L_j|\boldsymbol{p}_k)$, where $P(L_i|\boldsymbol{p}_k)$ represents the probability of the target point k being located in L_i, given the RSS vector of $\boldsymbol{p}_k$. According to Bayes' formula and assuming that the values of $P(L_i), \forall i$ are the same, we have the relationship of

$$P(L_i|\boldsymbol{p}_k) > P(L_j|\boldsymbol{p}_k) \propto P(\boldsymbol{p}_k|L_i) > P(\boldsymbol{p}_k|L_j) \tag{3.19}$$

for our decision concerning choosing L_i over L_j. Therefore, the decision rule obeys the maximum likelihood (ML) criterion. Naturally, a potential drawback of the RSS-based fingerprinting is the complexity of the full-search-based ML test: not only the feedback RSS $\boldsymbol{p}_k$ has to be compared with $\bar{\boldsymbol{p}}_i$, $i = 1, 2, \cdots, Q$, but also the comparison between each elements within the vectors has to be carried out. Therefore, the database obtained during the off-line stage and the number of APs in the room have a profound influence on the complexity of fingerprinting in visible light positioning.

Let us now investigate the positioning performance of fingerprinting in VLC-aided positioning when different size of tiles are used in the off-line database, which are the sizes of 0.5×0.5 m^2, 0.25×0.25 m^2 and 0.15×0.15 m^2, as shown in Figs. 3.15 - 3.17. Observe that, as expected, more accurate positioning results can be obtained, when smaller tiles are used during the off-line stage, although at the cost of higher

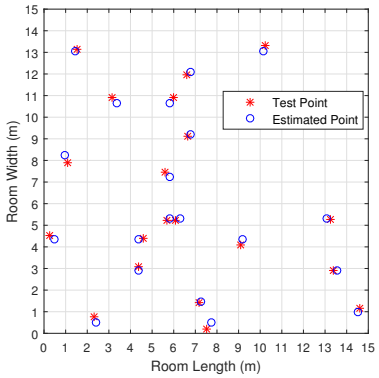

(a) Positioning results

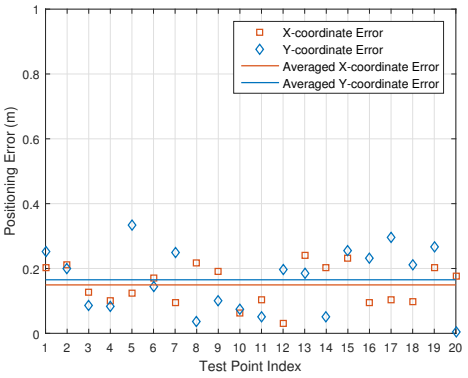

(b) Positioning errors of each test point

Figure 3.15: Fingerprinting-based visible light positioning with the tile size of 0.5×0.5 m^2 under $\Psi_{\text{FoV}} = 100^o$, considering both the LoS and the first reflected visible-light rays.

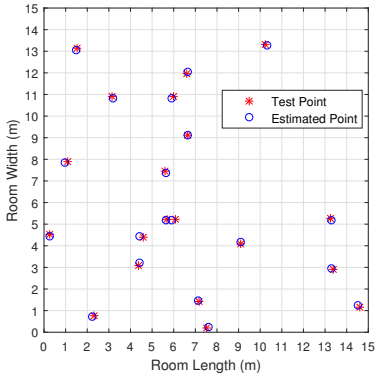

(a) Positioning results

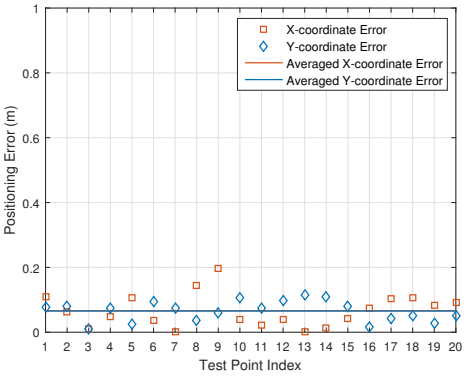

(b) Positioning errors of each test point

Figure 3.16: Fingerprinting-based visible light positioning with the tile size of 0.25×0.25 m^2 under $\Psi_{\text{FoV}} = 100^o$, considering both the LoS and the first reflected visible-light rays.

complexity. Furthermore, it can be found that the outage points seen in Fig. 3.7 can all be successfully estimated by fingerprinting, even though the tiles collected in database are sparse, as shown in Fig. 3.15. Additionally, even though the positioning error based on fingerprinting is not as small as that of the triangulation, it remains at a low level on the order of centimetres. Note that, in contrast to the triangulation where the reflected rays degraded the positioning performance, here the reflected rays are useful for improving fingerprinting. Figure 3.18 shows the positioning performance of the fingerprinting based only on the LoS rays, where all other parameters are the same as in Fig. 3.16. Since the comparison during the on-line stage of fingerprinting is between the vector $\bar{\boldsymbol{p}}_i$ and $\boldsymbol{p}_k$, having more non-zero values in the vectors makes the positioning more accurate. Moreover, we find that fingerprinting has a much better

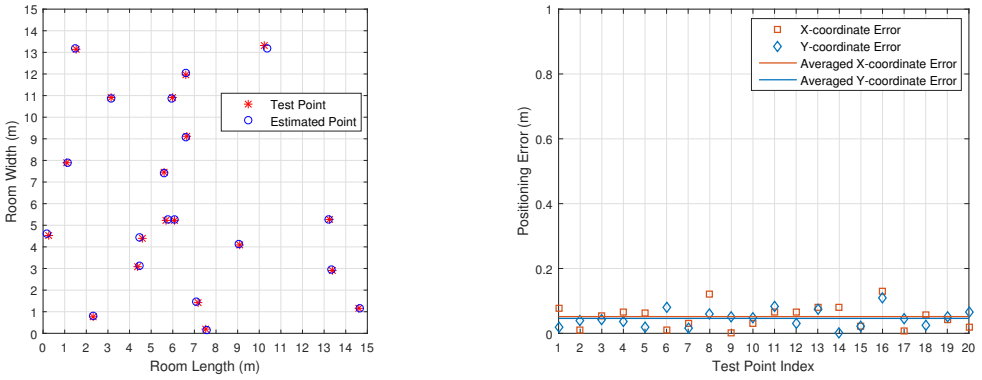

(a) Positioning results

(b) Positioning errors of each test point

Figure 3.17: Fingerprinting-based visible light positioning with the tile size of 0.15×0.15 m^2 under $\Psi_{\text{FoV}} = 100^o$, considering both the LoS and the first reflected visible-light rays.

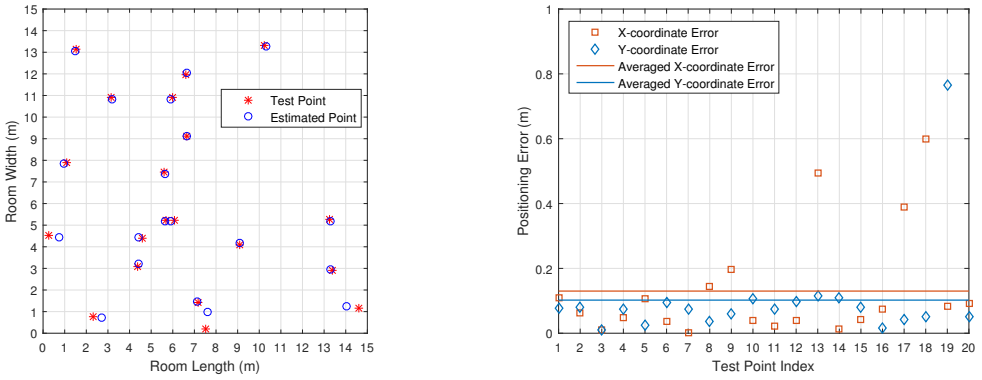

(a) Positioning results

(b) Positioning errors of each test point

Figure 3.18: Fingerprinting-based visible light positioning with the tile size of 0.25×0.25 m^2 under $\Psi_{\text{FoV}} = 100^o$, considering only the LoS visible-light rays.

performance than triangulation at small FoV values. Recall from Figs. 3.8 and 3.11 that the triangulation almost fails at $\Psi_{\text{FoV}} = 80^o$. By contrast, as demonstrated in Fig. 3.19, all test points can be successfully estimated, where the average positioning error is around 20 cm, which we believe can be further reduced upon increasing the tile density.

Based on these investigations, we have found that the VLC-aided positioning performance of fingerprinting is attractive. However, its high complexity is a major concern, when invoking this positioning technique in VLC. On the other hand, the positioning accuracy of triangulation is quite high in some scenarios. Inspired by these findings, instead of relying on a single positioning technique, a hybrid positioning is proposed for VLC-aided positioning, as detailed in the next section.

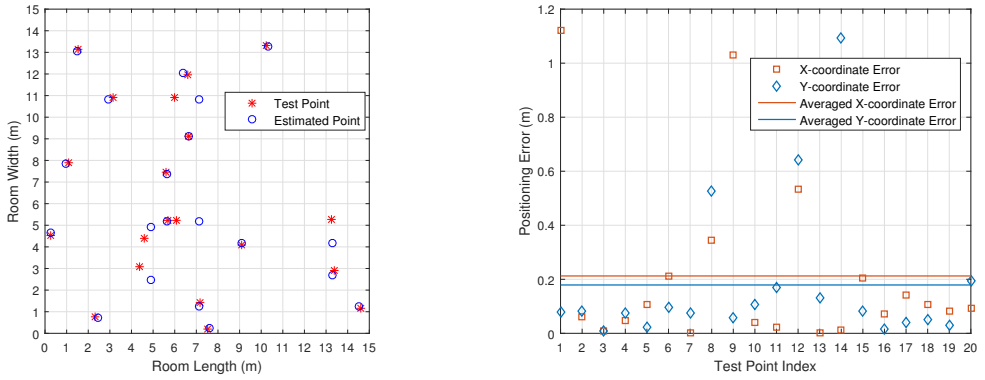

(a) Positioning results

(b) Positioning errors of each test point

Figure 3.19: Fingerprinting-based visible light positioning with the tile size of 0.25×0.25 m^2 under $\Psi_{\text{FoV}} = 80^o$, considering both the LoS and the first reflected visible-light rays.

3.4.3 Hybrid Positioning for VLC-Aided Positioning

Figure 3.20 shows the position error as a function of the FoV for both the triangulation and for the fingerprinting aided visible light positioning with different tile sizes in the database, while both the LoS and the reflected visible light rays are considered. In this figure, the position error is simply the Euclidean distance between the UE's true position and estimated position. As we can see, fingerprinting-based visible light positioning is capable of achieving a lower positioning error in a wide FoV range than that of the triangulation-based visible light positioning. Furthermore, we observe that, by collecting denser tiles in the database of the fingerprinting, more accurate positioning results can be expected, while its price is a higher complexity. As discussed above, triangulation-based positioning exhibits a low complexity and a beneficial scene independence, but its outage probability is approaching 1 when the FoV is insufficiently high, which implies that triangulation fails in those scenarios, as shown in Fig. 3.21. By contrast, although the accuracy of fingerprinting is not as high as that of triangulation, its outage probability is close to zero, regardless of the FoV values. Hence, we propose a hybrid positioning technique, combining the advantages of both to achieve a compelling balance between the complexity and accuracy.

More explicitly, there are four steps dedicated to realizing our hybrid positioning:

1. *Preliminary:* At this step, we build the fingerprinting database for the room, where the room is divided into $Q = q \times q$ number of tiles, while the location information associated with its RSS vector $\bar{\boldsymbol{p}}_i \in \mathbb{R}^{(|\mathcal{M}|\times 1)}$, $i = 1, 2, \cdots, Q$ is held in the database;

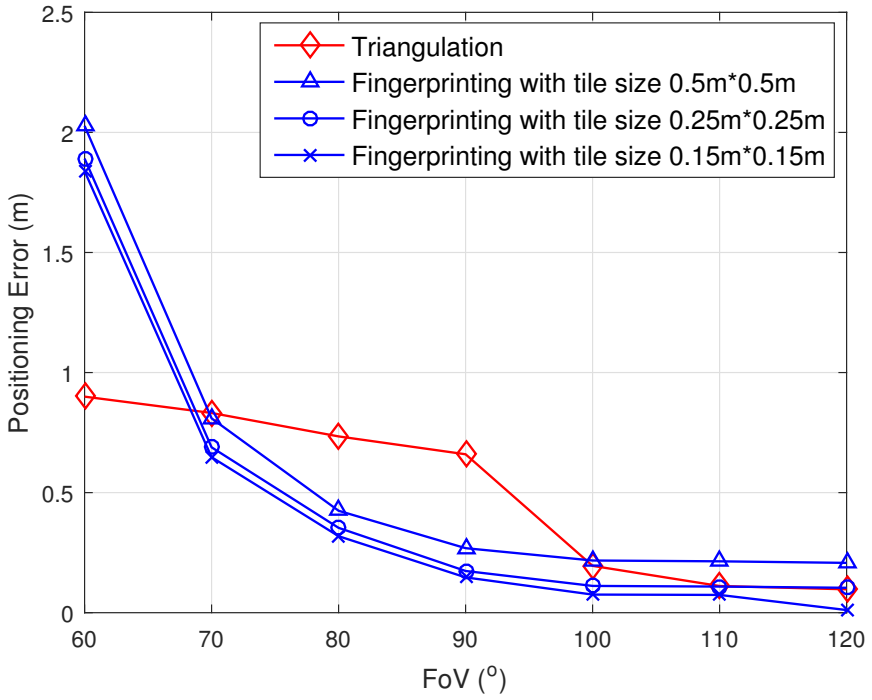

Figure 3.20: Positioning error as a function of the FoV for both the triangulation-based positioning and for the fingerprinting solution for a different tile size in database.

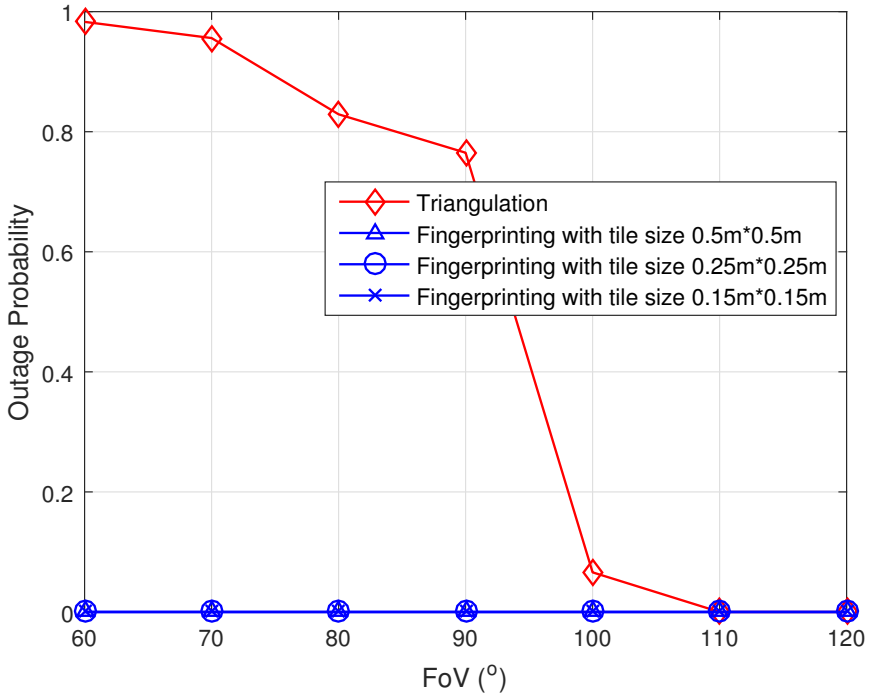

Figure 3.21: Probability of the outage points for both the triangulation and the fingerprinting based visible light positioning, according to Fig. 3.20.

2. *Coarse-Positioning:* At this step, the triangulation is invoked to estimate the UEs' positions. Each estimated position is classified into its corresponding tile of the database and returns the likelihood of being associated with that specific tile;

3. *Evaluation:* Since the location of the UE is unknown to the central controller during the positioning process, the RSS information is invoked for evaluating the triangulation-based positioning. If the RSS difference[3] between that of UE k and its associated tile is lower than a threshold Υ, UE k is deemed to belong to the accepted set. Otherwise, it belongs to the rejected set[4];

4. *Re-Positioning:* For those positioning results in the accepted set, no further actions will be applied and the estimated position is confirmed based on the triangulation. For those results in the rejected set, fingerprinting will be invoked for re-evaluating positioning.

By combining both positioning techniques, the total complexity is reduced compared to plain fingerprinting. At the same time, the average positioning accuracy may be enhanced at a wider range of FoV values, when compared to stand-alone triangulation-based positioning.

3.5 Performance Results

Let us now provide simulation results for characterizing the performance of the proposed hybrid positioning in UC-VLC system. The quality threshold Υ is set to $10e^{-5}$, where the databased is built with tile size of 0.25×0.25 m^2, balancing between the complexity and the positioning accuracy. More simulation parameters are summarized in Table 3.1. We rely on two criteria for evaluating the hybrid positioning, namely the positioning performance and the system throughput, respectively.

3.5.1 Positioning Performance

In this section, the positioning-aided VLC performance is evaluated, where the metrics of positioning accuracy, robustness and scalability are considered. To elaborate a little further, the accuracy of the hybrid positioning is measured based on the average Euclidean distance between the estimated location and the true location. Furthermore, the robustness metric is invoked for characterizing the hybrid positioning when some of

[3]The channel difference of UE k and its associated tile is defined as $|h_k - \bar{h}_i|$, where we have $h_k = \sum_n h_{k,n}$ for the UE and $\bar{h}_i = \sum_n h_{i,n}$ for the tile.

[4]Note that the positioning of some UEs may fail at the coarse-positioning stage due to the interference of reflected rays or insufficient FoVs. Those UEs will be automatically included in the rejected set for re-positioning.

I-1. Environment-Related Parameters	
room size	$15\times15\times3$ m^3
AP height H_t	2.5 m
number of APs $\lvert\mathcal{N}\rvert$ (changed in Fig. 3.27, 3.28)	8×8
UE height H_r	0.85 m
number of UEs $\lvert\mathcal{K}\rvert$ (change in Fig. 3.22)	20
blocking probability $\mathbb{P}_{\text{bl}}$ (changed in Fig. 3.24, 3.25)	0
I-2. VLC Channel-Related Parameters	
semi-angle at half-illumination $\phi_{1/2}$	60^o
gain of optical filter $g_{of}(\psi)$	1
gain of optical concentrator $g_{oc}(\psi)$	1
physical area for a PD receiver A_s	1 cm^2
reflection coefficient ρ	0.75
refractive index ϱ	1.5
O/E conversion efficiency γ	0.53 A/W
FoV ψ_{FoV} (change in Fig. 3.22, 3.29 - 3.31)	90^o
I-3. Positioning-Related Parameters	
quality threshold Υ	$10e^{-5}$
tile size $q \times q$	0.25m × 0.25m
I-4. Physical-Link-Related Parameters	
modulation bandwidth B	20 MHz
AWGN power spectral density N_0	10^{-22} A^2/Hz
transmit power $P_{\text{Tx,elec}}$	1 W
DC bias in DCO-OFDM P_{bias}	10 mW
limited linear power range $[P_L, P_H]$	[1 mW, 30 mW]
I-5. Clustering-Related Parameters	
radius r in radius based UC-clustering	4 m
UE distance threshold d_u in centre-dynamic UC-clustering	2 m
AP distance threshold d_a in centre-dynamic UC-clustering	3 m

Table 3.1: List of Parameters in Chapter 3

the RSS values are blocked, which is commonly encountered in VLC due to the LoS-dominated propagation characteristics. Moreover, we also consider the scalability of the proposed hybrid positioning in various AP density scenarios.

3.5.1.1 Accuracy

We quantify the accuracy of the proposed hybrid positioning, when the number of target UEs $\lvert\mathcal{K}\rvert$ equals to 10, 20 and 30, under various FoV values, as shown in Fig. 3.22. Observe in the figure that the outage probability of the proposed hybrid positioning is close to zero, regardless of the FoV value. Since we know that the majority of UE locations cannot be estimated by triangulation when the FoV is narrow, according to Fig. 3.21, the second-stage of our hybrid positioning is invoked, therefore the outage probability can be significantly reduced. Furthermore, since triangulation performs poorly for all

UEs when the FoV is insufficient, the positioning error of the hybrid positioning is similar to that of fingerprinting (shown in Fig. 3.20). Upon increasing the FoV value, the positioning error of the hybrid positioning becomes capable of approaching that of the triangulation, where the fingerprinting will only be applied to a small fraction of UEs, which remarkably reduces the positioning complexity.

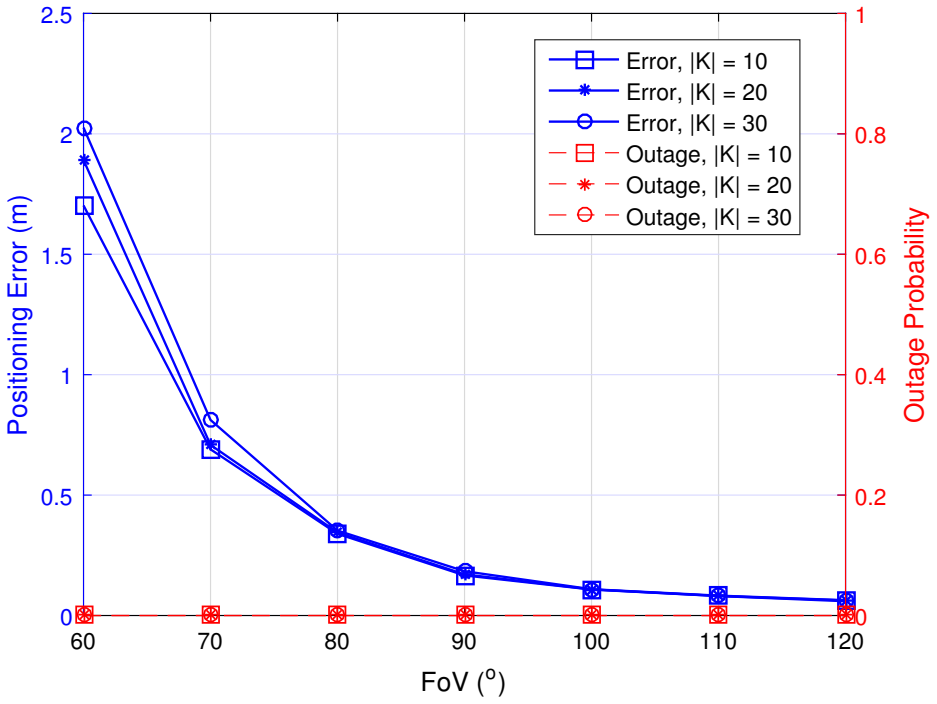

Figure 3.22: Positioning error associated with the outage probability of the hybrid positioning technique in visible light positioning as a function of FoV in different UE density scenarios.

3.5.1.2 Robustness

We are also interested in characterizing the robustness of the proposed hybrid positioning. Since the LoS ray can be blocked, in this situation, the positioning has to use its incomplete information to estimate the locations. As a benchmark, Fig. 3.23 presents the positioning results of both triangulation and of hybrid positioning at every location of the simulated room without any blocking. For visual clarity, the positioning error tolerance ι is set to 0.3 m, so that if the difference of the estimated position and the true position is larger than ι, the position will be marked by blue color, otherwise, it will be yellow color. It can be observed from Fig. 3.23(b) that hybrid positioning succeeds in most of the locations, only a few locations at the edge of the room cannot satisfy the threshold ι. By contrast, the accepted positioning set of the triangulation is much smaller than that of the hybrid positioning, as shown in Fig. 3.23(a), only the points

located at the propagation intersection of several APs can be estimated with an error less than ι.

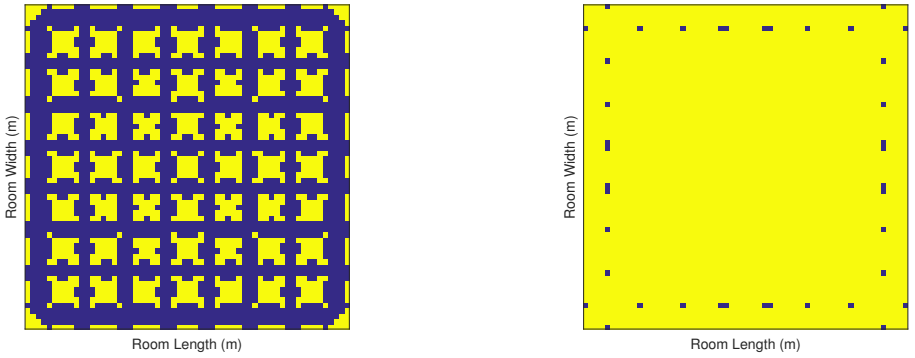

(a) Triangulation positioning (b) Hybrid positioning

Figure 3.23: Positioning for the whole room aided by (a) triangulation and (b) hybrid positioning with blocking probability $\mathbb{P}_{\text{bl}} = 0$, under FoV of 90^o. Blue area presents the estimated position with error larger than 0.3 m, while the yellow area represents the acceptable positioning results with the positioning error is less than 0.3 m.

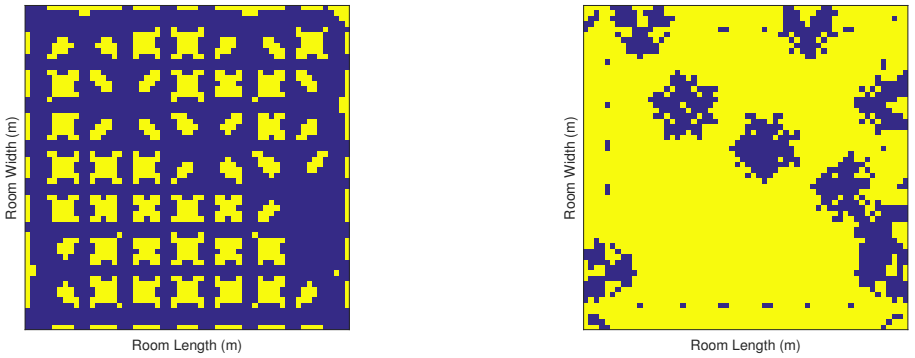

(a) Triangulation positioning (b) Hybrid positioning

Figure 3.24: Positioning for the whole room aided by (a) triangulation and (b) hybrid positioning with blocking probability $\mathbb{P}_{\text{bl}} = 0.15$, under FoV of 90^o. The acceptable estimated locations are marked by yellow color, while blue color for those unacceptable locations.

To explore the influence of the LoS blocking probability $\mathbb{P}_{\text{bl}}$ on the positioning results, Figs. 3.24 and 3.25 characterize the triangulation and the hybrid positioning at blocking probabilities of 0.15 and 0.23, respectively. Specifically, in Fig. 3.24, a total of 10 randomly selected APs are blocked, which means that no position estimates are available for those 10 APs. Compared to the no-blocking scenario, the probability of unacceptable positioning results of both the triangulation and of the hybrid positioning

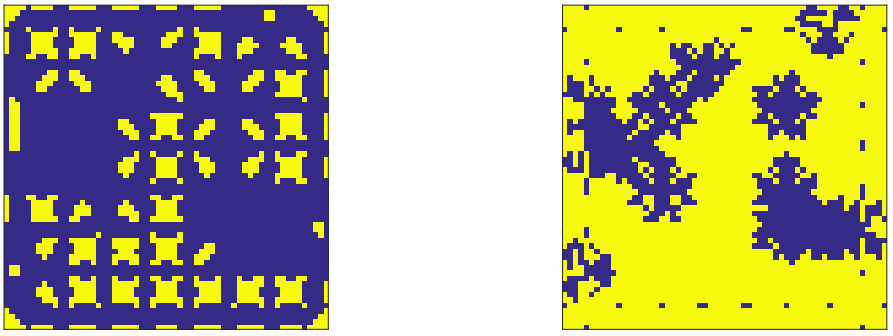

(a) Triangulation positioning (b) Hybrid positioning

Figure 3.25: Positioning for the whole room aided by (a) triangulation and (b) hybrid positioning with blocking probability $\mathbb{P}_{\text{bl}} = 0.23$, under FoV of 90^o. The acceptable estimated locations are marked by yellow color, while blue color for those unacceptable locations.

is increased, but hybrid positioning still outperforms triangulation. When the blocking probability is increased, say a total of 15 APs are blocked, observe in Fig. 3.25 that the hybrid positioning is still capable of estimating the majority of locations within the error tolerance. Therefore, it may be inferred that the proposed hybrid positioning has a higher robustness than that of triangulation, since the hybrid positioning is still capable of functioning adequately, when some of the APs are blocked.

3.5.1.3 Scalability

The scalability is used for characterizing the performance of positioning, when the positioning scope changes. We evaluate the scalability in terms of two aspects, which are the UE density and the AP density for the given room. To elaborate a little further, as shown in Fig. 3.22, we see that the positioning error in a dense UE scenario is higher than that of the sparse UE scenario. However, this difference may be eliminated upon increasing the FoV values. To explore the influence of AP density, the logarithmic positioning error relying on a total of $8 \times 8 = 64$ APs is evaluated across the entire room, as shown in Fig. 3.26. The corresponding normalized AP density is defined as the number of APs divided by the room area, which is $0.28/\text{m}^2$. Observe by comparing Fig. 3.26(b) and Fig 3.26(a) that the positioning error recorded for our hybrid technique at the edge of the room is reduced to about 1 m from about 10 m seen for the triangulation-based positioning. When we reduce the normalized AP density to $0.1/\text{m}^2$ by reducing the number of APs to $5 \times 5 = 25$, triangulation-based positioning and hybrid positioning may be compared in Fig. 3.27. As expected, the performance of triangulation is significantly degraded, whilst the positioning accuracy relying on hybrid positioning is only

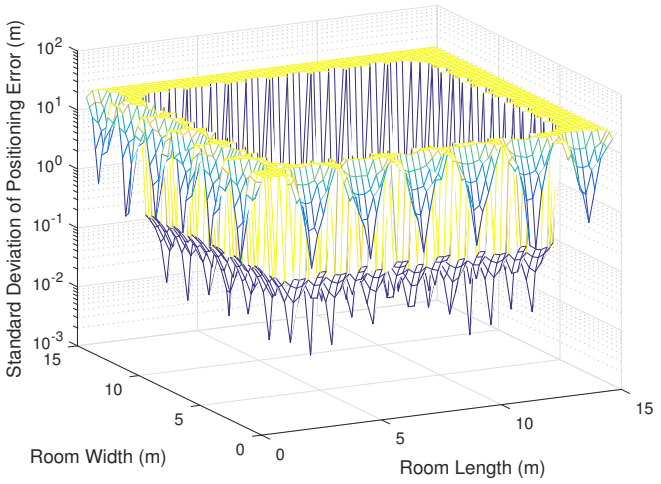

(a) Standard deviation of positioning error distribution using triangulation based positioning

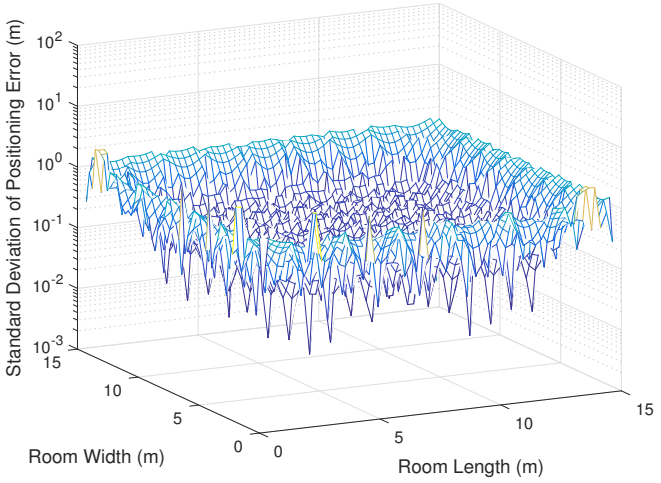

(b) Standard deviation of positioning error distribution using hybrid positioning

Figure 3.26: Comparison of positioning accuracy between hybrid positioning and triangulation based positioning with AP density of $0.28/\mathrm{m}^2$.

slightly reduced. Finally, when increasing the AP density to $0.87/\mathrm{m}^2$, observe in Fig. 3.28 that triangulation still has an estimation standard deviation of about 10 m at the corner points, where it suffers from the strongest reflections and scattering. By contrast, our hybrid positioning reduces it to around 1 m in the corners and to about 0.1 m or less in other positions. In general, the positioning performance degrades when the distance between the AP and the UE increases. We find that the positioning performed by the proposed hybrid positioning technique is capable of resisting that issue, even in quite sparse AP distribution (in Fig. 3.27), most of the position can be estimated at centimetre-level. Based on the above observations, it can be inferred that

the proposed hybrid positioning is quite accurate right across the room considered with high-level scalability, while dispensing with the full ML test of all UEs relied upon by fingerprinting-based positioning.

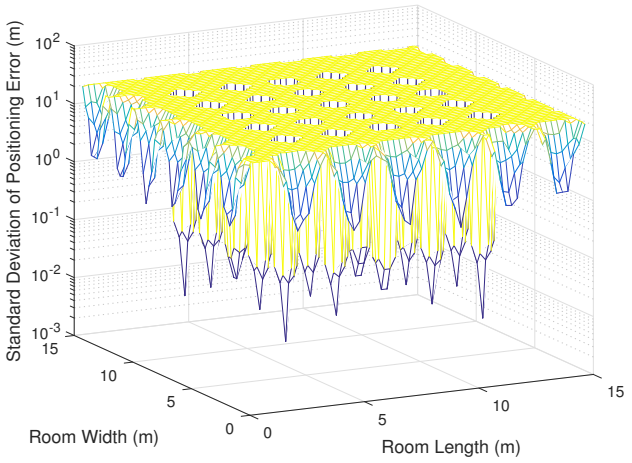

(a) Standard deviation of positioning error distribution using triangulation based positioning

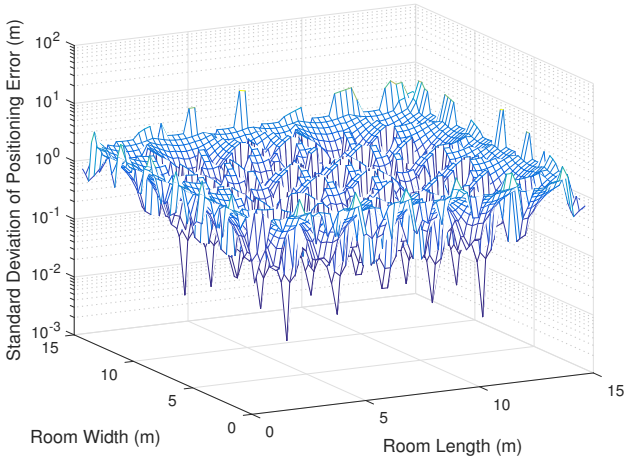

(b) Standard deviation of positioning error distribution using hybrid positioning

Figure 3.27: Comparison of positioning accuracy between hybrid positioning and triangulation based positioning with AP density of $0.1/\mathrm{m}^2$.

3.5.2 System Throughput

In this section, the throughput is evaluated in our proposed UC-VLC system relying on UC-clustering. For each transmission link, ACO-OFDM is adopted. The UC-clusters are constructed based on the estimated UE locations. The system's throughput can be calculated according to Table 2.1, as we analysed in Chapter 2. The throughput achieved

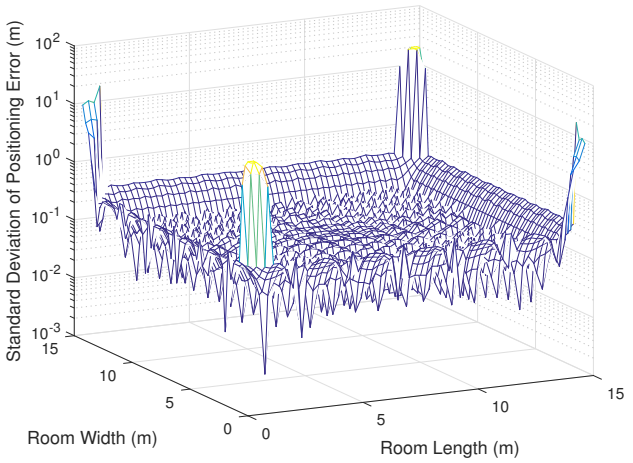

(a) Standard deviation of positioning error distribution using triangulation based positioning

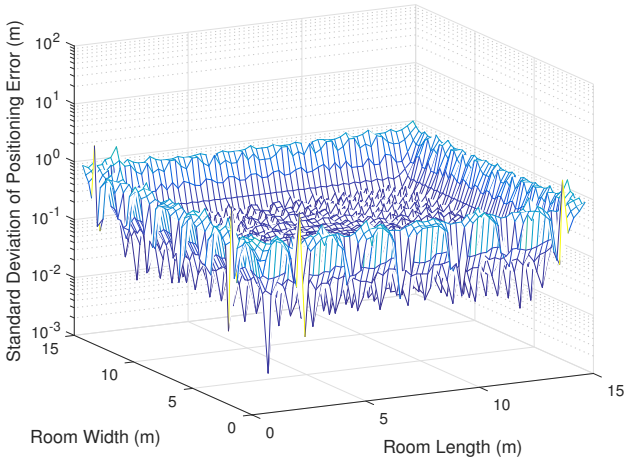

(b) Standard deviation of positioning error distribution using hybrid positioning

Figure 3.28: Comparison of positioning accuracy between hybrid positioning and triangulation based positioning with AP density of $0.87/m^2$.

with the aid of perfect/imperfect positioning for different FoV values is explored in the absence of clipping distortion in Fig. 3.29 and in the presence of clipping distortion in Fig. 3.30. When compared to triangulation-based positioning, the hybrid positioning performs significantly better for low FoV values in both scenarios. Explicitly, when the FoV is lower than 70^o, triangulation-based positioning fails, because the FoV is too low for adequately selecting three different reference APs required for positioning. On the other hand, the system's throughput achieved with the aid of hybrid positioning tends to be similar to that of fingerprinting, despite its lower complexity. Finally, both the fingerprinting and the hybrid positioning achieve a similar system throughput to that of perfect positioning, regardless of the specific level of performance considered.

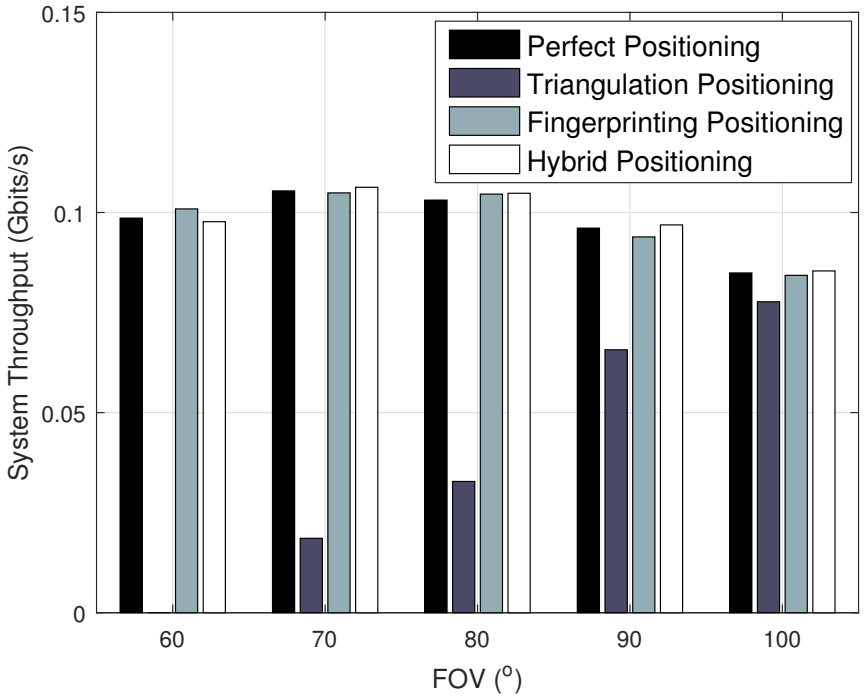

Figure 3.29: System throughput comparison between different positioning techniques as a function of FoV values in the absence of clipping distortion.

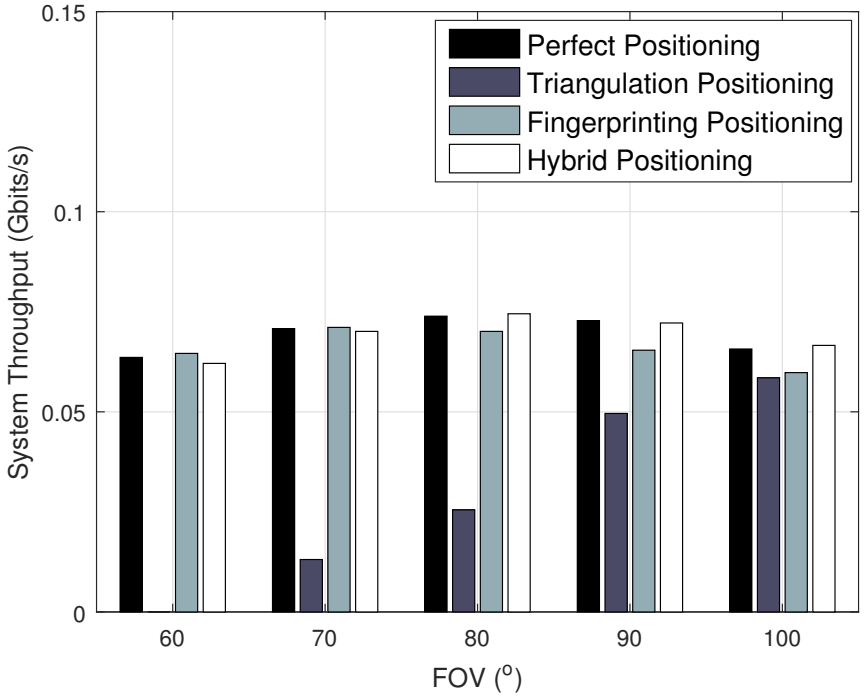

Figure 3.30: System throughput comparison between different positioning techniques v.s. the FoV, with non-negligible clipping distortion.

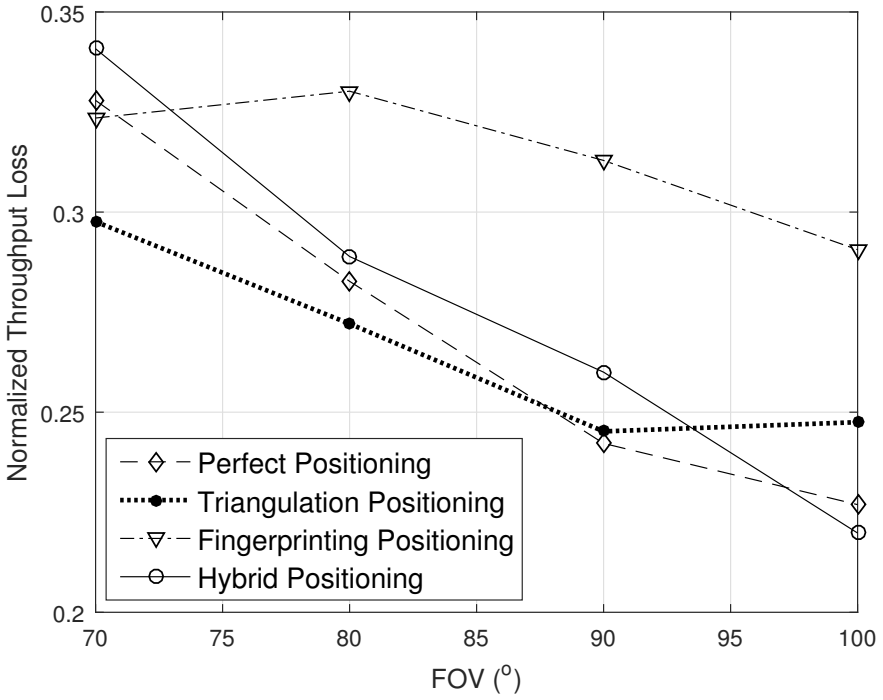

Figure 3.31: Normalized throughput loss as a function of the FoV for different positioning techniques.

Explicitly, Fig. 3.31 shows the normalized throughput loss of all positioning techniques due to the clipping distortion. The normalized throughput loss is calculated as the difference between the throughput associated with no clipping distortion and having non-negligible clipping distortion, which is further normalized with respect to the throughput associated with no clipping. It can be seen from this figure that when the FoV is high, the proposed hybrid positioning suffers from the lowest normalized throughput loss, approaching the throughput of the perfect positioning scenarios. On the other hand, fingerprinting based positioning suffers from the most grave normalized throughput loss. Finally, a common trend for all positioning techniques is that the normalized throughput loss becomes higher, when the FoV is lower. This is because when the FoV is low, the clipping distortion effects tend to dominate, while the interference effects dominate for higher FoVs.

3.6 Chapter Conclusions

In this chapter, we proposed a novel hybrid positioning technique for achieving the flexible construction of UC-clusters for indoor VLC under practical LED linearity constraints in the face of both clipping distortion and noise. More explicitly, by amalgamating the benefits both of triangulation and of fingerprinting, the proposed hybrid positioning

technique becomes capable of achieving a much higher positioning accuracy than triangulation at a lower complexity than fingerprinting, right across the entire room and for a range of FoV values. Furthermore, the robustness and the scalability of the proposed technique were demonstrated to be better than that of triangulation. The resultant system throughput is also similar to that of perfect positioning, even under contamination by clipping distortion.

3.7 Chapter Summary

As the key technique of supporting the UC-clustering conceived in Chapter 2, the positioning techniques conceived for indoor VLC UEs have been investigated in this chapter. The feasibility of relying on visible light to estimate indoor locations was outlined in Section 3.3, yielding the concept of visible light positioning. In Section 3.4, two indoor positioning techniques, namely triangulation and fingerprinting were analysed in the context of VLC-aided positioning. The estimated locations obtained by triangulation were observed to be affected by the FoV and by the reflected visible light rays, as shown in Figs. 3.6 - 3.11. Furthermore, the robustness and the scalability of triangulation in VLC-aided positioning is quite poor, as seen in Figs. 3.12 - 3.14, since both the blocking and the number of APs have a serious impact on its positioning performance. As for fingerprinting in VLC-aided positioning, we demonstrated in Section 3.4.2 that its positioning accuracy strongly relies on how dense the tiles in the database are. As expected, the smaller the size of the tiles we hold in the database for the room, the more accurate positioning results can be obtained, as shown in Figs. 3.15 - 3.17. As demonstrated in Fig. 3.21, the probability of outage points was approaching to zero in fingerprinting under all simulated FoV values, while triangulation was rather disfunctional when the FoV was small. However, the price of using fingerprinting is its increased complexity, since during the on-line stage, the comparison between each target point and each tile obtained during off-line stage is based on a degree of $|\mathcal{N}|$. The complexity was expected to be significantly increased, if smaller tiles were used by the databased to attain a higher accuracy. Based on the advantages and the disadvantages both of triangulation and of fingerprinting, a hybrid positioning scheme was proposed for visible light positioning in Section 3.4.3, where triangulation is invoked for coarse-positioning, while fingerprinting for second-stage positioning, so that the outage probability becomes low and the complexity is also reduced. The performance of hybrid positioning was evaluated in terms of its accuracy (Fig. 3.22), its robustness (Figs. 3.23 - 3.25) and scalability (Figs. 3.27 - 3.28), which shows that the positioning accuracy is quite low across the room, while hybrid positioning becomes capable of operating in the face of blocking. Moreover, due to its accurate positioning, the throughput achieved by our UC-VLC system relying on hybrid positioning approaches that of the one relying on perfect positioning, which was

verified both in the absence of clipping distortion (Fig. 3.29) and in the presence of clipping distortion (Fig. 3.30).

Chapter 4

Dynamic Resource Allocation

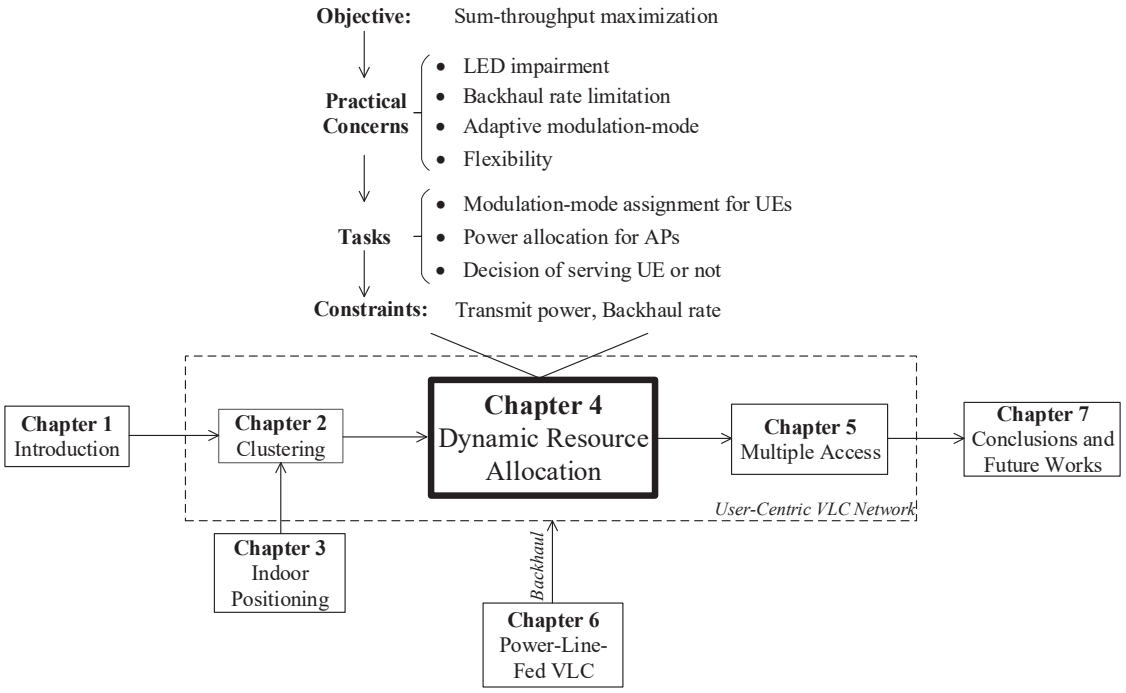

Figure 4.1: Block diagram of Chapter 4.

4.1 Introduction

The concept of centre-shifting UC-clusters invoked for VLC was shown to offer extra throughput benefits over the conventional NC-VLC, which was demonstrated in Chapter 2. Note that the position information required by UC-clustering can be obtained by the hybrid positioning we proposed in Chapter 3. However, this improvement was quantified

based on a number of idealized simplifying assumptions, such as operating exactly at the Shannon capacity. Furthermore, greedily supporting all the UEs in the system may in fact reduce the achievable throughput, when the transmit power is restricted. To provide more practical performance estimates, in this chapter, we will explore an efficient resource allocation conceived for ensuring that the sum-throughput of the UC-VLC system is maximized under a range of practical considerations, such as LED impairments. To elaborate a little further, instead of relying on the Shannon-capacity-based throughput, channel-quality-dependent adaptive modulation-mode assignment will be introduced into our UC-VLC network. To maximize the sum-throughput, dynamic resource allocation will be proposed, where the modulation-mode assignment will be jointly optimized with the power allocation, under both transmit power and backhaul rate constraints.

The remainder of this chapter is organized as follows. Section 4.2 discusses four practical considerations in the resource allocation of our UC-VLC systems. Then a constrained throughput maximization problem is formulated in Section 4.3. In Section 4.4, we propose a dynamic-programming-based resource allocation strategy aims for solving this maximization problem by jointly assigning the modulation-modes and power. Next, our performance results are provided in Section 4.5. Finally, the chapter is concluded in Section 4.6.

4.2 Practical Considerations

Before investigating the resource allocation of our UC-VLC network, several practical considerations are discussed in this section. As shown in Figure 4.2, the clipping-distortion has a detrimental impact on the UC-VLC performance, but there is a paucity of contributions on this issue in VLC system-level design. Besides, since the VLC network relies on a wired backbone, any backhaul rate constraint will have a profound impact on it, especially on the multi-AP-multi-UE structure of UC-VLC. Instead of relying on Shannon capacity for our system-level design, each UE is assigned a specific practical modulation-mode, which is coupled with the required transmission power, leading to much more sophisticated resource allocation. Furthermore, flexibility is another important factor when considering the resource allocation in this multi-AP-multi-UE scenario. The standard greedy resource allocation has to be re-examined in our resource-limited scenario. Our more detailed discussion are as follows.

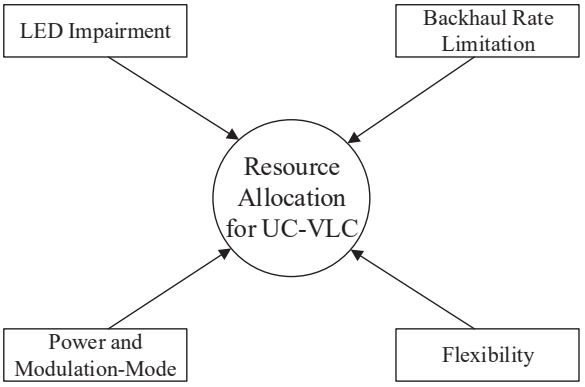

Figure 4.2: Practical considerations for UC-VLC when we deal with the resource allocation.

4.2.1 LED Impairments

Due to the non-ideal current-voltage transfer characteristic of LED, there is only a limited linear dynamic range for high-quality transmission, which is maximized by the signal pre-distortion [130]. Therefore, the signal peaks exceeding this linear range have to be distorted and clipped, which imposes undesirable non-linear clipping-distortion [129]. More details on clipping-distortion are provided in Section 2.2. According to the simulation results provided in Section 2.5, the non-negligible clipping-distortion degrades the throughput to different degrees, depending on the FoV and on the UE density. Additionally, a DC-bias is required by both ACO/DCO-OFDM to mitigate the impairments imposed by clipping-distortion, as we discussed in Section 2.2. Considering DCO-OFDM as an example, the more the DC-bias approaches half of the dynamic range, the lower the clipping-distortion becomes. However, the more the power is used for biasing, the less power can be allocated for transmission, when the total transmit power is restricted. Therefore, the power allocation has to be carefully considered when we take into account the LED's impairments.

4.2.2 Backhaul-Rate Limitation

The backbone of the VLC network also requires special attention [135]. Thanks to the power lines already installed behind the LEDs, it is a natural candidate for supporting VLC, and acting as the backhaul [92]. Figure 4.3 depicts the wiring system of VLC, where the power line is invoked for connecting VLC with the backbone network. To this end, the integration of power lines and VLC is cost efficient, where the power line is exploited to provide both data transmission and powering, while the dual function of LED is that of lighting and communications. For simplicity, in this chapter we omit the transmission loss in power line, and set the backhaul rate constraint for each AP to R^{BH},

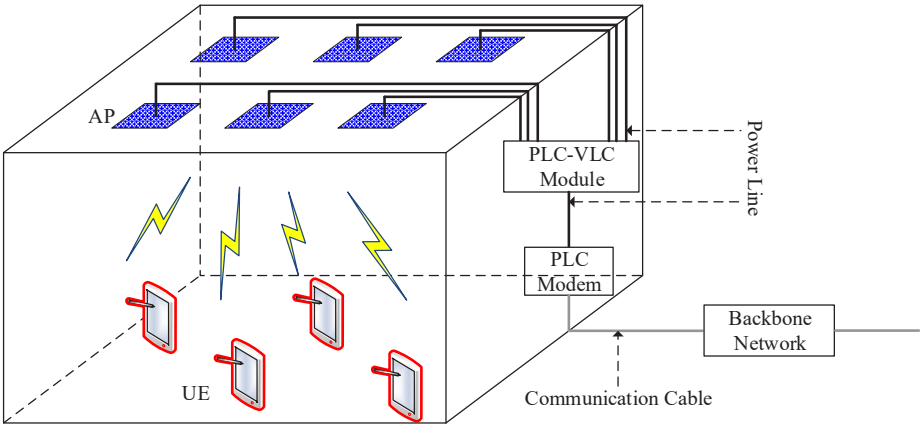

Figure 4.3: PLC-fed VLC network.

which means that the maximum affordable tele-traffic of each AP should not exceed this value. Note that the detailed investigation of the integration of power line and VLC will be explored in Chapter 6. Therefore, with the aim of simultaneously supporting several UEs by invoking VT within each UC-cluster, each AP faces the challenge of limited backhaul rate. This will have a profound impact on the QoS, since the UEs are considered only if their associated APs have sufficient backhaul capacity [136]. Therefore, the limited backhaul rate constraint may restrict the transmission capability of each AP, potentially resulting in a throughput bottleneck. We will consider this important issue when designing resource allocation for our UC-VLC system.

4.2.3 Adaptive Modulation-Mode Assignment

Most of the previous researches in terms of resource allocation relied on the idealized simplifying assumption of operating exactly at Shannon capacity [29, 60, 76]. Although the Shannon capacity is capable of providing the theoretical upper-bound of the system's transmission capability under idealized settings, it fails to reflect the practically achievable throughput. Specifically, the sum-throughput of various UEs is hard to attain, when those UEs experience different channel conditions and are assigned by individual realistic modulation-modes. Hence, we will quantify the modulation-mode-dependent throughput in this section. To elaborate, instead of evaluating the Shannon-capacity-based throughput in the UC-VLC network, we are more interested in the throughput attained by practical modulation-modes, such as the classic multi-level quadrature amplitude modulation (M-QAM). In order to obtain the maximum sum-throughput in UC-VLC, an efficient adaptive modulation-mode assignment algorithm is required. By employing the VT within each constructed UC-cluster, the modulation-mode decision of a specific UE is related not only to the channel condition of itself, but also to the channel qualities and modulation-modes of the other UEs in the same cluster. Hence, it

is a challenging multi-user-dependent modulation-mode assignment. Furthermore, it is plausible that a higher-order modulation-mode leads to a higher rate, but the associated cost in terms of its power requirement is also increased. Since in practice the transmit power of each AP is confined, the modulation-mode assignment of UEs has to be considered in conjunction with the power allocation of the associated APs. It indicates that the pair of variables namely the power and the modulation-mode are coupled with each other. To be specific, the modulation-mode assignment indicates the power allocation, however, due to the power constraint, the modulation-mode assignment, in turn, is affected by the power. This interdependent relationship between the power allocation and the modulation-mode assignment makes the maximization problem even more complex. However, most of the previous allocation strategies fix one of the variables and optimize the other one, which is inefficient [137–139]. In this chapter, we aim for maximizing the sum-throughput in UC-VLC by jointly allocating the power to each AP and the modulation-mode to each UE.

4.2.4 Flexibility

Most of the previous research on sum-throughput maximization greedily supported all of the UEs in the system, which may in fact be inefficient, especially under limited transmit power and backhaul rate scenario. Specifically, if the channel qualities of certain UEs are unsatisfactory, allocating more power to them is futile, because it wastes resource and imposes excessive interference. Furthermore, if the sum-throughput exceeds the backhaul rate constraint, all the UEs' packets have to be dropped due to the greedy strategy, instead of reducing the number of served UEs. Against this background, we propose to selectively serve the UEs. To elaborate a little further, rather than greedily supporting all the UEs, the number of served UEs in the UC-VLC is dynamically selected, purely relying on the principle of sum-throughput maximization. Furthermore, due to the multi-user-dependent feature we discussed above, the modulation-mode assignment is also dynamically adjusted for the UEs. Therefore, the sum-throughput is maximized depending on dynamically determining the number of served UEs as well as the adaptive modulation-mode assignment, which significantly increases the flexibility of the network.

4.3 Constrained Problem Statement

In this section, our maximization problem is formulated under the practical impairments and distortions mentioned above. To begin with, the TPC is invoked within each constructed UC-cluster to eliminate the MUI. Then the achievable throughput is considered in the face of non-negligible clipping-distortion. Finally, the MUI-free but

clipping-distortion-contaminated throughput maximization problem is proposed under practical backhaul rate and transmit power constraints.

4.3.1 Link-Level Transmission

Unfortunately, the constructed multi-AP-multi-UE structure within each UC-clusters sustains MUI. To eliminate, VT is employed in link level with the aid of TPC. Furthermore, each transmission link between an AP and a UE invokes either ACO-OFDM or DCO-OFDM, which suffers from clipping distortion due to the non-linear characteristics of LEDs. Explicitly, In each UC-cluster, MUI is imposed in the overlapping coverage area of two or more attocells. Here the coverage area of attocell is defined as the area receiving both the LoS and the first reflected rays, provided that its RSS is higher than a certain minimum acceptable value. To mitigate the MUI, we invoke the ZF-based VT technique at the AP-end. To be more explicit, the multi-user system model within cluster $\mathcal{C}_c$ may be formulated as:

$$\boldsymbol{y}_c = \boldsymbol{H}_c \boldsymbol{G}_c \boldsymbol{P}_c \boldsymbol{x}_c + \boldsymbol{\tau}_c, \tag{4.1}$$

which processes the transmit signal vector $\boldsymbol{x}_c \in \mathbb{R}^{(|\mathcal{K}_c|\times 1)}$ by the TPC matrix $\boldsymbol{G}_c \in \mathbb{R}^{(|\mathcal{N}_c|\times|\mathcal{K}_c|)} = \boldsymbol{H}_c^H(\boldsymbol{H}_c\boldsymbol{H}_c^H)^{-1}$ and by the optical channel matrix $\boldsymbol{H}_c \in \mathbb{R}^{(|\mathcal{K}_c|\times|\mathcal{N}_c|)}$, hence resulting in the MUI-free received signal $\boldsymbol{y}_c \in \mathbb{R}^{(|\mathcal{K}_c|\times 1)}$. Furthermore, $\boldsymbol{P}_c = \text{diag}\{\boldsymbol{p}_c\}$ is the allocated power matrix, which needs to be determined, where the kth element of $\boldsymbol{p}_c$ is the power required by UE k in the cth cluster. Moreover, we have $\boldsymbol{\tau}_c = [\tau_{c,1}, \tau_{c,2}, \cdots, \tau_{c,|\mathcal{K}_c|}]^T$, where $\tau_{c,k} = N^{\text{awgn}} + N_{c,k}^{\text{clip}} + I_{c,k}$. To elaborate, N^{awgn} stands for the AWGN having a variance of σ_{awgn}^2, while $N_{c,k}^{\text{clip}}$ and $I_{c,k}$ denote the clipping distortion having a variance of $\sigma_{\text{clip},c,k}^2$, and the ICI of UE k in the cth cluster, respectively.

4.3.2 Problem Formulation

To provide flexibility, a number of $|\mathcal{M}|$ modulation-modes are available for UEs, which is held in the modulation-mode set $\mathcal{M}$. To elaborate a little further, for the mth modulation-mode in the set $\mathcal{M}$, a specific square QAM scheme having the constellation size of 2^{2m} is employed. Given a specific target BER, the minimum SINR γ_m required for the mth modulation-mode is derived from [140]:

$$\gamma_m = \frac{2(2^{2m}-1)}{3}\left[\text{erfc}^{-1}\left(\frac{m2^m\text{BER}}{2^m-1}\right)\right]^2. \tag{4.2}$$

Taking into account the aforementioned clipping-distortions, the power required by UE k in the cth cluster, assigned with the mth modulation-mode, is represented as:

$$p_{c,k,m} = \gamma_m \eta (\sigma^2_{\text{awgn}} + \sigma^2_{\text{clip},c,k} + I_{c,k}), \tag{4.3}$$

where we have [129]:

$$\begin{aligned} \eta =& \frac{G_{\text{B}}^2}{\left[Q(\lambda_{\text{bottom}}) - Q(\lambda_{\text{top}})\right]^2 G_{\text{DC}}}, \quad \sigma^2_{\text{clip},c,k} = \frac{\sigma^2 G_{\text{DC}}}{G_{\text{B}} \sum\limits_{n \in \mathcal{N}_n} [\boldsymbol{G}_c]^2_{(n,k)}}, \\ I_{c,k} =& \frac{1}{\eta} \sum_{l=1, l \neq n}^{|\mathcal{C}|} \sum_{n \in \mathcal{N}_l} [\boldsymbol{H}_l]^2_{(k,n)} P^{\text{tx}}_{\max}. \end{aligned} \tag{4.4}$$

Note that the variance of clipping-distortion σ^2 and the attenuation factor G_{DC} can be obtained for both the ACO-OFDM and the DCO-OFDM according to Eqs. (2.7), (2.9), (2.15) and (2.16). In addition, G_{B} represents the bandwidth utilization factor, where in DCO-OFDM it approximates to 1, while in ACO-OFDM is 0.5. Moreover, $\sigma^2_{\text{awgn}} = N_0 B$ is the AWGN noise, where N_0 is the power spectral density, and $\sigma^2_{\text{clip},c,k}$ shows the clipping distortion for UE k in the cth cluster. Finally, $I_{c,k}$ denotes the ICI for the UE k arriving from all other cells except for the current cell. Note that $P^{\text{tx}}_{\max}$ represents the maximum transmit power allowance, assuming that the ICI power always remains under its maximum level.

By observing (4.3), it implies that once the modulation-mode assignment is settled for the UEs, their required power can be determined. However, due to the transmit power constraint of each AP, the modulation-mode assignment, in turn, is affected by the power. This interdependent relationship between the modulation-mode assignment and the power allocation makes our maximization problem complicated. Furthermore, global optimization in a joint multi-cluster fashion would result in an excessive complexity. By contrast, our maximization may be independently implemented within each efficiently-constructed cluster, since the UC-clusters are beneficially constructed based on the centre-dynamic UC-clustering strategy proposed in Chapter 2. Rather than greedily supporting all the UEs within each cell, the number of served UEs is dynamically selected, purely relying on the principle of sum-throughput maximization. Here, we define the served UEs as the UEs that can successfully receive information from their associated APs, ensuring both the backhaul constraint and the transmit power constriant. Based on these, the sum-throughput maximization strategy is invoked within each cluster for dynamically determining the number of served UEs, associated with the adaptive modulation-mode assignment as well as power allocation, hence pursuing system level sum-throughput maximization. Mathematically, the maximization problem

of the cth cluster is formulated as:

$$\max_{\mathcal{M}_c^*} \sum_{k=1}^{|\mathcal{K}_c|} \sum_{m=1}^{|\mathcal{M}|} r_{c,k,m} x_{c,k,m} \tag{4.5a}$$

$$\text{s.t. } x_{c,k,m} \in \{0,1\}, \quad \forall k \in \mathcal{K}_c, \ \forall m \in \mathcal{M}; \tag{4.5b}$$

$$\sum_{m=1}^{|\mathcal{M}|} x_{c,k,m} \in \{0,1\}, \quad \forall k \in \mathcal{K}_c; \tag{4.5c}$$

$$\sum_{k=1}^{|\mathcal{K}_c|} \sum_{m=1}^{|\mathcal{M}|} r_{c,k,m} x_{c,k,m} \leq R^{\mathrm{BH}}; \tag{4.5d}$$

$$\sum_{k=1}^{|\mathcal{K}_c|} \sum_{m=1}^{|\mathcal{M}|} p_{c,k,m} x_{c,k,m} \left[\boldsymbol{G}_c\right]_{(n,k)}^2 \leq P_{\max}^{\mathrm{tx}}, \ \forall n \in \mathcal{N}_c. \tag{4.5e}$$

We have $r_{c,k,m}$ to denote the rate attained by UE k in the cth cluster, relying on the modulation-mode $m \in \mathcal{M}$. Note that, if DCO-OFDM is considered, the achievable rate is confined to $r_{c,k,m} = \frac{B}{2}\log_2(2^{2m}) = mB$, where $\frac{B}{2}$ is the information carrying bandwidth due to the Hermitian symmetry. When ACO-OFDM is employed, the achievable rate is further halved. Furthermore, the binary index $x_{c,k,m}$ represents modulation-mode decision of UE k:

$$x_{c,k,m} = \begin{cases} 1, & \text{if } m\text{th mode is assigned to UE } k \in \mathcal{K}_c, \\ 0, & \text{if } m\text{th mode is not assigned to UE } k \in \mathcal{K}_c. \end{cases} \tag{4.6}$$

We aim to obtain the feasible modulation-mode assignment $\mathcal{M}_c^*$ of the cth cluster. Since the binary index $x_{c,k,m}$ is in the objective function (4.5a) and in the constraints (4.5b) - (4.5e), the resultant maximization problem is therefore a mixed combinational non-convex problem.

4.4 Dynamic Resource Allocation for UC-VLC

To elaborate, constraint (4.5c) is imposed to indicate that each UE can be assigned a specific modulation-mode or in fact a no-transmission-mode due to the constraints (4.5d) and (4.5e), which represent the backhual rate and the transmit power constraints for each AP. Note that if the value of $\sum_{m=1}^{|\mathcal{M}|} x_{c,k,m}$ for a specific UE k turns out to be zero, a no-transmission-mode is assigned to UE k during the current time-slot. Furthermore, it can be found from the constraint (4.5e) that to ensure the exploitation of the maximum power allowance for every AP in the cth cluster, the modulation-mode decision of UE k is related not only to the channel conditions of itself, but also to the channel qualities

and modulation-modes of the other UEs in the same cluster. Hence, the resultant multi-user-dependent maximization problem becomes prohibitively complex. Since not only the number of served UE is time-variant, but also their modulation-mode assignment across the entire cluster, which is further coupled with the power allocation strategy.

For tractability, the original problem (4.5) is divided into two sub-problems and solved step-by-step. The step one $\boldsymbol{\mathcal{S}1}$ mainly deals with the modulation-mode assignment and power allocation consecutively for each UE under maximum sum-throughput principle, by taking into account that only one specific AP's power is restricted at a time. Then, step two $\boldsymbol{\mathcal{S}2}$ aims to find a global solution ensuring that all APs in the cell simultaneously satisfy the constraints (4.5d) and (4.5e). To this end, the maximized sum-throughput associated with the globally implementable modulation-mode assignment and power allocation strategy under the practical considerations is obtained within each cluster.

Theorem 4.1. *The solution obtained by successively solving* $\boldsymbol{\mathcal{S}1}$ *and* $\boldsymbol{\mathcal{S}2}$ *is equivalent to the globally optimal solution of the original problem (4.5).*

Proof. Please see Appendix 4.7.1. □

4.4.1 Step One $\mathcal{S}1$: Limited-Power Scenario for Single AP

We first formulate the problem of $\boldsymbol{\mathcal{S}1}$ for a specific power-restricted AP (i.e. AP n) in the cth cluster. Then we propose a heuristic dynamic-programming-based algorithm for maximizing the single-AP-power-limited sum-throughput.

4.4.1.1 Problem Formulation for $\mathcal{S}1$

Mathematically, the sub-problem of $\boldsymbol{\mathcal{S}1}$ is formulated as:

$$\max_{\mathcal{M}_c^*} \sum_{k=1}^{|\mathcal{K}_c|} \sum_{m=1}^{|\mathcal{M}|} r_{c,k,m} x_{c,k,m} \tag{4.7a}$$

$$\text{s.t. } x_{c,k,m} \in \{0,1\}, \quad \forall k \in \mathcal{K}_n, \ \forall m \in \mathcal{M}; \tag{4.7b}$$

$$\sum_{m=1}^{|\mathcal{M}|} x_{c,k,m} \in \{0,1\}, \quad \forall k \in \mathcal{K}_c; \tag{4.7c}$$

$$\sum_{k=1}^{|\mathcal{K}_c|} \sum_{m=1}^{|\mathcal{M}|} p_{c,k,m} x_{c,k,m} \left[\boldsymbol{G}_c\right]_{(n,k)}^2 \leq P_{\max}^{\text{tx}}, \tag{4.7d}$$

where (4.7d) indicates only AP n is under power constraint, whilst the power restriction of other APs and the backhaul rate constraint (4.5d) are neglected in step $\boldsymbol{\mathcal{S}1}$. Compared

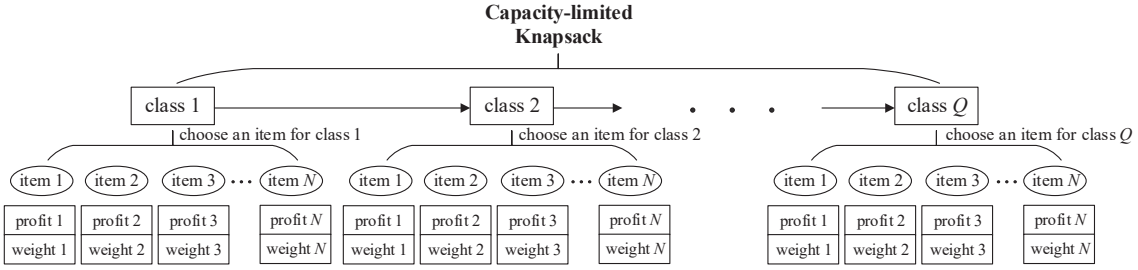

(a) Diagram of the multi-choice knapsack problem

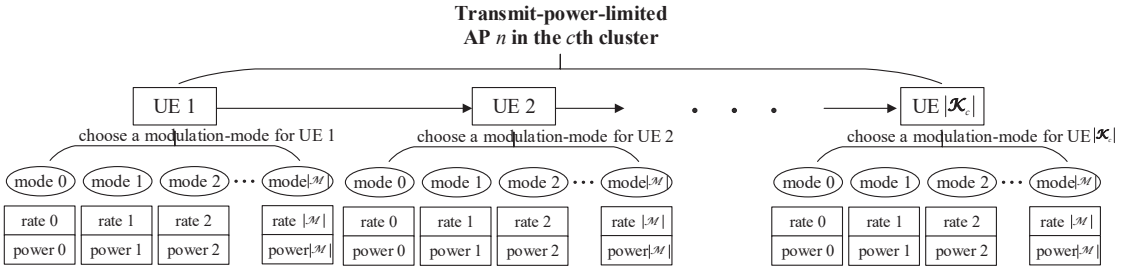

(b) Diagram of the problem in **S1**

Figure 4.4: The diagram of the both the *multi-choice knapsack* problem and our problem in step ***S*1**.

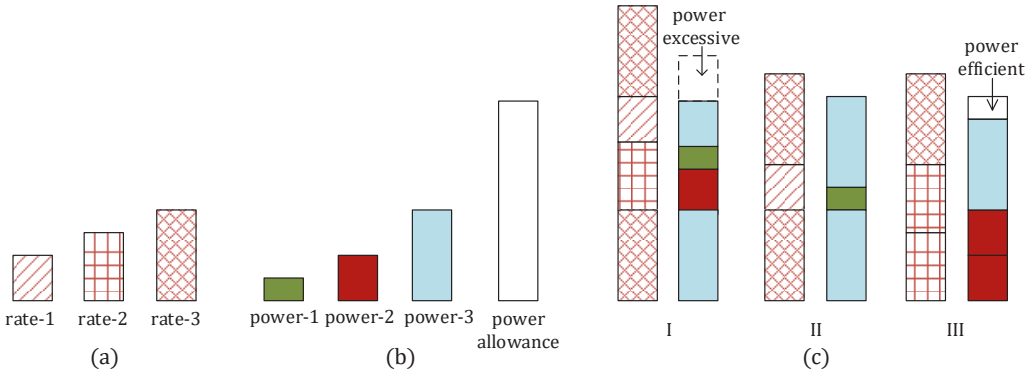

Figure 4.5: An example of our multi-choice knapsack problem. (a) shows the rate set of three modulation-mode, which are available to be assigned to each UE; (b) gives the set of required power levels corresponding to the modulation-modes and our maximum transmit power allowance; (c) depicts three possible modulation-mode and power allocation assignments.

to the original problem, the complexity of ***S*1** is determined by a $(|\mathcal{K}_c| \times 1)$-element channel matrix, rather than by a $(|\mathcal{K}_c| \times |\mathcal{N}_c|)$-element one. Hence the computational complexity is tremendously reduced.

We find that the problem of ***S*1** is similar to a multi-choice knapsack problem. As shown in Fig. 4.4, for each UE (*class*) associated with a specific modulation-mode

(*item*) m, it has an achievable rate (*profit*) $r_{c,k,m}$ and power consumption (*weight*) $p_{c,k,m}$. $\boldsymbol{S1}$ aims to determine the specific modulation-mode for each UE, so that we arrive at the maximized sum-throughput (*sum profit*), obeying the maximum power constraint (*capacity*) of AP (*knapsack*) n. It is worth mentioning that the choice of modulation-mode also includes the no-transmission-mode, enabling the system to selectively support UEs, with reference to "mode 0" in Fig. 4.4(b). Since the capacity is limited for a knapsack, as shown in Fig. 4.4(a), class i is considered for assigning an item if and only if there is still some capacity remaining after including class 1 to $i-1$ in the knapsack. Similarly, in our problem $\boldsymbol{S1}$, UE k is taken into account for assigning a specific modulation-mode when there are still some power and backhaul rate remaining after supporting UE 1 to $k-1$ by AP n.

Let us elaborate a little further. For example, a specific cluster contains four UEs, where each UE can either select one of three possible modes or no-transmission-mode, guaranteeing the corresponding sum power consumption dose not exceed the transmit power constraint. As shown in Fig. 4.5(c)-I, although all the four UEs are assigned by a specific modulation-mode, their total required power exceeds the maximum power allowance. By the contrast, Fig. 4.5(c)-II and (c)-III satisfy the power constraint, whilst three out of four UEs are supported by a given AP. Furthermore, compared to Fig. 4.5(c)-II, the modulation-mode assignment provided in Fig. 4.5(c)-III is more desirable, because it requires less power to attain the same sum-throughput. Therefore, there are numerous feasible solutions for $\boldsymbol{S1}$, especially when a dynamically fluctuating number of served UEs is considered. To obtain the suitable modulation-mode assignment and power allocation in the single-AP limited-power scenario, a heuristic dynamic-programming-based algorithm is invoked, which has the inherent advantage of solving $\boldsymbol{S1}$ with the aid of a recursive process.

4.4.1.2 Principle of UE-Recursion

According to the dynamic programming philosophy, the strategy of maximization relies on considering the UEs one-by-one. Explicitly, at each stage, the sum-throughput of all the UEs considered is obtained as the sum of the current UE's throughput and the sum-throughput of all the previously considered UEs, whilst ensuring the fulfilment of the power constraint. We term this process as UE-recursion. Within each UE-recursion stage, there are UE-end modulation-layer iterations and AP-end power-layer iterations, which benefits to dynamically adjusting the modulation-mode combinations for the UEs considered under transmit power constraint. Note that we may tighten the power constraint to a lower value than the value of $P_{\max}^{\text{tx}}$, provided that this does not lead to a reduction of the sum-throughput. To elaborate, we discretize the value of $P_{\max}^{\text{tx}}$ into J levels, where the tightened power constraint is then confined to be one of the

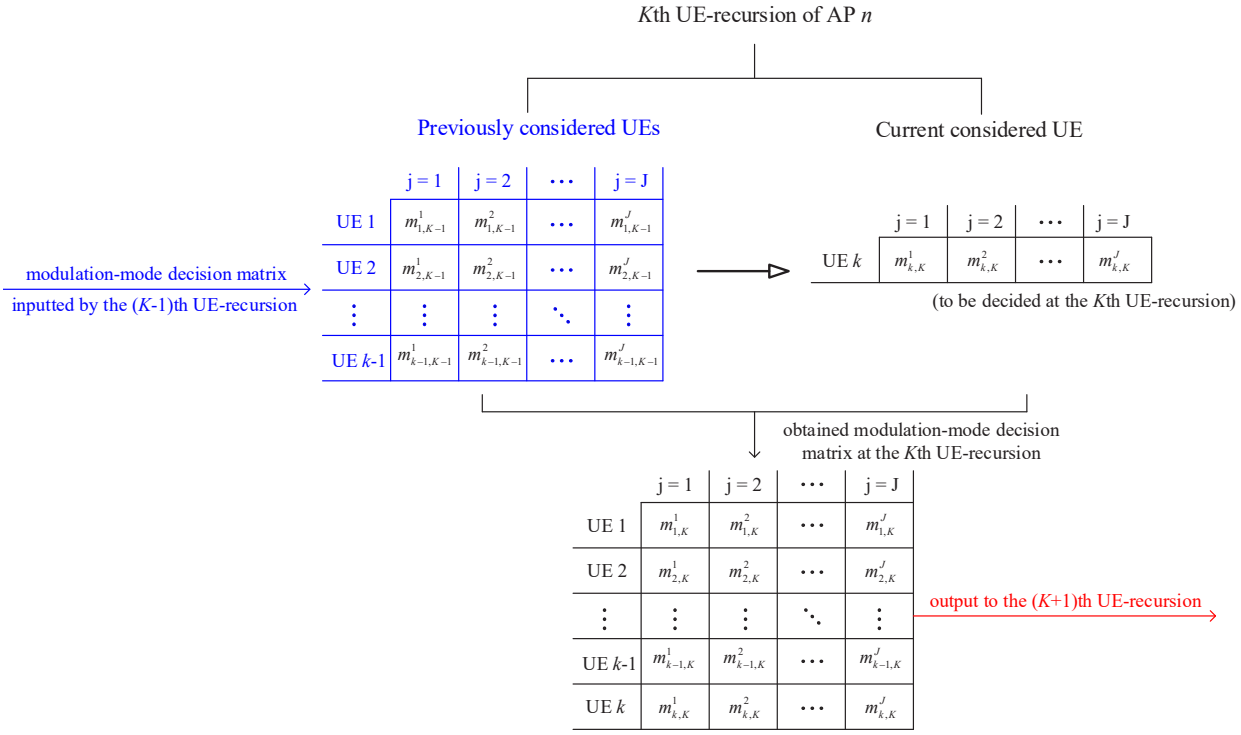

Figure 4.6: A diagram of the Kth UE-recursion and the relationship between it and the $(K-1)$th and the $(K+1)$th UE-recursion, where $m_{k,K}^{j}$ denotes the modulation-mode decided for UE k at the Kth UE-recursion when the power of AP n is restricted by p_j^{tx}.

levels expressed as:

$$\left\{p_j^{\text{tx}} = jP_{\max}^{\text{tx}}/J:\ j=1,2,\cdots,J\right\}. \tag{4.8}$$

Without loss of generality, we define the Kth UE-recursion as that of finding the maximum sum-throughput of all the previously considered $(K-1)$ UEs and the kth considered UE, which is randomly selected, for all the J power constraint levels. The relationship between the Kth UE-recursion and the $(K-1)$th and the $(K+1)$th UE-recursion is provided in Fig. 4.6. In this manner, $\boldsymbol{S1}$ can then be deemed to be successfully solved, when K approaches $|\mathcal{K}_c|$.

4.4.1.3 Dynamic-Programming-Based Algorithm

Before implementing the proposed algorithm, we consider a hypothetical scenario with no UE served in the nth cluster as initialization:

$$T_{c,n,0}(p_j^{\text{tx}}) = 0,\ p_{c,0,m} = 0,\ \left[\boldsymbol{H}_c\right]_{(0,n)} = 0,\ (\forall c, \forall n, \forall j, \forall m), \tag{4.9}$$

which indicates the throughput achieved by the virtual UE in any cluster is always zero, when served by any AP under any arbitrary power constraint. Its power consumption

and channel gain are set to zero for any arbitrary modulation-mode, regardless of which AP it is connected to.

Let us now detail the dynamic-programming-based algorithm. At the Kth UE-recursion, when the transmit power of AP n is restricted by p_j^{tx}, we first check whether the maximum excess power of $p_j^{\text{tx}} - \langle p_{c,k,1} \rangle^{\text{tx}}$ is non-negative or not by randomly picking a UE in the set $\mathcal{K}_c$ as the kth considered UE. Even if this UE is assigned the lowest-throughput-modulation-mode ($m = 1$), the excess power is still negative, there is no feasible solution for AP n supporting a total of K UEs under the power constraint p_j^{tx}. Therefore, we have:

$$T_{c,n,K}(p_j^{\text{tx}}) = -\infty, \quad \text{for } p_j^{\text{tx}} - \langle p_{n,k,1} \rangle^{\text{tx}} < 0, \tag{4.10}$$

where $T_{c,n,K}(p_j^{\text{tx}})$ represents the maximum sum-throughput upon supporting a total of K UEs, when the transmit power of AP n is restricted to p_j^{tx}.

Otherwise, search all the legitimate modulation-modes for the kth considered UE, whilst ensuring a positive excess transmit power of $p_j^{\text{tx}} - \langle p_{c,k,m} \rangle^{\text{tx}}$. This part of power is used for supporting a number of $(K-1)$ UEs, as represented by $T_{c,n,K-1}\big(\lfloor p_j^{\text{tx}} - \langle p_{c,k,m} \rangle^{\text{tx}} \rfloor\big)$, which is one of the maximized results during the $(K-1)$th UE-recursion. By doing so, the maximum value of $T_{c,n,K}(p_j^{\text{tx}})$ can be acquired by the following recursive formula:

$$T_{c,n,K}(p_j^{\text{tx}}) = \max_m \Big\{ T_{c,n,K-1}\big(\lfloor p_j^{\text{tx}} - \langle p_{c,k,m} \rangle^{\text{tx}} \rfloor\big) + r_{c,k,m} : \; p_j^{\text{tx}} - \langle p_{c,k,m} \rangle^{\text{tx}} \geq 0, \; m \in \mathcal{M} \Big\}. \tag{4.11}$$

Here we employ $\langle p_{c,k,m} \rangle^{\text{tx}}$ to express $[\boldsymbol{G}_c]^2_{(n,k)} p_{c,k,m}$. It may happen that the result of $p_j^{\text{tx}} - \langle p_{c,k,m} \rangle^{\text{tx}}$ is not equal to any of the power constraint levels, hence the floor-operation of $\lfloor \bullet \rfloor$ is invoked to obtain a round value corresponding to the nearest lower level. This recursive formula is assisted by previous UE-recursion, guaranteeing that the total required transmit power dose not exceed p_j^{tx}. The associated modulation-mode of the kth UE considered is selected from one of the legitimate modulation-modes and the corresponding counterparts for all the previously considered UEs are collected from one of the results during the last-stage recursion. The Kth UE-recursion is realized by iteratively increasing the power constraint level from p_1^{tx} to p_J^{tx}, where the flowchart of the Kth UE-recursion process is displayed in Fig. 4.7. When all UEs in set $\mathcal{U}_n$ have been considered, problem $\boldsymbol{S1}$ is successfully solved, having the AP-n-power-limited sum throughput set $\mathcal{T}_{c,n} \in \mathbb{R}^{(|\mathcal{K}_c| \times J)}$ as $\mathcal{T}_{c,n} = \Big\{ T_{c,n,K}(p_j^{\text{tx}}) : \; j = 1, 2, \cdots, J, \; K = 1, 2, \cdots, |\mathcal{K}_c| \Big\}$. The general expression of this dynamic-programming-based process is formulated in (4.12).

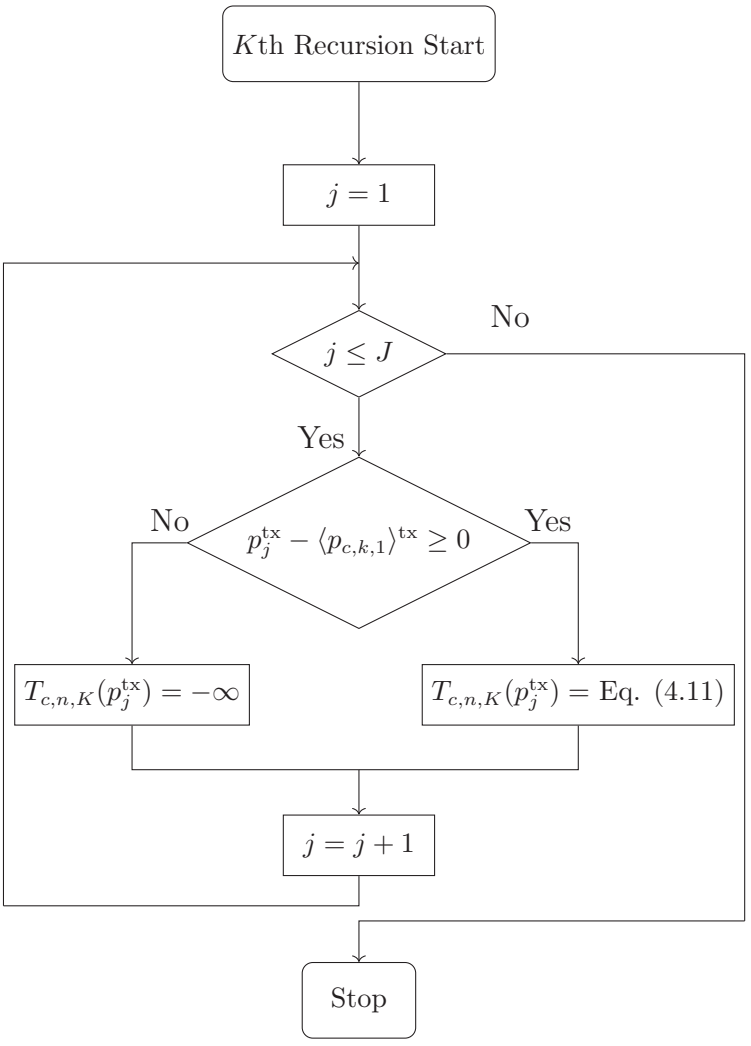

Figure 4.7: The flow diagram of the dynamic-programming-based UE-recursion for the kth UE.

$$T_{c,n,K}(p_j^{\mathrm{tx}}) = \begin{cases} -\infty, & \text{for } p_j^{\mathrm{tx}} - \langle p_{n,k,1} \rangle^{\mathrm{tx}} < 0,\ 1 \leq j \leq J,\ 1 \leq K \leq |\mathcal{K}_c|; \\ \max\limits_{m} \Big\{ T_{c,n,K-1}\big(\lfloor p_j^{\mathrm{tx}} - \langle p_{c,k,m} \rangle^{\mathrm{tx}} \rfloor \big) + r_{c,k,m} :\ p_j^{\mathrm{tx}} - \langle p_{c,k,m} \rangle^{\mathrm{tx}} \geq 0,\ m \in \mathcal{M} \Big\}, & \\ & \text{for } p_j^{\mathrm{tx}} - \langle p_{c,k,1} \rangle^{\mathrm{tx}} \geq 0,\ 1 \leq j \leq J,\ 1 \leq K \leq |\mathcal{K}_c|. \end{cases} \tag{4.12}$$

4.4.2 Step Two *S*2: Limited-Power-and-Backhaul Scenario for Multiple APs

In this section, we aim for maximizing both the power-limited and the backhaul-rate-limited sum-throughput for all the APs in the cell from the results in ***S*1** in conjunction

with an appropriate modulation-mode assignment and power allocation strategy.

4.4.2.1 Objective and Problem Formulation for *S*2

Upon completing a total of $|\mathcal{K}_c|$ UE-recursions for AP n, the results associated with the maximum sum-throughput set $\mathcal{T}_{c,n}$ are the candidate modulation-mode assignment and the power allocation strategies, which are stored in the sets $\mathcal{M}_{c,n,K} \in \mathbb{R}^{(K\times J)}$ and $\mathcal{P}_{c,n,K} \in \mathbb{R}^{(K\times J)}$, where $K \in \{1, 2, \cdots, |\mathcal{K}_c|\}$. Note that each column of the sets, expressed as $\left[\mathcal{M}_{c,n,K}\right]_{(:,j)}$ and $\left[\mathcal{P}_{c,n,K}\right]_{(:,j)}$, respectively, provides a potential modulation-mode assignment and power allocation assignment for K UEs. By collecting the results of $\mathcal{T}_{c,n}$ for all the APs of the cth cluster, the resultant sum-throughput set is given by:

$$\mathcal{T}_c = \Big\{\mathcal{T}_{c,n} :\ n = 1, 2, \cdots, |\mathcal{N}_c|\Big\}, \tag{4.13}$$

along with the obtained candidate modulation-mode assignment set as:

$$\mathcal{M}_c = \Big\{\mathcal{M}_{c,n,K} :\ K = 1, 2, \cdots, |\mathcal{K}_c|,\ n = 1, 2, \cdots, |\mathcal{N}_c|\Big\}, \tag{4.14}$$

and the power allocation set as

$$\mathcal{P}_c = \Big\{\mathcal{P}_{c,n,K} :\ K = 1, 2, \cdots, |\mathcal{K}_c|,\ n = 1, 2, \cdots, |\mathcal{N}_c|\Big\}. \tag{4.15}$$

Based on the results of ***S*1**, the aim of ***S*2** is to select one of the solutions from the sets $\mathcal{M}_c$ and $\mathcal{P}_c$ so that the corresponding maximum sum throughput in $\mathcal{T}_c$ is realized not only by observing the maximum transmit power limit $P_{\max}^{\text{tx}}$ for all the APs in the cluster, but also observing the maximum backhaul rate constraint R^{BH}. Therefore, ***S*2** can be mathematically formulated as:

$$\max_{n,j,K}\ \big\{\mathcal{T}_c\big\}, \tag{4.16a}$$

$$\text{s.t.}\quad \sum_{k=1}^{K}\left[\mathcal{M}_{c,n,K}\right]_{(k,j)} \le R^{\text{BH}}; \tag{4.16b}$$

$$\Big\langle\left[\mathcal{P}_{c,n,K}\right]_{(:,j)}\Big\rangle^{\text{tx}} \preceq P_{\max}^{\text{tx}}\cdot\mathbf{1}_{|\mathcal{K}_c|\times 1}, \tag{4.16c}$$

where $\mathbf{1}_{|\mathcal{K}_c|\times 1}$ represents an all-one vector having a size of $\big(|\mathcal{K}_c|\times 1\big)$.

4.4.2.2 Limited-Power-and-Backhaul Throughput Maximization Process

Specifically, there are three stages invoked for multi-AP-power-and-backhaul-limited maximization algorithm in ***S*2**:

1. Set the sum throughput values in $\mathcal{T}_c$ exceeding the maximum tolerance backhaul rate R^{BH} to $-\infty$, which guarantees that the rest of the values in the set $\mathcal{T}_c$ obey constraint (4.16b).

2. Find the values of $\{n, j, K\}$[1] maximizing the updated set $\mathcal{T}_c$ as: $\{n^*, j^*, K^*\} = \arg\max_{n,j,K} \mathcal{T}_c$. By doing so, the maximum sum throughput is achieved when the AP n^* serving K^* number of UEs under the power constraint $p_{j^*}^{\mathrm{tx}}$. The set $\mathcal{T}_c$ is then updated by setting the value of $T_{c,n^*,K^*}(p_{j^*}^{\mathrm{tx}})$ to $-\infty$. Accordingly, the candidate power allocation strategy is extracted from $\left[\mathcal{P}_{c,n^*,K^*}\right]_{(:,j^*)}$.

3. If $\left[\mathcal{P}_{c,n^*,K^*}\right]_{(:,j^*)}$ satisfies the constraint (4.16c), which means that by employing this power allocation strategy, all APs in the set $\mathcal{N}_c$ can transmit by satisfying both the backhaul-limit and the power-limit to a total of K^* UEs simultaneously. The maximization for the cth cluster is finished by allocating the transmit power to each AP based on $\left\langle \left[\mathcal{P}_{c,n^*,K^*}\right]_{(:,j^*)} \right\rangle^{\mathrm{tx}}$ and assigning the modulation-modes for the served UEs according to $\left[\mathcal{M}_{c,n^*,K^*}\right]_{(:,j^*)}$. Otherwise, repeat the same procedure from Stage 2) until all APs satisfy both the maximum backhaul rate constraint and the maximum transmit power constraint.

If there is no legitimate result after completing the above three stages, the whole cell has to be abandoned in the current time slot, since one or possibly several APs cannot afford transmission due to the excessive power or rate required. However, this limitation can be circumvented by appropriately designing the size of UC-cells and by dynamically enabling/disabling the UEs.

4.4.3 Solutions

To this end, the globally maximized sum-throughput $T_{c,n^*,K^*}(p_{j^*}^{\mathrm{tx}})$ for the cth cluster is fulfilled. Correspondingly, the appropriate modulation-mode assignment strategy $\mathcal{M}_c^*$ is based on $\left[\mathcal{M}_{c,n^*,K^*}\right]_{(:,j^*)}$ for K^* UEs and the feasible power allocation strategy relies on $\left\langle [\mathcal{P}_{c,n^*,K^*}]_{(:,j^*)} \right\rangle^{\mathrm{tx}}$ for $|\mathcal{N}_c|$ APs supported in the cth cluster. In a nutshell, by solving ***S*1** and ***S*2** successively, we have obtained the solution for the original problem (4.5) under a pair of constraints. Then, by aggregating all the solutions obtained in a total of $|\mathcal{C}|$ UC-clusters, we have completed both the modulation-mode assignment and power allocation for the UEs and the APs in the system, while achieving the maximum sum-throughput under practical considerations.

[1]When choosing the maximum sum throughput in set $\mathcal{T}_c$, the priority order of the three variables are: $K > j > n$. For example, if $T_{c,n,K}(p_j^{\mathrm{tx}}) = T_{c,n',K'}(p_{j'}^{\mathrm{tx}})$, regardless of the values of n, n', j, j', higher priority will be given to $T_{c,n,K}(p_j^{\mathrm{tx}})$ when $K > K'$ for the sake of reducing the UE outage. Furthermore, if $T_{c,n,K}(p_j^{\mathrm{tx}}) = T_{c,n',K}(p_{j'}^{\mathrm{tx}})$, where we have $p_j^{\mathrm{tx}} < p_{j'}^{\mathrm{tx}}$, a higher priority will be given to $T_{c,n,K}(p_j^{\mathrm{tx}})$, regardless of the value of n and n', with the aim of energy conservation.

4.4.4 Complexity Analysis

It is conceptually plausible that the optimal modulation assignment and power allocation can be found by exhaustive search. Upon considering a specific UC-cluster (i.e. the cth cluster) as an example, in this $|\mathcal{K}_c|$-UE $|\mathcal{M}|$-modulation-mode cluster, there are a total of $(|\mathcal{M}|+1)^{|\mathcal{K}_c|}$ modulation-mode assignments, bearing in mind that some of the UEs may not be served. The corresponding search complexity is on the order of $\mathcal{O}\Big((|\mathcal{M}|+1)^{|\mathcal{K}_c|}\Big)$. In our proposed algorithm, the complexity of $\boldsymbol{S1}$ relying on the dynamic-programming-based algorithm using twin-layer iterations is $\mathcal{O}\big(J|\mathcal{M}||\mathcal{K}_c|\big)$ for each AP, and the complexity of $\boldsymbol{S2}$ associated with the multi-AP-power-and-backhaul-limited sum throughput maximization algorithm is $\mathcal{O}\big(J|\mathcal{N}_c|\big)$. Hence the computational complexity of the proposed algorithm is significantly lower than that of the exhaustive search, since the former is increased polynomially, while the latter exponentially. Furthermore, the convergence of our proposed algorithm is also characterized. Recall that the proposed algorithm requires us to discretize the power constraint $P_{\max}^{\text{tx}}$ into J levels, which may result in a difference between the results obtained by our algorithm and the optimum one. To characterize the convergence, a small indoor UC-VLC network is considered due to its low complexity. Figure 4.8 shows that upon increasing J, the result obtained by our algorithm approaches to the optimum one, thus it is convergent.

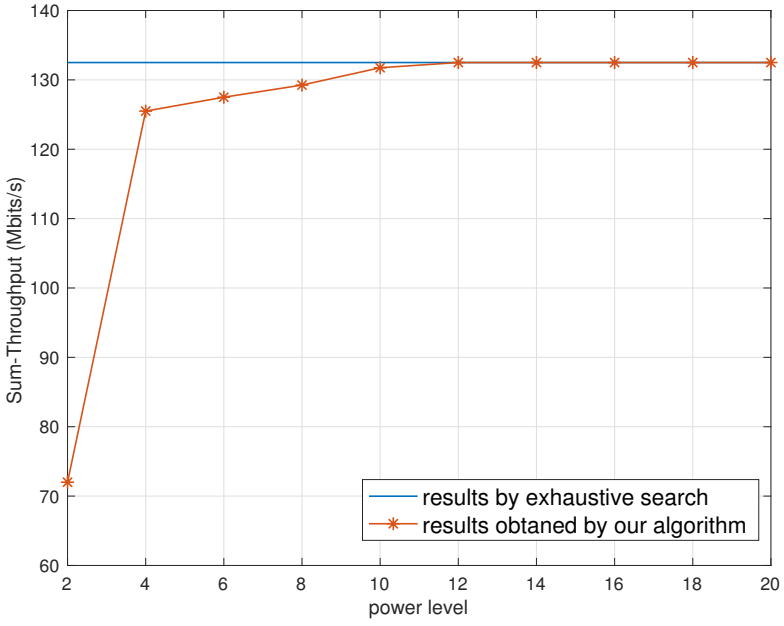

Figure 4.8: Convergence demonstration of our proposed algorithm in a 3×3×3 m^3 indoor room, where a total of two APs located on (0.75,1.5,2.5) and on (2.25,1.5,2.5) to support two UEs. The available modulation-mode are 4-QAM, 16-QAM and 64-QAM, associated with ACO-OFDM scheme. The results are averaged over 100 independent UE distributions.

I-1. Environment-related Parameters	
room size	15×15×3 m^3
AP height	2.5 m
number of APs $\lvert\mathcal{N}\rvert$	8×8
LED array per AP	60×60
UE height	0.85 m
number of UEs $\lvert\mathcal{K}\rvert$ (changed in Fig. 4.10, 4.14 - 4.17, 4.20, 4.21)	25
I-2. VLC Channel-related Parameters	
semi-angle at half-illumination $\phi_{1/2}$	60^o
gain of optical filter $g_{of}(\psi)$	1
gain of optical concentrator $g_{oc}(\psi)$	1
physical area for a PD receiver S	1 cm^2
reflection efficiency ρ	0.75
field-of-view Ψ_{FoV} (changed in Fig. 4.9, 4.18, 4.19)	85^o
I-3. UC-Cells Construction-related Parameters	
UE distance threshold d_u (changed in Fig. 4.22 - 4.24)	2.5 m
AP distance threshold d_a	3 m
I-4. Physical-layer-related Parameters	
target BER	10^{-5}
modulation bandwidth B	50 MHz
AWGN power spectral density N_0	10^{-22} A^2/Hz
DC bias in ACO-OFDM P_{bias} (changed in Fig. 4.17)	1 mW/LED
DC bias in DCO-OFDM P_{bias} (changed in Fig. 4.16)	10 mW/LED
limited linear power range $[P_l, P_h]$	[1mW, 30mW]
I-5. Dynamic-programming-related Parameters	
transmit power constraint $P_{\max}^{\text{tx}}$	10 W/AP
backhaul constraint R^{BH} (changed in Fig. 4.22 - 4.24)	100 - 800 Mbits/s
number of power limit levels J	20

Table 4.1: List of Parameters in Chapter 4

4.5 Performance Results

This section provides our numerical simulations for characterising the modulation-mode-dependent throughput of the UC-VLC system under practical constraints. Specifically, we consider BPSK, 4-QAM, 16-QAM, 64-QAM and 256-QAM modulation-modes for adaptive modulation-mode assignment. Note that our results are averaged over hundreds independent UE distributions. All simulation parameters are summarised in Table 4.1.

4.5.1 Effect of Positioning Errors

When constructing the UC-clusters, the position information for UEs is required, as we discussed in Chapter 2. Primarily, we compare the achievable throughput both with and without perfect positioning. To elaborate, Fig. 4.9 shows that the average throughput, as a function of FoV, achieved by ACO/DCO-OFDM transmission scheme,

is similar for both positioning techniques. Here we define the average throughput as the modulation-mode-dependent throughput per served UE. Note that in the imperfect positioning scenario, the positioning error is set up to 10 cm, which can be realized by most of the indoor positioning techniques [13]. Furthermore, the outage performance associated with imperfect positioning is close to the one achieved by perfect positioning. Note that the outage probability is defined as the probability that the achieved throughput of UEs is lower than a certain minimum acceptable value. To elaborate a little further, the minimum acceptable value is confined to be 15 Mbits/s, below which the UE is viewed as the outage UE. It is noteworthy that the outage UEs are consisted of both the un-assigned UEs and un-served UEs, where the former results from anchoring process, while the latter is decided by the dynamic resource allocation algorithm. The same tendency is also observed in Fig. 4.10, where both the average throughput and the outage probability are as a function of the UE densities. Moreover, the normalized throughput and outage difference as a function of the maximum positioning error is shown in the Fig. 4.11, which are defined as:

$$\overline{\mathrm{TP}} = \frac{|\mathrm{TP} - \mathrm{TP}_e|}{\mathrm{TP}}, \tag{4.17}$$

$$\overline{\mathrm{OP}} = \frac{|\mathrm{OP} - \mathrm{OP}_e|}{\mathrm{OP}} \tag{4.18}$$

Note that TP and OP are the average throughputs associated with the outage probability whilst relying on perfect positioning, while TP_e and OP_e are those associated with imperfect positioning. This implies that the proposed system is capable of tolerating realistic positioning errors. Therefore, in the following simulations, we rely on the perfect positioning assumption to reduce the computational complexity of our investigations.

4.5.2 UC-VLC v.s. NC-VLC

The performance of VLC network highly depends on its topology due to the specific propagation characteristics of visible light. Since the network association has a strong relationship with the received signal to interference ratio, it is valuable to observe the performance of our proposed UC-VLC for various UC-cluster sizes. As a benchmark, the radical UFR strategy aided conventional NC-VLC system is employed, which has already been introduced in Chapter 2. Since we consider not only the LoS path of the VLC channel, but also the first reflected propagation path, the UEs located at the edge or in the corner of the room tend to suffer from more grave interference than the UEs located in the center area of the room. Therefore, the distribution of UEs has an influence on the system's performance. Furthermore, investigating the density of UEs is capable of reflecting on the individual UE capacity within the system we constructed. In light of these, we are interested in exploring the influence of UE density on our proposed system,

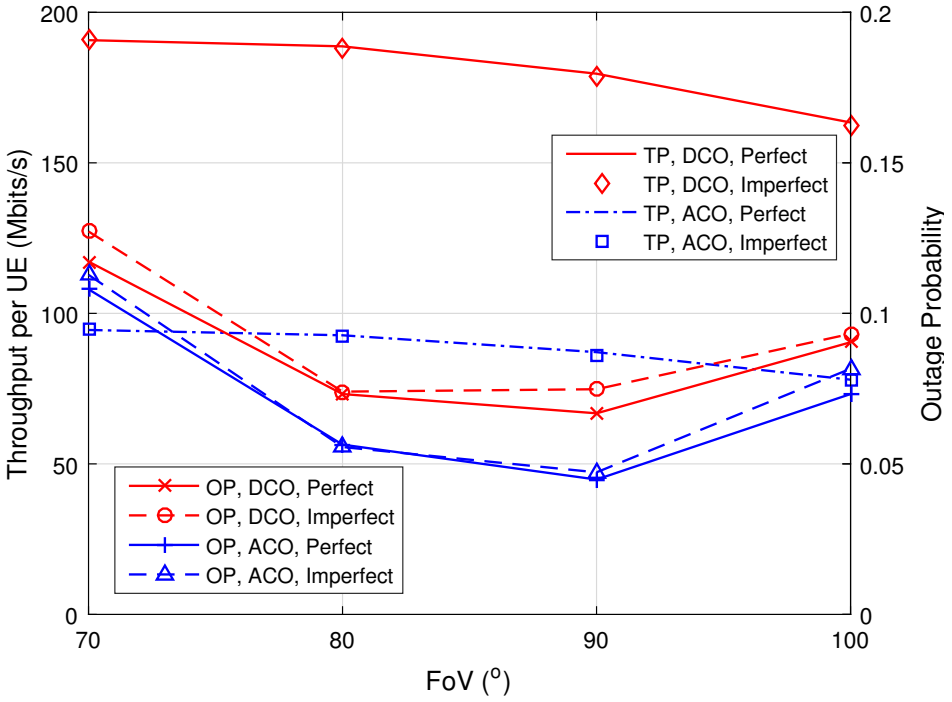

Figure 4.9: Throughput (TP) and outage probability (OP) of the UC-VLC network *v.s.* the FoV for both perfect and imperfect positioning, using the parameters of Table 4.1.

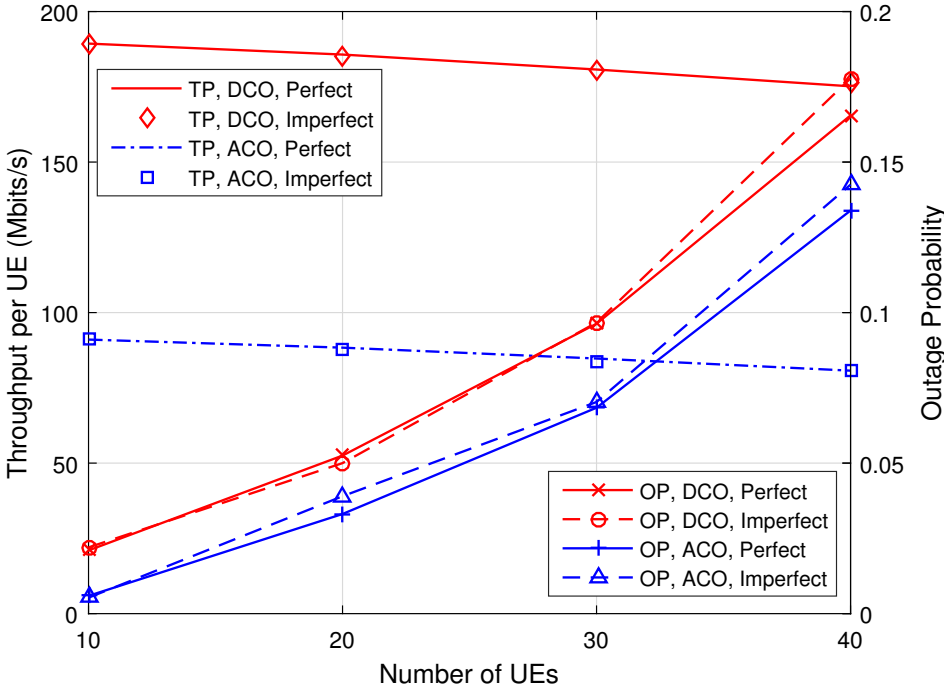

Figure 4.10: Throughput and outage probability of the UC-VLC network *v.s.* the number of UEs for both perfect and imperfect positioning, using the parameters of Table 4.1.

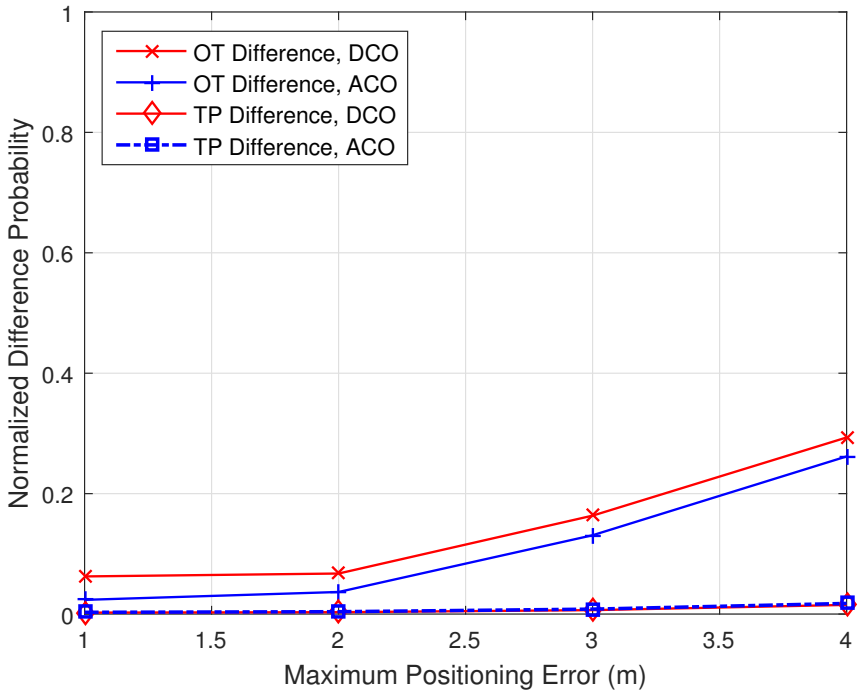

Figure 4.11: Normalized throughput and outage probability difference for various positioning errors, using the parameters of Table 4.1.

since the location and density of UEs are vital in terms of the system's robustness. Note that for each simulation, a number of UEs are uniformly distributed in the room. To fully explore all the locations, our results are averaged over hundreds of random independent UE distributions. In addition, the value of FoV at the UE-end seriously impacts the received signal/interference strength. For a smaller FoV, a given UE tends to receive signal/interference from less APs, and vice versa. Therefore, we will consider a range of FoV values to investigate its impact on both the achievable throughput and on the outage probability in the following sections.

4.5.2.1 Throughput Distribution

To begin with, let us have a glance at the distribution of the modulation-mode-dependent throughput in both the UC/NC-VLC networks. As shown in Figs. 4.12 and 4.13, the throughput distribution achieved by DCO-OFDM and ACO-OFDM is provided, respectively. It demonstrates that, for both the transmission schemes, the proposed UC-VLC system exhibits a better throughput performance, since the majority of UEs can achieve a higher rate than the NC-VLC system. Moreover, we observe that the throughputs achieved by DCO-OFDM in both the UC/NC-VLC systems are roughly twice that of the scenario associated with ACO-OFDM, which confirms the theoretical analysis of an ideal system operating without any practical impairments and constraints. These

observations give us the general result that UC-VLC system supports a substantially higher throughput than NC-VLC system.

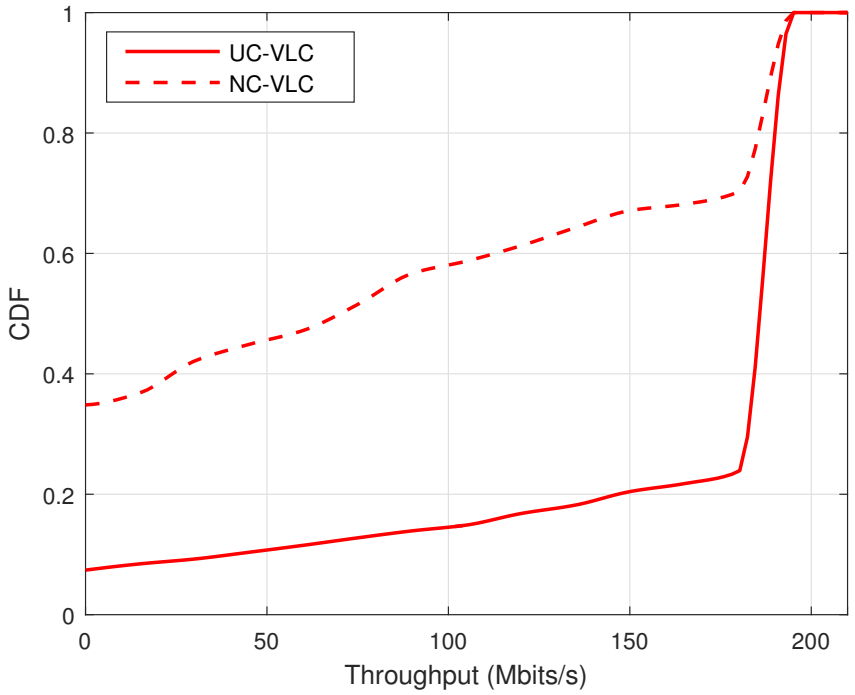

Figure 4.12: Cumulative distribution function (CDF) of the modulation-mode-dependent throughput distribution in DCO-OFDM aided UC/NC-VLC network, using the parameters of Table 4.1.

4.5.2.2 Sum-Throughput Performance

In the indoor VLC system constructed, where a total of 8×8 APs are uniformly distributed, it is able to simultaneously support a maximum of 64 UEs per time slot. Therefore, Figs. 4.14 and 4.15 observes the total achievable throughput attained in NC-VLC and UC-VLC associated with various sizes of UC-clusters as a function of the number of UEs, in both the ACO/DCO-OFDM. As seen in Fig. 4.14, the NC-VLC system arrives at its overall best performance when supporting around 30 UEs. Upon further increasing the number of UEs, the sum-throughput of the NC-VLC exhibits an obvious drop due to inefficient UE-AP association strategy. By contrast, the UC-cluster aided UC-VLC system's throughput is steadily increased with the number of UEs up to a maximum, beyond which it exhibits a slight degradation. There are two reasons behind this degradation. Firstly, given the high UE density, some UEs fail to find their unique anchoring APs, which are termed as the un-assigned UEs. This situation leads to an outage. Secondly, the associated UEs have to compete with each other during the resource allocation, where some UEs may not be supported due to the limited resources,

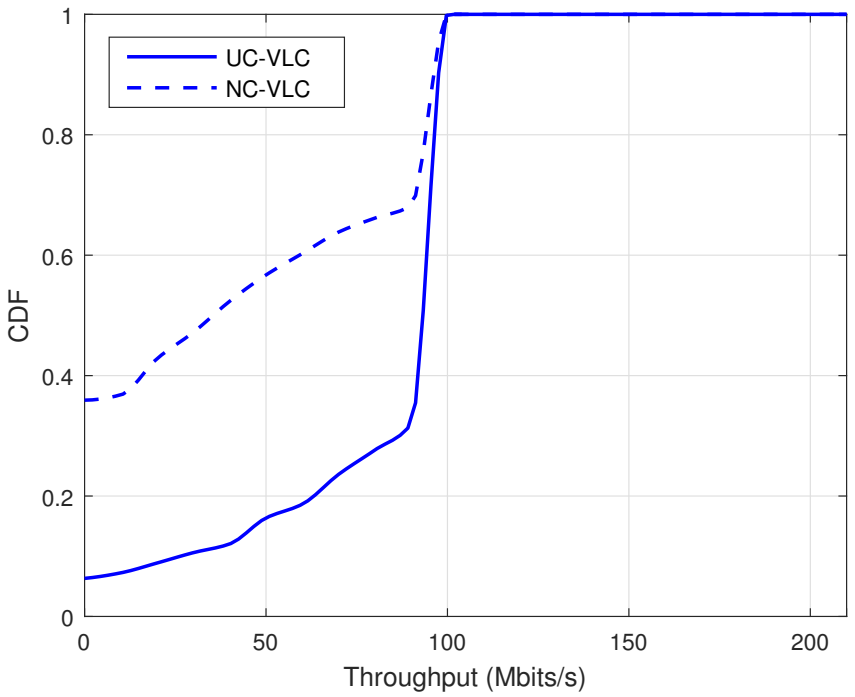

Figure 4.13: CDF of the modulation-mode-dependent throughput distribution in ACO-OFDM aided UC/NC-VLC network, using the parameters of Table 4.1.

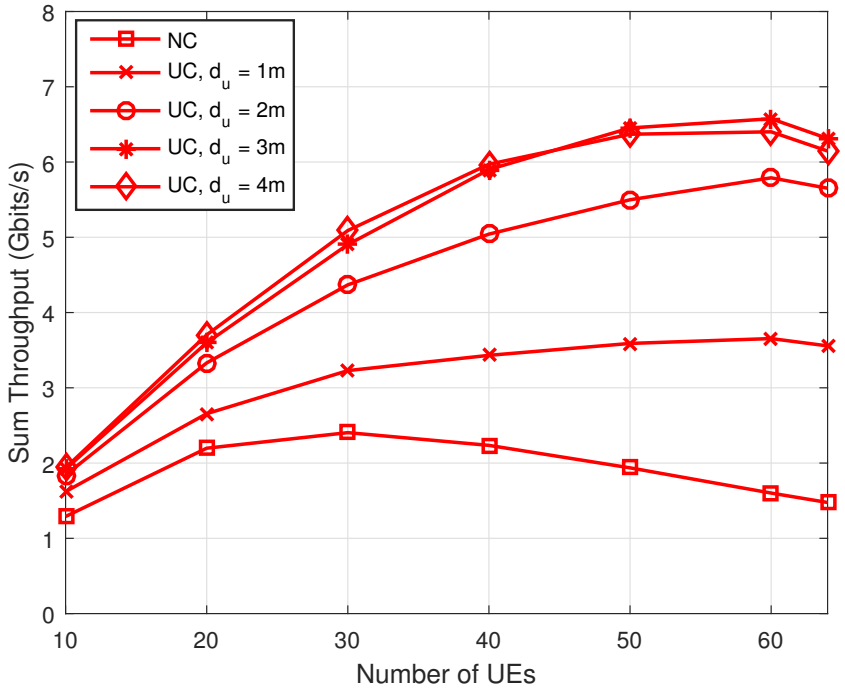

Figure 4.14: Sum-throughput of the DCO-OFDM as a function of the number of UEs, compared between the UC-VLC with various sized of UC-clusters and NC-VLC, using the parameters of Table 4.1.

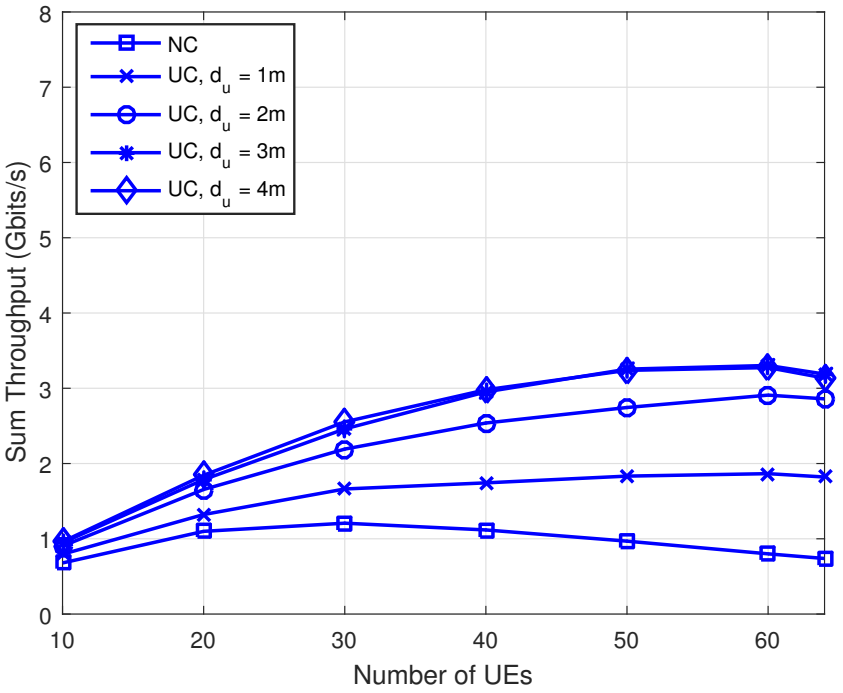

Figure 4.15: Sum-throughput of the ACO-OFDM as a function of the number of UEs, compared between the UC-VLC with various sized of UC-clusters and NC-VLC, using the parameters of Table 4.1.

which are termed as the un-served UEs. Observe in Fig. 4.15 that our proposed UC-VLC system relying on ACO-OFDM outperforms the NC-VLC system under practical constraints, especially for dense UE populations.

Furthermore, we also observe from Figs. 4.14 and 4.15 that the larger the UC-clusters employed, the higher the sum-throughput becomes, although the attained throughput tends to become saturated upon increasing d_u. Although the VT aided multi-AP-multi-UE regime improves the throughput, the larger UC-clusters tend to require more resources (power and backhaul) for simultaneously supporting their target UEs. However, the transmit power as well as the backhaul rate of our system are restricted. Therefore, it is not always true that the larger d_u becomes, the better the throughput. The best choice of d_u strongly relies on the specific topology of the network.

In addition, the influence of LED impairments on the UC-VLC system relying on the ACO/DCO-OFDM transmission scheme is explored in Figs. 4.16 and 4.17 under various UE densities. It can be seen from Eqs. (2.7) and (2.9) of Chapter 2 that the clipping-distortion strongly depends on the value of DC-bias, when the LED's dynamic range is fixed. Due to the particular characteristics of DCO-OFDM, typically a higher DC-bias than that of ACO-OFDM is required. Therefore, we observe the clipping-distortion's

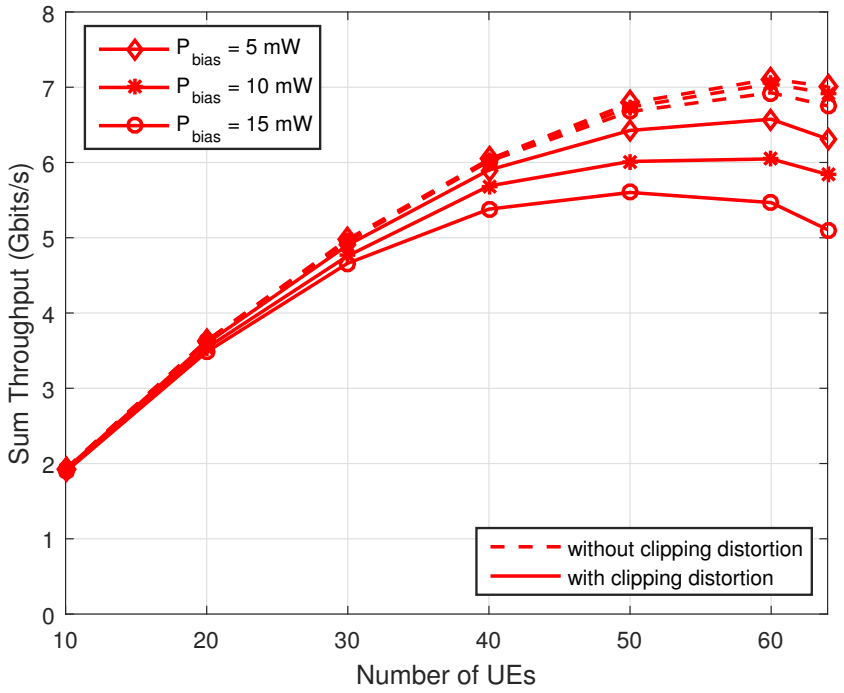

Figure 4.16: Influence of clipping-distortion on the sum-throughput of DCO-OFDM as a function of the number of UEs, using the parameters of Table 4.1. Note that the solid lines and dash lines represent the achievable sum-throughput with and without LED impairment consideration, respectively.

influence on the sum-throughput for DC-bias values of $P_{\text{bias}} = 5$, 10, 15 mW for DCO-OFDM, while $P_{\text{bias}} = 1$, 3, 5 mW for ACO-OFDM. Note that the power used for biasing is reduced from $P_{\max}^{\text{tx}}$. Therefore, the higher the bias we have, the less the clipping-distortion imposed, however, the less the power is available for data transmission. It can be observed from Fig. 4.16 that the clipping-distortion has a more obvious impact on denser UE distributions, which is justified as follows. Upon increasing the UE density, more UEs tend to be supported within each cluster. Naturally, a higher transmit power is required for simultaneously supporting the increased number of UEs within each UC-cluster. However, due to the clipping-distortion and power constraint, the UEs tend to select low-rate modulation-modes, if the cluster cannot provide sufficient power. To this end, the sum-throughput under LED impairments suffers from a reduction compared to that without LED impairments, when increasing the UE density. Moreover, the sum-throughput is reduced more obviously upon increasing the value of P_{bias}, since the higher DC-bias requires more power. Note that the impact of P_{bias} on DCO-OFDM and ACO-OFDM is different. It is more profound on DCO-OFDM owing to its power-inefficiency nature. However, the scenario without LED impairment consideration is unrealistic, since the LED impairments do exist and cannot be eliminated.

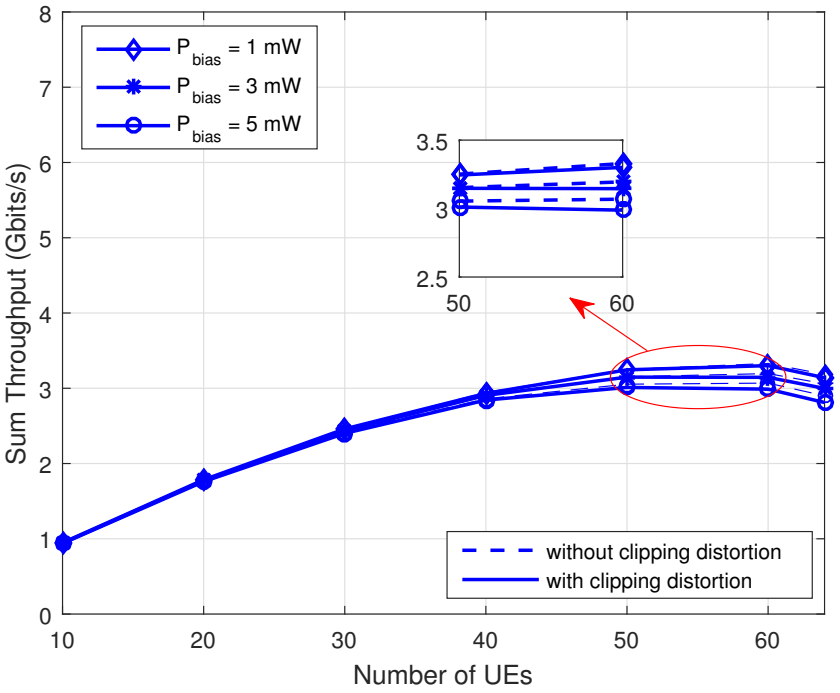

Figure 4.17: Influence of clipping-distortion on the sum-throughput of ACO-OFDM as a function of the number of UEs, using the parameters of Table 4.1. Note that the solid lines and dash lines represent the achievable sum-throughput with and without LED impairment consideration, respectively.

4.5.2.3 Effects of Various FoVs

The FoV is one of the most important parameters in VLC, since it has a far-reaching impact both on the channel gain and on the interference. Figure 4.18 compares the modulation-mode-related average throughput of UC-VLC and NC-VLC relying on the ACO/DCO-OFDM schemes for various FoV values. The first important point to note is that the larger the FoV we have, the lower the average throughput becomes for both UC/NC-VLC systems due to the increased ICI, regardless of the choice of the transmission scheme. We also observe that the UC-cluster aided UC-VLC system exhibits a consistently higher average throughput than the NC-VLC system for all FoV values, which illustrates the superiority of the UC-VLC philosophy under practical concerns. As expected, the benefit of UC-VLC is much more substantial at higher FoV values. It shows that the NC-VLC system has poor resistance to ICI, which means that the UC-VLC system relying on the multi-AP-multi-UE structure has better performance than that of the single-AP-single-UE structure in NC-VLC, in the face of grave ICI. Moreover, the dashed lines and dash-dot lines seen in Fig. 4.18 suggest that instead of dynamically deciding upon the number of served UEs, the greedy strategy relying on rate-fairness and hence aiming for serving all the UEs within each UC-cluster results

in a throughput reduction. According to the greedy strategy, once the cluster cannot afford to support all UEs, the whole cluster has to be dropped rather than reducing the number of served UEs in our dynamic strategy. Therefore, it can be found from Fig. 4.18 that the throughput reduction is more serious under large FoV values, due to the increased ICI.

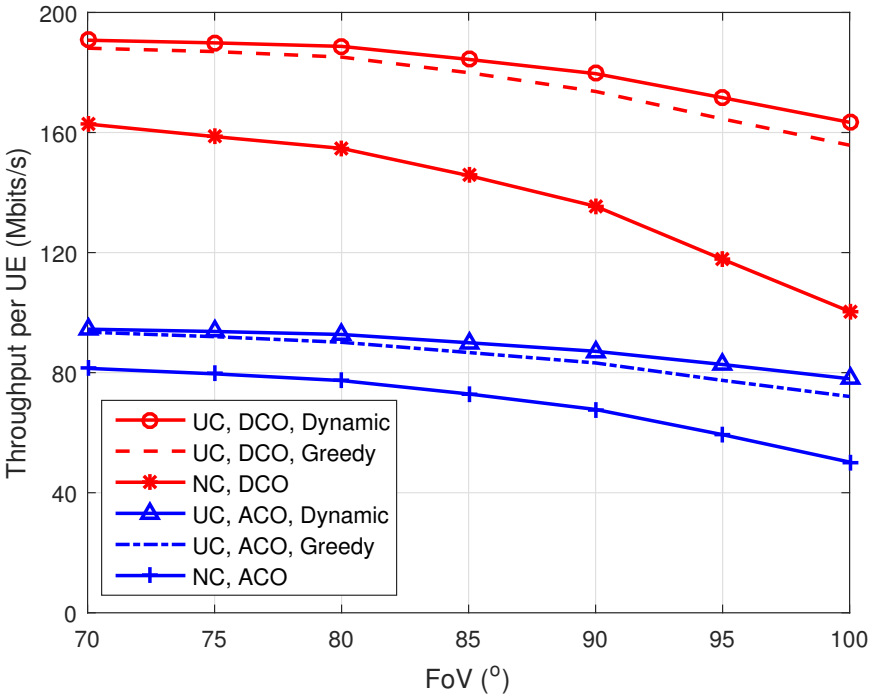

Figure 4.18: Modulation-mode-related throughput per served UE for both the UC and NC-VLC networks supported by ACO/DCO-OFDM *v.s.* the FoV values, using the parameters in Table 4.1.

Furthermore, the advantage of the UC-VLC system is also observed in terms of its outage probability performance, which can be seen in Fig. 4.19. Explicitly, the UC-VLC system has a substantially lower outage probability than the NC-VLC system for both transmission schemes, regardless of the specific FoV. This is an explicit benefit of the multi-AP-multi-UE structure, since the transmit power required is jointly supplied by the APs. Furthermore, we also observe that the outage probability of our UC-VLC is first decreased and then increased, upon increasing the value of FoV, where the best performance is obtained when we have FoV around to 90^o. For insufficient FoV, the number of candidate anchoring APs for a given UE is limited, which may lead to facing an increased number of un-assigned UEs. By contrast, a large value of FoV may result in an increased number of un-served UEs. Furthermore, we observe that the outage probability of the DCO-OFDM scheme is lower than that of the ACO-OFDM scheme in the context of the NC-VLC system, which is due to the higher bandwidth efficiency of DCO-OFDM. However, this trend is completely reversed in the UC-VLC system,

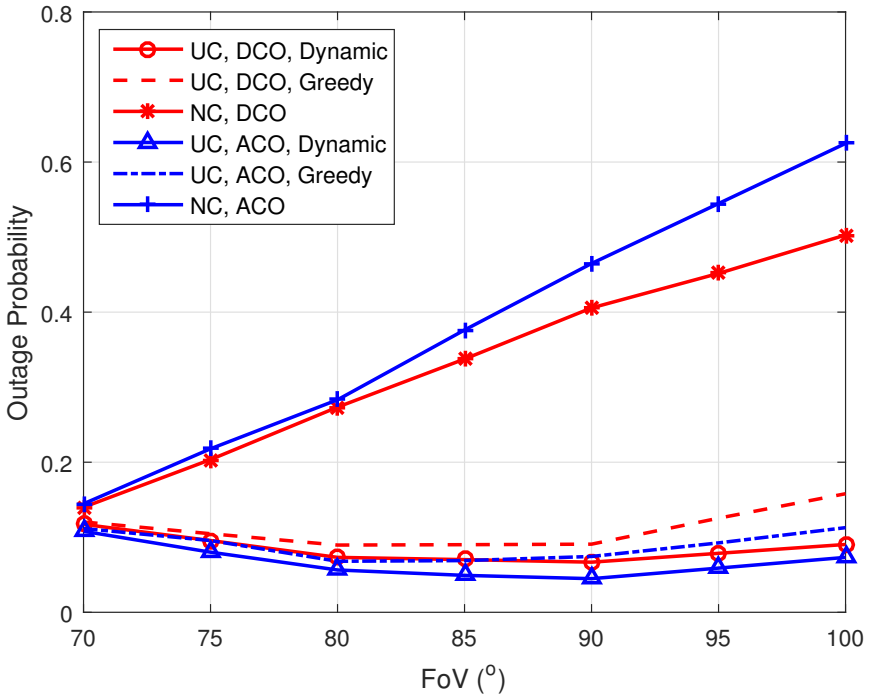

Figure 4.19: Corresponding UE outage probability of Fig. 4.18 *v.s.* the FoV values.

where the outage probability of the ACO-OFDM scheme is always lower than that of the DCO-OFDM scheme. This suggests that the power efficiency of ACO-OFDM plays a significant role in predetermining the system's overall power limitation. Moreover, the greedy strategy based UC-VLC experiences a higher outage probability, compared to the one relying on dynamical decisions. As we have analysed above, the greedy strategy intends to jointly support all clustered UEs, or to abandon all of them. This inevitably leads to an increased outage probability upon increasing the value of FoV. Note that this outage probability increase is much more serious for the DCO-OFDM scheme due to its power-inefficient nature.

4.5.2.4 Effects of Various UE Densities

In this section, the influence of UE density is explored. To elaborate, Fig. 4.20 shows the modulation-mode-related average throughput performance in both the UC and NC-VLC systems as a function of the number of UEs $|\mathcal{K}|$. By observing, it can be found when the UE density is fairly low, for example $|\mathcal{K}| = 10$, the UC-cluster aided UC-VLC tends to degenerate into a single/multi-AP-single-UE network, hence the throughput difference between the UC-VLC and the NC-VLC relying on the ACO/DCO-OFDM schemes becomes modest. However, the average throughput in UC-VLC keeps nearly stationary among various UE densities, where in NC-VLC system, an obvious drop is

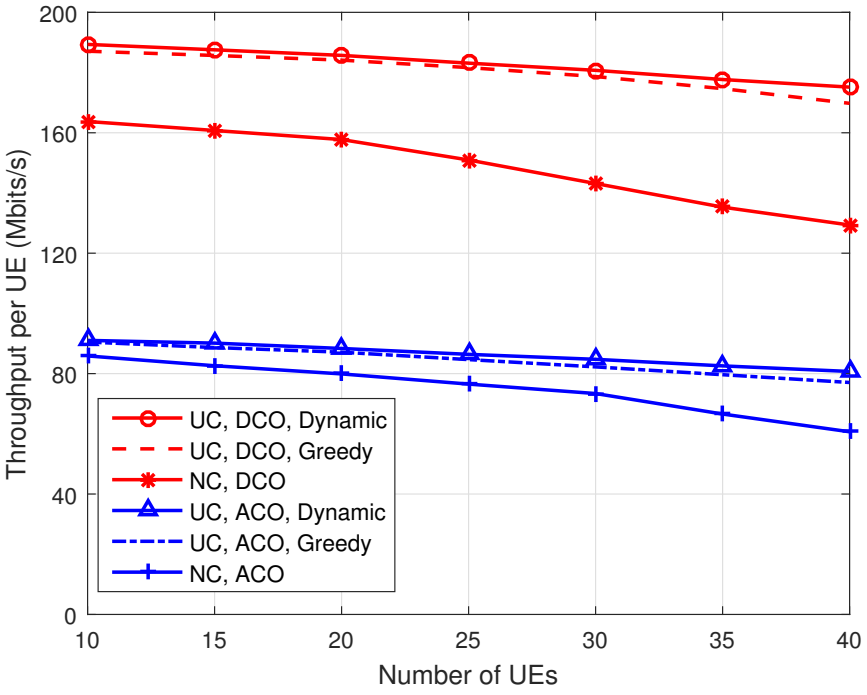

Figure 4.20: Average throughput of the UC/NC-VLC network applying the ACO/DCO-OFDM transmission schemes *v.s.* the UE densities, using the parameters in Table 4.1.

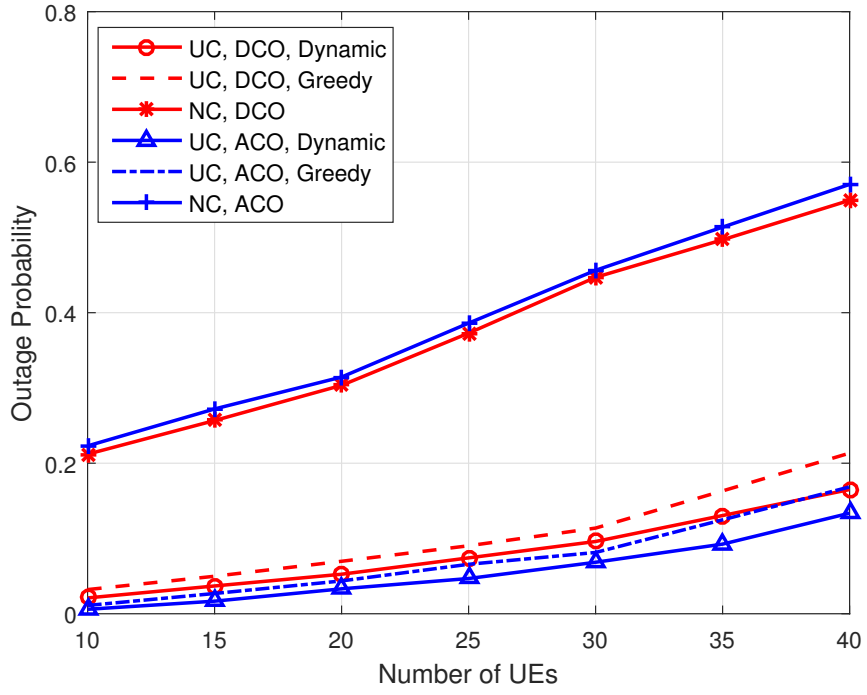

Figure 4.21: Corresponding UE outage probability of Fig. 4.20 *v.s.* the UE densities.

observed upon increasing the UE density. Therefore, it can be inferred that the UC-VLC system is capable of operating in a higher UE-density scenario, than the NC-VLC system. Furthermore, the average throughput reduction due to the greedy strategy is more visible in a high UE density scenario. In order to serve all associated UEs under the greedy strategy, it may allocate lower-order modulation-modes for UEs under constraints, which leads to a service quality reduction.

Although the average throughput of the UC-VLC system remains near-constant as a function of UE density, the Fig. 4.21 shows that the outage probability is gradually increased in the higher UE-density scenarios. Having said that, it still remains substantially lower than that of the NC-VLC system. This implies that the proposed UC-VLC system is capable of maintaining a higher quality of service for the UEs both for the DCO-OFDM and ACO-OFDM schemes even in dense user-scenarios. Again, the outage probability in the greedy strategy based UC-VLC is substantially increased, compared to the dynamic one. Since the simulations of Fig. 4.21 are conducted at a fixed FoV value, the number of associated UE is the same in both the dynamical strategy and the greedy strategy. Upon increasing the number of UEs, it may be too difficult to serve all the associated UEs only by reducing their modulation-mode-order, hence leading to an increased outage probability for the UEs. Therefore, our proposed dynamic UE-support strategy achieves a much higher throughput, whilst supporting more UEs, regardless of the FoV and of the UE density.

4.5.3 Effect of Backhaul Rate Constraint on UC-VLC

In the single-AP-single-UE network, the backhaul rate constraint becomes redundant for NC-VLC systems. Therefore, in this section, we focus our attention on the effect of backhaul rate constraints in the proposed UC-VLC system.

To explore, the effect of the backhaul rate constraint R^{BH} on the sum-throughput of the UC-VLC system with DCO-OFDM and ACO-OFDM are provided in Figs. 4.22 and 4.23, respectively. As shown in the two figures, the backhaul rate constrained sum-throughput is presented as a function of the UC-cluster size. Compared to the ideal backhaul scenario (dash line), which represents that the sum-throughput achieved with infinite sufficient backhaul rate constraint, we find that the sum-throughput of various UC-cluster sizes is reduced, regardless of whether DCO-OFDM or ACO-OFDM is used. Furthermore, the more the rigid backhaul rate constraint, the higher the throughput reduction becomes. We also observe that the achievable sum-throughput relying on larger UC-clusters tends to be more seriously limited by the backhaul rate constraint. This is because the APs in a larger UC-cluster have to carry higher downlink traffic. These trends are also true for the ACO-OFDM scheme, as shown in the Fig. 4.23, albeit

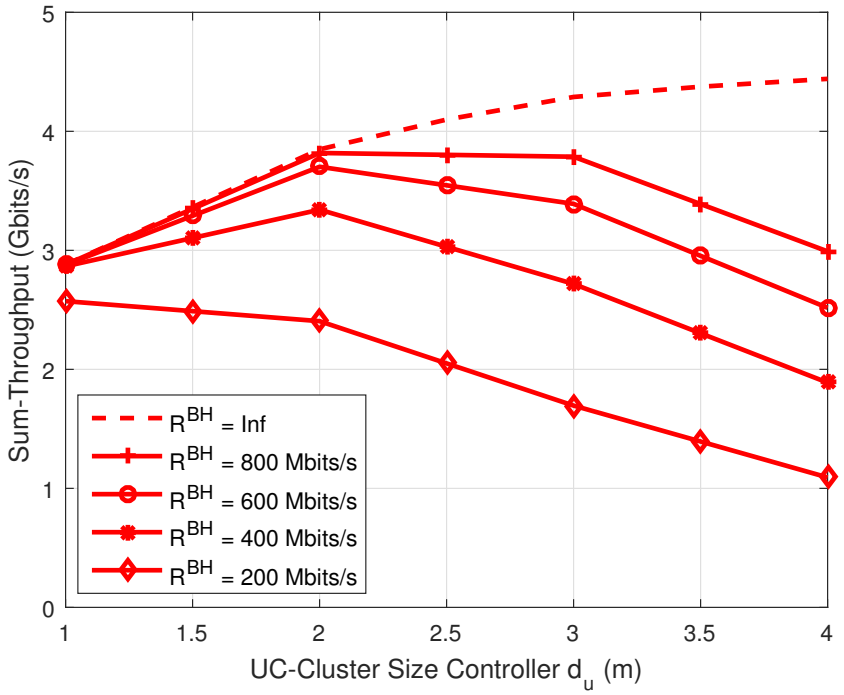

Figure 4.22: Influence of the backhaul rate constraint R^{BH} on the sum-throughput in the UC-VLC network relying on DCO-OFDM scheme for various UC-cluster sizes, using the parameters in Table 4.1.

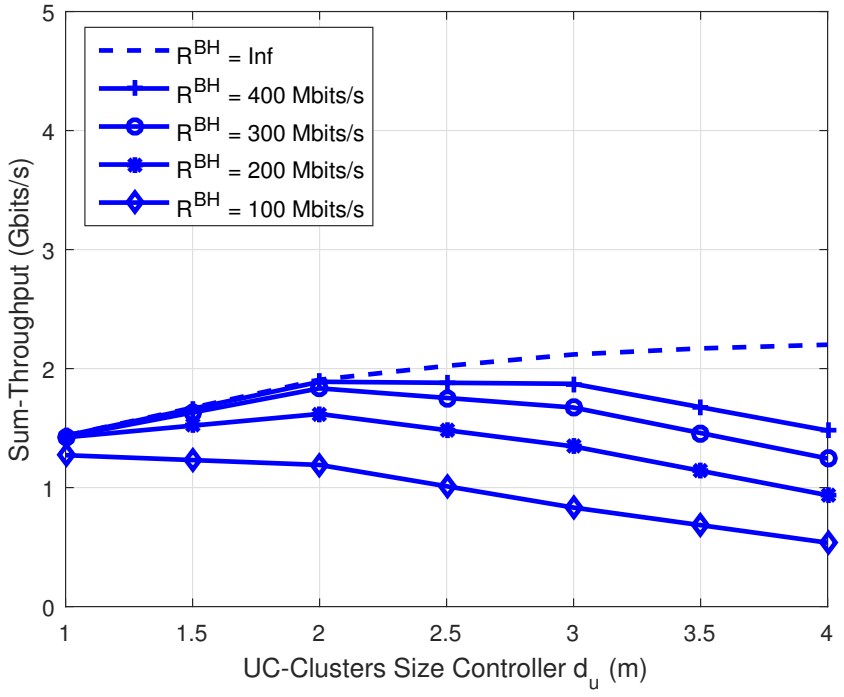

Figure 4.23: Influence of the backhaul rate constraint R^{BH} on the sum-throughput in the UC-VLC network relying on ACO-OFDM scheme for various UC-cluster sizes, using the parameters in Table 4.1.

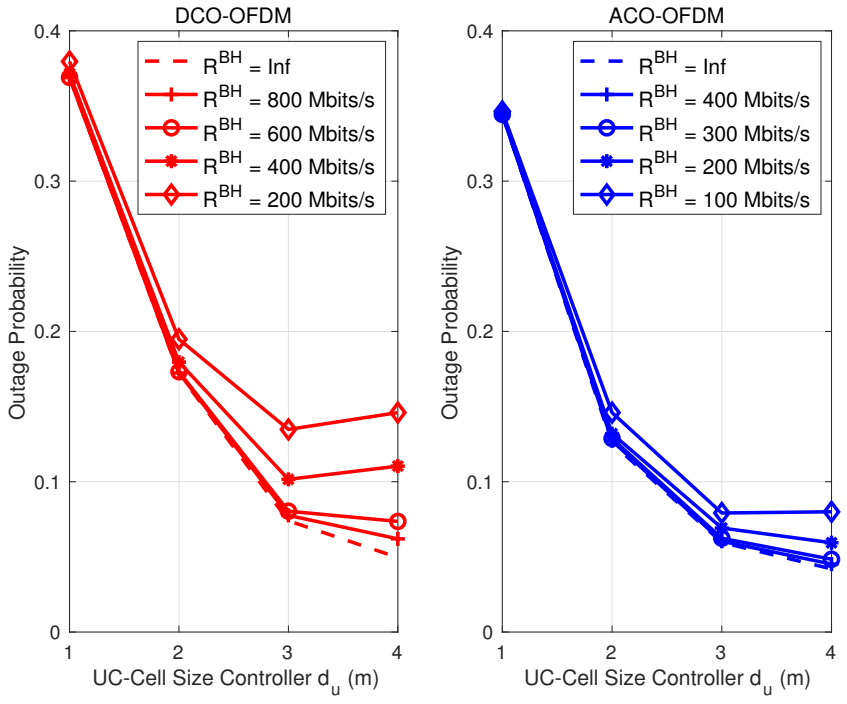

Figure 4.24: UE outage probability as a function of the backhaul rate constraint R^{BH} for our UC-VLC system at various UC-Cell sizes, using the parameters of Table 4.1.

the backhaul limitation of ACO-OFDM is not as grave as that of the DCO-OFDM scheme due to its lower sum-throughput.

Let us now investigate the impact of backhaul rate constraint on both the DCO-OFDM and the ACO-OFDM schemes in terms of outage probability, as shown in Fig. 4.24. By observing, the outage probability of all the UC-cluster size control parameter d_u is reduced upon increasing the backhaul rate constraint, which can be observed for both the DCO-OFDM and ACO-OFDM schemes. Furthermore, Fig. 4.24 shows that the UC-VLC system relying on larger UC-clusters experiences a lower outage probability, under having ideal backhaul constraint. This is because for larger control parameters d_u, the number of UC-clusters supporting the UE population is reduced as a benefit of the reduced ICI. Notably, $d_u = 4$ m results in an increased outage probability, when the backhaul limitation is stringent, because to meet the stringent backhaul constraint, the system will eventually shrink the cluster size and hence will serve fewer UEs per UC clusters.

4.6 Chapter Conclusion

In this chapter, the modulation-mode-related throughput was maximized in our UC-VLC system relying on the proposed dynamic resource allocation strategy. Explicitly, the practical concerns peculiar to the UC-VLC system were discussed in Section 4.2. Upon taking into account these practical concerns, our constrained maximization problem was formulated in Section 4.3. To handle the multi-user-dependent maximization problem, the original problem was divided into two steps, where we proved that it is optimum by successively solving those two steps. In Section 4.4, we found that the RA of UC-VLC can be modelled by the multi-choice knapsack problem, thus a dynamic-programming-based resource allocation strategy was proposed. Upon relying on this strategy, the modulation-mode assignment for UEs and the power allocation for APs were jointly decided, where the decision concerning the number of served UEs was also dynamically configure according to the communication environment. Compared to the adaptive modulation assignment using exhaustive search, the calculation complexity was significantly reduced, where the convergence of our proposed strategy was demonstrated in Fig. 4.8.

As for the numerical results, we first demonstrated that the proposed system is capable of readily tolerating positioning errors upto 10cm, as shown in Figs. 4.9 - 4.11, which can be achieved by most of the indoor positioning techniques, including our proposed hybrid positioning of Chapter 3. The UFR aided NC-VLC was used as our benchmarker. As seen in Figs. 4.12 and 4.13, the UEs are encouraged to achieve much higher throughput in UC-VLC, where the same resource allocation strategy is invoked. To elaborate, we investigated the maximized sum-throughput, when supporting various number of UEs both with and without clipping-distortion, which were characterized in Figs. 4.14 - 4.17. As a Benefit of UC-clustering, the UC-VLC enjoys a multi-UE gain in terms of its sum-throughput, where the size of UC-clusters influences the multi-UE gain. In the realistic clipping-distortion scenario, the power of DC-bias intended for clipping-distortion-elimination has to be jointly considered with the power allocated for transmission under our power constraint. The superiority of UC-VLC is also reflected in terms of its average throughput as well as its outage probability, for various FoV values and UE densities, as seen in Figs. 4.18 - 4.21. Additionally, the backhaul rate constraint was taken into account and it was contrasted to the ideal backhaul scenario, as demonstrated in Figs. 4.22 - 4.24. By carefully designing the size of UC-clusters, the impairments on throughput and outage probability due to the strict backhaul restriction can be readily relaxed.

4.7 Appendix: Proof of Theorem 4.1

The method of contradiction is adopted to prove **Theorem 4.1**. The detailed derivation is provided in the following.

We assume that the globally optimal modulation-mode assignment of the original problem is $\mathcal{M}_{\mathrm{g}}^{*}$. Its elements represent the modulation-mode decision of each specific UE. Accordingly, the globally optimal sum throughput can be obtained by $f^{T}(\mathcal{M}_{\mathrm{g}}^{*})$, where $f^{T}(\cdot)$ is the throughput function and $f^{T}(\mathcal{M}_{\mathrm{g}}^{*})$ satisfies the backhaul constraint. The globally optimal power allocation strategy $\mathcal{P}_{\mathrm{g}}^{*}$ can also be obtained, where each element satisfies our transmit power constraint. We assume that the modulation-mode assignment obtained by successively solving $\boldsymbol{S1}$ and $\boldsymbol{S2}$ is $\mathcal{M}_{\mathrm{s}}^{*}$, which is associated with the achievable sum throughput $f^{T}(\mathcal{M}_{\mathrm{s}}^{*})$ and the power allocation strategy $\mathcal{P}_{\mathrm{s}}^{*}$.

To prove **Theorem 4.1**, we assume $f^{T}(\mathcal{M}_{\mathrm{g}}^{*}) > f^{T}(\mathcal{M}_{\mathrm{s}}^{*})$, which means that the proposed algorithm cannot obtain the global optimum solution. Upon comparing constraint (4.5e) to (4.7d), it can be found that the power constraint is only applied to a specific AP at a time in $\boldsymbol{S1}$, not to all the APs indicated in the original problem. Furthermore, the backhaul constraint in $\boldsymbol{S1}$ can be viewed as infinity. The problem formulation of $\boldsymbol{S1}$ is then be rephrased as:

$$\max_{\mathcal{M}_{c}^{*}} \sum_{k=1}^{|\mathcal{K}_{c}|} \sum_{m=1}^{|\mathcal{M}|} r_{c,k,m} x_{c,k,m} \tag{4.19a}$$

$$\text{s.t. } x_{c,k,m} \in \{0,1\}, \quad \forall k \in \mathcal{K}_{c},\ \forall m \in \mathcal{M}; \tag{4.19b}$$

$$\sum_{m=1}^{|\mathcal{M}|} x_{c,k,m} \in \{0,1\}, \quad \forall k \in \mathcal{K}_{c}; \tag{4.19c}$$

$$\sum_{k=1}^{|\mathcal{K}_{c}|} \sum_{m=1}^{|\mathcal{M}|} p_{c,k,m} x_{c,k,m} \left[\boldsymbol{G}_{c}\right]_{(n,k)}^{2} \leq P_{\max}^{\mathrm{tx}}, \tag{4.19d}$$

$$\sum_{k=1}^{|\mathcal{K}_{c}|} \sum_{m=1}^{|\mathcal{M}|} r_{c,k,m} x_{c,k,m} \leq +\infty. \tag{4.19e}$$

Hence compare to the original problem, both the backhaul constraint and the power constraint in $\boldsymbol{S1}$ are more relaxed than that in the original problem. According to our assumption, the power allocation strategy $\mathcal{P}_{\mathrm{g}}^{*}$ satisfying the constraints (4.5d) and (4.5e) should also satisfy the constraints (4.19e) and (4.19d). It means that the modulation-mode assignment $\mathcal{M}_{\mathrm{g}}^{*}$ associated with the power strategy $\mathcal{P}_{\mathrm{g}}^{*}$ is also one of the solutions of $\boldsymbol{S1}$. When moving to $\boldsymbol{S2}$, it aims to pick one of the solutions obtained in $\boldsymbol{S1}$ under the sum throughput maximization principle so that all the APs fulfil their power constraint as well as the backhaul constraint. However, the result of $\boldsymbol{S2}$ is $\mathcal{M}_{\mathrm{s}}^{*}$, which represents

$f^T(\mathcal{M}_{\mathrm{g}}^*) < f^T(\mathcal{M}_{\mathrm{s}}^*)$ that is in contrast to our assumption. Therefore we may conclude that our proposed algorithm is capable of finding the global optimum.

Chapter 5

Multiple Access Design

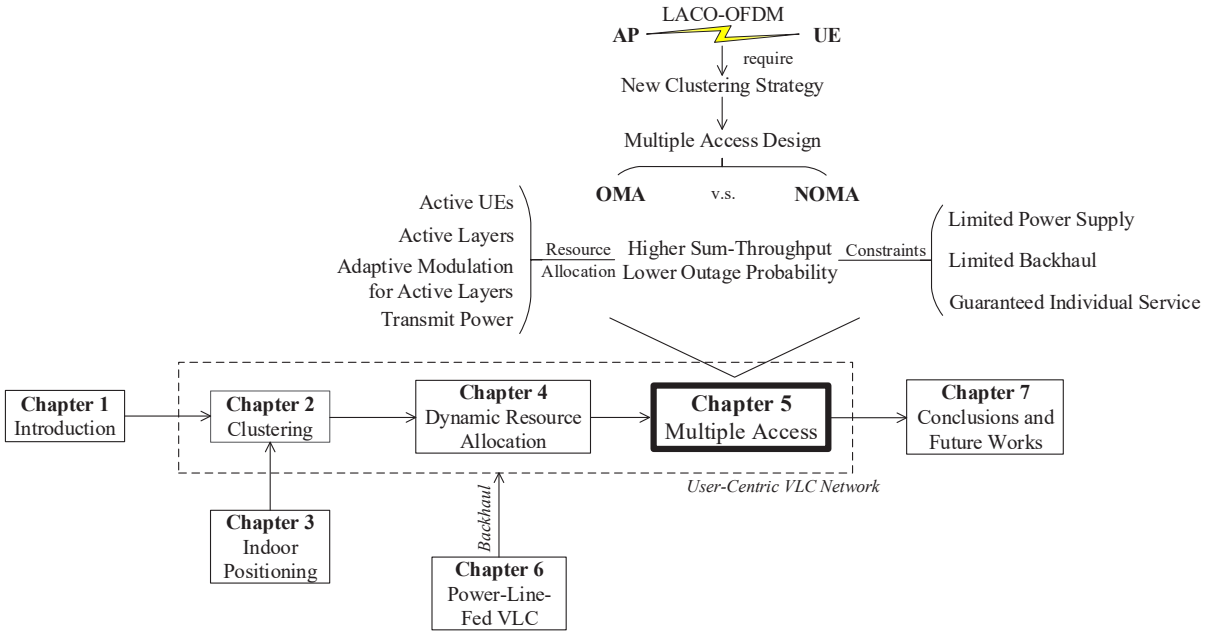

Figure 5.1: Block diagram of Chapter 5.

5.1 Introduction

Given the limited power-efficiency of DCO-OFDM and the modest bandwidth-efficiency of ACO-OFDM, our quest in this chapter is to investigate a more advanced transmission scheme for improving the overall system-level design of our UC-VLC system. LACO-OFDM [19] is one of the most efficient VLC transmission techniques, which exhibits substantial flexibility, because the number of active layers may be conveniently adapted

among the different UEs. Similarly, the modulation-mode of each active layer may also be different. Therefore, in this chapter, we investigate LACO-OFDM in our UC-VLC system. As indicated in [10], the merged-cell construction assisted by TPC techniques is capable of supporting a high throughput, as shown in Chapter 4. However, since the demodulation of the LACO-OFDM is carried out in a layer-by-layer manner, TPC cannot be readily invoked in LACO-OFDM for multi-user transmission. Therefore, a radical paradigm shift and a new system architecture is required for our LACO-OFDM aided VLC network, where dynamic resource allocation is proposed for exploiting the flexibility of LACO-OFDM at the system-level. In order to handle the severe ICI encountered by VLC systems when relying on densely-deployed APs, we propose a hybrid NOMA/OMA scheme for enhancing the performance with the aid of dynamic resource allocation.

The remainder of this chapter is organized as follows. Section 5.2 reviews the background of LACO-OFDM and demonstrates that the previously proposed UC-clustering is not applicable. In Section 5.3, we propose an overlapped clustering strategy for the sake of intrinsically amalgamating LACO-OFDM with our VLC system, which is based on a directed bipartite graph. In Section 5.4, the conventional NOMA scheme is introduced first and then a hybrid NOMA/OMA scheme is proposed for reducing the outage probability in the face of ICI. To attain the maximum sum-throughput, a two-tier resource allocation strategy is proposed in Section 5.5, which is capable of allocating a different number of active layers and different modulation-modes for the different layers. The simulation results of Section 5.6 characterize the achievable performance of our proposed hybrid MA schemes. Finally, this chapter is concluded in Section 5.7, which is then followed by the chapter's summary in Section 5.8.

5.2 Review of LACO-OFDM

Although the ACO-OFDM and DCO-OFDM constitute a pair of widely employed modulation schemes in VLC, they have their own limitations. According to [16], explicitly, ACO-OFDM utilizes only half the subcarriers for transmission, hence resulting in a data rate loss. By contrast, a DC bias is required by DCO-OFDM to generate positive signals, which wastes precious power [15]. Therefore, more advanced transmission schemes have been proposed, such as LACO-OFDM, which has drawn substantial research attention due to its power- and bandwidth-efficiency. Specifically, it improves the traditional ACO-OFDM by actively employing more subcarriers in a layer-based manner, hence attaining a higher transmission rate than ACO-OFDM, despite requiring a lower transmit power than DCO-OFDM. Furthermore, it provides a beneficial design flexibility by dynamically determining the number of active layers, and striking a trade-off among complexity, power efficiency and throughput.

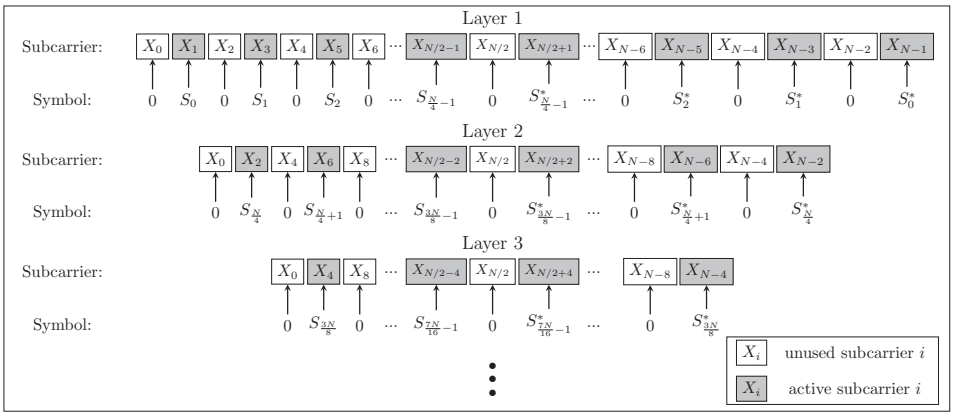

Figure 5.2: Schematic of LACO-OFDM relying on N subcarriers, where the superscript $(\bullet)^*$ is the conjugate operator to guarantee the reality of the signal.

To expound a little further, Fig. 5.2 demonstrates the operation of LACO-OFDM. A block of N frequency-domain samples is represented by $\boldsymbol{X} = [X_0, X_1, \cdots, X_{N-1}]$ and the OFDM source symbol is denoted by $\boldsymbol{S} = [S_0, S_1, \cdots, S_{N-1}]$, which is the result of the appropriately mapped source bit stream according to the specific modulation scheme chosen, such as M-QAM. It can be observed that the first layer of LACO-OFDM operates exactly as the conventional ACO-OFDM having N subcarriers, as seen in Fig. 5.2, which can only accommodate $N/4$ symbols and leaving $N/2$ unused subcarriers denoted as $[X_0, X_2, X_4, \cdots, X_{N-2}]$. Note that following the IFFT-based modulation in order to obtain a real-valued positive signal, the first layer's signal is then asymmetrically clipped at zero in the time-domain, where the clipping-distortion manifests itself in the frequency-domain by contaminating the previously unused even-indexed subcarriers, resulting in undesired ILI. To efficiently exploit the entire OFDM bandwidth, the unused subcarriers of the first layer can now be filled by ACO-OFDM again in the second layer as seen in Fig. 5.2, yielding $N/8$ more transmitted symbols, but bearing in mind that these subcarriers were also contaminated by the clipping-distortion generated by the first layer. Following the IFFT-based modulation in the second layer, clipping the resultant time-domain signal also generates new clipping-distortion, which affects the higher layers. The remaining layers obey the same philosophy of populating the unused subcarriers, resulting in efficient spectrum utilization, where the clipping-distortion generated by one layer will contaminate the symbols of higher layers. Upon increasing the number of layers, more subcarriers are utilized for data transmission, hence leading to an increased data rate. After zero-clipping the time-domain signals $\lfloor s_l \rfloor$ of the lth active layer are superimposed on each other, which are then transmitted through the VLC channel. For a more detailed graphical portrayal of the entire LACO-OFDM process, please refer to [21].

Before introducing the receiver of LACO-OFDM, we first analyse the power consumption of the LACO-OFDM. According to [141], the relationship between the power

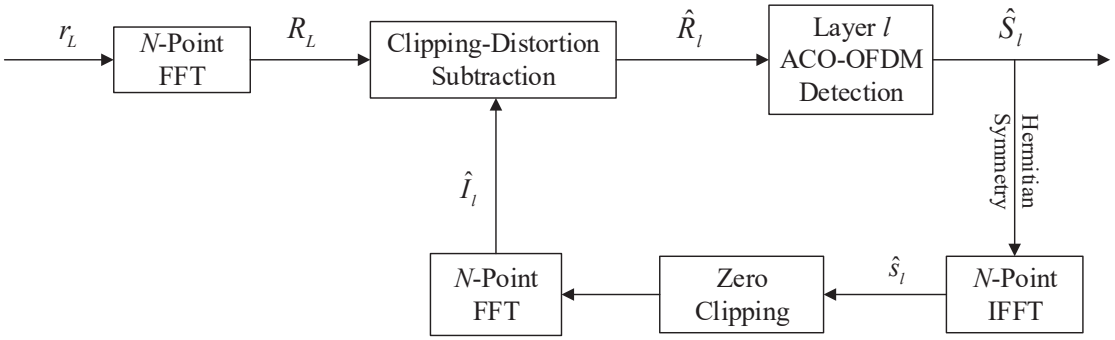

Figure 5.3: Block diagram of the LACO-OFDM receiver.

and variance of the lth layer is given by:

$$p_l = \mathbb{E}\left[\lfloor s_l \rfloor^2\right] = \frac{\sigma_l^2}{2}. \tag{5.1}$$

The mean and variance of the time-domain signal $\lfloor s_l \rfloor$ can be expressed as [21]:

$$\mathbb{E}\left[\lfloor s_l \rfloor\right] = \frac{\sigma_l}{\sqrt{2\pi}}; \tag{5.2}$$

$$\mathbb{D}\left[\lfloor s_l \rfloor\right] = \mathbb{E}\left[\lfloor s_l \rfloor^2\right] - \mathbb{E}^2\left[\lfloor s_l \rfloor\right] = \frac{\pi - 1}{2\pi}\sigma_l^2. \tag{5.3}$$

Since the signal $\lfloor s_l \rfloor$ of the different layers $l = 1, \cdots, L$ are independent of each other, the co-variance between any two of them is zero. Hence the mean and the variance of the superposed signal $x_L = \sum_{l=1}^{L} \lfloor s_l \rfloor$ becomes:

$$\mathbb{E}\left[x_L\right] = \sum_{l=1}^{L} \mathbb{E}\left[\lfloor s_l \rfloor\right] = \sum_{l=1}^{L} \frac{\sigma_l}{\sqrt{2\pi}} \tag{5.4}$$

$$\mathbb{D}\left[x_L\right] = \sum_{l=1}^{L} \mathbb{D}\left[\lfloor s_l \rfloor\right] = \sum_{l=1}^{L} \frac{\pi - 1}{2\pi}\sigma_l^2. \tag{5.5}$$

By further combining (5.1), (5.4) and (5.5), the relationship between the power of a total of L layers and the lth layer in LACO-OFDM can be expressed as:

$$\begin{aligned} P_L &= \mathbb{E}\left[x_L^2\right] = \mathbb{D}\left[x_L\right] + \mathbb{E}^2\left[x_L\right] \\ &= \frac{\pi - 1}{\pi}\sum_{l=1}^{L}\sigma_l^2 + \frac{1}{2\pi}\left(\sum_{l=1}^{L}\sigma_l\right)^2 \\ &= \frac{\pi - 1}{\pi}\sum_{l=1}^{L} p_l + \frac{1}{\pi}\left(\sum_{l=1}^{L}\sqrt{p_l}\right)^2. \end{aligned} \tag{5.6}$$

which implies that the total power of all L layers is not equal to the sum of the power of each layer.

At the receiver shown in Fig. 5.3, the received signal r_L is detected in a layer-by-layer manner. As we discussed above, the first layer has no clipping-distortion contamination, i.e. it is free from ILI. Therefore, it can be directly detected exactly as in ACO-OFDM, yielding the frequency-domain detected bits $\hat{S}_1$. Since the clipping-distortion generated by the first layer is imposed on all the even-indexed subcarriers, ILI decontamination has to be carried out before detecting the second layer. Fortunately, the estimated time-domain signal $\hat{s}_1$ of the first layer can be locally re-generated with the aid of $\hat{S}_1$, where the frequency-domain clipping-distortion can also be estimated by the fast-Fourier-transform (FFT) of $\hat{s}_1$ after zero clipping, as seen in Fig. 5.3. By subtracting the re-generated clipping-distortion $\hat{I}_1$ from the received signal eliminates the ILI imposed by the first layer, hence the transmitted bits carried by the second layer can be perfectly detected. The estimated bits $\hat{S}_2$ of the second layer may be invoked for re-generating the clipping-distortion imposed on the higher-order layers, using the same procedure as mentioned above. By using the iterative procedure of Fig. 5.3, the ILI-free information transmitted by all L layers can be detected layer-by-layer. However, as expected, any estimation error lead to residual interference, which corrupts the re-generation process. As a consequence, the residual ILI accumulates, when we move to higher layers. Hence, the higher layers tend to suffer a worse transmission environment.

Compared to the conventional ACO-OFDM, the LACO-OFDM associated with L layers is hence capable of transmitting $\sum_{l=2}^{L} N/2^{l+1}$ more source symbols without adding a DC bias. As a further benefit, the flexibility of the VLC system can be significantly improved by invoking LACO-OFDM. For example, the number of active layers may be varied across the UEs, where for each active layer, the choice of modulation-mode may also be different. Therefore, we amalgamate the advanced LACO-OFDM with our UC-VLC system for attaining an improved performance. As the UC-clustering results in the multi-AP-multi-UE structure, TPC may be employed for eliminating the MUI, which poses a challenge when conceiving LACO-OFDM with our current UC-VLC system. To elaborate a little further, an important feature of LACO-OFDM is that the detection quality of higher layers relies on the signal re-generation quality of the lower layers. The problem is that by employing TPC, the transmit signal of each layer contains the information of not only a single but of several UEs. Since detection is carried out separately by each individual UE, unfortunately the clipping-distortion cannot be re-generated locally. Therefore, a paradigm shift from our current UC-VLC system is required in order to fully explore the flexibility of LACO-OFDM at the system-level design.

5.3 Network Association

By considering LACO-OFDM, a new network association design has to be conceived, because additionally the deployment of AP in VLC tends to be more dense than that of the RF. Owing to the densification of APs, a given UE may be in the vicinity of multiple APs. Although the channel gain offers a straightforward mean of determining the topology, the UE-AP association purely relying on it would remain inefficient. This is because the UEs located at the corner or edge of the room are more likely to receive strong reflections from the walls [121]. However, it is not beneficial to associate a UE with an AP providing strong reflections if their Euclidean distance is high. As a further parameter, the transmission distance may also be considered. Inspired by [142], the association between a pair of distinct entities, such as the APs and UEs, allows us to invoke bipartite graph theory. In order to fully explore the coverage overlap of APs, an overlapped clustering strategy based on graph-theory is proposed in this section.

5.3.1 Overlapped Clustering

In order to carry out the association relying on the channel conditions and on the propagation distance, based on graph theory, we aim to build a directed bipartite graph, $\mathcal{G}_{\text{asso}} = (\mathcal{V}_{\text{asso}}, \mathcal{E}_{\text{asso}})$, where the vertex set is given by $\mathcal{V}_{\text{asso}} = \mathcal{K} \cup \mathcal{N}$. Note that the UE set $\mathcal{K}$ and the AP set $\mathcal{N}$ are two distinct classes and no edges are expected within each class. The edge set $\mathcal{E}_{\text{asso}} = \mathcal{E}_{\text{asso}}^{\text{ue}\to\text{ap}} \cap \mathcal{E}_{\text{asso}}^{\text{ue}\leftarrow\text{ap}}$ accommodates the intersection of the set, $\mathcal{E}_{\text{asso}}^{\text{ue}\to\text{ap}}$, holding edges spanning from the UE-end to the AP-end and the set, $\mathcal{E}_{\text{asso}}^{\text{ue}\leftarrow\text{ap}}$, containing edges emerging from the AP-end to the UE-end. To complete this directed bipartite graph $\mathcal{G}_{\text{asso}}$, we conceive three stages detailed as follows.

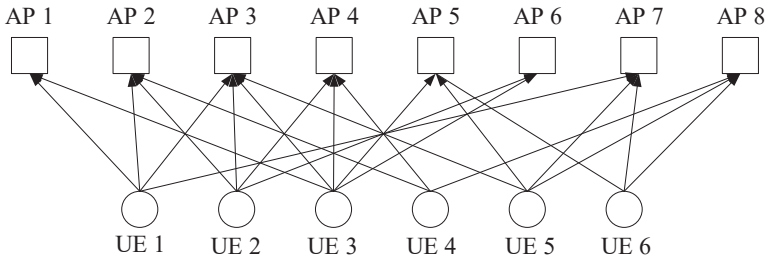

Figure 5.4: An example of the UE-end channel-strength-guaranteed matching (directed edges are represented by solid arrows).

(a) *Channel-Gain-Guaranteed Matching*: In this stage, the preference of association is based on the channel gain. If the aggregated channel gain $h_{k,n}$ between AP n and UE k is larger than a pre-defined quality threshold H_{thr}, an edge $e_{k\to n}$ is built with a direction from UE-end to AP-end. Otherwise, no edge between them at

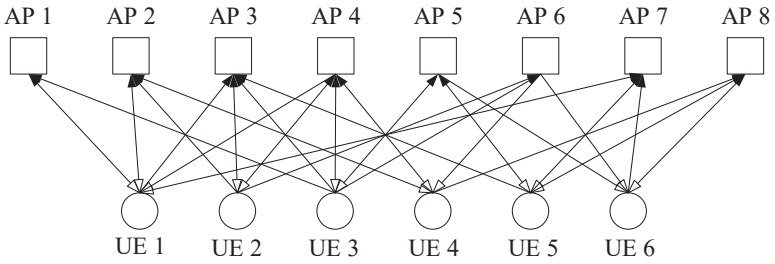

Figure 5.5: An example of the AP-end transmission-distance-restricted matching (directed edges are given by hollow arrows).

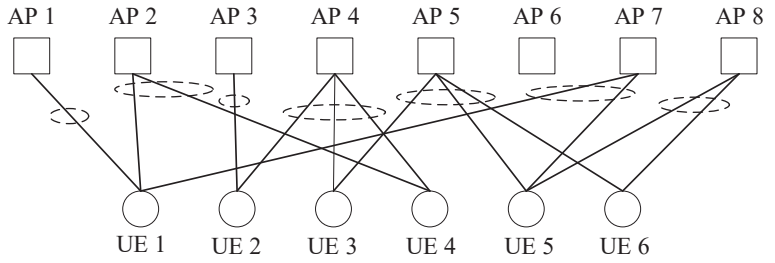

Figure 5.6: The constructed clusters based on the proposed overlapped clustering.

this stage. Each UE in $\mathcal{K}$ fully explores all potential APs and the resultant edges are held in $\mathcal{E}_{\text{asso}}^{\text{ue}\to\text{ap}}$, which is expressed as:

$$\mathcal{E}_{\text{asso}}^{\text{ue}\to\text{ap}} = \left\{ e_{k\to n} : \ h_{k,n} \geq H_{\text{thr}}, \quad \forall k \in \mathcal{K}, \ \forall n \in \mathcal{N} \right\}. \tag{5.7}$$

This UE-end matching is exemplified in a 6-UEs-8-APs scenario shown in the Fig. 5.4, where all directed edges in $\mathcal{E}_{\text{asso}}^{\text{ue}\to\text{ap}}$ are denoted by solid arrows.

(b) *Transmission-Distance-Restricted Matching*: In this stage, we conceive a transmission-distance restriction as a complementary matching metric. Explicitly, for a given AP n, an edge $e_{k\leftarrow n}$ will be constructed with a direction emerging from AP n to UE k, if the Euclidean distance between them is below the pre-defined distance threshold D_{thr}. Each AP searches through the set of all the potential UEs and the edges generated in this stage are held in the set $\mathcal{E}_{\text{asso}}^{\text{ue}\leftarrow\text{ap}}$ as:

$$\mathcal{E}_{\text{asso}}^{\text{ue}\leftarrow\text{ap}} = \left\{ e_{k\leftarrow n} : \ D_{k,n} \leq D_{\text{thr}}, \quad \forall n \in \mathcal{N}, \ \forall k \in \mathcal{K} \right\}. \tag{5.8}$$

This AP-end matching is displayed in Fig. 5.5, where the directed edges in $\mathcal{E}_{a}^{\text{ue}\leftarrow\text{ap}}$ are given by hollow arrow tips.

(c) *Confirmation*: After the above two stages, the topology ends up with four different types of associations: unidirectional connection from UE-end to AP-end, unidirectional connection from AP-end to UE-end, bidirectional connection and

no connection. By satisfying both the channel gain and transmission distance criteria, we confirm the association between the APs and UEs, provided that they are connected bidirectionally, as depicted in Fig. 5.6.

The association graph $\mathcal{G}_{\text{asso}}$ contributes to our overlapping clusters, where a given AP may have more than one target UE, while a given UE may be associated with multiple APs, ending up with a *many-to-many* matching solution. As shown in Fig. 5.6, a total of seven clusters are constructed for the example, where each cluster consists of an AP and its associated UEs. Note that since no associated UEs are found for AP 6, hence this AP switches to a "sleep" mode for energy saving.

5.3.2 Complexity Analysis

We assume that the number of candidate APs providing adequate links for UE k at Stage (a) is Q_k and the number of candidate UEs located within the maximum tolerance distance from AP n at Stage (b) is K_n. For the first two stages, the complexity order is given by $\mathcal{O}\big(\sum_{k=1}^{|\mathcal{K}|} Q_k\big)$ and $\mathcal{O}\big(\sum_{n=1}^{|\mathcal{N}|} K_n\big)$, respectively. During the last stage, we have to check the possible connections in the second stage for each possible association between the two players paired in the first stage. This implies an extra complexity order of $\sum_{k=1}^{|\mathcal{K}|}\big(Q_k \sum_{n=1}^{|\mathcal{N}|} K_n\big)$. Thus, the total complexity of our proposed overlapping clustering strategy amounts to:

$$\mathcal{O}\left(\sum_{k=1}^{|\mathcal{K}|} Q_k + \sum_{n=1}^{|\mathcal{N}|} K_n + \sum_{k=1}^{|\mathcal{K}|}\left(Q_k \sum_{n=1}^{|\mathcal{N}|} K_n\right)\right), \tag{5.9}$$

which corresponds to a polynomial order. As a benchmark, we compare it to the optimal clustering solution based on the exhaustive search. Since it is a *many-to-many* matching problem, for a given AP n, there are $\sum_{\tau=0}^{|\mathcal{K}|}\binom{|\mathcal{K}|}{\tau}$ possible UE association combinations. For a total of $|\mathcal{N}|$ APs, the computational complexity order of the exhaustive search is given by:

$$\mathcal{O}\left(\left(\sum_{\tau=0}^{|\mathcal{K}|}\binom{|\mathcal{K}|}{\tau}\right)^{|\mathcal{N}|}\right). \tag{5.10}$$

This shows that the optimal association problem scales exponentially with the number of APs, which becomes excessive in VLC since the value of $|\mathcal{N}|$ is normally high. Therefore, the proposed overlapped clustering is capable of spectacularly reducing the computation complexity.

5.4 Hybrid Multiple Access Design

Efficiently organizing the multi-user access for each constructed cluster is a challenging problem in the ultra-dense VLC network. The most straightforward arrangement is OMA, relying on TDMA or FDMA. In TDMA, the APs offer access to their associated UEs in orthogonal time-slots, whilst FDMA allows the UEs to be multiplexed in the frequency-domain, so that they can be supported simultaneously. However, OMA may not work efficiently in VLC, since the number of UEs supported by a given AP may be high, while a transmission link between a given AP and its associated UE may also be interfered by a number of other APs. Moreover, due to the dense deployment of APs in VLC networks, a UE may be associated to more than one AP, and similarly, an AP could be found by more than one UE. This bidirectional multi-association scenario makes the network access management much more complex than that of conventional wireless networks. Therefore, simply relying on conventional OMA techniques may be deemed inefficient. As a parallel development, NOMA has drawn substantial research attention [54–66]. In contrast to OMA techniques, NOMA allows multiple UEs to access the network by multiplexing them in the power-domain, where SIC is applied at the receiver side to separate the information of each individual UE [54]. It is clearly beneficial that multiple UEs are capable of simultaneously using the same time- and spectral-slots. In this manner, the performance of UEs near the attocell's edge can be significantly improved. Since in VLC the main limitation is the narrow modulation bandwidth of LEDs, the NOMA concept can be invoked for enhancing the achievable throughput in the downlink of VLC networks [55].

In this section, we will demonstrate that the emerging NOMA may be vulnerable to ICI in the context of VLC relying on densely deployed APs, leading to an excessive UE outage probability[1]. To overcome this problem, we design a hybrid NOMA/OMA scheme for the sake of eliminating the ICI and improving the outage probability to attain an increased sum-throughput in our VLC networks.

5.4.1 Conventional NOMA Scheme

Consider a specific cluster $\mathcal{C}_c$, where AP n aims for supporting $|\mathcal{K}_c|$ UEs[2]. We assume that the maximum UE-load of each AP is fixed to Λ. Based on the NOMA principle, $K_n = \min(|\mathcal{K}_n|, \Lambda)$ number of UEs are supported at different levels of power. Note that if we have $|\mathcal{K}_n| > \Lambda$, the AP randomly selects one of the UE combinations based on $\binom{|\mathcal{K}_n|}{\Lambda}$, leaving the rest of the UEs unsupported for the current time-slot. Without loss

[1] We define the UE's outage probability in this chapter as the probability of having unsupported UEs, which may occur due to various reasons, such as an inadequate individula rate.

[2] Note that the index of cluster is similar to the index of AP according to the association in this chapter, we will use the subscript n to express both the AP and cluster index, for avoiding misunderstanding

of generality, the selected UEs are sorted[3] based on their channels as $|h_{1,n}|^2 \geq |h_{2,n}|^2 \geq \cdots \geq |h_{K_n,n}|^2$. Therefore, the NOMA-based information $\boldsymbol{x}_n$ transmitted to all K_n UEs using the superposition coding technique is expressed as:

$$\boldsymbol{x}_n = \sum_{k=1}^{K_n} \sqrt{P_{n,k}} s_{n,k}, \tag{5.11}$$

where $s_{n,k}$ conveys the desired signal of the kth UE transmitted by AP n in cluster $\mathcal{C}_c$ and its allocated power is $P_{n,k}$. At the receiver side, the observation at the kth UE is:

$$\begin{aligned} y_{n,k} &= \boldsymbol{x}_n h_{k,n} + w_{n,k} \\ &= \underbrace{\sqrt{P_{n,k}} h_{k,n} s_{n,k}}_{\text{desired signal of } k\text{th UE}} + \underbrace{\sum_{\substack{q=1 \\ q \neq k}}^{K_n} \sqrt{P_{n,q}} h_{k,n} s_{n,q}}_{\text{intra-cell interference}} + \underbrace{\sigma^2 + \boldsymbol{I}_{n,k}}_{\text{noise and interference}}, \end{aligned} \tag{5.12}$$

where $w_{n,k}$ represents the sum of both the AWGN and ICI. For the sake of decoding its own signal, the kth UE has to decode and subtract the signal of other UEs having a lower channel gain, based on SIC. By successfully removing part of the intra-cell interference $\sum_{q=k+1}^{K_n} \sqrt{P_{n,q}} h_{k,n} s_{n,q}$, the kth UE then decodes its desired signal. As a result, the residual intra-cell interference, namely $\sum_{q=1}^{k-1} \sqrt{P_{n,q}} h_{k,n} s_{n,q}$, is treated as noise. Therefore, the SINR of the kth UE becomes:

$$\gamma_{n,k} = \frac{|h_{k,n}|^2 P_{n,k}}{\sum\limits_{q=1}^{k-1} |h_{k,n}|^2 P_{n,q} + \sigma^2 + \boldsymbol{I}_{n,k}}. \tag{5.13}$$

The variance of AWGN noise is based on $\sigma^2 = N_0 B$, where N_0 is the noise spectrum, and B is the available bandwidth. The ICI imposed on the kth UE is given by:

$$\boldsymbol{I}_{n,k} = \sum_{f=1, f \neq n}^{|\mathcal{N}|} I_{n,k}^{[f]}, \tag{5.14}$$

which emanates from all other clusters, except for $\mathcal{C}_n$. Explicitly, if there is no association between a specific AP in cluster $\mathcal{C}_f$ and the kth UE in cluster $\mathcal{C}_n$, the ICI arriving from $\mathcal{C}_f$ is:

$$I_{n,k}^{[f]} = |h_{k(n),f}|^2 P_{\max}, \tag{5.15}$$

where $h_{k(n),f}$ is the channel gain between the kth UE in $\mathcal{C}_n$ and the AP in $\mathcal{C}_f$, while $P_{\max}$ represents the maximum transmit power of $\mathcal{C}_f$. Otherwise, if the kth UE is also

[3]To avoid misunderstanding, UE k has the same meaning as the kth UE after sorting process.

associated with the AP in $\mathcal{C}_f$, the ICI is given by:

$$I_{n,k}^{[f]} = \frac{\varsigma_{f,k(n)} - 1}{|\mathcal{K}_f|} |h_{k(n),f}|^2 P_{\max}, \tag{5.16}$$

where $1 \leq \varsigma_{f,k(n)} \leq |\mathcal{K}_n|$ denotes the sorting order of the UE in $\mathcal{C}_f$. Due to the NOMA regime, only the residual intra-cell interference of the cluster $\mathcal{C}_f$ imposes the ICI to the kth UE in $\mathcal{C}_n$, which implies that the overlapping nature of the proposed clustering mitigates the ICI.

5.4.2 Hybrid NOMA/OMA Scheme

However, apart from the maximum UE-load limitation, the outage probability of the conventional NOMA scheme may be further degraded, when additional practical constraints are also taken into account, such as individual rate requirement, backhaul restrict and transmit power limitation. Furthermore, the ICI becomes more severe in VLC because of the dense deployment of APs, which further impairs the performance of conventional NOMA. As a remedy, we therefore propose a hybrid NOMA/OMA scheme, which can flexibly introduce both the OMA technique, such as FR and TDMA-based scheduling, further combined with the conventional NOMA scheme. To elaborate a little further, by employing the FR technique, the ICI can be readily controlled by relying on the most appropriate selection of the reuse factor τ, while the TDMA-based scheduling is capable of mitigating the UE's outage probability by re-considering the UEs, which were in outage or unselected due to the load limitation during the previous time slots.

5.4.2.1 Graph-Coloring Based Frequency-Resource Block Allocation

Again, to cope with the ICI, the classic FR technique may be invoked, where the entire spectrum is partitioned into τ frequency-resource blocks (FRBs) and allocated to each cluster so that the ICI can be eliminated by ensuring that adjacent APs do not share the same spectrum. We realize that the bandwidth partitioning inevitably imposes a sum-throughput reduction. Hence, there is a trade-off between the achievable throughput and the ICI-mitigation. To identify the best FR pattern, we propose a graph-coloring based FRB allocation strategy, which is followed by graph building, sorting and coloring stages.

We say that $z_{c,f} = 1$ represents that two clusters $\mathcal{C}_c$ and $\mathcal{C}_f$ are overlapped, if their associated UEs are partially or entirely duplicated, which is indicated by:

$$z_{c,f} = \begin{cases} 1, & \sum_{k \in \mathcal{K}} x_{c,k} x_{f,k} > 0; \\ 0, & \sum_{k \in \mathcal{K}} x_{c,k} x_{f,k} = 0. \end{cases} \tag{5.17}$$

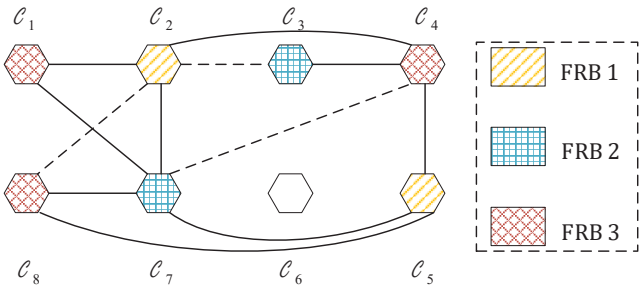

Figure 5.7: Graph-coloring based FRB allocation example using $\tau = 3$, according to the constructed clusters in Fig. 5.6.

The index of $x_{c,k} = 1$ indicates that UE k is associated with $\mathcal{C}_c$, otherwise it is $x_{c,k} = 0$. Consider the association scenario of Fig. 5.6 as an example. A coloring graph, $\mathcal{G}_{\text{color}} = (\mathcal{V}_{\text{color}}, \mathcal{E}_{\text{color}})$, is aimed to be constructed, where $\mathcal{V}_{\text{color}}$ is the vertex set containing all the clusters and the edge set $\mathcal{E}_{\text{color}}$ holding the relationship between any two vertices. To elaborate, an edge is constructed between any two vertices if we have $z_{n,f} = 1$, as indicated by the solid lines shown in Fig. 5.7. Additionally, when the ICI between the non-overlapping clusters is higher than the threshold I_{thr}, an edge is also added between them, as indicated by the dashed lines in Fig. 5.7. To this end, the graph $\mathcal{G}_{\text{color}}$ has been built.

Vertex	Degree	Weighted Degree
v_1	2	2
v_2	5	4
v_3	2	1.5
v_4	4	3.5
v_5	3	3
v_6	0	0
v_7	5	4.5
v_8	3	2.5

Table 5.1: Degree and weighted degree of vertices in Fig. 5.7

At the sorting stage, we define that the degree $\deg(v_n)$ of the vertex n as the number of edges it connects with, where the weighted degree $\overline{\deg}(v_n)$ takes into account the weighting factors ω_{s} and ω_{d} for the solid edges and dashed edges, respectively. Let us assume that we have $\omega_{\text{s}} = 1$ and $\omega_{\text{d}} = 0.5$. Then, according to our definitions, both the degrees and the weighted degrees of all vertices seen in Fig. 5.7 are summarized in Table 5.1. However, purely relying on the degree is inefficient, because for example both the vertex v_2 and v_7 have the same degree of 5, whilst the weighted degree is $v_2 = 4$ and that of v_7 is 4.5. Therefore, the sorting takes into account both the degree and the weighted degree, albeit a higher priority is assigned to the degree. Therefore, the sorting

Algorithm 2 TDMA-based Scheduling

Input: The cluster $\mathcal{C}_n = \{\mathcal{N}_n, \mathcal{K}_n\}$ and its channel matrix H_n

Require: I: Scheduling

Initialisation: $\mathcal{K}_n^{\textcircled{S}} = \emptyset$, $g = 0$, $|\mathcal{K}_{n,g}^{\textcircled{S}}| = +\infty$.

while $\mathcal{K}_n^{\textcircled{S}} \neq \mathcal{K}_n$ & $|\mathcal{K}_{n,g}^{\textcircled{S}}| \neq 0$ **do**

  $g = g + 1$;

  AP n in cluster $\mathcal{C}_n$ attempts to support a number of $\begin{cases} \min(|\mathcal{K}_n|, \Lambda), & g = 1; \\ \min(|\mathcal{K}_n| - \sum_{e=1}^{g-1} |\mathcal{K}_{n,e}^{\textcircled{S}}|,\ \Lambda), & g > 1, \end{cases}$ UEs in NOMA fashion;

  The successfully served UEs at this iteration are held in set $\mathcal{K}_{n,g}^{\textcircled{S}}$;

  $\mathcal{K}_n^{\textcircled{S}} = \mathcal{K}_n^{\textcircled{S}} \cup \mathcal{K}_{n,g}^{\textcircled{S}}$;

end while

$\mathcal{K}_n^{\varnothing} = \mathcal{K}_n \setminus \mathcal{K}_n^{\textcircled{S}}$, flag $= g$;

Require: II: Time-Resource Allocation

if $|\mathcal{K}_{n,\text{flag}}^{\textcircled{S}}| \neq 0$ **then**

  for $g = 1 \rightarrow$ flag **do**

    $t_g = \frac{|\mathcal{K}_{n,g}^{\textcircled{S}}|}{|\mathcal{K}_n|} \times T$;

  end for

else

  for $g = 1 \rightarrow$ flag $- 1$ **do**

    $t_g = \left(\frac{|\mathcal{K}_{n,g}^{\textcircled{S}}|}{|\mathcal{K}_n|} + \frac{|\mathcal{K}_n^{\varnothing}| \times |\mathcal{K}_{n,g}^{\textcircled{S}}|}{|\mathcal{K}_n| \times |\mathcal{K}_n^{\textcircled{S}}|} \right) \times T$;

  end for

end if

result of Fig. 5.7 is given by:

$$v_7 \geq v_2 \geq v_4 \geq v_5 \geq v_8 \geq v_1 \geq v_3 \geq v_6. \tag{5.18}$$

In the ensuing coloring stage, the first τ vertices having the highest sorting order are colored first, and the remaining vertices are then assigned by a random color, which is different from that of their adjacent vertices. The coloring result of the example can be found in Fig. 5.7, where the whole spectrum is partitioned into three FRBs. Note that if τ is not high enough, it may happen that two adjacent vertices are assigned by the same FRB, yielding ICI.

5.4.2.2 TDMA-based Scheduling

If the FR factor τ is insufficiently high, ICI still exists, leading to excessive outage probability. The TDMA-based scheduling is therefore invoked within each cluster for reducing the UE's outage probability with the aid of time-domain iterations. To be specific, it consists of two stages: round-robin scheduling and time-resource allocation, which is presented in **Algorithm 2**. To proceed, let us first introduce some notations. The sets $\mathcal{K}_n^{\textcircled{S}}$ and $\mathcal{K}_n^{\varnothing}$ are employed to hold the identity of the served UEs and of the

unsupported UEs of cluster $\mathcal{C}_n$, respectively, where the set $\mathcal{K}_n^{\textcircled{S}}$ is updated in every iteration. During the gth iteration, the supported UEs are saved in the active-UE group $\mathcal{K}_{n,g}^{\textcircled{S}}$.

To start with, constrained by the maximum load limitation Λ, the AP in cluster $\mathcal{C}_n$ intends to randomly support $K_{n,1} = \min(|\mathcal{K}_n|, \Lambda)$ number of UEs following the conventional NOMA principle. The successfully served UEs[4] are then held in $\mathcal{K}_{n,1}^{\textcircled{S}}$ as well as in $\mathcal{K}_n^{\textcircled{S}}$. Note that if we have $|\mathcal{K}_n| < \Lambda$ and $\mathcal{K}_{n,1}^{\textcircled{S}} = \mathcal{K}_n$, which means that the AP is able to serve all its associated UEs at the same time-slot, then cluster $\mathcal{C}_n$ does not need the scheduling process. Otherwise, when we arrive at $\mathcal{K}_n^{\textcircled{S}} \neq \mathcal{K}_n$, those unsupported UEs are re-considered in the following iterations. The set $\mathcal{K}_n^{\textcircled{S}}$ is expanded step-by-step, when more UEs can be supported, until we reach $\mathcal{K}_n^{\textcircled{S}} = \mathcal{K}_n$. Note that if we end up with $\mathcal{K}_{n,g}^{\textcircled{S}} = \emptyset$, the scheduling process will be suspended and the remaining unsupported UEs are classified as being in outage, since the AP cannot afford to support them.

For the time-resource allocation stage, we assume that the total time duration available for each cluster is T and that each UE is assigned an equal amount of time resource $T/|\mathcal{K}_n|$. After completing the scheduling stage, if it arrives at $|\mathcal{K}_{n,\text{flag}}^{\textcircled{S}}| \neq 0$, which implies that all UEs in $\mathcal{K}_n$ can be supported, then the time resource t_g allocated to the gth group is proportional to the number of its served UEs, which is given by:

$$t_g = \frac{|\mathcal{K}_{n,g}^{\textcircled{S}}|}{|\mathcal{K}_n|} \times T. \tag{5.19}$$

Otherwise, the time-resource of those unsupported UEs, which is amounted to $T|\mathcal{K}_n^{\varnothing}|/|\mathcal{K}_n|$, is proportionally re-allocated to each active UE group according to $|\mathcal{K}_{n,g}^{\textcircled{S}}|$. Hence, for the gth group, the allocated time-resource is expressed as:

$$t_g = \left(\frac{|\mathcal{K}_{n,g}^{\textcircled{S}}|}{|\mathcal{K}_n|} + \frac{|\mathcal{K}_n^{\varnothing}| \times |\mathcal{K}_{n,g}^{\textcircled{S}}|}{|\mathcal{K}_n| \times |\mathcal{K}_n^{\textcircled{S}}|} \right) \times T. \tag{5.20}$$

To this end, each scheduled UE in cluster $\mathcal{C}_n$ can find its group with respect to the transmission time. The TDMA-based scheduling is summarized in **Algorithm 2**.

Remark 1. *The computational complexity of* ***Algorithm 2*** *is determined by the number of iterations and the complexity at each iteration. Upon considering the worst case, we have* $|\mathcal{K}_{n,g}^{\textcircled{S}}| = 1,\ g = 1, \cdots, |\mathcal{K}_n|$. *Therefore, the complexity of the algorithm can be approximated at most as* $\mathcal{O}\left(\sum_{g=1}^{|\mathcal{K}_n|} \kappa_g + |\mathcal{K}_n|\right)$, *where* κ_g *denotes the complexity of the resource allocation strategy we will discuss later.*

[4]Note that the decision of whether a given UE is served or not will be discussed in Section 5.5, which implies that during every iteration, it may arrive at $|\mathcal{K}_{n,g}^{\textcircled{S}}| \leq K_{n,g}$.

Upon introducing the TDMA-based scheduling, the number of served UEs may be accelerated within each cluster by grouping the associated UEs of a given AP into active orthogonal time-domain UE groups having different amounts of time resources. However, the price of improving the outage probability is the reduction of sum-throughput due to the time-resource partitioning. Furthermore, we observe that there are still situations, where we have $\mathcal{K}_n^{\textcircled{S}} \neq \mathcal{K}_n$, which is mainly due to the grave ICI. Therefore, both FR and TDMA-based scheduling may be dynamically invoked in our LACO-OFDM aided VLC system, depending on the communication environment.

5.5 Dynamic Resource Allocation for LACO-OFDM Based UC-VLC

The decision as to whether to support a given UE or not is formulated in this section, along with an efficient resource allocation strategy relying on the sum-throughput maximization principle. Explicitly, we focus our attention on the adaptive modulation-mode assignment for each UE supported, as well as on the power allocation for each active AP. Since the high-flexibility LACO-OFDM scheme is employed, this allows the UE to select different numbers of active layers and also allows each active layer to be assigned various modulation-modes. However, this inevitably increases the complexity. Note that these decisions depend not only on the UE's own received signal strength, but also on that of the other UEs, hence leading to a complex multi-user-dependent and multi-layer-dependent maximization problem. Furthermore, in practical UC-VLC networks, the APs have a limited transmit power and limited backhaul-rate, which may be the bottleneck of the system's performance. In addition, it is important to guarantee a minimum rate for each UE in order to offer some degree of fairness. Hence, in this section, this challenging sum-throughput maximization problem is formulated under practical considerations and is then solved by our proposed two-tiers dynamic resource allocation strategy.

5.5.1 Problem Formulation

Let us assume that the available modulation-modes are stored in the set $\mathcal{M}$, where mode m is a square QAM set with the constellation size of 2^{2m}. To fulfil the target BER, we also assume each active layer has to meet the same target BER and thus the relationship between the BER and the SINR $\gamma_{n,k,l}^{[m]}$ required for the lth layer of UE k in cluster $\mathcal{C}_n$

employing modulation-mode m is indicated as [140]:

$$\mathrm{BER} = \frac{2^m - 1}{m2^m} \mathrm{erfc}\left(\sqrt{\frac{3\gamma_{n,k,l}^{[m]}}{2(2^{2m}-1)}}\right). \tag{5.21}$$

Recalling (5.13), the transmit power required by layer l for the modulation-mode m of UE k is:

$$p_{n,k,l}^{[m]} = \frac{\gamma_{n,k,l}^{[m]} \beta_l \Big(\sum_{j=1}^{k-1} P_{n,j} |h_{k,n}|^2 + \sigma^2 + \boldsymbol{I}_{n,k} \Big)}{|h_{k,n}|^2}, \tag{5.22}$$

where $\beta_l = N_l/N$ is the ratio of the number of active subcarriers in the lth layer to the total number of subcarriers.

According to Eq. (5.6), the relationship between the UE's total required power and its power assigned to each active layer is not simply additive one. This is because the higher layers only have half the number of subcarriers for carrying information compared to the previous layers, where we have $\beta_l = \frac{1}{2}\beta_{l-1}$, if the same modulation-mode is applied to all layers. The power relationship of the different layers can be expressed as:

$$p_{n,k,l} = \frac{1}{2} p_{n,k,l-1} = \cdots = \frac{1}{2^{l-1}} p_{n,k,1}. \tag{5.23}$$

When we assume that different modulation-modes are assigned to the various layers, this power relationship is amended as follows:

$$p_{n,k,l}^{[m_{k,l}]} = \frac{1}{2} \cdot \frac{q_{m_{k,l}}}{q_{m_{k,l-1}}} p_{n,k,l-1}^{[m_{k,l-1}]} = \cdots = \frac{1}{2^{l-1}} \cdot \frac{q_{m_{k,l}}}{q_{m_{k,1}}} p_{n,k,1}^{[m_{k,1}]}, \tag{5.24}$$

where $q_{m_{k,l}}$ denotes the number of bits per symbol, when the modulation-mode $m_{k,l}$ is employed for UE k at the lth layer. Recall from Eq. (5.6) that the power of UE k having L layers along with various modulation-modes is given by:

$$P_{n,k} = \frac{\pi - 1}{\pi} \sum_{l=1}^{L} p_{n,k,l}^{[m_{k,l}]} + \frac{1}{\pi} \left(\sum_{l=1}^{L} \sqrt{p_{n,k,l}^{[m_{k,l}]}} \right)^2. \tag{5.25}$$

Equations (5.22) and (5.25) imply that the power required by UE k is related not only to the modulation-mode assignment and to the power allocation of each layer itself, but also affected by the residual intra-cell interference in the same cluster and the ICI arriving from other clusters. When further considering the practical constraints, the interdependence between the modulation-mode assignment and the power allocated to each layer of each UE becomes prohibitively complicated. Mathematically, the maximization problem of the achievable sum-throughput is formulated for the cluster n as:

$$\max_{\mathcal{M}_n^*, \mathcal{P}_n^*} \sum_{k=1}^{|\mathcal{K}_n|} \sum_{l=1}^{L} \sum_{m=1}^{|\mathcal{M}|} r_{k,l}^{[m]} y_{k,l}^{[m]} \tag{5.26a}$$

$$\text{s.t.} \sum_{m=1}^{|\mathcal{M}|} y_{k,l}^{[m]} = \{0,1\}, \quad y_{k,l}^{[m]} \in \{0,1\}, \ \forall k, \forall l, \forall m; \tag{5.26b}$$

$$\sum_{l=1}^{L} \sum_{m=1}^{|\mathcal{M}|} r_{k,l}^{[m]} y_{k,l}^{[m]} \geq R_{k,\min}, \quad \forall k; \tag{5.26c}$$

$$\sum_{k=1}^{|\mathcal{K}_n|} \sum_{l=1}^{L} \sum_{m=1}^{|\mathcal{M}|} r_{k,l}^{[m]} y_{k,l}^{[m]} \leq R_{\max}; \tag{5.26d}$$

$$\sum_{k=1}^{|\mathcal{K}_n|} P_{n,k} \leq P_{\max}. \tag{5.26e}$$

Notation $r_{k,l}^{[m]}$ represents the lth layer's achievable throughput for UE k using modulation-mode m. The binary indicator $y_{k,l}^{[m]}$ is employed for determining the modulation-mode assignment:

$$y_{k,l}^{[m]} = \begin{cases} 1, & \text{mode } m \text{ is assigned to the } l\text{th layer of UE } k, \\ 0, & \text{mode } m \text{ is not assigned to the } l\text{th layer of UE } k. \end{cases} \tag{5.27}$$

Note that if we arrive at $y_{k,l}^{[m]} = 0, \forall m$, the lth layer is not activated for UE k. Given $y_{k,l}^{[m]} = 0, \forall m, \forall l$, the UE k is not supported during the current time slot. The feasible modulation-mode assignment and power allocation obtained for every layer of every UE in cluster $\mathcal{C}_n$ is held in the sets $\mathcal{M}_n^*$ and $\mathcal{P}_n^*$, respectively.

To elaborate, constraint (5.26b) indicates that the UEs are able to adaptively select the layers for their transmission. For the sake of power efficiency, it is not necessary to ensure that the lth layer is utilized only if the $(l-1)$st layer is activated. Constraint (5.26c) indicates the minimum transmission rate $R_{k,\min}$ required by UE k, while (5.26d) expresses that the total affordable transmission rate should not exceed the backhaul allowance of $R_{\max}$. The transmit power constraint is presented in (5.26e), where the total power required should not exceed the maximum transmit power $P_{\max}$. It can be concluded that the problem in (5.26) is an interdependent mixed binary integer non-convex problem. It involves both binary modulation-mode-related variables $y_{k,l}^{[m]}$ and continuous power-allocation-related variables $p_{n,k,l}^{[m]}$. In general, the problem is hard to tackle by popular tools. In a nutshell, the task of our problem is to make decision on the modulation-mode assignment for each layer of each UE, bearing in mind that the no-transmission-mode is considered for each layer, so that the sum-throughput is maximized, without having each UE's rate less than its minimum rate requirement

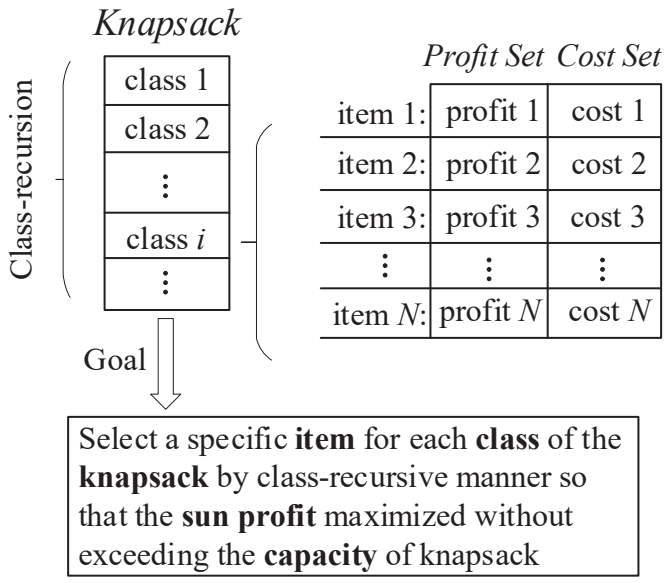

Figure 5.8: The schematic diagram of the original *multi-choice knapsack* problem.

and the total rate of UEs to exceed the maximum rate constraint, at the same time satisfying the transmit power constraint. For the sake of tractability, we transfer the original problem to a two-tiers connected maximization problem, where the 1st-tier focuses on the specific modulation-mode assignment for each layer of a given UE, while the 2nd-tier deals with the power allocation for each associated UE to a given AP. To be more specific, the 1st-tier takes into account the constraints (5.26c) and (5.26d), which aims for finding the potential rate-satisfied modulation-mode assignments for each layer of each UE, while ignoring the power constraint. Feasible solutions of the 1st-tier will then be further considered by the 2nd-tier, which aims for finding the power allocation solutions for multiple UEs in a specific clusters. To this end, the sum-throughput is maximized under the feasible modulation-mode assignment and power allocation.

5.5.2 1st-Tier Single-UE Modulation-Mode Assignment

Upon reviewing the *multi-choice knapsack* problem shown in Fig. 5.8, we find that the 1st-tier maximization problem can also be modelled by a *multi-choice knapsack* problem, which is presented in Fig. 5.9. Specifically, the adaptive modulation-mode decision is made for a given UE by considering the modulation-mode assignment of each layer of the UE, while the rate requirement of the UE can be readily satisfied. Note that as a special case of the *multi-choice knapsack* problem, both the profit and the cost estimated at the 1st-tier are restricted to the achievable rate, since at this tier we only consider the rate-related constraints, while ignoring the power-related constraints. Due to the

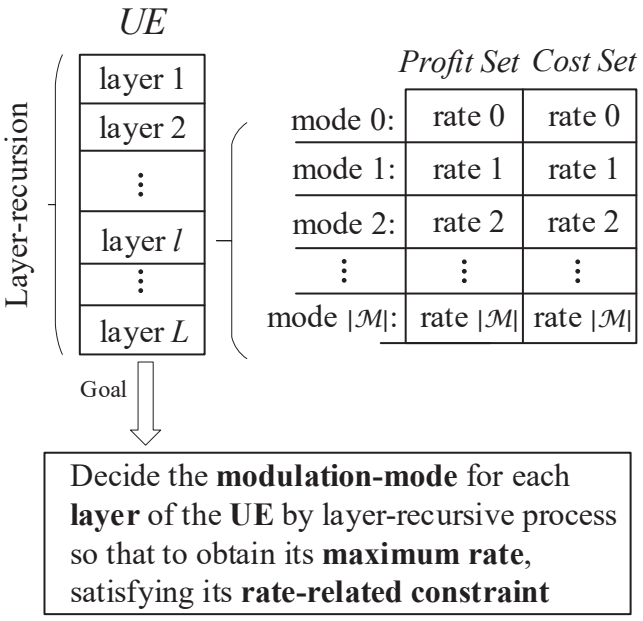

Figure 5.9: The schematic diagram of 1st-tier problem, which is based on the *multi-choice knapsack* problem. Note that, the profit and cost of mode 0 are virtual, which means that the layer will not be assigned a specific modulation-mode if mode 0 is decided for it, so that no profit contribution and no cost is associated with this layer.

NP-hard nature of the knapsack problem, we invoke dynamic programming for solving it in a layer-recursive manner, which implies that the modulation-mode decision of the lth layer is based on the modulation-mode assigned to the $(l-1)$st layer [143].

5.5.2.1 Sub-Problem Formulation

To explore the modulation-mode assignment for a single UE k, the problem of guaranteeing the transmission-quality of UE k at the 1st-tier can be mathematically formulated

as:

$$\max_{\mathcal{M}_{n,k}} \sum_{l=1}^{L} \sum_{m=1}^{|\mathcal{M}|} r_{k,l}^{[m]} y_{k,l}^{[m]} \tag{5.28a}$$

$$\text{s.t.} \quad \sum_{m=1}^{|\mathcal{M}|} y_{k,l}^{[m]} \in \{0,1\}, \; y_{k,l}^{[m]} \in \{0,1\}, \; \forall l, \forall m; \tag{5.28b}$$

$$\sum_{l=1}^{L} \sum_{m=1}^{|\mathcal{M}|} r_{k,l}^{[m]} y_{k,l}^{[m]} \geq R_{k,\min}; \tag{5.28c}$$

$$\sum_{l=1}^{L} \sum_{m=1}^{|\mathcal{M}|} r_{k,l}^{[m]} y_{k,l}^{[m]} \leq R_{\max}. \tag{5.28d}$$

Note that in contrast to Eq. (5.26e), here we apply the backhaul-rate constraint $R_{\max}$ to every individual UE for the convenience of the 1st-tier process and we will check every AP's backhaul-rate at a later stage. It can be found that the action of the 1st-tier is focused on finding the potential modulation-mode assignment for each layer of each individual UE. To elaborate, when every layer of UE k has been assigned a specific modulation-mode or the no-transmission-mode, its correspond rate can be evaluated. The maximization process at the 1st-tier entails making a decision on the specific modulation-mode assignment for each layer of UE k for the sake of achieving its maximum sum-throughput, whilst meeting the rate-related constraints of (5.28c) and (5.28d).

5.5.2.2 Methodology

According to the principle of dynamic-programming, the modulation-modes assignment are considered during each layer-specific recursion for the sake of dynamically adjusting the best modulation-mode combination of both the current layer considered and of the previous ones. To solve the problem of optimizing the 1st-tier, we commence by discretizing the maximum throughput allowance $R_{\max}$ into J levels, while the maximum rate constraint is then imposed on the J levels as follows:

$$\left\{ R_j = jR_{\max}/J : \; j = 1, \cdots, J \right\}. \tag{5.29}$$

Accordingly, the task of the lth layer-specific recursion is to obtain the maximized sum-throughput of UE k by searching for the best modulation-mode combinations commencing from layer 1 to l, under all the J rate-constraint levels. Note that during the lth layer-specific recursion, the modulation-mode assignment is divided into two parts, which are the previously considered modulation-mode assignment for layer 1 to layer $(l-1)$ and the currently considered modulation-mode assignment for layer l. This means that

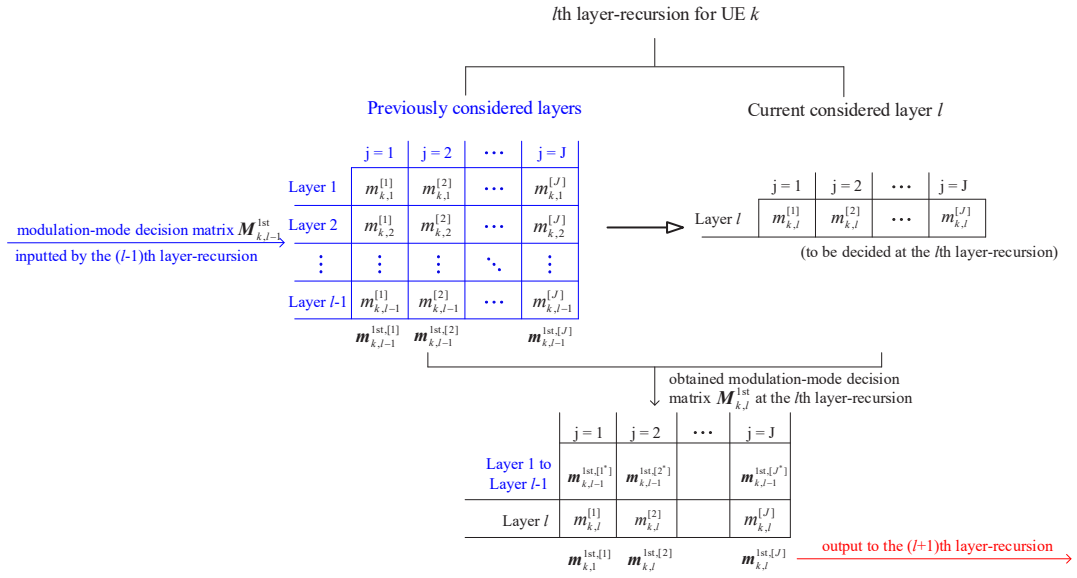

Figure 5.10: A diagram of the lth layer-specific recursion and the relationship between it and the $(l-1)$st and the $(l+1)$st layer-recursion, where $m_{k,l}^{[j]}$ denotes the modulation-mode decided for the lth layer under rate constraint R_j. Note that the modulation-mode assignment vector $\boldsymbol{m}_{k,l}^{1\text{st},[j]}$ for layer 1 to layer l is obtained for the UE k at the 1st-tier, under the rate constraint R_j, where the modulation-mode assignment decision at the lth layer-recursion is held by the matrix $\boldsymbol{M}_{k,l}^{1\text{st}}$.

the modulation-mode decision of the lth layer-recursion is based on the $(l-1)$st layer-specific recursion, as shown in Fig. 5.10. The problem of the 1st-tier is deemed to be solved when we arrive at the Lth layer-specific recursion, in a layer-by-layer manner.

Explicitly, considering a specific rate constraint R_j during the lth layer-specific recursion, the maximum achievable sum-throughput $\mathrm{T}_{k,l}(R_j)$ of UE k is obtained with the aid of the results of the $(l-1)$st layer-recursion, which is:

$$\begin{aligned} \mathrm{T}_{k,l}(R_j) &= \max_m \left\{ \mathrm{T}_{k,l-1}\left(\left\lfloor R_j - r_{k,l}^{[m]} \right\rfloor \right) + r_{k,l}^{[m]} \right\} \\ \text{s.t. } & R_j - r_{k,l}^{[m]} \geq 0, \quad \forall m \in \mathcal{M}, \end{aligned} \tag{5.30}$$

where we invoke the floor-operator $\lfloor \bullet \rfloor$ to obtain a rounded value corresponding to the nearest lower level of $\left(R_j - r_{k,l}^{[m]}\right)$, since the value of $\left(R_j - r_{k,l}^{[m]}\right)$ is not equal to any of the rate constraint levels. After considering all available modulation-modes for the lth layer, if we still cannot satisfy the condition in (5.30), we conclude that:

$$\mathrm{T}_{k,l}(R_j) = 0, \text{ if } R_j - r_{k,l}^{[m]} < 0, \ \forall m \in \mathcal{M}, \tag{5.31}$$

since no solution was found for UE k to afford a total of l layers under the constraint R_j. Therefore, the no-transmission-mode is assigned to the lth layer of UE k under the

rate constraint R_j. Otherwise, the legitimate modulation-mode of the lth layer of UE k under the rate constraint R_j is stored and denoted by $m_{k,l}^{[j]}$. Hence, the modulation-mode assignment vector $\boldsymbol{m}_{k,l}^{1\text{st},[j]}$ for UE k at the 1st-tier having a total of l layers under rate constraint R_j can be collected by combining $m_{k,l}^{[j]}$ and its counterparts in the previously considered $(l-1)$ layers, which are obtained from one of the combinations during the $(l-1)$st layer-specific recursion. We assume that the modulation-mode combinations of the previous $(l-1)$ layers have already been held in the matrix $\boldsymbol{M}_{k,l-1}^{1\text{st}} \in \mathbb{R}^{[(l-1)\times J]}$ formulated as:

$$\begin{aligned}\boldsymbol{M}_{k,l-1}^{1\text{st}} &= \left[\boldsymbol{m}_{k,l-1}^{1\text{st},[1]};\ \boldsymbol{m}_{k,l-1}^{1\text{st},[2]};\cdots;\boldsymbol{m}_{k,l-1}^{1\text{st},[J]}\right] \\ &= \begin{bmatrix} m_{k,1}^{[1]} & m_{k,1}^{[2]} & \cdots & m_{k,1}^{[J]} \\ m_{k,2}^{[1]} & m_{k,2}^{[2]} & \cdots & m_{k,2}^{[J]} \\ \vdots & \vdots & \ddots & \vdots \\ m_{k,l-1}^{[1]} & m_{k,l-1}^{[2]} & \cdots & m_{k,l-1}^{[J]} \end{bmatrix}.\end{aligned} \tag{5.32}$$

By solving (5.30), the modulation-mode decision of the lth layer $m_{k,l}^{[j]}$ associated with the decisions concerning the previous $(l-1)$ layers $\boldsymbol{m}_{k,l-1}^{1\text{st},[j^*]}$ has been obtained. Note that $\boldsymbol{m}_{k,l-1}^{1\text{st},[j^*]}$ is selected from one column of the matrix $\boldsymbol{M}_{k,l-1}^{1\text{st}}$. The two parts together meet the condition indicated in (5.30). The modulation-mode assignment $\boldsymbol{m}_{k,l}^{1\text{st},[j]}$ of all l layers under the constraint R_j is therefore expressed as:

$$\begin{aligned} & \boldsymbol{m}_{k,l}^{1\text{st},[j]} = \left[\boldsymbol{m}_{k,l-1}^{1\text{st},[j^*]},\ m_{k,l}^{[j]}\right] \\ \text{s.t.}\quad & \mathrm{T}_{k,l-1}(R_{j^*}) \geq \mathrm{T}_{k,l-1}(R_{j'}),\ \forall j', j^* \in \{1,\cdots,j\}; \\ & r_{k,l}^{m_{k,l}^{[j]}} + \mathrm{T}_{k,l-1}(R_{j^*}) \leq R_j. \end{aligned} \tag{5.33}$$

If we arrive at $\mathrm{T}_{k,l}(R_j) = 0$, the modulation-mode vector $\boldsymbol{m}_{k,l}^{1\text{st},[j]}$ is assigned an all-zero vector $\mathbf{0}_{(l\times 1)}$. The matrix $\boldsymbol{M}_{k,l}^{1\text{st}}$ can be fully constructed during the lth layer-specific recursion upon increasing the rate constraint level for approaching R_J. Note that the layer-recursion based maximization of the 1st-tier as well as of the modulation-mode assignment for UE k is summarized in Fig. 5.11.

5.5.2.3 Results Obtained at the 1st-Tier

When all L layers of UE k have been considered by obeying the aforementioned layer-by-layer operation, the candidate sum-throughput set, $\mathcal{T}_{n,k}$, for UE k as well as the corresponding modulation-mode assignment set $\mathcal{M}_{n,k}$ of the 1st-tier problem are obtained as:

$$\mathcal{T}_{n,k} = \left\{\mathrm{T}_{k,l}(R_j):\ j = 1,\cdots,J,\ l = 1,\cdots,L,\ k \in \mathcal{K}_n\right\}; \tag{5.34}$$

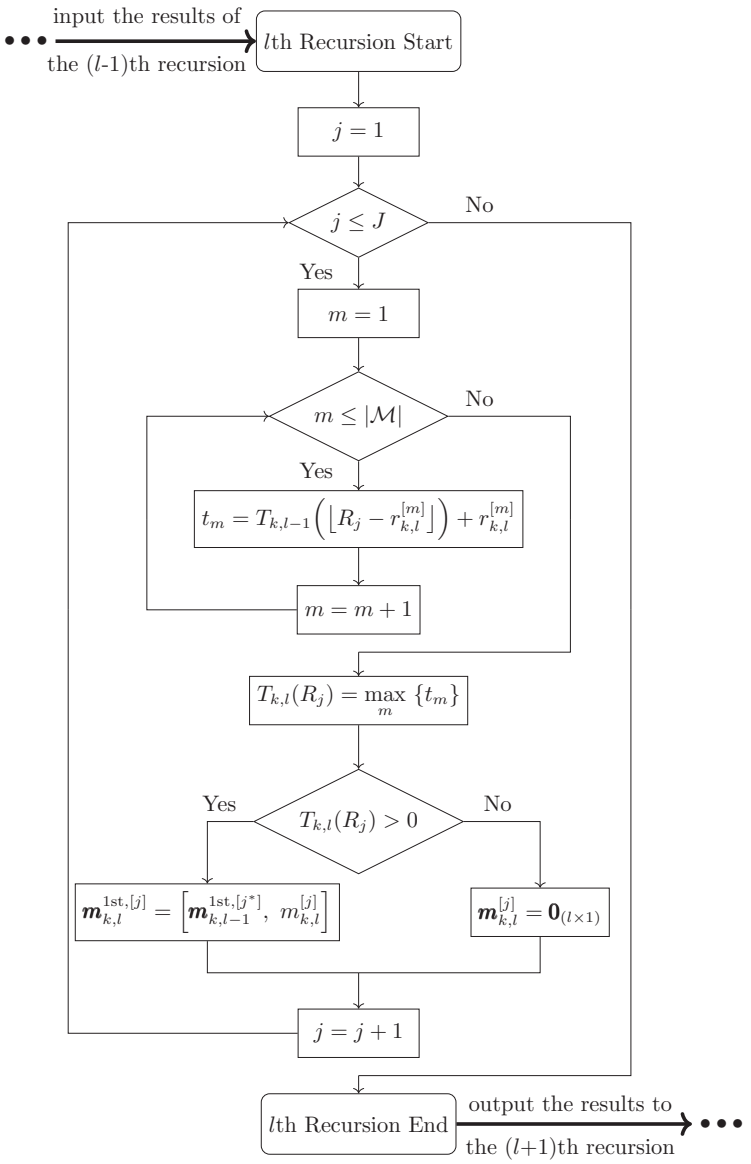

Figure 5.11: The flow diagram of the dynamic-programming-based lth layer-specific recursion.

$$\mathcal{M}_{n,k} = \left\{ \boldsymbol{M}_{k,l}^{1\text{st}} :\ l = 1, \cdots, L,\ k \in \mathcal{K}_n \right\}. \tag{5.35}$$

Due to the minimum rate $R_{k,\min}$ required by UE k as shown in (5.28c), the items in $\mathcal{T}_{n,k}$ which are lower than $R_{k,\min}$ have to be removed associated with the corresponding modulation-modes in the set $\mathcal{M}_{n,k}$. The number of remaining throughput items satisfying the rate constraint for UE k is given by Δ_k, where we have $\Delta_k \leq (J \times L)$. Therefore, the set $\mathcal{T}_{n,k}$ is reassigned to $\mathcal{T}_{n,k}^{\text{r}}$ holding the remaining throughput solutions of UE k in the 1st-tier as:

$$\mathcal{T}_{n,k}^{\text{r}} = \left\{ \text{T}_{n,k,1}^{\text{r}}, \text{T}_{n,k,2}^{\text{r}}, \cdots, \text{T}_{n,k,\Delta_k}^{\text{r}} \right\}, \tag{5.36}$$

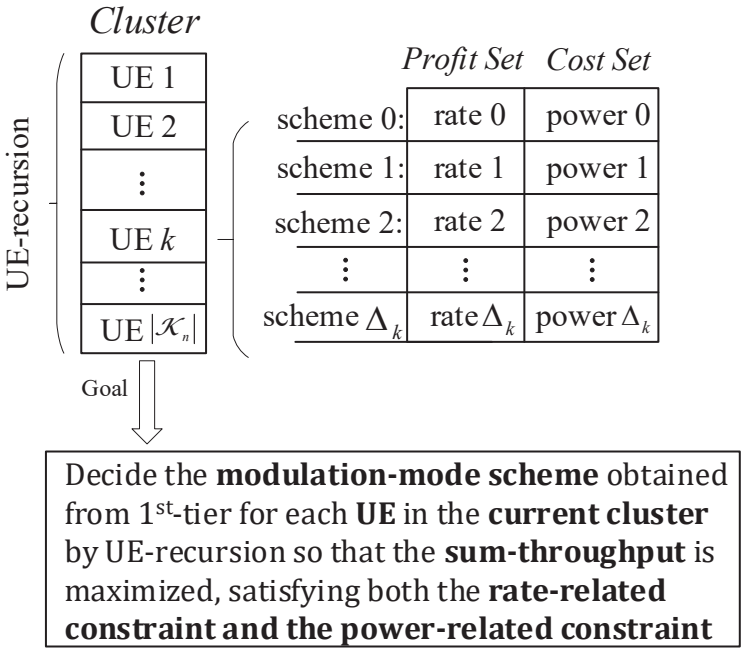

Figure 5.12: The schematic diagram of the 2nd-tier problem, which is based on the *multi-choice knapsack* problem. Note that, the profit and cost associated to scheme 0 are virtual, which means that the UE will not be supported if scheme 0 is assigned to it, so that no profit contribution and no cost is associated with this UE.

along with the updated modulation-mode scheme set as:

$$\mathcal{M}^{\mathrm{r}}_{n,k} = \left\{ \mathrm{m}^{\mathrm{r}}_{n,k,1}, \mathrm{m}^{\mathrm{r}}_{n,k,2}, \cdots, \mathrm{m}^{\mathrm{r}}_{n,k,\Delta_k} \right\}. \tag{5.37}$$

Note that the variables $\mathrm{T}^{\mathrm{r}}_{n,k,\delta}$ and $\mathrm{m}^{\mathrm{r}}_{n,k,\delta}$ represent the δth candidate throughput and modulation-mode arrangement for UE k, respectively. Hence the modulation-mode assignment for UE k has been successfully explored, under the rate constraints consideration. The 1st-tier is completed with k approaching to $|\mathcal{K}_n|$, where the obtained results $\mathcal{T}^{\mathrm{r}}_{n,k}$, $\mathcal{M}^{\mathrm{r}}_{n,k}$, $\forall k \in \mathcal{K}_n$ are delivered to the following the 2nd-tier.

5.5.3 2nd-Tier Multi-UEs Power Allocation

As indicated in Fig. 5.12, the 2nd-tier can also be modelled as a *multi-choice knapsack* problem, where a total of Δ_k schemes are obtained for UE k from the 1st-tier. By including the virtual scenario of scheme 0, some of the UEs considered may not be supported during the current time-slot, relying on the maximum sum-throughput principle. Again, the dynamic-programming based allocation strategy is invoked in a UE-specific recursion manner, where the resource allocation of the kth UE is based on the resources

allocated to the $(k-1)$st UE, working similar to the layer-specific recursion as shown in Fig. 5.11.

5.5.3.1 Sub-Problem Formulation

For simplifying our notation, we assume that in cluster $\mathcal{C}_n$, a total of $|\mathcal{K}_n| < \Lambda$ UEs are associated with AP n. In the proposed hybrid NOMA/OMA scheme, if we have $\mathcal{K}_n^{\text{Ⓢ}} \neq \mathcal{K}_n$ and $|\mathcal{K}_{n,g}^{\text{Ⓢ}}| \neq 0$, the corresponding UEs will be re-scheduled in later iterations, as indicated by **Algorithm 2**, whilst using the same maximization methodology. Therefore, both the conventional NOMA and the proposed scheme are discussed jointly in the following, where we focus our attention on the first iteration of the proposed scheme. Armed with the results of the 1st-tier, the maximization problem of the 2nd-tier for cluster $\mathcal{C}_n$ is formulated as:

$$\max_{\mathcal{K}_n^{\text{Ⓢ}},\mathcal{M}_n,\mathcal{P}_n} \sum_{k=1}^{|\mathcal{K}_n|}\sum_{\delta=1}^{\Delta_k} \mathrm{T}_{k,\delta}^{\mathrm{r}} v_{n,k}^{[\delta]} \tag{5.38a}$$

$$\text{s.t.} \quad \sum_{\delta=1}^{\Delta_k} v_{n,k}^{[\delta]} \in \{0,1\} : \; v_{n,k}^{[\delta]} \in \{0,1\}, \quad \forall \delta, \; \forall k; \tag{5.38b}$$

$$\sum_{k=1}^{|\mathcal{K}_n|} \Big(\sum_{\delta=1}^{\Delta_k} v_{n,k}^{[\delta]} \Big) P_{n,k} \leq P_{\max}; \tag{5.38c}$$

$$\sum_{k=1}^{|\mathcal{K}_n|}\sum_{\delta=1}^{\Delta_k} \mathrm{T}_{k,\delta}^{\mathrm{r}} v_{n,k}^{[\delta]} \leq R_{\max}, \tag{5.38d}$$

where the binary indicator $v_{n,k}^{[\delta]} = 1$ if UE k is supported using the δth modulation-mode combination $\mathrm{m}_{n,k,\delta}^{\mathrm{r}}$ in the set $\mathcal{M}_{n,k}^{\mathrm{r}}$, otherwise, it is zero, as defined in the following:

$$v_{n,k}^{[\delta]} = \begin{cases} 1, \text{ UE } k \text{ can be served using the } \delta\text{th modulation-mode combination in } \mathcal{M}_{n,k}^{\mathrm{r}}; \\ 0, \text{ UE } k \text{ cannot be served using the } \delta\text{th modulation-mode combination in } \mathcal{M}_{n,k}^{\mathrm{r}}. \end{cases} \tag{5.39}$$

For notational convenience, $P_{n,k}^{[\delta_k]}$ is utilized to represent $\big(\sum_{\delta=1}^{\Delta_k} v_{n,k}^{[\delta]}\big) P_{n,k}$, which quantifies the transmit power required for UE k, when the modulation-mode combination $\mathrm{m}_{n,k,\delta}^{\mathrm{r}}$ is applied. Note that if we have $\sum_{\delta=1}^{\Delta_k} v_{n,k}^{[\delta]} = 0$, none of the modulation-mode combinations is applied to UE k, hence UE k is in outage upon using the conventional NOMA transmission scheme, but it will be re-considered in the proposed hybrid NOMA/OMA scheme. As a result, the actually served UEs associated with their most appropriate modulation-mode assignment as well as the allocated power satisfying constraints (5.38c) and (5.38d) are held in the sets $\mathcal{K}_n^{\text{Ⓢ}}$, $\mathcal{M}_n$ and $\mathcal{P}_n$.

5.5.3.2 Methodology

Closer scrutiny of the objective function formulated in (5.38a) shows that our 2nd-tier maximization process is based on an individual AP, where for a specific AP n, it aims for exploring the most appropriate modulation-mode assignment for the associated UEs obtained during the 1st-tier process under the associated power constraint consideration. Similarly, the maximization problem of the 2nd-tier can also be solved by invoking dynamic-programming with aid of our UE-specific recursion. To be more specific, during the kth UE-specific recursion, all the Δ_k modulation-mode combinations of UE k are considered for determining, whether UE k can or cannot be adequately served under the relevant power constraint consideration, according to the result of the $(k-1)$st UE-specific recursion. To proceed, we discretize the maximum transmit power constraint $P_{\max}$ in (5.38c) into I levels, so that the resultant maximum transmit power allowance can be expressed as:

$$\{p_i = iP_{\max}/I : i = 1, 2. \cdots, I\}. \tag{5.40}$$

Thus, the objective of the kth UE-specific recursion is to explore the maximum sum-throughput for supporting a total of k UEs relying on our modulation-mode assignment and power allocation for each of them under all the I power constraint levels. According to Eq. (5.22) and (5.25), the required transmit power of UE k can be only determined if the power of the preceeding UEs having a higher channel gain than UE k, have already been found. Therefore, to ensure that the required sum-power of a total of k UEs does not exceed a specific power constraint p_i during the kth UE-specific recursion, the sum-throughput $\mathrm{S}_{n,k}(p_i)$ of all k UEs is attained based on the result of the $(k-1)$st UE-specific recursion as:

$$\begin{aligned} &\mathrm{S}_{n,k}(p_i) = \max_{\delta,j} \left\{ \mathrm{S}_{n,k-1}(p_j) + \mathrm{T}^{\mathrm{r}}_{n,k,\delta} \right\} \\ &\text{s.t.} \sum \boldsymbol{P}^{[j]}_{n,k-1} + P^{[\delta_k]}_{n,k} \,|^{j}_{k-1} \leq p_i, \; j \in \{1, \cdots, i\}, \; \delta \in \{1, \cdots, \Delta_k\}, \end{aligned} \tag{5.41}$$

where the vector $\boldsymbol{P}^{[j]}_{n,k-1} \in \mathbb{R}^{[(k-1)\times 1]}$ holds the power required for a total of $(k-1)$ UEs under the maximum transmit power constraint p_j, which is one of the results of the $(k-1)$st UE-specific recursion. Furthermore, $P^{[\delta_k]}_{n,k} \,|^{j}_{k-1}$ denotes the required transmit power of UE k, whose modulation-mode assignment is decided by the $\mathrm{m}^{\mathrm{r}}_{n,k,\delta}$, while the intra-cell interference imposed is $\boldsymbol{P}^{[j]}_{n,k-1}$.

Note that after attempting every possible combinations for UE k, if there is still no feasible solution for AP n to afford all the k UEs under the power constraint p_i satisfying (5.41), then we have $\mathrm{S}_{n,k}(p_i) = 0$. Otherwise, the maximized sum-throughput is acquired as $\mathrm{S}_{n,k}(p_i) = \mathrm{S}_{n,k-1}(p_{i^*}) + \mathrm{T}^{\mathrm{r}}_{n,k,\delta^{(i)}_k}$. Correspondingly, to explore the modulation-mode

assignment and power allocation, we assume that the modulation-mode assignment result of the (k-1)st UE-recursion is already stored in $\boldsymbol{M}_{n,k-1}^{\text{2nd}}$ as:

$$\boldsymbol{M}_{n,k-1}^{\text{2nd}} = \left[\boldsymbol{m}_{n,k-1}^{\text{2nd},[1]};\ \boldsymbol{m}_{n,k-1}^{\text{2nd},[2]};\cdots;\boldsymbol{m}_{n,k-1}^{\text{2nd},[I]}\right], \tag{5.42}$$

where we have

$$\boldsymbol{m}_{n,k-1}^{\text{2nd},[i]} = \left[\mathrm{m}^{\text{r}}_{n,1,\delta_1^{(i)}},\ \mathrm{m}^{\text{r}}_{n,2,\delta_2^{(i)}},\cdots \mathrm{m}^{\text{r}}_{n,k-1,\delta_{k-1}^{(i)}}\right]. \tag{5.43}$$

The candidate combinations in $\boldsymbol{M}_{n,k-1}^{\text{2nd}}$ containing the modulation-mode assignment for each layer of each of the $(k-1)$ UEs considered satisfy both the individual rate and power constraint. Accordingly, the power allocation result of the $(k-1)$st UE-specific recursion is contained by the matrix $\boldsymbol{P}_{n,k-1}$ formulated as:

$$\boldsymbol{P}_{n,k-1} = \left[\boldsymbol{P}_{n,k-1}^{[1]};\ \boldsymbol{P}_{n,k-1}^{[2]};\ \cdots;\ \boldsymbol{P}_{n,k-1}^{[I]}\right]. \tag{5.44}$$

For the kth UE-specific recursion carried out under a specific power constraint p_i, if the legitimate modulation-mode combination $\mathrm{m}^{\text{r}}_{n,k,\delta_k^{(i)}}$ is obtained by solving (5.41), the modulation-mode assignment for all k UEs under the constraint p_i is formulated as:

$$\begin{aligned} &\boldsymbol{m}_{n,k}^{\text{2nd},[i]} = \left[\boldsymbol{m}_{n,k-1}^{\text{2nd},[i^*]},\ \mathrm{m}^{\text{r}}_{n,k,\delta_k^{(i)}}\right] \\ \text{s.t.}\quad &\mathrm{S}_{n,k-1}(p_{i^*}) \geq \mathrm{S}_{n,k-1}(p_{i'}),\ \forall i^*, i' \in \{1,2,\cdots,i\}; \\ &\sum \boldsymbol{P}_{n,k-1}^{i^*} + P_{n,k}^{[\delta_k^{(i)}]}\ |_{k-1}^{i^*} \leq p_i. \end{aligned} \tag{5.45}$$

After determining $\mathrm{m}^{\text{r}}_{n,k,\delta_k^{(i)}}$ for UE k during the kth UE-specific recursion under the power limitation p_i, the required transmit power of the k UEs is collected as:

$$\boldsymbol{P}_{n,k}^{[i]} = \left[\boldsymbol{P}_{n,k-1}^{[i^*]},\ P_{n,k}^{[\delta_k^{(i)}]}\ |_{k-1}^{i^*}\right]. \tag{5.46}$$

In the same manner, the kth recursion is completed, when i approaches I.

5.5.3.3 Solutions for the Original Problem

After considering all $|\mathcal{K}_n|$ UEs in the cluster $\mathcal{C}_n$ following the aforementioned procedure, we obtain the candidate sum-throughput set $\mathcal{S}_n$ associated with the modulation-mode assignment combination set $\mathcal{M}_n$ and the power allocation strategy set $\mathcal{P}_n$ for cluster $\mathcal{C}_n$

as:

$$\mathcal{S}_n = \left\{ \mathrm{S}_{n,k}(p_i) : \quad i = 1, \cdots, I, \ k \in \mathcal{K}_n \right\}, \tag{5.47a}$$

$$\mathcal{M}_n = \left\{ \boldsymbol{M}_{n,k}^{\mathrm{2nd}} : \ k \in \mathcal{K}_n \right\}, \tag{5.47b}$$

$$\mathcal{P}_n = \left\{ \boldsymbol{P}_{n,k} : \ k \in \mathcal{K}_n \right\}. \tag{5.47c}$$

As a reminder, the specific values in $\mathcal{S}_n$ exceeding the backhaul-rate constraint $R_{\max}$ in (5.38d) have to be removed. The resultant sum-throughput values are therefore held in the set $\mathcal{S}_n^{\mathrm{r\&p}}$ as:

$$\mathcal{S}_n^{\mathrm{r\&p}} = \left\{ \mathrm{S}_{n,1}^{\mathrm{r\&p}}, \cdots, \mathrm{S}_{n,\chi_n}^{\mathrm{r\&p}} \right\}. \tag{5.48}$$

Accordingly, the items failing to satisfy the backhaul-rate are also removed from the set $\mathcal{M}_n$ and $\mathcal{P}_n$, respectively, ultimately resulting in the feasible modulation-mode assignment set $\mathcal{M}_n^*$ and the transmit power allocation set $\mathcal{P}_n^*$. Therefore, the solutions we obtained satisfy all the constraints of the original problem (5.26). Under the principle of sum-throughput maximization, the solution $\mathrm{S}_{n,\epsilon^*}^{\mathrm{r\&p}}$ is obtained from the set $\mathcal{S}_n^{\mathrm{r\&p}}$ associated with the ϵ^*th modulation-mode assignment obtained from $\mathcal{M}_n^*$ and the ϵ^*th power allocation strategy suggested by $\mathcal{P}_n^*$. It is worth mentioning that the sum-throughout $\mathcal{S}_{n,\epsilon^*}^{\mathrm{r\&p}}$ is contributed to by $|\mathcal{K}_n^{\textcircled{S}}|$ number of UEs, which may be less than $|\mathcal{K}_n|$. Those currently unsupported UEs will be re-considered according to **Algorithm 2**. Note that after completing all the maximization processes for the current cluster, the sum-throughput values obtained for each group are further combined with their associated time duration t_g, obtained based on **Algorithm 2**, to realize the achievable throughput for the cluster within T duration.

5.5.4 Complexity Analysis

The optimal resource allocation can be found by the exhaustive search, which is on the order of $\mathcal{O}\left((|\mathcal{M}|+1)^{L|\mathcal{K}|}\right)$. It is difficult to implement it in the UD-VLC due to the large $|\mathcal{K}|$. By contrast, the complexity of the modulation-mode assignment during the 1st-tier in our proposed strategy is $\mathcal{O}(JL|\mathcal{M}|)$ for each UE, and the complexity of the power allocation for a number of $K_{n,g}$ UEs in the 2nd-tier is $\mathcal{O}\left(I\sum_{k=1}^{K_{n,g}}\Delta_k\right)$. Therefore, the computational complexity of the proposed algorithm is significantly reduced to polynomial-level than that of the optimal exhaustive search.

5.6 Performance Results

In this section, we characterize our proposed *many-to-many* association strategy in comparison to a specific *one-to-many* association and demonstrate the superiority of

I-1. Environment-related Parameters	
room size	$15\times15\times3$ m^3
AP height	2.5 m
number of APs $\lvert\mathcal{N}\rvert$	8×8
LED array per AP	60×60
UE height	0.85 m
number of UEs $\lvert\mathcal{K}\rvert$	25
(changed in Fig. 5.13 - 5.18, 5.19, 5.20, 5.24 - 5.26)	
I-2. VLC Channel-related Parameters	
semi-angle at half-illumination $\phi_{1/2}$	60^o
gain of optical filter $g_{of}(\psi)$	1
gain of optical concentrator $g_{oc}(\psi)$	1
physical area for a PD receiver S	1 cm^2
reflection efficiency ρ	0.75
field-of-view Ψ_{FoV} (changed in Fig. 5.21, 5.22, 5.23)	85^o
I-3. Physical-layer-related Parameters	
target BER	10^{-5}
modulation bandwidth B	50 MHz
AWGN power spectral density N_0	10^{-22} A^2/Hz
Maximum number of layers L in LACO-OFDM	4
I-4. Network-construction-related Parameters	
channel quality threshold H_{thr}	10^{-6}
transmission distance threshold D_{thr}	5 m
ICI threshold I_{thr}	10^{-7}
FR factor τ (changed in Fig. 5.19 - 5.21)	2
I-5. Resource-allocation-related Parameters	
maximum load constraint Λ (changed in Fig. 5.27, 5.28)	2 - 5 UE/AP/time-slot
transmit power constraint $P_{\max}$	10 W/AP
individual minimum rate requirement $R_{k,\min}$	0-150 Mbits/s
backhaul constraint $R_{\max}$	1 Gbits/s
number of rate limit levels J	100
number of power limit levels I	20

Table 5.2: List of Parameters in Chapter 5

the proposed hybrid NOMA/OMA schemes in comparison to the conventional TDMA and NOMA arrangements. The modulation-mode-related sum-throughput is maximized with the aid of the proposed dynamic resource allocation strategy, where each UE can dynamically select upto four layers for LACO-OFDM. The modulation-modes available in the set $\mathcal{M}$ for each layer are BPSK, 4-QAM, 16-QAM, 64-QAM and 256-QAM. Our results are averaged over hundreds independent UE distributions. The rest of the simulation-related parameters are summarized in Table 5.2.

5.6.1 Achievable Rate Distribution

Let us first consider the achievable rate of the UEs in a single distribution. Figure 5.13 shows the modulation-mode-related rates both in the context of conventional TDMA

and of NOMA, while the achievable rate in the same UE distribution aided by our proposed hybrid schemes are provided in Fig. 5.14. Note that the left sub-figure of Fig. 5.14 is a special case of our proposed hybrid NOMA/OMA scheme, where a reuse factor of $\tau = 1$ is applied, while the right sub-figure of it has $\tau = 2$. It can be found from Fig. 5.13 that the conventional TDMA scheme has the lowest performance since most of the UEs are in outage, while the achievable rates of those served UEs are quite low. The conventional NOMA scheme provides much higher rate for its served UEs, as a benefit of its improved spectral efficiency and time efficiency. However, its performance is unsatisfactory when the UEs are close to each other. By observing the Fig. 5.14, the proposed hybrid NOMA/TDMA scheme is capable of slightly increasing the number of UEs supported. When the FR technique is adopted, the number of UEs supported is significantly increased in conjunction with a more fair rate distribution.

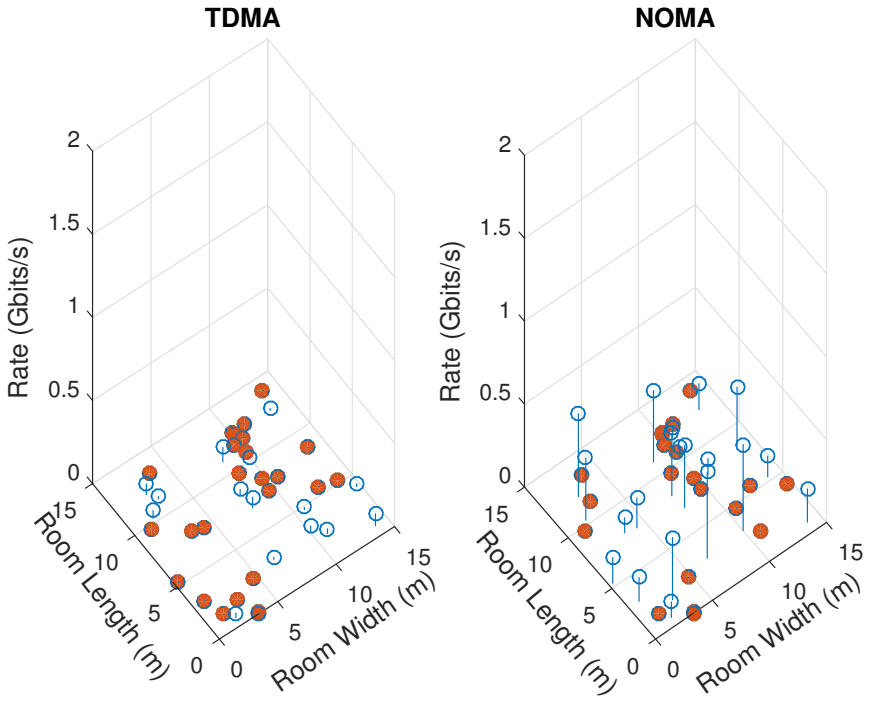

Figure 5.13: Achievable rate distribution of a total of $|\mathcal{K}| = 40$ UEs randomly located in an indoor environment supported by our UC-VLC network using TDMA (left) and NOMA (right) schemes under FoV $= 100^o$, where the UEs in outage are marked by solid circles.

To expound a little further, a more clear comparison of the four schemes is provided in Figs. 5.15 - 5.18, associated with their individual UE rate and the averaged rate. It can be found in Fig. 5.15 that the TDMA scheme fails in the face of the intense-AP-intense-UE scenario. Upon comparing the Fig. 5.16 to Fig. 5.17, we find that by invoking TDMA-based scheduling, the issue of high UE outage can be mitigated. Therefore, the averaged rate is slightly increased accordingly. Upon employing the FR

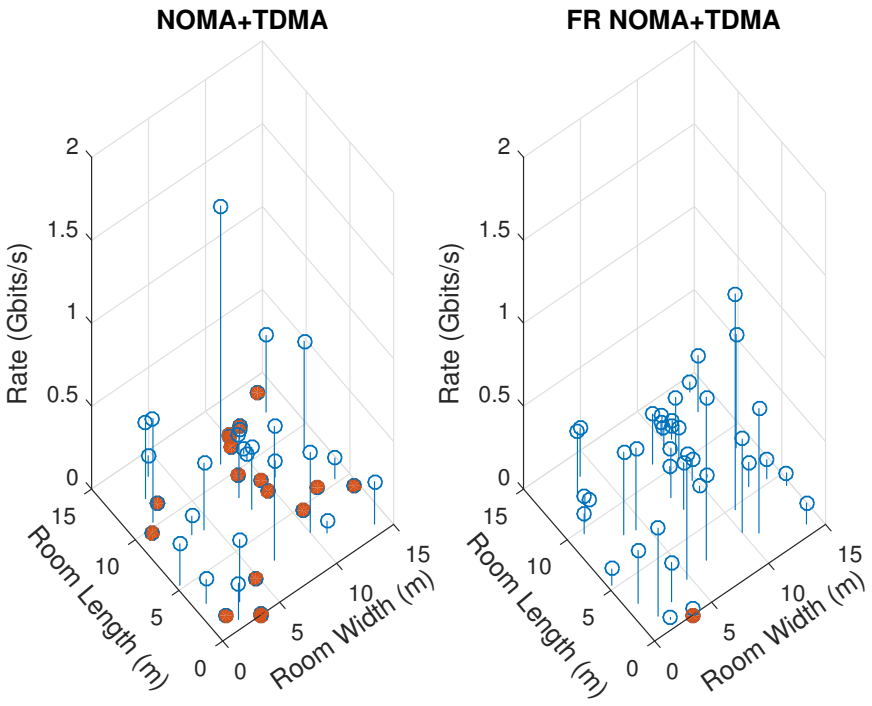

Figure 5.14: Achievable rate of the same UE distribution as in Fig. 5.13 supported by our UC-VLC network using the hybrid NOMA/TDMA scheme (left) and the FR aided hybrid NOMA/TDMA (right) schemes under FoV = 100^o, where the UEs in outage are marked by solid circles.

regime, the outage probability can be significantly reduced. As a benefit of the ICI elimination, the averaged UE rate is improved, despite the bandwidth being partitioned into two sub-bands. Next, we will investigate the performance of those four schemes averaged over hundreds of UE location distributions.

5.6.2 Effects of FR Factor

The value of the reuse factor τ has a profound impact on both the achievable throughput as well as on ICI elimination. Based on the proposed graph-coloring aided FBR allocation algorithm, we investigate the effect of various reuse factors τ on the system's performance. In this section, we compare the FR aided NOMA schemes and the FR aided hybrid NOMA/TDMA scheme, whilst using the conventional NOMA and the hybrid NOMA/TDMA benchmarkers.

To be specific, Fig. 5.19 demonstrates the achievable sum-throughput for various FR factors. By observing this figure, a high reuse factor closer to unity results in a low sum-throughput in all the two schemes, while the sum-throughput attained by the FR aided hybrid NOMA/TDMA scheme is higher than that of the FR aided NOMA scheme

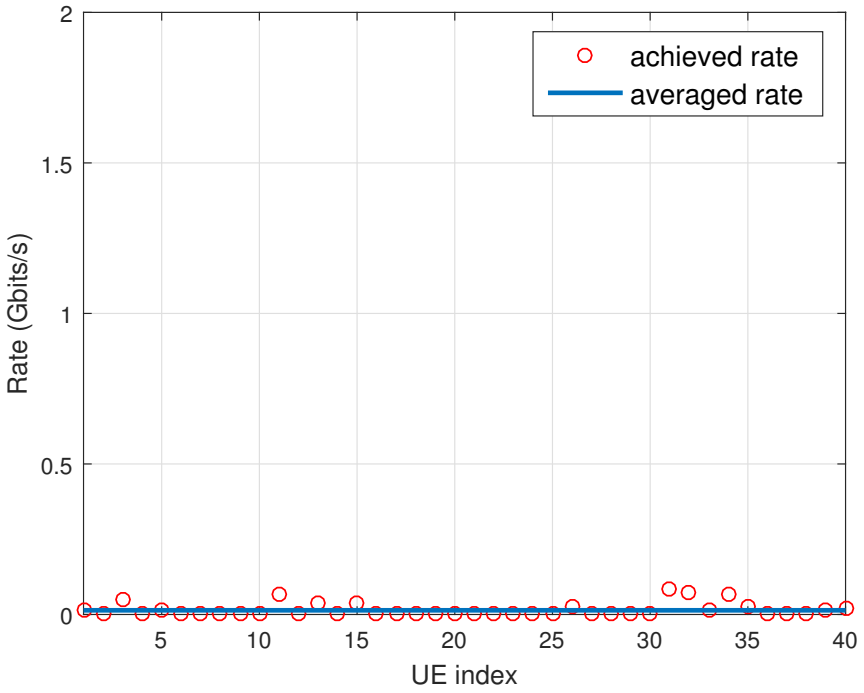

Figure 5.15: The individual UE rates and the average rate of the left subfigure of Fig. 5.13.

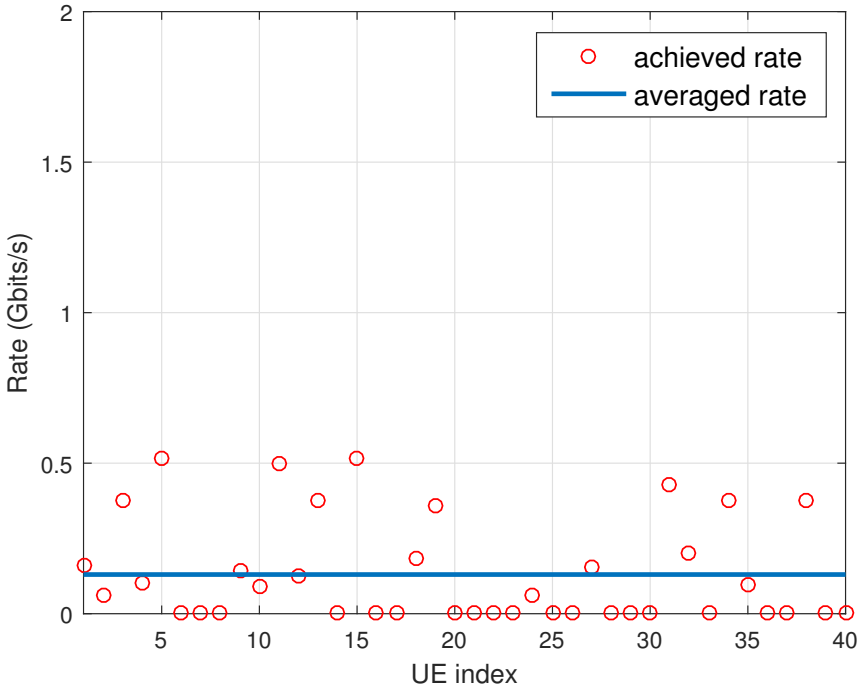

Figure 5.16: The individual UE rates and the average rate of the right subfigure of Fig. 5.13.

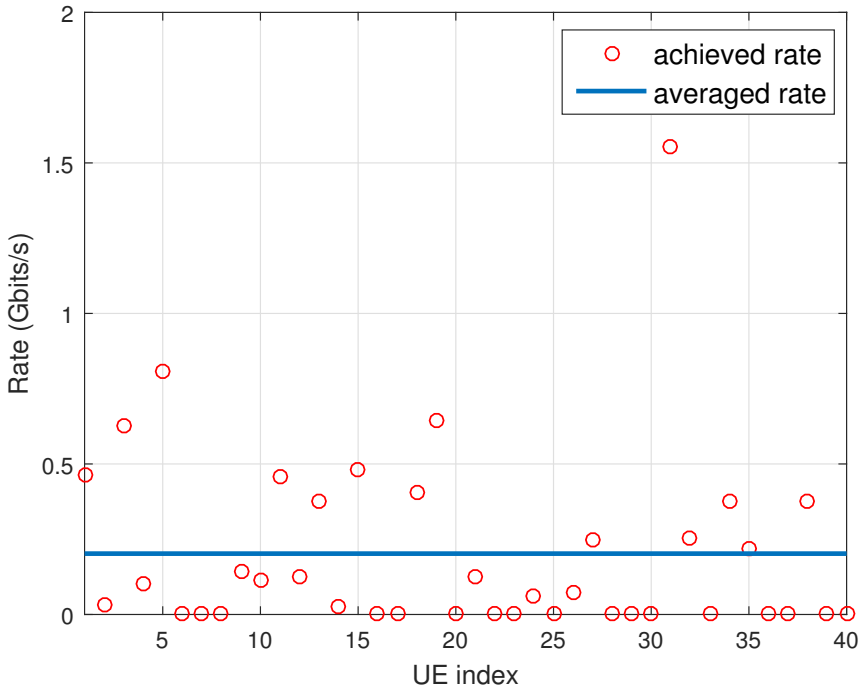

Figure 5.17: The individual UE rates and the average rate of the left subfigure of Fig. 5.14.

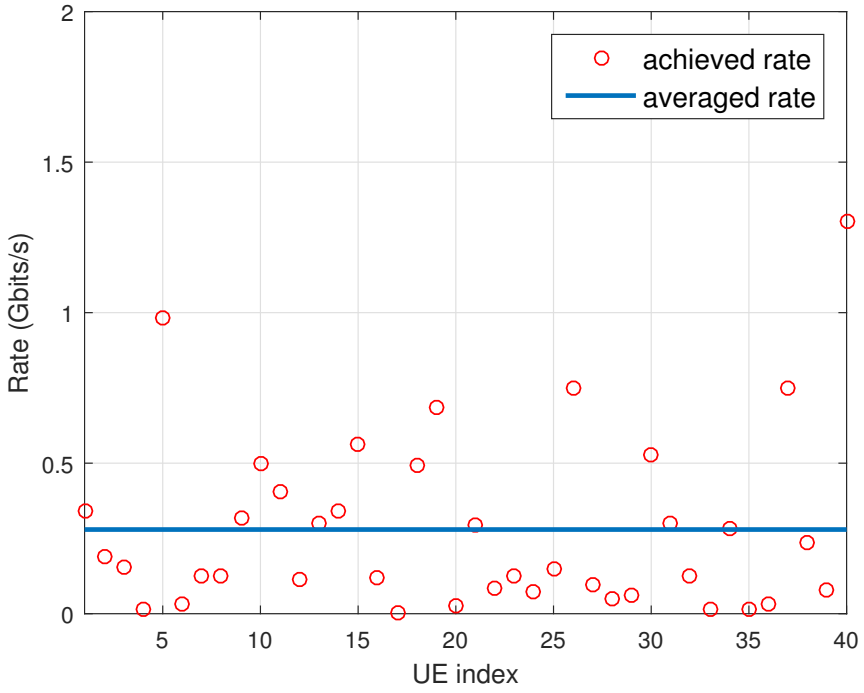

Figure 5.18: The individual UE rates and the average rate of the right subfigure of Fig. 5.14 with $\tau = 2$.

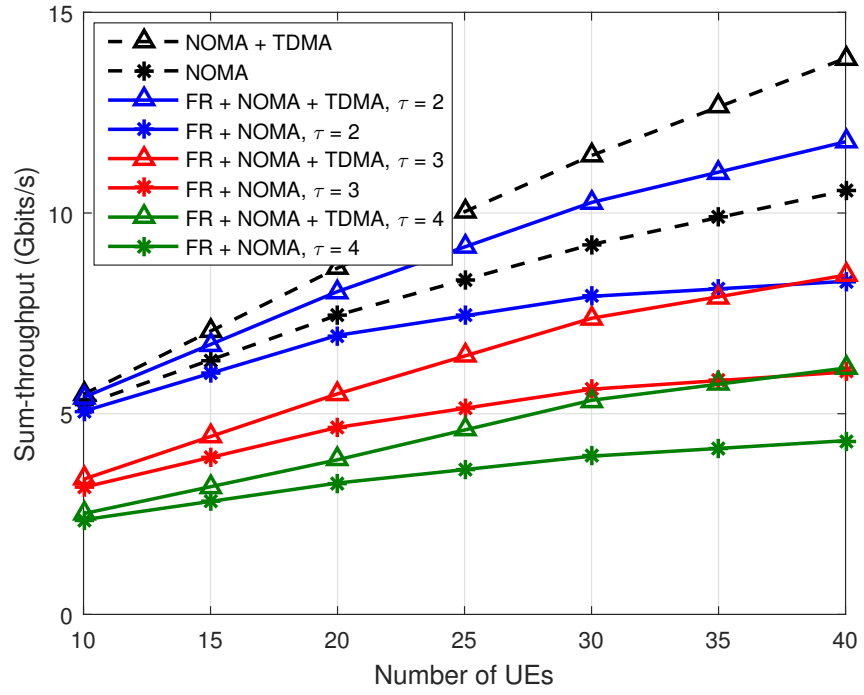

Figure 5.19: Achievable sum-throughput with various FR factor τ for the FR aided NOMA scheme and the FR aided hybrid NOMA/TDMA scheme, supporting various number of UEs.

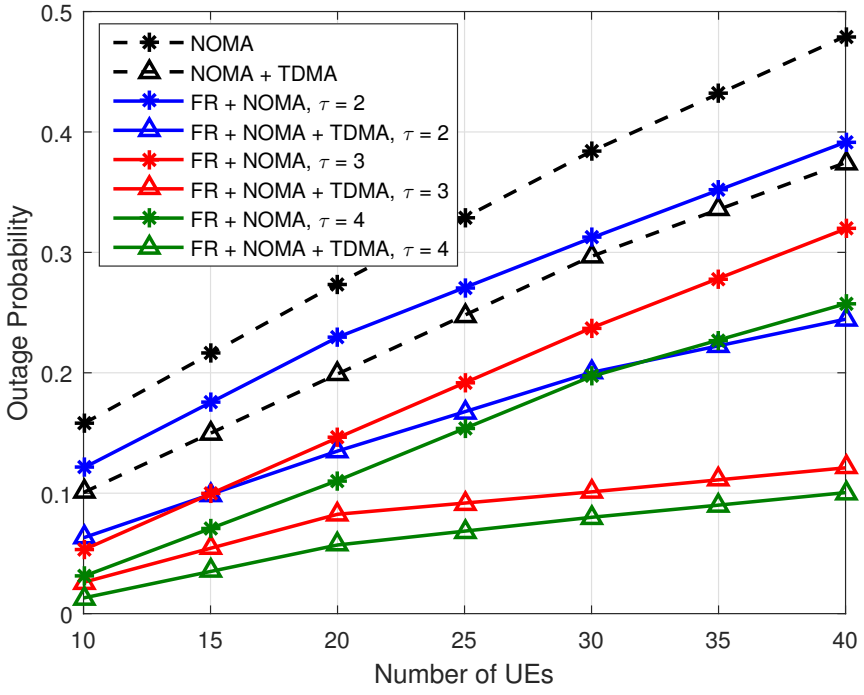

Figure 5.20: Outage probability with various FR factor τ for the FR aided NOMA scheme and the FR aided hybrid NOMA/TDMA scheme, supporting various number of UEs.

for the different FR factors. However, we found that by partitioning the bandwidth into, for example two blocks, the achievable sum-throughput is not reduced to half of the conventional NOMA or of the hybrid NOMA/TDMA scheme. This implies that by invoking the technique of FR, the ICI can be mitigated. Furthermore, we draw attention to an observation concerning the outage probability of various FR factors, as shown in Fig. 5.20. Explicitly, a high reuse factor has a low UE outage as a benefit of its reduced ICI, albeit at a reduced sum-throughput. We also found that the outage improvement is reduced upon increasing the FR factor τ. By invoking TDMA-based scheduling, the time-slot is divided into groups, but as we mentioned above, the sum-throughput attained by the hybrid NOMA/TDMA remains consistently higher than that of the NOMA. This is because the TDMA-based scheduling is capable of reducing the UE's outage probability, which facilitates a better performance for the hybrid NOMA/TDMA scheme.

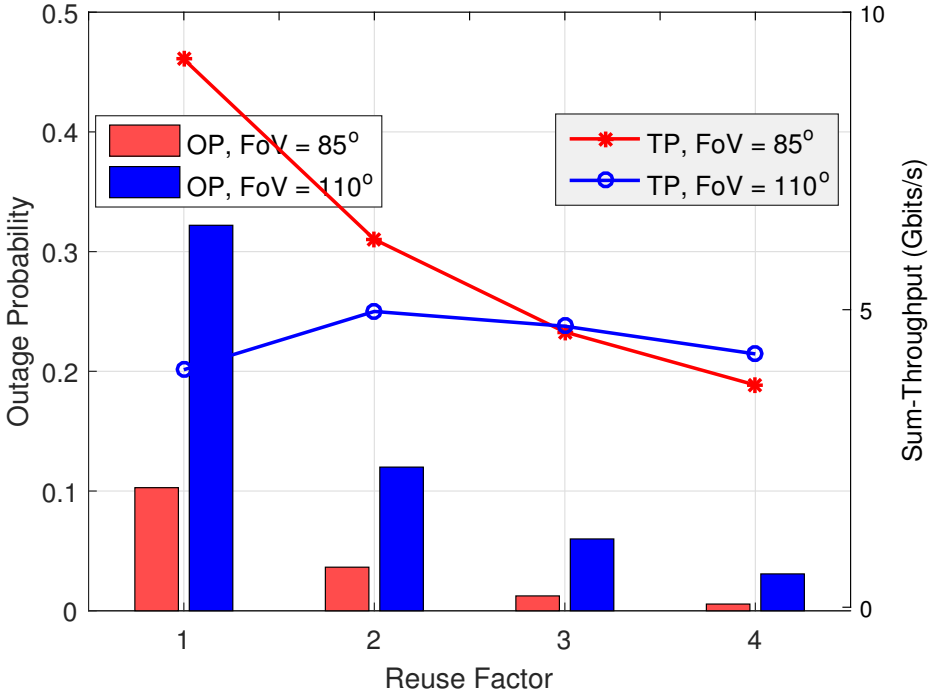

Figure 5.21: Effects of various FR factor on the sum-throughput and the outage probability based on the hybrid NOMA/TDMA scheme, compared under different FoV values.

Moreover, as shown in Fig. 5.21, we observe that for a moderate FoV value (say $\Psi_{\text{FoV}} = 85^o$), further increasing the FR factor results in a substantial sum-throughput reduction, even though the improvement of the UE outage is not so prominent. Since the ICI is not so strong, it is futile to employ a high reuse factor. By contrast, when the system suffers from serious ICI due to large FoV value (say $\Psi_{\text{FoV}} = 110^o$), moderately

increasing the FR factor strikes a trade-off between a high sum-throughput and a low outage probability.

5.6.3 Effects of FoV

Let us now investigate the effects of various FoVs on the performance of our UC-VLC network, where the FR factor of $\tau = 3$ is adopted. Observe in Fig. 5.22(a) that the sum-throughput of TDMA is continuously reduced upon increasing the FoV, hence TDMA almost completely fails in a high FoV value scenario. The sum-throughput achieved by the conventional NOMA scheme is initially slightly increased, but then sharply decays upon further increasing the value of FoV. It is interested to notify that with purely relying on the TDMA scheduling and without invoking the FR technique, the realized sum-throughput of the hybrid NOMA/TDMA scheme is very close to the one of conventional NOMA scheme, which will be explained later. Furthermore, we observe that for $\Psi_{\text{FoV}} \leq 100^o$ the sum-throughput of the FR aided hybrid NOMA/TDMA scheme associated with $\tau = 3$ is continuously improved upon increasing the value of FoV, but still remains lower than that of the hybrid NOMA/TDMA scheme due to the spectrum partitioning. However, this observation is completely reversed for the scenario of $\Psi_{\text{FoV}} \geq 110^o$, which indicates that as a benefit of the FR technique, the proposed FR aided hybrid NOMA/TDMA scheme becomes capable of mitigating the hostile ICI.

The throughput performance is also compared to the network relying on *one-to-many* association, where an AP may serve more than one UE, while the UE can only be served by a single AP. By observing Fig. 5.22, we find that the proposed UD-VLC relying on *many-to-many* association achieves a continuous throughput gain compared to the one on the *one-to-many* association, under all the simulated FoV values. Furthermore, we observe that all plots in Fig. 5.22(b) decrease, upon increasing FoV. As we analysed before, the overlapped area of several clusters of the proposed *many-to-many* association is capable of mitigating the ICI when NOMA is invoked. However, since no overlapped association in the *one-to-many* benchmark, the ICI impairs its performance, especially when FoV is large. It implies that, in UD-VLC, much higher throughput can be expected when UEs can be served by multiple APs, benefiting from the *many-to-many* association.

To expound further, Fig. 5.23 presents the outage probability for the same range of FoV values relying on the four MA schemes. By observing Fig. 5.23(a), the UE's outage probability achieved by the conventional NOMA scheme is better than that of TDMA, because as a benefit of overlapped clustering, the ICI can be mitigated in the context of using NOMA. Furthermore, as a benefit of TDMA-based scheduling, the proposed hybrid NOMA/TDMA scheme mitigates the outage probability, whilst its sum-throughput approaches that of the conventional NOMA scheme, despite its partial erosion by the time-domain partitioning. However, the outage probability achieved these

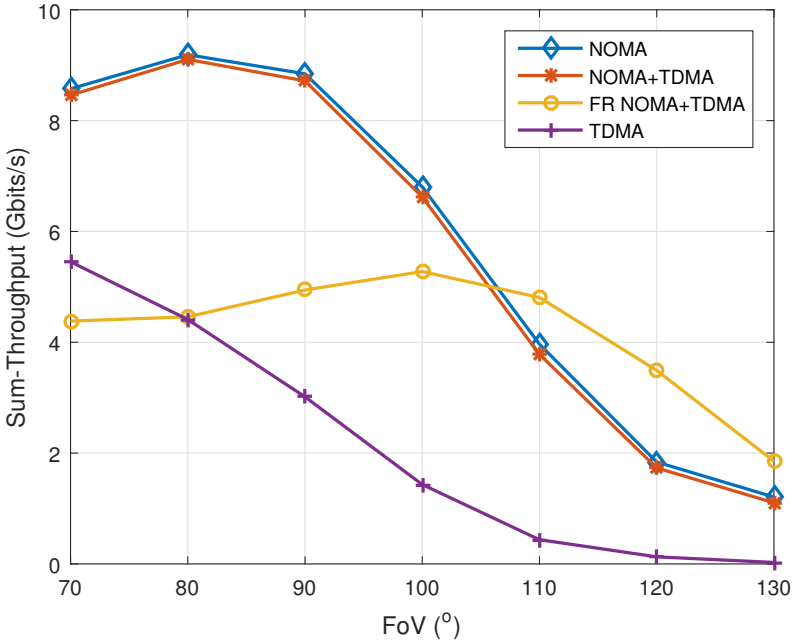

(a) *Many-to-many* association

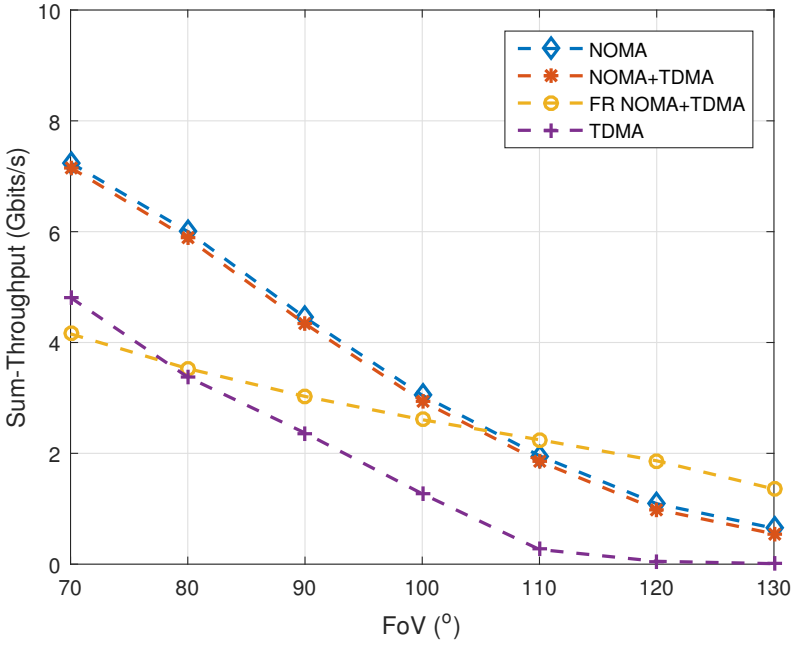

(b) *One-to-many* association

Figure 5.22: Achievable sum-throughput of different MA schemes for various FoV values using the parameters of Table 5.2.

schemes still remain unsatisfactory. Remarkably, we observe that the outage probability of the FR aided hybrid NOMA/TDMA scheme continuously remains much lower than that of the other three schemes even in large-FoV-scenarios which is an explicit benefit of

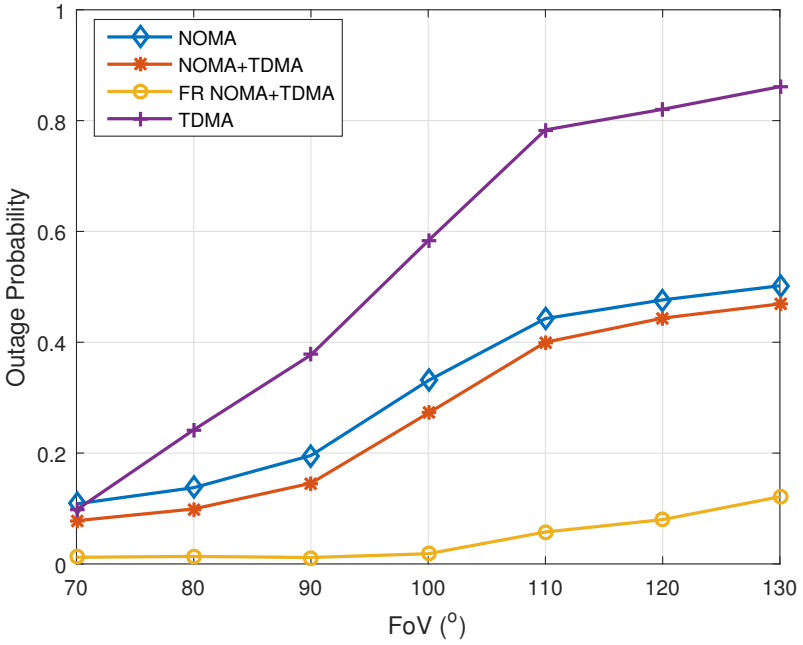

(a) *Many-to-many* association

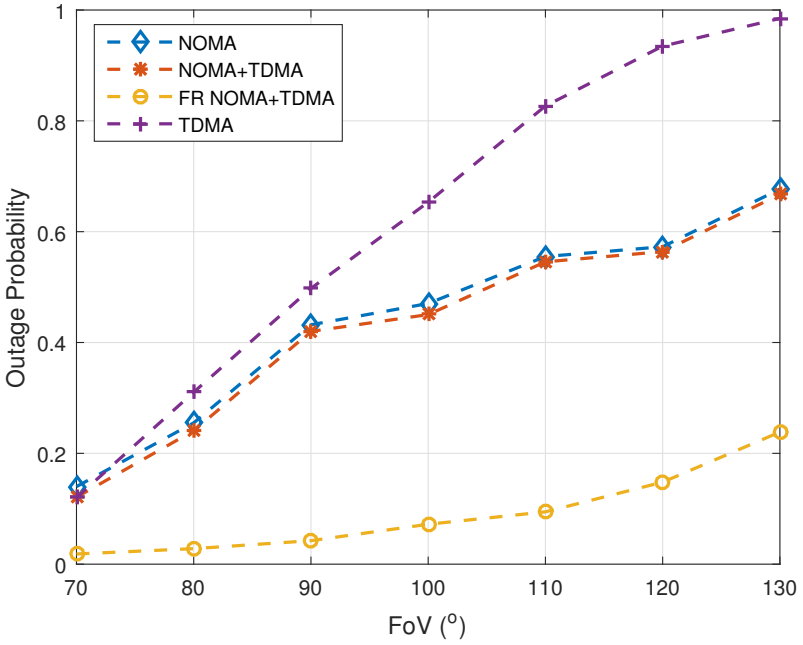

(b) *One-to-many* association

Figure 5.23: Outage probability for various FoV values.

our interference management technique. As expected, the outage probability of the *one-to-many* association is observed to be higher than that of the *many-to-many* association, as shown in Fig. 5.23(b). To explore, if the UE can not be supported by its associated AP when *one-to-many* association is adopted, it contributes the outage since all other

APs imposed ICI to it. On the contrary, since the UE may be associated to several APs according to the proposed *many-to-many* association, the outage probability can be significantly reduced.

In the light of the above simulation results, we suggest that purely relying on the conventional TDMA or NOMA schemes fails to provide a good service in the VLC networks. The proposed hybrid NOMA/TDMA achieve a great trade-off between the higher sum-throughput and acceptable outage probability in moderate-ICI environments, while by further adopting the FR technique into the hybrid scheme, it performs well in ICI-contaminated scenarios.

5.6.4 Effect of UE Density

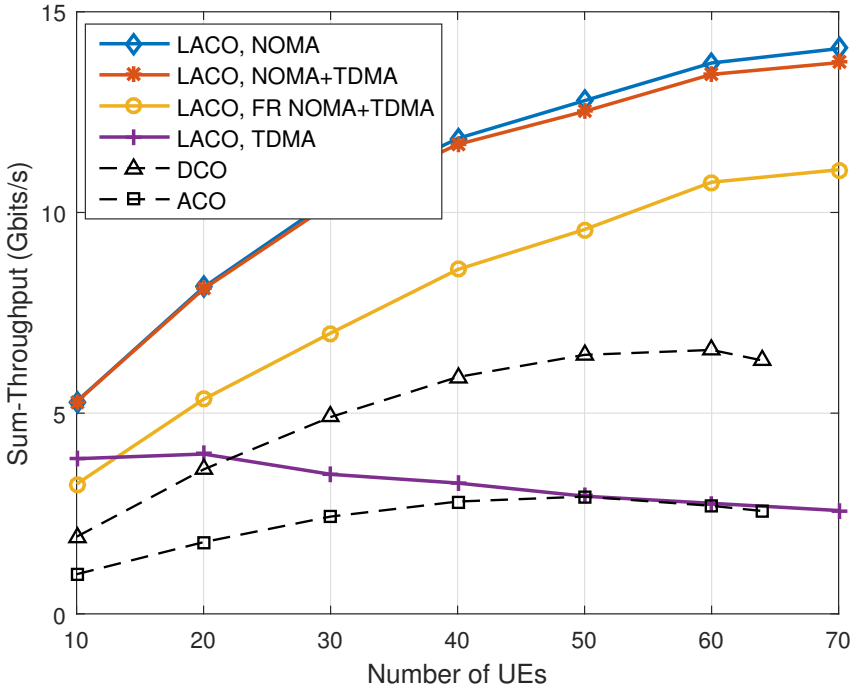

Figure 5.24: Sum-throughput vs. the number of UEs.

In this section, we observe the performance of the UC-VLC network for various UE densities at $\Psi_{FoV} = 85^o$. As seen in Fig. 5.24, upon increasing the number of UEs $|\mathcal{K}|$, both the conventional NOMA and the hybrid NOMA/OMA scheme achieve an increased sum-throughput, while TDMA-aided UC-VLC achieves a much lower throughput, which is further reduced upon increasing the UE density. We observe that the conventional NOMA scheme enjoys a higher multi-user gain than the proposed scheme, because the achievable sum-throughput of the hybrid schemes is degraded both by TDMA-based

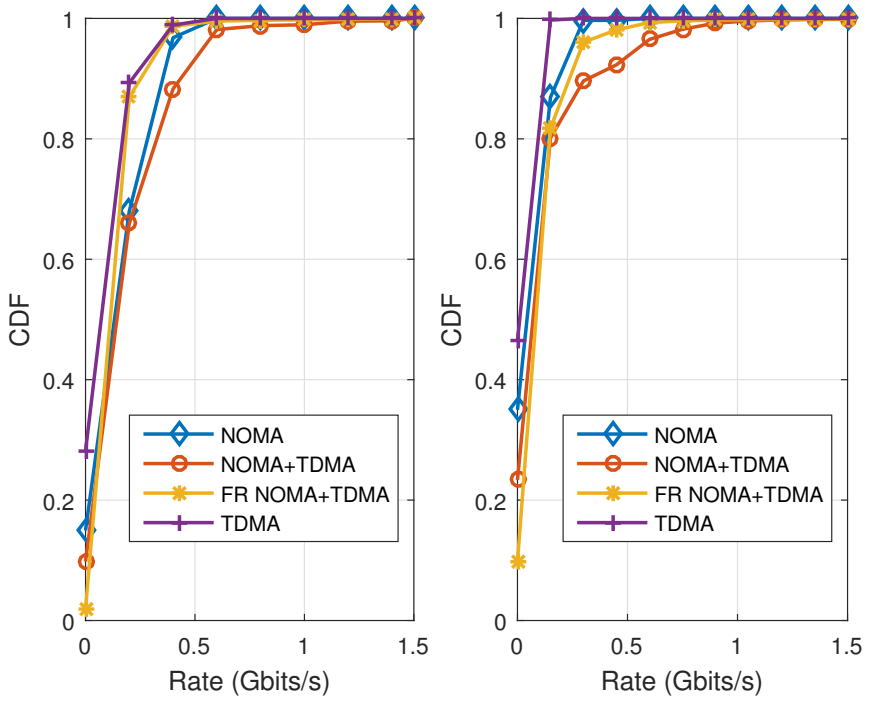

Figure 5.25: CDF of individual UE rate in both sparse and intense UE density scenarios. Left: $|\mathcal{K}| = 20$; Right: $|\mathcal{K}| = 60$.

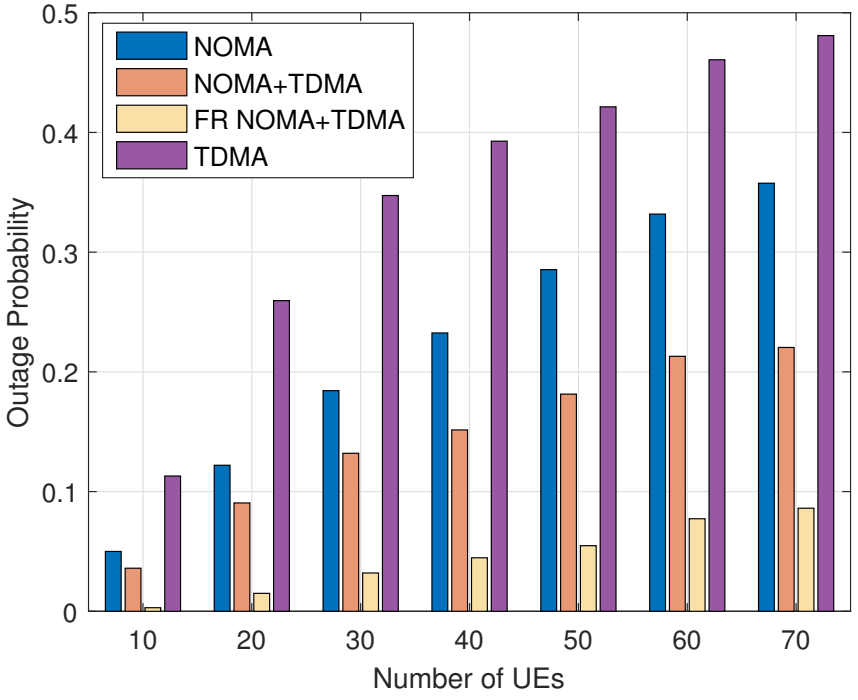

Figure 5.26: Outage probability vs. the number of UEs.

scheduling and by spectrum partitioning. However, the multi-user gain of the conventional NOMA scheme remains modest compared to both hybrid schemes. This is because due to the transmit power and backhaul-rate constraint, the number of UEs supported by the NOMA scheme remains limited. Therefore, without the TDMA-based scheduling, the achievable sum-throughput remains limited. Furthermore, by invoking NOMA in the constructed LACO-OFDM aided UC-VLC, its achieved throughput is much higher than that of the ACO/DCO-OFDM aided VLC relying on the multi-AP-multi-UE clustering we conceived in Chapter 4. Moreover, due to the employed TPC, the number of served UEs is limited to the number of APs in the ACO/DCO-OFDM aided UC-VLC network, as shown in Fig. 5.24 that the dashed lines end at $|\mathcal{K}| = |\mathcal{N}|$, which is not a problem for our proposed network.

More specifically, Fig. 5.25 characterizes the rate distribution observed for both sparse and high UE densities under the desired FoV value. This implies that the proposed hybrid NOMA/TDMA scheme encourages its target UEs to aim for higher individual rates, regardless of how dense the network is. Furthermore, the superiority of the proposed FR aided hybrid NOMA/TDMA scheme is demonstrated in densely deployed UE scenarios compared to the conventional NOMA scheme, which is however still worse than that of the hybrid NOMA/TDMA scheme.

On the other hand, the outage probability of the hybrid NOMA/TDMA and the FR aided hybrid NOMA/TDMA schemes shown in Fig. 5.26 is much better, regardless of the UE density. Note that the outage probability improvement is more remarkable, when the FR technique is invoked, albeit at the cost of a sum-throughput reduction. As a consequence, we would advice that when the UEs are quite dense, it is better to consider the proposed hybrid NOMA/TDMA scheme to pursue satisfactory achievable sum-throughput, whilst supporting more UEs during a single time duration.

5.6.5 Effects of UE-Load Restrictions

It is worth mentioning that the above simulation results were obtained under loose UE-load considerations. Since the UE-load restriction has an impact both on the complexity and stability of the transceiver design, we now take into account the effects of various UE-load restrictions imposed on both the conventional NOMA and on the proposed hybrid NOMA/OMA schemes[5]. As seen in Fig. 5.27 and Fig. 5.28, compared to the ideal unconstrained load scenario, there is a throughput loss for all three schemes under a load constraint and the outage probabilities are also deteriorated. Note that the ideal unconstrained load scenario refers to the virtual situation that the number

[5]According to the definition of the maximum load in Section 5.4.1, the limitation has impacts on the scenario when multiple UEs are supported at the same time period. Therefore, in this section, the TDMA is not considered since it serves only a single UE at a time.

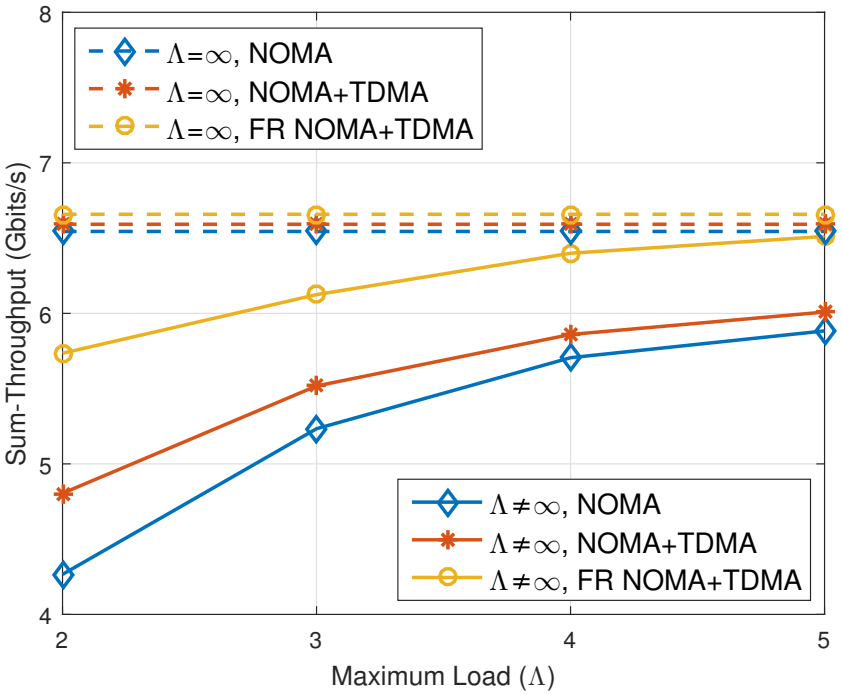

Figure 5.27: Achievable sum-throughput as a function of the maximum load Λ, investigated in three MA schemes compared to the ideal load scenario (denoted by the dashed lines).

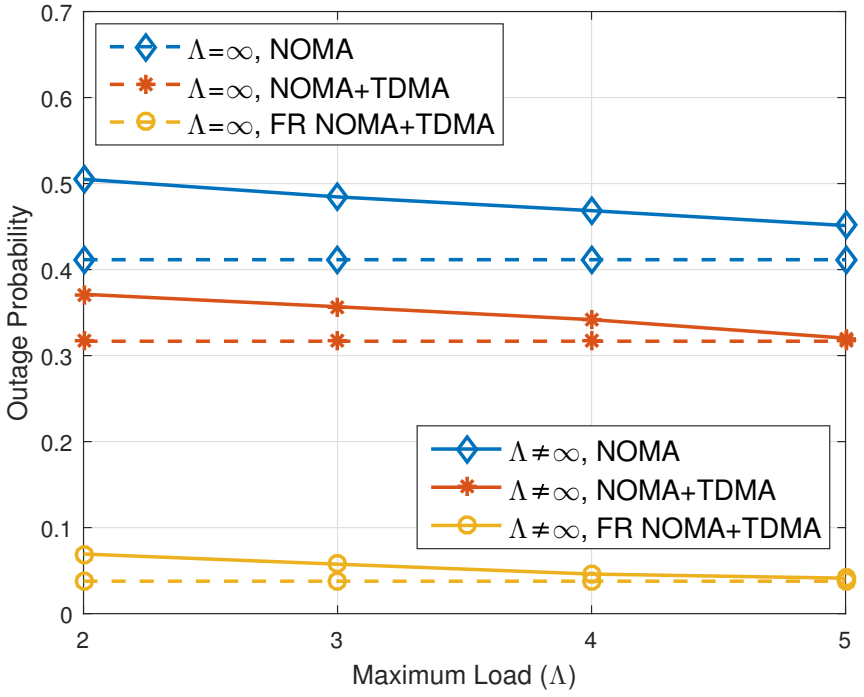

Figure 5.28: Achievable outage probability as a function of the maximum load Λ, investigated in three MA schemes compared to the ideal load scenario (denoted by the dashed lines).

of UEs served by a single AP during a single time period is not restricted, which is naturally unrealistic. This implies that the performance erosion of the conventional NOMA is imposed by the load constraint. As for the conventional NOMA scheme, if the number of target UEs of a specific AP is higher than Λ, it randomly selects only Λ UEs to serve, leaving the remaining UEs unsupported, which leads to an obvious loss in terms of both the sum-throughput and outage probability. By contrast, upon introducing the TDMA-based scheduling, Λ UEs are first randomly selected to be served, and then thanks to the re-consideration mechanism, the dropped or unsupported UEs may be served during the forth coming time-slots. Therefore, the outage probability of the hybrid schemes approaches the one in the ideal loading scenario in conjunction with an increased load restriction. Furthermore, thanks to the proficient interference management, the performance degradation of FR aided hybrid NOMA/TDMA scheme is beneficially mitigated in terms of both the sum-throughput and the outage probability. Based on this, when considering the practical load constraint of VLC networks, the proposed FR aided hybrid NOMA/TDMA scheme only has a modest throughput loss, while keeping the outage probability as low as possible.

5.7 Chapter Conclusions

An overlapped clustering algorithm has been proposed for the LACO-OFDM aided VLC system, which offered beneficial throughput gains, associated with the proposed compelling MA scheme, in seriously ICI-contaminated scenarios. With the aid of the conceived dynamic resource allocation strategy, each AP is capable of allocating different transmit power, whilst each UE dynamically explores its set of modulation-modes as well as the number of activated subcarriers thanks to the adoption of LACO-OFDM. In pursuit of a further enhanced performance, a hybrid NOMA/OMA scheme has been proposed, which outperforms the conventional TDMA and NOMA schemes in terms of both its sum-throughput and UE outage probability. Our simulation results demonstrated that the proposed scheme employing a carefully chosen FR factor performs better in hostile communication environments than the benchmarks. Furthermore, our simulation results also demonstrated that the proposed LACO-OFDM aided VLC network performs better than that of the ACO/DCO-OFDM aided VLC network in Chapter 4 and has no hard limitation on the UE capacity.

5.8 Chapter Summary

Section 5.2 reviewed the transmitter and the receiver of the LACO-OFDM, where we highlighted that due to the layer-by-layer detection at the receiver, the multi-user transmission based UC-clustering strategy proposed in Section 2.4 cannot be directly applied to the LACO-OFDM aided UC-VLC system. Therefore, in Section 5.3.1, we designed a specific *many-to-many* overlapped clustering strategy for the LACO-OFDM aided VLC system. This considered both the channel gain and the transmission distance, where the clusters were constructed according to graph theory, as shown in Figs. 5.4 - 5.6. The complexity analysis of the proposed clustering strategy was provided in Section 5.3.2, which exhibited a substantial reduction compared to the exhaustive search. To explore the MA for the LACO-OFDM aided UC-VLC system, the NOMA scheme was first analysed in Section 5.4.1. Upon considering the maximum tolerable load restriction, the NOMA scheme may not perform well in UC-VLC, especially in ICI-limited scenarios. To handle this, in Section 5.4.2, a hybrid NOMA/OMA scheme was conceived by dynamically combining the FR and the TDMA-based scheduling. To obtain the maximized sum-throughput, a two-tier dynamic resource allocation strategy was proposed in Section 5.5 for fully exploring the flexibility of LACO-OFDM at the system-level.

The attainable performance of the LACO-OFDM aided UC-VLC relying on the conventional TDMA, NOMA and the hybrid NOMA/OMA schemes was characterized in Section 5.6. It was demonstrated that our proposed hybrid scheme of Fig. 5.14 operating both with and without FR tended to outperform the conventional TDMA and NOMA schemes of Fig. 5.13. Figures 5.15 to 5.18 demonstrated that the proposed hybrid schemes achieved an increased throughput. Figures 5.19 to 5.21 investigated the influence of various FR factors on the sum-throughput and the outage probability. They indicated that the specific selection of the FR factor strongly depended on the communication environment, such as the FoV value and the UE density, striking on a trade off between the ICI elimination and the throughput erosion imposed by the associated spectrum partitioning. We also quantified the sum-throughput and the outage probability of the four schemes, namely of the conventional TDMA, NOMA, hybrid NOMA/TDMA and the FR aided hybrid NOMA/TDMA, under various FoV values, as shown in Figs. 5.22 and 5.23. It can be inferred that by introducing the FR technique, our proposed FR aided hybrid NOMA/TDMA scheme performs well in large-FoV-value scenarios to mitigate the grave ICI and its outage probability remains at the lowest level in various FoV values among the four schemes. Furthermore, the superiority of our proposed *many-to-many* association was demonstrated over the *one-to-many* association, as a benefit of our overlapped clustering structure. When the UE density is changed, the performance of the four schemes was explored in Figs. 5.24 - 5.26, where we found that the proposed hybrid NOMA/TDMA scheme struck a compelling sum-throughput

vs outage probability. Furthermore, the influence of load restriction was investigated in Figs. 5.27 and 5.28. Observe in Fig. 5.27 that the sum-throughput achieved by conventional NOMA was eroded in the face of load restrictions. As expected, due to the postponed re-consideration of UEs in the hybrid schemes, the outage probability degradation increasing caused by the load restriction is gradually reduced upon increasing the maximum UE load Λ.

Chapter 6

Power-Line-Fed VLC Network

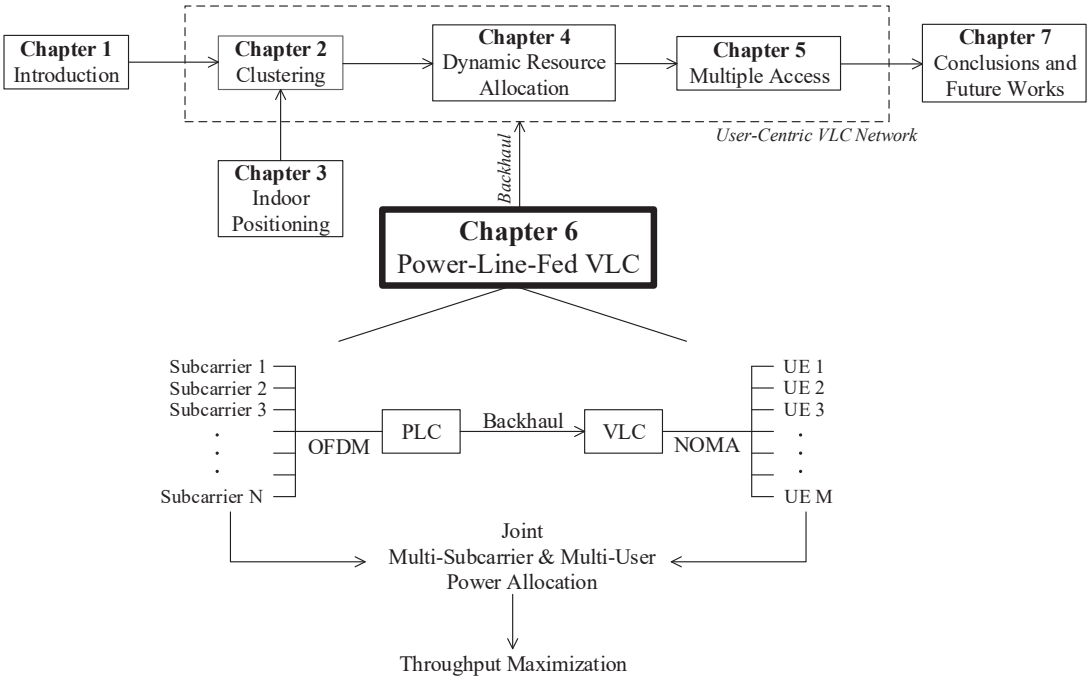

Figure 6.1: Block diagram of Chapter 6.

6.1 Introduction

Recall from previous chapters that the influence of backhaul has a significant impact on the VLC network's performance. However, in the previous chapters, we have stipulated the idealized simplifying assumption that the backhaul has a zero delay and BER, as well as infinite capacity. Naturally, in practice this is never achieved. Fortunately,

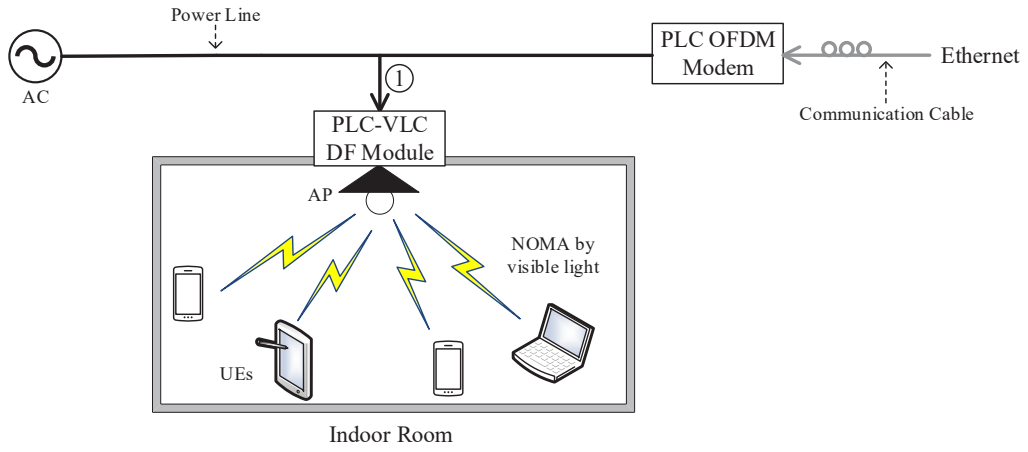

Figure 6.2: Schematic of the conceived PLC-VLC network.

since the LEDs are supplied by the mains voltage, the ubiquitous mains power line constitutes a natural backbone feed for VLC. Therefore, a power-line-fed VLC network is conceived in this chapter, where the source data is fed by PLC into the VLC network. We refer to it as a PLC-VLC network, where the power-line feds the LED-AP with data without requiring a duplicated fibre-backbone. Then the information is forwarded to multiple UEs via visible light. The main challenge of the PLC-VLC network is that the PLC constitutes a hostile medium due to the impulsive noise and multipath effects, which may become the bottleneck of the performance in PLC-VLC network. Fortunately, sophisticated OFDM-based PLC is capable of mitigating these effects in high-speed transmission [92]. Hence the PLC-VLC network conceived is expected to be an economical candidate for the smart-home network of the near future. In this chapter, the achievable throughput is maximized for the PLC-VLC network, with the aid of sophisticated resource allocation. To increase the downlink bit rate, the NOMA principle is invoked in VLC for supporting multiple UEs. For the sake of maximizing the sum-throughput of the PLC-VLC network conceived, we propose a JPA strategy, where the power is dynamically allocated in both the PLC and VLC networks, relying on the near-instantaneous communication conditions of the UEs.

The remainder of this chapter is organized as follows. The system model of the PLC-VLC network conceived is introduced in Section 6.2. In Section 6.3, the constrained optimization problem statement is presented, which is solved by the proposed JPA in Section 6.4. Our performance results are discussed in Section 6.5. Finally, the chapter is concluded in Section 6.6 and summarized in Section 6.7.

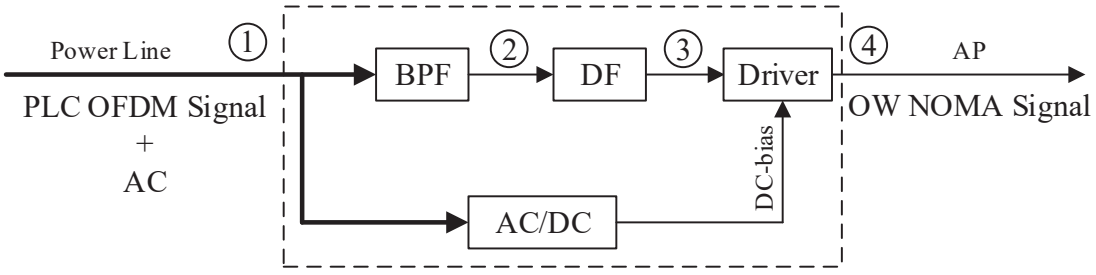

Figure 6.3: Structure of the PLC-VLC DF module, where the signal at ① consists of both the PLC OFDM signal and the AC, the signal at ② is only the PLC OFDM signal, the signal at ③ is the remodulated OW signal, and the signal at ④ is the OW signal suitable for LED transmission.

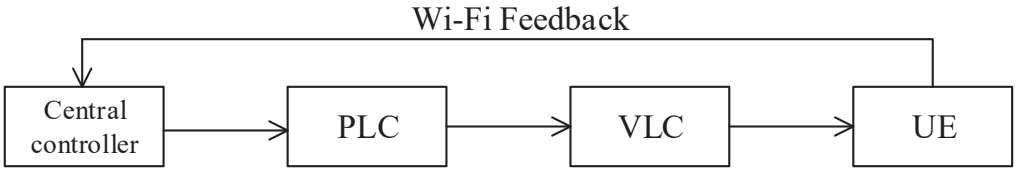

Figure 6.4: A centralized PLC-VLC network, relying on the feedback information from UE via WiFi uplink.

6.2 System Model

In an indoor scenario, we assume that an LED-AP faces downward providing access to M UEs, where the power line has already been installed behind it. Note that the power line is multiplexed for powering the AP as well as backhaul for VLC network. Explicitly, as seen in Fig. 6.2, the source data arriving from the Ethernet is fed into the power line through a PLC OFDM modem. As the output of the PLC OFDM modem, the PLC OFDM signal propagating along with the AC at 50 Hz (as shown at ①) is received by the PLC-VLC DF module. To elaborate a little further, the structure of the PLC-VLC DF module is depicted in Fig. 6.3. Since the frequency of the OFDM signal is much higher than 50 Hz, a bandpass filter (BPF) is employed in the PLC-VLC DF module to extract the PLC signal (as seen at ② of Fig. 6.3). The signal at ② is then demodulated and decoded by the DF unit, where the decoded bit stream is remodulated for the VLC optical wireless (OW) link, as shown at ③ of Fig. 6.3. Since the LED-AP is driven by DC, a DC-bias, obtained by an AC/DC converter, is added to the signal at ③, so that the OW signal suitable for LED transmission is obtained at ④ of Fig. 6.3. Note that the conceived PLC-VLC network is monitored by a central controller, which is responsible

for the power allocation relying on the feedback information received from UEs via WiFi uplink, as shown in Fig. 6.4.

6.2.1 OFDM-Based Power Line Transmission

Due to the of frequency-selective, time-varying characteristics of the power line additionally impaired by colored background and impulsive noise, the channel model requires special attention. Generally speaking, the PLC channel can be modelled by using either a bottom-up or a top-down approach. In this chapter, the transfer function $G(f)$ of the PLC channel based on the top-down approach is invoked upon relying on the parameters measured in [1], as shown in Fig. 6.5. In real power line topologies, more than one branch may be arranged. Therefore, the PLC signal propagation does not only take place along a direct LoS path. Mathematically, by combining the multipath propagation and frequency-depended attenuation, the PLC transfer function can be modelled as [1]:

$$G(f) = \sum_{i=1}^{L} w_i e^{-(a_0 + a_1 f^{\kappa}) d_i} e^{-j2\pi f (d_i / v_p)}, \tag{6.1}$$

where w_i is the weighting factor of the ith path, while a_0 and a_1 are the attenuation parameters. The constant κ is the exponent of the attenuation factor, while d_i represents the length of path i and v_p is the propagation velocity.

Since OFDM is employed in PLC for counteracting the frequency-selective channel and its grave-noise environment, the channel gain g_n at the nth subcarrier is obtained by averaging the function $g(f)$ over the surrounding N subcarriers and plotting the average at each band's central frequency, as shown in Fig. 6.5. To elaborate, the main noise source in PLC is colored background noise, with a variance of $\sigma^2_{\mathrm{p},n} = N_0^{\mathrm{p}} B$ at the nth subcarrier [144]. Note that B is the bandwidth of each subcarrier and we have the noise power spectral N_0^{p} as [144]:

$$N_0^{\mathrm{p}} = (a + b|f|^c), \tag{6.2}$$

where a, b and c are parameters depending on the location of measurement. Another impairment in PLC is the impulsive disturbance, which is non-stationary and usually occurs with a relatively low probability [104]. For simplicity, we denote the probability of the PLC channel being free from impulsive noise by ϱ [145]. Hence, the throughput of the OFDM-based PLC may be formulated as:

$$R_{\mathrm{plc}} = \varrho \sum_{n=1}^{N} B \log_2 \left(1 + \lambda_n p_{\mathrm{plc},n}\right), \tag{6.3}$$

where N is the number of subcarriers. The power allocated to the nth subcarrier is denoted by $p_{\mathrm{plc},n}$, where we have $\lambda_n = |g_n|^2 / \sigma^2_{\mathrm{p},n}$.

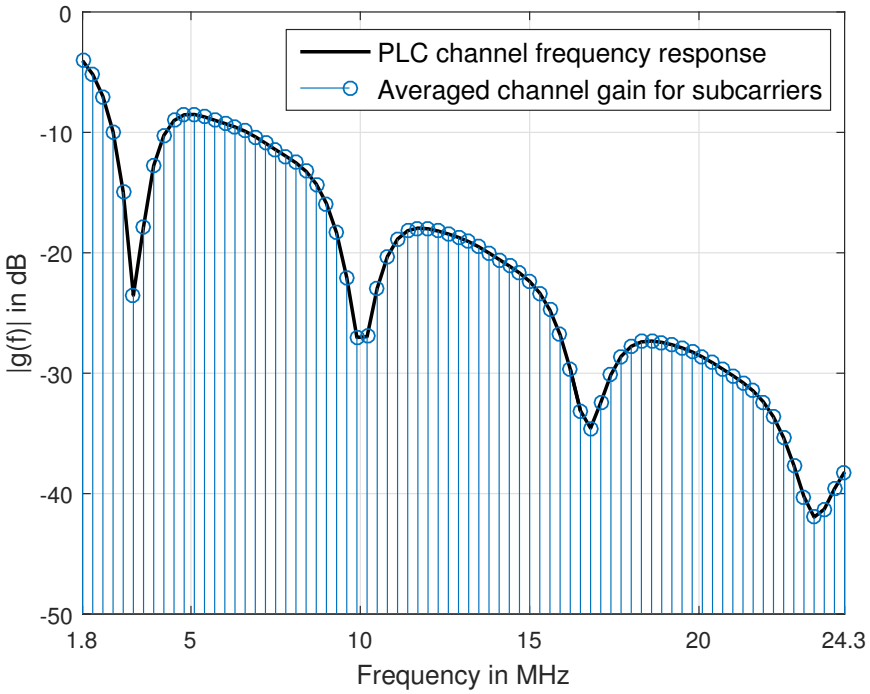

Figure 6.5: Frequency response of PLC channel modelled in [1], where the channel gain of the OFDM-subcarriers is obtained by averaging $G(f)$ at their centre frequencies.

6.2.2 NOMA Aided VLC Downlinks

Since the VLC channel can be modelled by a single-tap AWGN channel and the energy of its reflections decreases rapidly, a Lambertian model is considered for VLC-UEs. Recall from Chapter 2 that the LoS and the first reflected channel gain of UE m, denoted as $h_{\mathrm{LoS},m}$ and $h_{\mathrm{Ref},m}$, can be obtained by Eqs. (2.1) and (2.3), respectively. Hence, the aggregated VLC channel of UE m is obtained as:

$$h_m = h_{\mathrm{LoS},m} + h_{\mathrm{Ref},m}. \tag{6.4}$$

Without loss of generality, UEs are sorted in ascending order based on their channel gains, according to $|h_1|^2 \leq \cdots \leq |h_M|^2$. For supporting multi-user access, the power-domain NOMA principle is invoked, as shown in Fig. 6.6, so that all UEs are capable of sharing a given time-or-frequency-slot. To elaborate, the transmitted signal of the AP is expressed as:

$$x = \sum_{m=1}^{M} s_m \sqrt{p_{\mathrm{vlc},m}}, \tag{6.5}$$

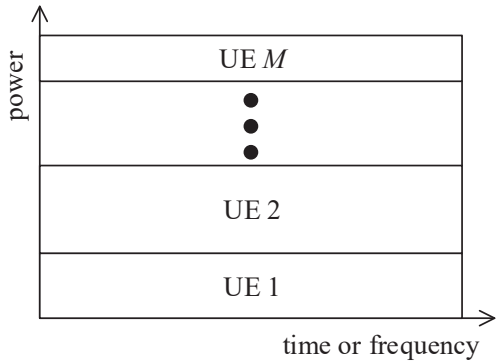

Figure 6.6: Demonstration of power-domain NOMA for multiple UEs.

while s_m is the signal intended for UE m and $p_{\mathrm{vlc},m}$ is its allocated power. According to the NOMA regime, the received VLC signal at UE m is given by:

$$y_m = h_m \sum_{l=1}^{M} s_l \sqrt{p_{\mathrm{vlc},l}} + n_m, \tag{6.6}$$

where n_m denotes the AWGN of UE m with variance σ_{v}^2. In SIC, the higher-power UE is detected first, because it is affected by the interference imposed by the lower-power UE to a lesser extent. Then its detected signal is remodulated and subtracted from the composite signal, hence decontaminating it. Therefore, the interference imposed on UE m only comes from the signal destined for UE $(m+1)$ to M. These SIC operations continue until we arrive at the signal of the lowest-power UE. Then the achievable throughput of UE m becomes:

$$R_{\mathrm{vlc},m} = B_{\mathrm{v}} \log_2 \left(1 + \frac{|h_m|^2 p_{\mathrm{vlc},m}}{|h_m|^2 \sum_{l=m+1}^{M} p_{\mathrm{vlc},m} + \sigma_{\mathrm{v}}^2} \right) \tag{6.7}$$

where B_{v} is the bandwidth of VLC. For notation expression simplification, here we define $P_{\mathrm{vlc},m} = \sum_{l=m}^{M} p_{\mathrm{vlc},m}$, so that the Eq. (6.7) can be re-written as:

$$R_{\mathrm{vlc},m} = B_{\mathrm{v}} \log_2 \left(\frac{\eta_m P_{\mathrm{vlc},m} + 1}{\eta_m P_{\mathrm{vlc},m+1} + 1} \right), \tag{6.8}$$

where we have $\eta_m = |h_m|^2/\sigma_{\mathrm{v}}^2$ for the UE m. Note that $P_{\mathrm{vlc},M+1} = 0$. It is noteworthy that $P_{\mathrm{vlc},1} = \sum_{m=1}^{M} p_{\mathrm{vlc},m}$ represents the required power for all M VLC UEs, where $P_{\mathrm{vlc},M} = p_{\mathrm{vlc},M}$ represents the required power for the Mth UE.

6.3 Constrained Problem Statement

In the conceived PLC-VLC network, our objective is to maximize the sum-throughput attained by a total of M UEs upon jointly considering the data-carrying power allocation of both the PLC and VLC component[1]. In this section, the sum-throughput maximization problem is formulated, along with its feasibility analysis.

6.3.1 Problem Formulation

Specifically, the total transmit power P_T is restricted in reality, which has to be carefully assigned to the individual OFDM-subcarriers in PLC and to the multiple VLC UEs, respectively. Furthermore, since PLC is invoked as the backhaul of VLC, the achievable sum-throughput of the PLC-VLC network is limited by the performance of PLC. To maintain fairness, the minimum rate requirement r_m of each UE has to be satisfied. Mathematically, our constrained throughput maximization problem is hence formulated as:

$$\max_{\boldsymbol{p}_{\text{plc}},\boldsymbol{p}_{\text{vlc}}} \sum_{m=1}^{M} R_{\text{vlc},m} \tag{6.9a}$$

$$\text{s.t. } P_{\text{plc}} + P_{\text{vlc},1} \leq P_T; \tag{6.9b}$$

$$\sum_{m=1}^{M} R_{\text{vlc},m} \leq R_{\text{plc}}; \tag{6.9c}$$

$$R_{\text{vlc},m} \geq r_m, \quad \forall m; \tag{6.9d}$$

$$\boldsymbol{p}_{\text{plc}} \geq \mathbf{0}_{N\times 1}; \tag{6.9e}$$

$$\boldsymbol{p}_{\text{vlc}} \geq \mathbf{0}_{M\times 1}, \tag{6.9f}$$

where we have

$$P_{\text{plc}} = \sum_{n=1}^{N} p_{\text{plc},n}, \tag{6.10}$$

$$\boldsymbol{p}_{\text{plc}} = [p_{\text{plc},1}, \cdots, p_{\text{plc},N}]^T, \ \boldsymbol{p}_{\text{vlc}} = [p_{\text{vlc},1}, \cdots, p_{\text{vlc},M}]^T. \tag{6.11}$$

Furthermore, $\mathbf{0}_{N\times 1}$ represents a N dimensional column zero vector, while $\mathbf{0}_{M\times 1}$ represents a M dimensional column zero vector. Observe the problem (6.9) that the maximum sum-throughput achieved is jointly determined by both PLC and VLC. Specifically, although the higher the throughput provided by PLC, the higher the throughput attained by VLC as shown in constraint (6.9c), but naturally, an increased power is required by PLC for increasing its throughput according to Eq. (6.3), where the total available

[1]We note that although data-carrying PLC power is only a small fraction of the illumination power, it is paramount to keep it as low as possible for avoiding the contamination of the PLC network.

power both for the PLC and for the VLC are limited, as shown in constraint (6.9b). To handle this dependent relationship between PLC and VLC, we aim for solving problem (6.9) jointly and hence propose a JPA strategy for maximizing the sum-throughput.

6.3.2 Feasibility Analysis

Before explore the JPA, the feasibility of problem (6.9) is considered in **Theorem 1**.

Theorem 6.1. *There exists at least one feasible solution of problem (6.9) if and only if the following condition is satisfied:*

$$\underbrace{\sum_{n=1}^{N}\left[2^{\left(\sum_m r_m-\varrho B\sum_n \log_2\lambda_n\right)/\varrho B_p}-\frac{1}{\lambda_n}\right]^+}_{\textit{Minimum power required by PLC}}+\underbrace{\sum_{m=1}^{M}2^{\sum_{j=1}^{m-1}r_j/B_v}\left(2^{r_m/B_v}-1\right)/\eta_m}_{\textit{Minimum power required by VLC}}\leq P_T. \tag{6.12}$$

Proof. To prove **Theorem 1**, we introduce the shorthand of

$$P=\min_{\boldsymbol{p}_{\text{plc}},\boldsymbol{p}_{\text{vlc}}} P_{\text{plc}}+P_{\text{vlc},1} \tag{6.13a}$$

$$\text{s.t. } (6.9c)-(6.9f). \tag{6.13b}$$

We say that the problem of (6.9) is feasible only if $P_T \geq P$, where P is the minimum power required by our constrained PLC-VLC network. Assume that the power $p_{\text{vlc},m}$ assigned to UE m relies on its achievable rate $R_{\text{vlc},m}$, where we have $R_{\text{vlc},m} > r_m$. Hence, the following relationship is obtained:

$$2^{R_{\text{vlc},m}/B_{\text{v}}}=1+\frac{\eta_m p_{\text{vlc},m}}{\eta_m P_{\text{vlc},m+1}+1}>2^{r_m/B_{\text{v}}}. \tag{6.14}$$

Accordingly, the power $p_{\text{vlc},m}$ allocated to user m satisfies

$$p_{\text{vlc},m}>(2^{r_m/B_{\text{v}}}-1)(\eta_m P_{\text{vlc},m+1}+1)/\eta_m. \tag{6.15}$$

This implies that the power $p_{\text{vlc},m}$ can be further reduced, so that P is decreased. Hence, the power allocated to UE m can be reduced to:

$$p'_{\text{vlc},m}=\frac{2^{r_m/B_{\text{v}}}-1}{\eta_m}(\eta_m P_{\text{vlc},m+1}+1)<p_{\text{vlc},m}, \tag{6.16}$$

when the achievable throughput is $R'_{\text{vlc},m}=r_m$. Meanwhile, for UE $l\in\{1,\cdots,m-1\}$, the reduction of $p_{\text{vlc},m}$ leads to an increased $R_{\text{vlc},l}$. Similarly, the power $p_{\text{vlc},l}$ allocated to UE l can be sequentially reduced to $p'_{\text{vlc},l}$, while still satisfying its minimum rate requirement. Hence, we infer that the constraint (6.9d) holds with equality for all UEs,

while minimizing the total power. To expound further, for the Mth UE, the minimum required power $p'_{\text{vlc},M}$ is obtained according to Eq. (6.8) as:

$$P_{\text{vlc},M} = \frac{2^{r_M/B_\text{v}} - 1}{\eta_M}. \tag{6.17}$$

Assisted by Eq. (6.17), the minimum power required by the $(M-1)$st UE is given by:

$$P_{\text{vlc},M-1} = \frac{2^{r_{M-1}/B_\text{v}} \left(2^{r_M/B_\text{v}} - 1\right)}{\eta_M} + \frac{2^{r_{M-1}/B_\text{v}} - 1}{\eta_{M-1}}. \tag{6.18}$$

Therefore, by using a recursive method, we arrive at $m = 1$, where the minimum power required for all M UEs is obtained as:

$$\begin{aligned} P_\text{v} &= \min P_{\text{vlc},1} \\ &= \sum_{m=1}^{M} \frac{2^{\sum_{j=1}^{m-1} r_j/B_\text{v}} \left(2^{r_m/B_\text{v}} - 1\right)}{\eta_m}. \end{aligned} \tag{6.19}$$

To this end, the problem in (6.13) can now be rewritten as:

$$P = \min_{\boldsymbol{p}_\text{plc}} P_\text{plc} + P_\text{v} \tag{6.20a}$$

$$\text{s.t.} \sum_m r_m \le R_\text{plc}; \tag{6.20b}$$

$$\boldsymbol{p}_\text{plc} \ge \mathbf{0}_{N\times 1}. \tag{6.20c}$$

Since P_v has been found in Eq. (6.19), we treat it as a constant of the problem (6.20). Furthermore, compared to the constraint (6.9c) of problem (6.13), the left term in constraint (6.20b) of problem (6.20) is changed to the sum of the minimum rate requirements of all the M UEs, according to the previous analysis. To solve the problem in (6.20), the associated Lagrangian function is given by:

$$\mathcal{L}(\boldsymbol{p}_\text{plc}, \xi) = \sum_n p_{\text{plc},n} - \xi \left[\varrho B \sum_n \log_2 \left(1 + p_{\text{plc},n}\lambda_n\right) - \sum_m r_m \right], \tag{6.21}$$

where ξ is the Lagrange multiplier. The associated Karush-Kuhn-Tucker (KKT) conditions are listed as follows:

$$\frac{\partial \mathcal{L}(\boldsymbol{p}_\text{plc}, \xi)}{\partial p_{\text{plc},n}} = 1 - \frac{\varrho B \xi \lambda_n}{\ln 2 \times (1 + \lambda_n p_{\text{plc},n})} = 0, \ \forall n; \tag{6.22a}$$

$$\xi \left[\varrho B \sum_n \log_2 \left(1 + p_{\text{plc},n}\lambda_n\right) - \sum_m r_m \right] = 0; \tag{6.22b}$$

$$\xi \ge 0. \tag{6.22c}$$

Upon solving Eq. (6.22a), we have:

$$p_{\mathrm{plc},n} = \frac{\varrho B \xi}{\ln 2} - \frac{1}{\lambda_n}. \tag{6.23}$$

To guarantee the positivity of $p_{\mathrm{plc},n}, \forall n$, $\xi \neq 0$ is required. Further combined with Eq. (6.22b), we may conclude that the equality holds in Eq. (6.22b), when the achievable throughput of the PLC link equals to the sum of the minimum rate requirements of all UEs, yielding:

$$\xi = \frac{\ln 2}{\varrho B} 2^{(\sum_m r_m - \varrho B \sum_n \log_2 \lambda_n)/\varrho B_{\mathrm{p}}}. \tag{6.24}$$

Therefore, the minimum power required by the PLC link is obtained as:

$$P_{\mathrm{p}} = \sum_{n=1}^{N} \left[2^{(\sum_m r_m - \varrho B \sum_n \log_2 \lambda_n)/\varrho B_{\mathrm{p}}} - \frac{1}{\lambda_n} \right]^+, \tag{6.25}$$

where we use the notation of $(x)^+ = \max\{0, x\}$.

Hence, having at least one feasible solution for (6.9) is guaranteed upon satisfying the condition in (6.12).

□

This feasibility analysis indicates that problem (6.9) is tractable when P_T meets condition (6.12), so that P_T has to be higher than the minimum power required by the PLC-VLC network under constraints (6.9b) - (6.9f).

6.4 Joint Power Allocation Algorithm

In this section, we will analyse the relationship between the PLC as well as VLC links within the feasible set and prove that the total power $P_{\mathrm{vlc},1}$ required by VLC is a function of the total power P_{plc} required by PLC. Therefore, with the aid of (6.9b), the power allocated to PLC and to VLC can be jointly decided. To elaborate, the Lagrangian

function of (6.9) is given by:

$$\begin{aligned}\mathcal{L}(\boldsymbol{p}_{\text{plc}}, \boldsymbol{p}_{\text{vlc}}, \alpha, \beta, \boldsymbol{\mu}) &= \sum_{m=1}^{M} B_{\text{v}} \log_2 \left(\frac{\eta_m P_{\text{vlc},m} + 1}{\eta_m P_{\text{vlc},m+1} + 1} \right) \\ &+ \alpha \left(P_T - P_{\text{plc}} - P_{\text{vlc},1} \right) + \beta \left[\varrho B \sum_{n=1}^{N} \log_2 \left(1 + \lambda_n p_{\text{plc},n} \right) \right. \\ &\left. - \sum_{m=1}^{M} B_{\text{v}} \log_2 \left(\frac{\eta_m P_{\text{vlc},m} + 1}{\eta_m P_{\text{vlc},m+1} + 1} \right) \right] \\ &+ \sum_{m=1}^{M} \mu_m \left[B_{\text{v}} \log_2 \left(\frac{\eta_m P_{\text{vlc},m} + 1}{\eta_m P_{\text{vlc},m+1} + 1} \right) - r_m \right],\end{aligned} \tag{6.26}$$

where α, β and $\boldsymbol{\mu} = [\mu_1, \cdots, \mu_M]^T$ are the Lagrange multipliers associated with the (6.9b) - (6.9d). The KKT conditions of (6.9) are listed as follows:

$$\frac{\partial \mathcal{L}}{\partial p_{\text{plc},n}} = -\alpha + \frac{\varrho \beta B \lambda_n}{\ln 2 (1 + \lambda_n p_{\text{plc},n})} = 0, \quad \forall n, \tag{6.27a}$$

$$\frac{\partial \mathcal{L}}{\partial p_{\text{vlc},m}} = -\alpha + \frac{B_{\text{v}}}{\ln 2} \left\{ \frac{\eta_1 (1 - \beta + \mu_1)}{\eta_1 P_{\text{vlc},1} + 1} + \sum_{l=2}^{m} \left[\frac{\eta_l (1 - \beta + \mu_l)}{\eta_l P_{\text{vlc},l} + 1} - \frac{\eta_{l-1} (1 - \beta + \mu_{l-1})}{\eta_{l-1} P_{\text{vlc},l} + 1} \right] \right\}, \ \forall m, \tag{6.27b}$$

$$\alpha \left(P_T - P_{\text{plc}} - P_{\text{vlc},1} \right) = 0, \tag{6.27c}$$

$$\beta \left(R_{\text{plc}} - \sum_{m=1}^{M} R_{\text{vlc},m} \right) = 0, \tag{6.27d}$$

$$\mu_m \left(R_{\text{vlc},m} - r_m \right) = 0, \quad \forall m, \tag{6.27e}$$

$$\alpha \geq 0, \ \beta \geq 0, \ \boldsymbol{\mu} \geq \mathbf{0}_{M \times 1}, \tag{6.27f}$$

$$(6.9b) - (6.9f). \tag{6.27g}$$

Considering $m = 1$ from (6.27b), we have

$$\alpha = \frac{B_{\text{v}} \eta_1 (1 - \beta + \mu_1)}{\ln 2 \times (\eta_1 P_{\text{vlc},1} + 1)}, \tag{6.28}$$

which can be further combined with (6.27a) to get:

$$\alpha = \frac{1 + \mu_1}{\ln 2 \times \left[\frac{\eta_1 P_{\text{vlc},1} + 1}{B_{\text{v}} \eta_1} + \frac{\lambda_n p_{\text{plc},n} + 1}{\varrho B \lambda_n} \right]}. \tag{6.29}$$

Observe that the denominator of (6.29) is always positive, regardless of the power allocation. Furthermore, because we have $\mu_1 \geq 0$ based on (6.27f), it can be inferred that $\alpha \neq 0$. Upon recalling (6.27c), we may formulate the first corollary for the problem (6.9), which is shown in **Corollary 1**.

Corollary 1: *The optimum solution of Problem (6.9) is reached when* $P_{plc}+P_{vlc,1}=P_T$.

Since (6.27a) implies that similarly to α, β is also positive, our second corollary may be readily formulated based on (6.27d), as seen in **Corollary 2**.

Corollary 2: *The optimum of Problem (6.9) is reached, when the sum-throughput* $\sum_m R_{vlc,m}$ *achieved by VLC equals to the throughput* R_{plc} *provided by PLC.*

Furthermore, by exploiting (6.27b), we arrive at:

$$\frac{\partial \mathcal{L}}{\partial p_{\mathrm{vlc},m}}-\frac{\partial \mathcal{L}}{\partial p_{\mathrm{vlc},m-1}}=\frac{B_{\mathrm{v}}}{\ln 2}\left[\frac{1-\beta+\mu_m}{P_{\mathrm{vlc},m}+1/\eta_m}-\frac{1-\beta+\mu_{m-1}}{P_{\mathrm{vlc},m}+1/\eta_{m-1}}\right]=0. \tag{6.30}$$

Upon taking into account that $|h_{m-1}|^2<|h_m|^2$,[2] we have $P_{\mathrm{vlc},m}+1/\eta_m<P_{\mathrm{vlc},m}+1/\eta_{m-1}$. It can hence be concluded that Eq. (6.30) equals to 0 if and only if $\mu_{m-1}>\mu_m$, leading to $\mu_1>\mu_2>\cdots>\mu_M\geq 0$. Upon relying on Eq. (6.27e), we may infer the third corollary formulated as:

Corollary 3: *The optimum of Problem (6.9) is reached, when* $R_{vlc,m}=r_m,\ m\in\{1,2,\cdots,M-1\}$.

Based on it, if provided that $\mu_M>0$ for the Mth UE, the throughput maximization problem of (6.9) is readily solved with the achievable sum-throughput in VLC given by $\sum_{m=1}^{M} r_m$. Accordingly, the power allocation of both VLC and PLC can be readily configured. By contrast, if we have $\mu_M=0$, according to the **Corollary 3**, the throughput attained by UE M is therefore given by:

$$R_{\mathrm{vlc},M}=R_{\mathrm{plc}}-\sum_{m=1}^{M-1} r_m, \tag{6.31}$$

yielding the power required by the Mth UE in the form of:

$$P_{\mathrm{vlc},M}=\frac{2^{\left(R_{\mathrm{plc}}-\sum_{l=1}^{M-1} r_l\right)/B_{\mathrm{v}}}}{\eta_M}-\frac{1}{\eta_M}. \tag{6.32}$$

Then, according to **Corollary 3**, for the $(M-1)st$ UE we have:

$$2^{r_{M-1}/B_{\mathrm{v}}}=\frac{\eta_{M-1}P_{\mathrm{vlc},M-1}+1}{\eta_{M-1}P_{\mathrm{vlc},M}+1}. \tag{6.33}$$

[2]Note that we will discuss the case of $|h_{m-1}|^2=|h_m|^2$ later.

By substituting the expression of $P_{\mathrm{vlc},M}$ in Eq. (6.32) into Eq. (6.33), the power $P_{\mathrm{vlc},M-1}$ can be obtained as:

$$P_{\mathrm{vlc},M-1} = \frac{2^{\left(R_{\mathrm{plc}} - \sum_{l=1}^{M-2} r_l\right)/B_{\mathrm{v}}}}{\eta_M} - \frac{(\eta_{M-1} - \eta_M) \times 2^{r_{M-1}/B_{\mathrm{v}}}}{\eta_{M-1}\eta_M} - \frac{1}{\eta_{M-1}}. \tag{6.34}$$

By recursively reducing UE-index, the general expression of $P_{\mathrm{vlc},m}$ may be formulated as:

$$P_{\mathrm{vlc},m} = \frac{2^{\left(R_{\mathrm{plc}} - \sum_{l=1}^{m-1} r_l\right)/B_{\mathrm{v}}}}{\eta_M} - \sum_{i=m}^{M-1} \frac{(\eta_i - \eta_{i+1}) \times 2^{\sum_{l=m}^{i} r_l/B_{\mathrm{v}}}}{\eta_i\eta_{i+1}} - \frac{1}{\eta_m}. \tag{6.35}$$

Hence the total power required by the VLC UEs is given by:

$$P_{\mathrm{vlc},1} = \frac{2^{R_{\mathrm{plc}}/B_{\mathrm{v}}}}{\eta_M} - \sum_{i=1}^{M-1} \frac{(\eta_i - \eta_{i+1}) \times 2^{\sum_{l=1}^{i} r_l/B_{\mathrm{v}}}}{\eta_i\eta_{i+1}} - \frac{1}{\eta_1}. \tag{6.36}$$

Recall from **Corollary 1** that the power allocated to VLC and PLC is P_T, hence yielding a function formulated as:

$$\Psi = P_{\mathrm{plc}} + P_{\mathrm{vlc},1} - P_T, \tag{6.37}$$

which denotes the power relationship between the PLC and VLC network. To elaborate a litter further, for a given PLC power, the maximum rate is attained, when the power allocation relies on the classic water-filling strategy. Therefore, the achievable throughput of PLC is given by:

$$R_{\mathrm{plc}} = \varrho B \sum_n \log_2 \left[\lambda_n \left(P_{\mathrm{plc}} + \sum_n 1/\lambda_n\right)/N\right], \tag{6.38}$$

where the power allocated to the nth subcarrier is:

$$p_{\mathrm{plc},n} = \left(\frac{1}{N}(P_{\mathrm{plc}} + \sum_m \frac{1}{\lambda_n}) - \frac{1}{\lambda_n}\right)^+. \tag{6.39}$$

Upon substituting R_{plc} of Eq. (6.38) into Eq. (6.36), we find that the function Ψ only has a single variable, which is P_{plc}. Hence the classic bisection method may be invoked for finding P^*_{plc} with respect to $\Psi = 0$. Furthermore, the power values of $P^*_{\mathrm{vlc},m}$, $\forall m$ can be jointly obtained based on (6.35). Accordingly, the power allocated to each VLC UE is given by:

$$p^*_{\mathrm{vlc},m} = \begin{cases} P^*_{\mathrm{vlc},m} - P^*_{\mathrm{vlc},m+1}, & \text{if } m = 1, \cdots, M-1 \\ P^*_{\mathrm{vlc},m}, & \text{if } m = M. \end{cases} \tag{6.40}$$

To this end, the throughput maximization problem of (6.9) is solved by our JPA strategy.

I-1. Environment-related Parameters	
room size	4×4×3 m^3
AP height	2.5 m
UE height	0.85 m
number of UE M (changed in Fig. 6.16, 6.17)	10
I-2. VLC-related Parameters	
semi-angle at half-illumination $\phi_{1/2}$	60^o
FoV Ψ_{FoV}	120^o
gain of optical filter $g_{of}(\psi)$	1
gain of optical concentrator $g_{oc}(\psi)$	1
physical area for a PD receiver S	1 cm^2
reflection efficiency ρ	0.75
bandwidth B_{v}	20 MHz
I-3. PLC-related Parameters	
number of subcarrier N	1024
bandwidth per subcarrier B	24.41 KHz
frequency range (changed in Fig. 6.10)	1.8 MHz - 24.3 MHz
noise-power-related parameter a	-140
noise-power-related parameter b	38.75
noise-power-related parameter c	-0.72
impulsive-noise-free probability ϱ	0.98
I-4. PA-related Parameters	
transmit power constraint P_T (changed in Fig. 6.11, 6.12, 6.13)	1 W
minimum rate requirement r_m (changed in Fig. 6.10, 6.14, 6.15)	20 Mbits/s
SPA factor α	0.3

Table 6.1: List of Parameters in Chapter 6

Let us now consider the special case that when there are two UEs having the same channel gain, i.e., $|h_m|^2 = |h_{m+1}|^2$. To handle this problem, a virtual UE m' is invoked, where we have $r_{m'} = r_m + r_{m+1}$. Then, the optimal power is allocated to UE $1, \cdots, m-1, m', m+1, \cdots, M$ following the above discussion and hence the power of $p^*_{\text{vlc},m'}$ is obtained. The power allocated to the mth and the $(m+1)$st UE has to ensure that $p^*_{\text{vlc},m} + p^*_{\text{vlc},m+1} = p^*_{\text{vlc},m'}$, while guaranteeing that $R^*_{\text{vlc},m} \geq r_m$ and $R^*_{\text{vlc},m+1} \geq r_{m+1}$. If we have $m+1 < M$, according to our power allocation strategy, we obtain $R^*_{\text{vlc},m'} = r_{m'}$ so that we have $R^*_{\text{vlc},m} = r_m$ and $R^*_{\text{vlc},m+1} = r_{m+1}$, respectively. Accordingly, their optimal power can be acquired according to (6.35) and (6.40). If we have $m+1 = M$, we arrive at $R^*_{\text{vlc},m'} \geq r_{m'}$ for our power allocation strategy. To determine the optimal power for both the UEs, the rates are set to $R^*_{\text{vlc},m} = r_m$ and $R^*_{\text{vlc},m+1} = r_{m'} - R^*_{\text{vlc},m}$.

6.5 Performance Results

In this section, simulations are conducted to investigate the performance of the proposed JPA designed for our PLC-VLC network, where a $4 \times 4 \times 3$ m^3 indoor room is considered. The associated parameters are summarized in Table 6.1.

6.5.1 Influence of PLC Channel

As we mentioned before, the PLC is expected to be the bottleneck of the PLC-VLC network. Therefore, in this section, we explore the influence of the PLC channel on the PLC-VLC network's performance, where three typical reference channels (RCs) are considered[3]. To be specific, the RC1 has the frequency response shown in Fig. 6.7 based on four paths, which is commonly used in PLC research [1].

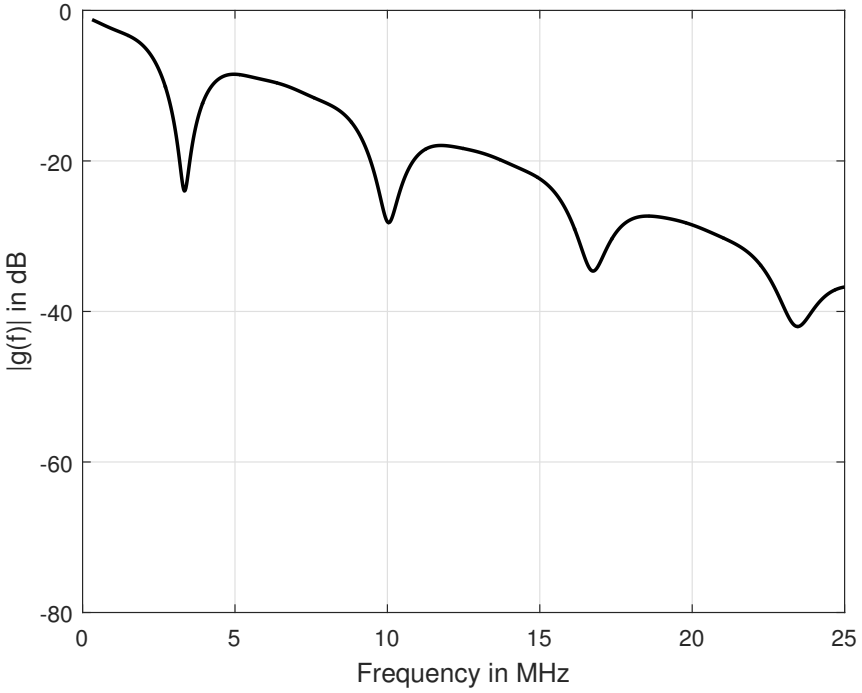

Figure 6.7: Frequency response of the RC1 PLC channel.

As shown in Fig. 6.8, RC2 represents a good PLC channel with only few reflection points and no obvious frequency domain troughs are observed. Furthermore, RC3 represents an extremely narrow-band PLC channel, as seen in Fig 6.9.

To explore the influence of PLC channel on our PLC-VLC network's performance, the power allocated to both the PLC and VLC links as well as the achievable sum-throughput are presented in Fig. 6.10. Again, the frequency response of RC3 is essentially limited to 10 MHz. Therefore, to have a fair comparison, the frequency range of all three PLC channels was restricted to span from 0.3 MHz to 10 MHz. As expected, under our transmit power constraint, the better the PLC channel we have, the lower the power allocated to the PLC link becomes. This increases the sum-throughput of the PLC-VLC network. Furthermore, it can also be seen in Fig. 6.10 that although RC1 exhibits frequency-selective fading, the power allocated to PLC link is only slightly reduced

[3]The complete parameters of these three RCs are provided in Appendix.

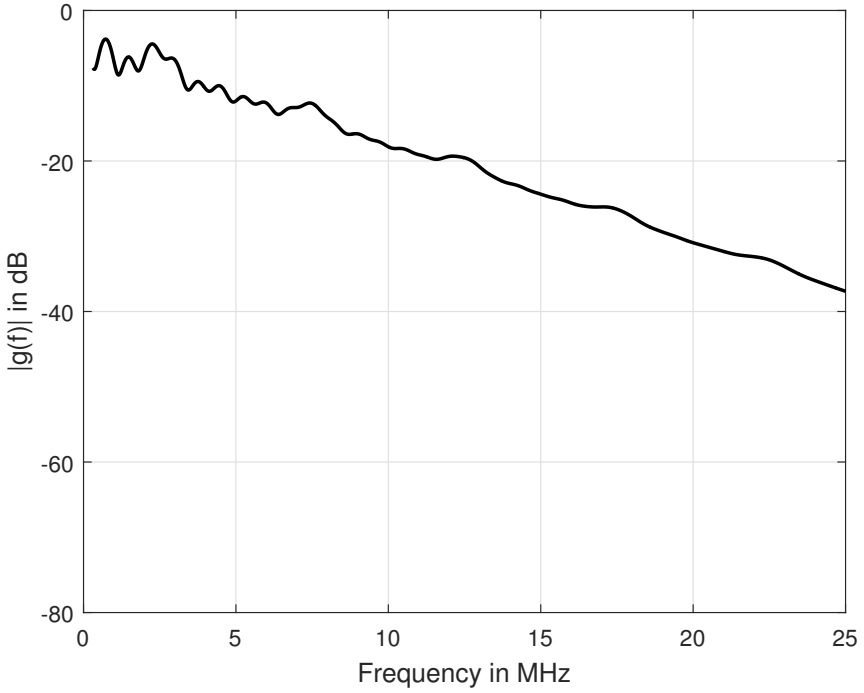

Figure 6.8: Frequency response of the RC2 PLC channel.

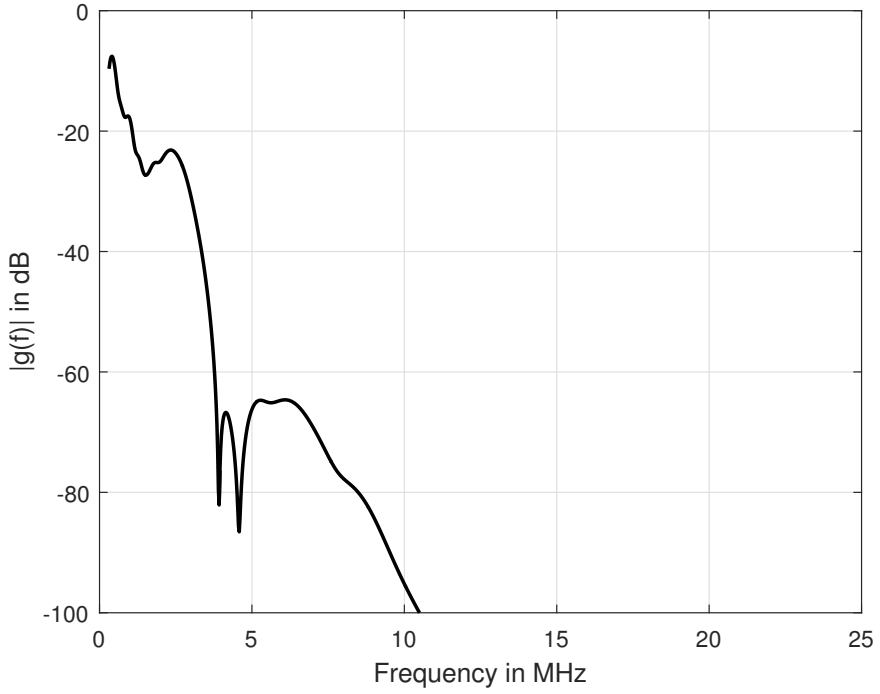

Figure 6.9: Frequency response of the RC3 PLC channel.

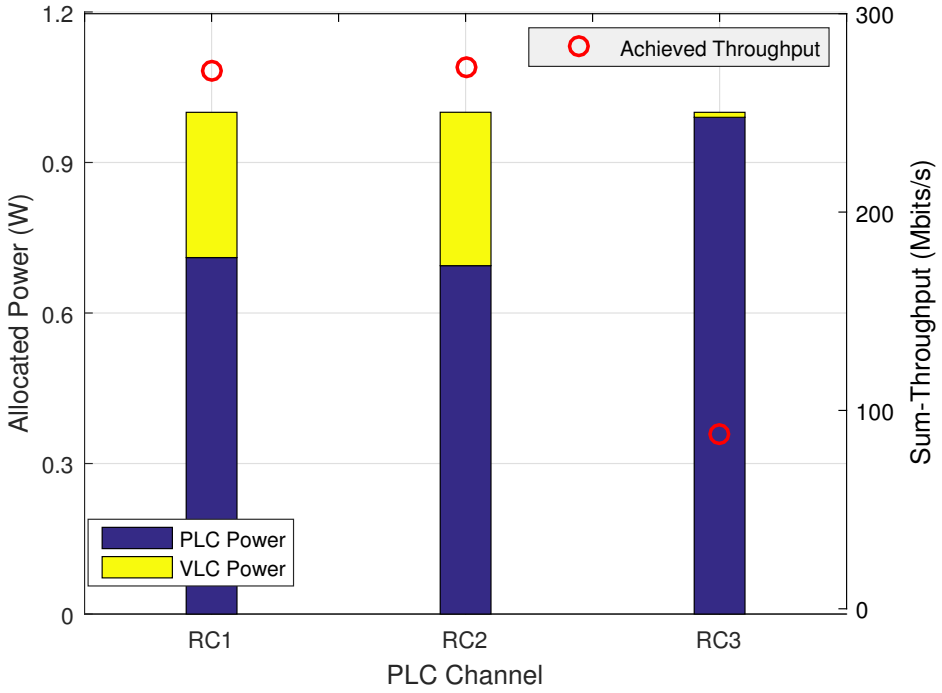

Figure 6.10: The power allocated to the PLC and VLC links as well as the sum-throughput achieved by the PLC-VLC network for the PLC channels of RC1, RC2 and RC3, under a minimum rate requirement of 5 Mbits/s. All other parameters are summarized in Table 6.1.

compared to the RC2 scenario. This implies that as expected, the OFDM scheme is capable of performing well. However, if the PLC channel is as hostile as RC3, the majority of the power has to be allocated to PLC link, leading to a substantially reduced sum-throughput. Based on these findings, in the following simulations, the RC1 will be employed in our PLC-VLC network, since it is also widely used in PLC research.

6.5.2 Influence of Transmit Power

In this section, we will investigate the influence of various transmit power constraints on our PLC-VLC network. First of all, the power allocated to the PLC and VLC links is investigated for various values of P_T, as shown in Fig. 6.11. Naturally, upon increasing the transmit power allowance, the power allocated to both PLC and VLC links is increased. It is interesting to find that the power allocated to VLC is higher than that of the PLC link. This trend is reversed compared to Fig. 6.10. This is because that the bandwidth of PLC RC1 in Fig. 6.11 is almost twice that in Fig. 6.10. This implies that the PLC-VLC network has benefited from employing a wider PLC band, since more power can be allocated to VLC for throughput improvement. Furthermore, we observe that the higher the transmit power allowance we have, the lower the power

ratio between PLC and VLC becomes. Again, more power can be allocated to VLC, hence resulting in a throughput improvement. Note that according to our JPA, the sum power of PLC and VLC is equal to the maximum transmit power allowance, where the PLC power ratio is defined as P_{plc}/P_T. As demonstrated in Fig. 6.12, the benefit of increasing the power of the VLC link is that the throughput achieved by the PLC-VLC network exhibits a steady growth upon increasing P_T.

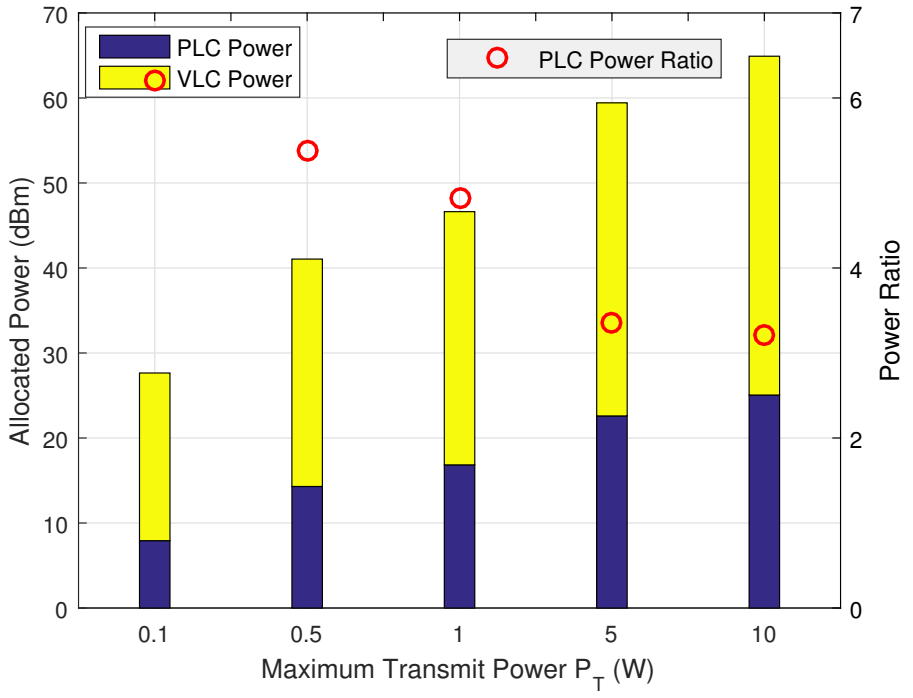

Figure 6.11: The power allocated to the PLC and VLC links based on our proposed JPA and RC1. All other parameters are summarized in Table 6.1.

To expound a little further, the achievable VLC-UE rate distribution of the proposed NOMA downlink in our PLC-VLC network relying on various transmit power allowances P_T is presented in Fig. 6.13. Observed that 90% UEs achieve a throughput of 20 Mbits/s in this scenario. Since a total of 10 UEs are supported during our simulation, all the VLC-UEs, excepted for the specific UE having the highest channel gain, can be guaranteed to have their minimum rate requirements satisfied. Since the simulations are conducted within the feasible set, the residual power is used for the highest-gain UE to achieve a throughput no lower than its minimum rate requirement, whilst relying on our proposed JPA. It can be observed from Fig. 6.13 that the higher power allowances encourage the highest-gain UE to aim for an increased rate.

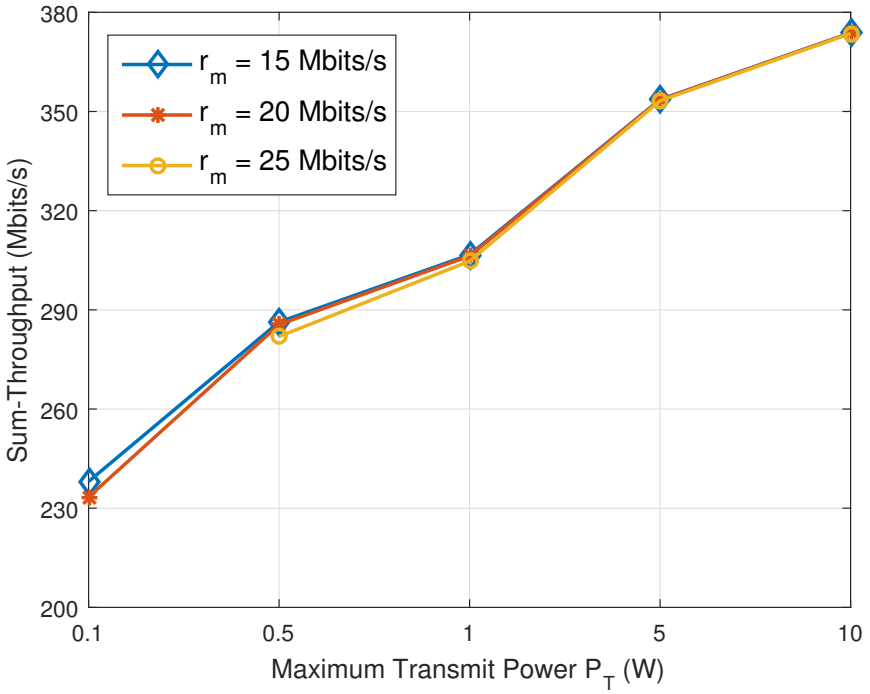

Figure 6.12: Sum-throughput attained by the PLC-VLC network relying on RC1 as a function of the transmit power P_T, under various minimum rate requirements. All other parameters are summarized in Table 6.1.

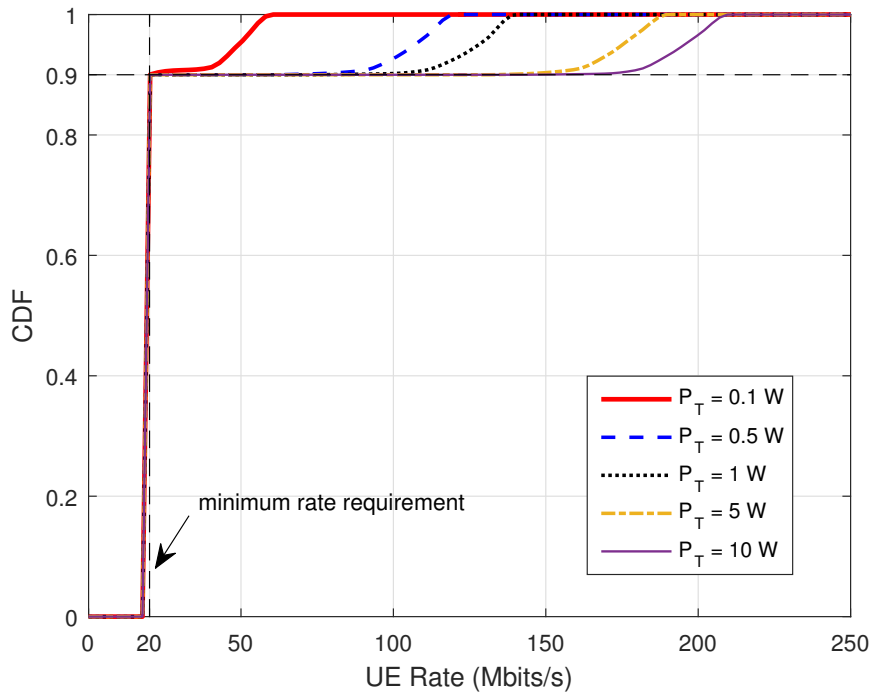

Figure 6.13: CDF of the VLC-UEs' achievable rate parameterized by various transmit power allowances P_T. All other parameters are summarized in Table 6.1.

6.5.3 Influence of Minimum Rate Requirement

In this section, the influence of various minimum rate requirements on the PLC-VLC network is explored. To elaborate, two typical NOMA PA schemes are included as benchmarkers for comparions, which are the statical power allocation (SPA) [55] and NGDPA [59]. Instead of dynamically controlling the power allocation in our PLC-VLC network as the proposed JPA, both SPA and NGDPA rely on a fixed power allocation strategy for the multiple VLC UEs. Specifically, the SPA strategy is formulated as [55]:

$$p_{\text{vlc},m} = \alpha p_{\text{vlc},m-1}, \tag{6.41}$$

where α is a factor, which satisfies $0 < \alpha < 1$. Instead of purely relying on the decoding order, the NGDPA strategy also includes the channel gain difference, which is expressed as [59]:

$$p_{\text{vlc},m} = \left(\frac{h_1 - h_{m-1}}{h_1}\right)^m p_{\text{vlc},m-1}. \tag{6.42}$$

Furthermore, the classic TDMA is also invoked in our PLC-VLC scheme as a benchmarker for our NOMA VLC downlink[4].

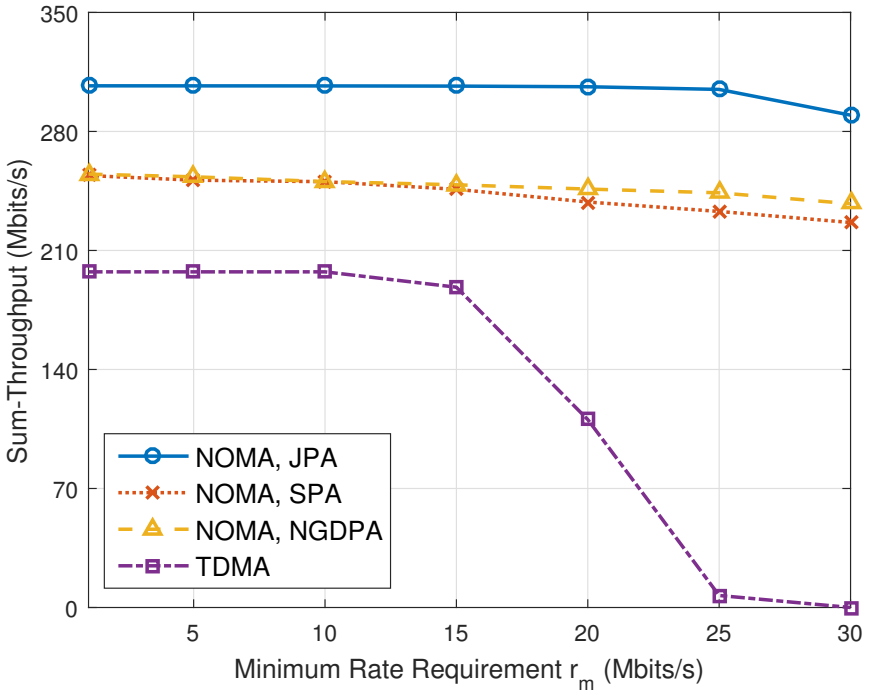

Figure 6.14: Sum-throughput attained by the PLC-VLC network v.s. minimum rate requirements, parameterized by different power allocation strategies and MA techniques. All other parameters are summarized in Table 6.1.

[4]The JPA for TDMA-based VLC-downlink is provided in Appendix 6.2.

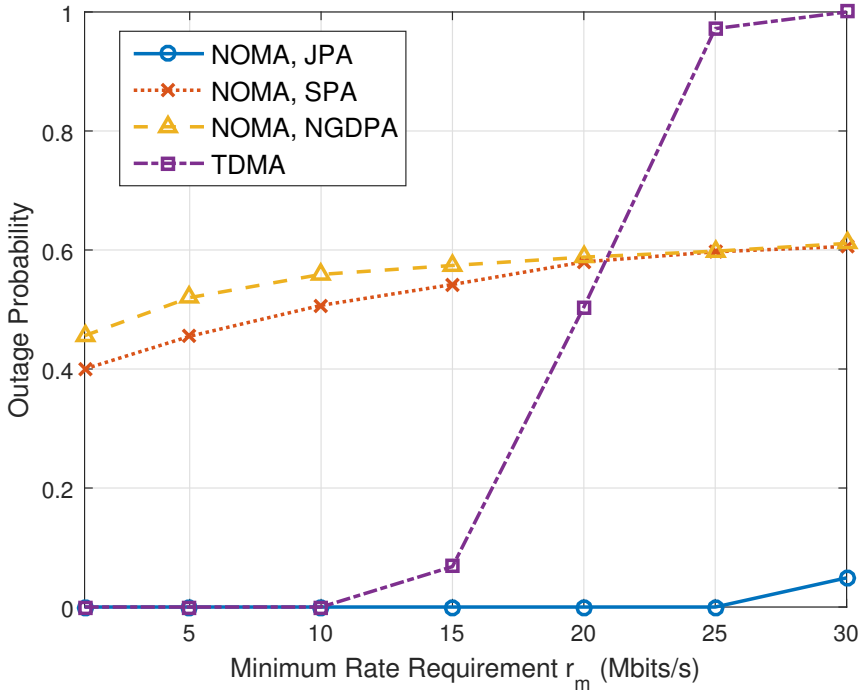

Figure 6.15: Outage probability of the PLC-VLC network vs the minimum rate requirement. All other parameters are summarized in Table 6.1.

Figure 6.14 shows the sum-throughput attained by our PLC-VLC network under various minimum rate requirements, in conjunction with different power allocation and MA strategies. Observed that NOMA downlink exhibits the best performance, whilst TDMA falters under strict minimum rate requirements. Regardless of the specific power allocation strategy, the sum-throughput attained by NOMA-VLC downlink tends to be slightly reduced upon increasing the minimum rate requirement of each UE. This is because increasing the minimum rate requirement of each UE results in allocating more power to the specific UEs having worse channels, hence leading to a power reduction for PLC. We also observe that the sum-throughput attained by our proposed JPA is higher than that of the SPA and of the NGDPA benchmarkers, which is an explicit benefit of considering not only the decoding order and channel gains, but also the transmission integrity. Furthermore, the associated outage probability is observed in Fig. 6.15, where the outage probability is defined as the probability of having UEs that cannot be supported at their minimum rate requirement. Upon imposing stricter minimum rate requirements, the outage probability of TDMA exhibits a sharp increase, and approaches 1, when the transmission rate of 30 Mbits/s is requested by every UE. By contrast, we observe that the outage probability of the NOMA based PLC-VLC network relying on the proposed JPA remains close to zero for most of the r_m values, and it is only slightly increased even when the minimum rate requirement is as high as 30 Mbits/s. As for the SPA and NGDPA strategies, their outage probabilities are much higher than that of the

JPA, for all the minimum rate requirements considered. This implies that the power is efficiently allocated to both the PLC and VLC by our proposed JPA, so that it can achieve an increased throughput, while keeps the outage probability as low as possible, right across a wide range of minimum rate requirements.

6.5.4 Influence of UE Density

In this section, we investigate the influence of UE density on the PLC-VLC network. Specifically, Fig. 6.16 portrays the sum-throughput attained by different power allocation strategies and MA techniques, in various UE density scenarios. Again, we find an obvious sum-throughput drop for the TDMA technique, which becomes inadequate, when the UE density becomes $\sim 0.9/\mathrm{m}^2$. We also observe that the sum-throughput attained by the proposed JPA is higher than that of SPA and NGDPA, regardless of UE density. It is interesting to observe that the sum-throughput acquired by JPA steadily increases upon increasing the UE density and then slightly decreases, while that of the other two PA strategies monotonically decreases. Since JPA succeeds in maintaining the required minimum rate even for those UEs which do not have the highest channel gain, it encourages the UEs having the highest channel gain to aim for the highest possible throughput within the affordable power budget.

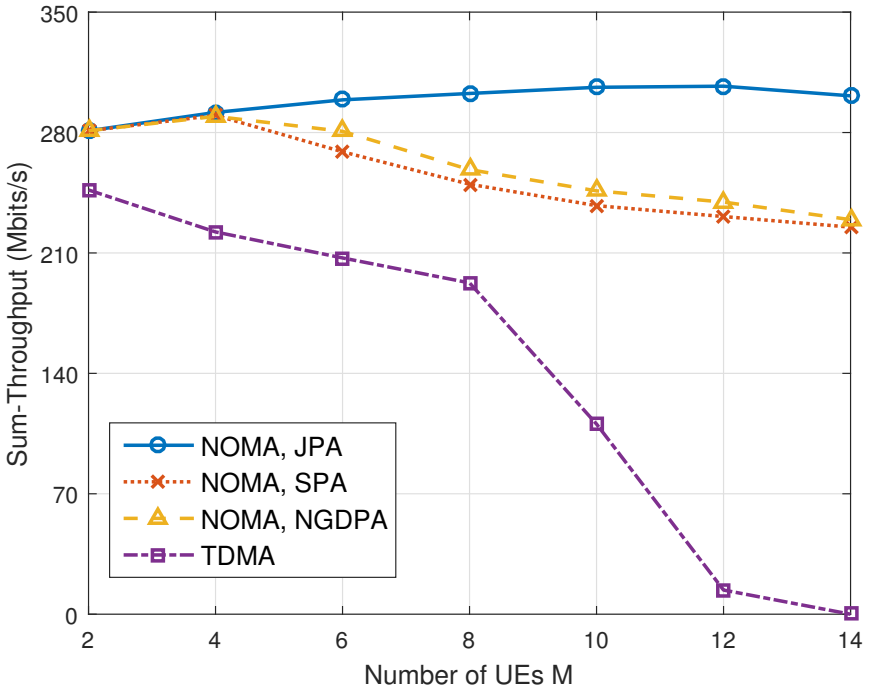

Figure 6.16: Sum-throughput attained by the PLC-VLC network as a function of UE density, parameterized by the different power allocation strategies and MA techniques. All other parameters are summarized in Table 6.1.

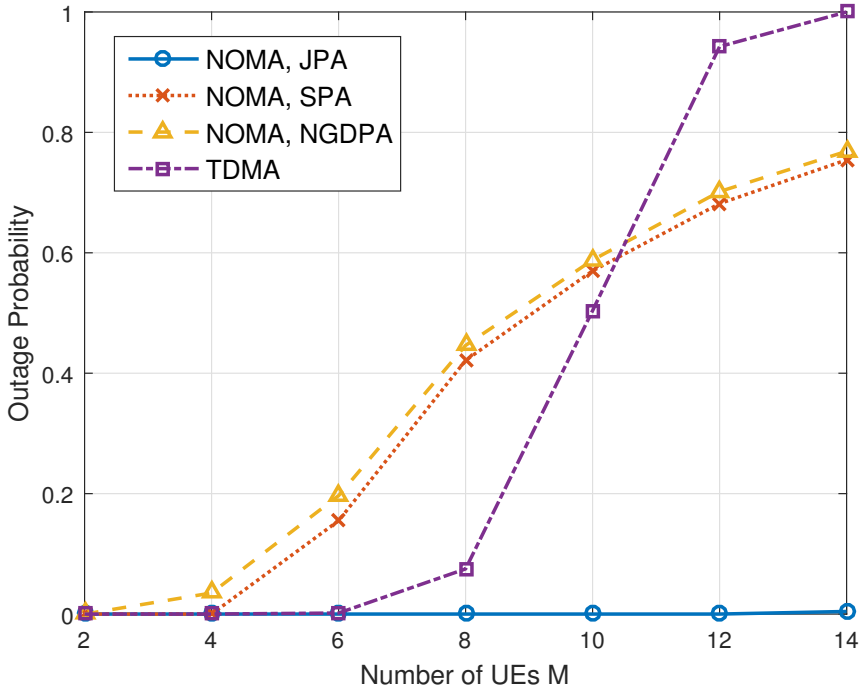

Figure 6.17: Outage probability of the PLC-VLC network vs the number of UE, relying on various power allocation strategies and MA techniques. All other parameters are summarized in Table 6.1.

Moreover, the outage probability is investigated in Fig. 6.17. As seen in the figure, the outage probability of TDMA is significantly increased approaching 1 upon increasing the UE density, while the outage probability of both the SPA and of the NGDPA is also increased. Instead, we find that the outage probability of our proposed JPA remains near-zero for a variety of UE density scenarios, We conclude that the proposed JPA aided PLC-VLC network is capable of efficiently supporting multiple UEs.

6.6 Chapter Conclusions

In this chapter, we explored a multi-user PLC-VLC downlink scenario, where PLC acted as the backbone of our VLC system. A constrained throughput maximization problem was formulated, which was solved by our proposed JPA. Our simulations demonstrated that as expected, the NOMA technique was capable of attaining a higher throughput than OMA. Furthermore, we also demonstrated that the proposed JPA outperformed the previously published SPA and NGDPA benchmarkers [55, 59], under diverse minimum rate requirements and UE densities. It is inferred that the PLC-VLC network assisted by the JPA is capable of efficiently supporting multiple UEs under a wide range of minimum rate requirements, while maintaining a close-to-zero outage probability.

6.7 Chapter Summary

In this chapter, PLC was invoked for feeding VLC network, resulting in the conceived PLC-VLC networks. Broadband OFDM was employed by the PLC component, which was briefly introduced in Section 6.2.1. As shown in Figs. 6.10 and 6.11, upon relying on broadband OFDM, a majority of the power can be allocated to VLC for increasing the throughput of the proposed PLC-VLC networks. To support multiple UEs, in Section 6.2.2, NOMA based VLC was proposed for increasing the throughput. As demonstrated in Figs. 6.14 - 6.17, TDMA aided PLC-VLC network fails in the scenario of high minimum rate requirement and in dense UE population scenarios. By contrast, relying on NOMA regime, our PLC-VLC network achieves a high throughput, while significantly reduced the number of UEs in outage. To solve our sum-throughput maximization problem, sophisticated power allocation was proposed in Section 6.3. Upon exploiting the relationship between PLC and VLC links, an optimal JPA strategy was proposed in Section 6.4, where the power allocated to each subcarrier in PLC and to each of the VLC-UE was jointly decided. The CDF of the throughput achieved upon relying on JPA and shown in Fig. 6.13 implied that the JPA was capable of guaranteeing the minimum rate requirement of the individual UEs, while the UE having the highest channel gain is encouraged to increase its throughput, provided that the associated power consumption is affordable for the network. Furthermore, a pair of typical power allocation strategies were also included as benchmarkers, namely the SPA and the NGDPA. The throughput and outage probability of Figs. 6.14 and 6.15 suggested that the proposed JPA outperformed the other two strategies, yielding both a higher throughput as well as a reduced outage probability, even in the face of strict minimum rate requirements. Moreover, the influence of the UE density was also quantified in Figs. 6.16 and 6.17, which reflected that the proposed JPA is capable of achieving a near-zero outage probability when the UE density below 0.9 UE/m^2.

6.8 Appendix 6.1: Parameters of Three PLC Channels

The parameters of the reference channels RC1, RC2 and RC3 are provided in Tables 6.2, 6.3 and 6.4, respectively.

Attenuation Term		
$\kappa = 1$	$a_0 = 0$	$a_1 = 7.8 \times 10^{-10}$
Path Parameter		
i	w_i	d_i
1	0.64	200
2	0.38	222.4
3	-0.15	244.8
4	0.05	267.5

Table 6.2: Parameters of RC1

Attenuation Term		
$\kappa = 1$	$a_0 = 0$	$a_1 = 1.5 \times 10^{-9}$
Path Parameter		
i	w_i	d_i
1	0.6	100
2	-0.08	130
3	0.08	160
4	-0.08	190
5	0.15	300

Table 6.3: Parameters of RC2

Attenuation Term			$\kappa = 1$		$a_0 = 0$		$a_1 = 4.5 \times 10^{-9}$	
Path Parameter								
i	w_i	d_i	i	w_i	d_i	i	w_i	d_i
1	0.17	211.5	5	0.33	278	9	0.05	390
2	0.25	228	6	-0.37	306	10	-0.15	420
3	-0.1	243	7	0.18	330	11	0.15	540
4	-0.12	254	8	-0.2	360	12	-0.15	740

Table 6.4: Parameters of RC3

6.9 Appendix 6.2: Power Allocation for the TDMA VLC-Downlink

When employing TDMA, the VLC-UEs are multiplexed in the time-domain, where there is only a single UE is supported within a single time-slot. Upon assuming that the time-resources T is averaged over all UEs, the sum-throughput maximization over T duration is equivalent to maximizing the throughput within a single time-slot. As the time-slots are independent from each other, the throughput maximization can be operated within each single time-slot. To elaborate, the JPA conceived for the TDMA aided PLC-VLC network is introduced as follows.

According to our assumption, the maximization problem of UE m is mathematically formulated as:

$$\max_{\boldsymbol{p}_{\text{plc}}, p_{\text{vlc},m}} \frac{B_{\text{v}}}{M} \log_2 \left(1 + \eta_m p_{\text{vlc},m}\right) \tag{6.43a}$$

$$\text{s.t. } P_{\text{plc}} + p_{\text{vlc},m} \leq P_T; \tag{6.43b}$$

$$\frac{B_{\text{v}}}{M} \log_2 \left(1 + \eta_m p_{\text{vlc},m}\right) \leq R_{\text{plc}}; \tag{6.43c}$$

$$\frac{B_{\text{v}}}{M} \log_2 \left(1 + \eta_m p_{\text{vlc},m}\right) \geq r_m; \tag{6.43d}$$

$$\boldsymbol{p}_{\text{plc}} \geq \mathbf{0}_{N\times 1}; \tag{6.43e}$$

$$p_{\text{vlc},m} \geq 0. \tag{6.43f}$$

The Lagrangian function of Problem (6.43) is therefore obtained as:

$$\begin{aligned} \mathcal{L}\left(\boldsymbol{p}_{\text{plc}}, p_{\text{vlc},m}, \delta, \gamma, \tau\right) &= \frac{B_{\text{v}}}{M} \log_2 \left(1 + \eta_m p_{\text{vlc},m}\right) + \delta \left(P_T - P_{\text{plc}} - p_{\text{vlc},m}\right) \\ &+ \gamma \left[R_{\text{plc}} - \frac{B_{\text{v}}}{M} \log_2 \left(1 + \eta_m p_{\text{vlc},m}\right)\right] + \tau \left[\frac{B_{\text{v}}}{M} \log_2 \left(1 + \eta_m p_{\text{vlc},m}\right) - r_m\right], \end{aligned} \tag{6.44}$$

where δ, γ and τ represent the Lagrange multipliers associated with the constraints (6.43b) - (6.43d). Accordingly, the KKT conditions of it are listed as follows:

$$\frac{\partial \mathcal{L}}{\partial p_{\text{plc},n}} = \frac{\gamma \varrho B}{\ln 2} \times \frac{\lambda_n}{1 + \lambda_n p_{\text{plc},n}} - \delta = 0, \ \forall n; \tag{6.45a}$$

$$\frac{\partial \mathcal{L}}{\partial p_{\text{vlc},m}} = \frac{B_{\text{v}}(1 - \gamma + \tau)}{M \ln 2} \times \frac{\eta_m}{1 + \eta_m p_{\text{vlc},m}} - \delta = 0; \tag{6.45b}$$

$$\delta \left(P_T - P_{\text{plc}} - p_{\text{vlc},m}\right) = 0; \tag{6.45c}$$

$$\gamma \left[R_{\text{plc}} - \frac{B_{\text{v}}}{M} \log_2 \left(1 + \eta_m p_{\text{vlc},m}\right)\right] = 0; \tag{6.45d}$$

$$\tau \left[\frac{B_{\text{v}}}{M} \log_2 \left(1 + \eta_m p_{\text{vlc},m}\right) - r_m\right] = 0; \tag{6.45e}$$

$$\delta \geq 0, \ \gamma \geq 0, \ \tau \geq 0; \tag{6.45f}$$

$$(6.43b) - (6.43f). \tag{6.45g}$$

Upon combining Eq. (6.45a) and (6.45b), we have:

$$\gamma = \frac{B_{\text{v}}(1 + \tau)}{M} \times \frac{\frac{\eta_m}{1 + \eta_m p_{\text{vlc},m}}}{\frac{\varrho B \lambda_n}{1 + \lambda_n p_{\text{plc},n}} + \frac{B_{\text{v}} \eta_m}{M(1 + \eta_m p_{\text{vlc},m})}}. \tag{6.46}$$

Observe that Eq. (6.46) remains positive, regardless of the power value of $p_{\text{plc},n}$ and $p_{\text{vlc},m}$, yielding $\gamma > 0$. Therefore, Eq. (6.45d) only remains zero when the throughput achieved by VLC UE m equals to the throughput provided by the PLC links, which is

expressed as:

$$R_{\text{plc}} = \frac{B_{\text{v}}}{M} \log_2 \left(1 + \eta_m p_{\text{vlc},m}\right). \tag{6.47}$$

Furthermore, Eq. (6.45a) implies that similar to γ, δ is also positive. Hence it can be readily seen that Eq. (6.45c) is only satisfied, when we have:

$$P_{\text{plc}} + p_{\text{vlc},m} = P_T. \tag{6.48}$$

For the sake of satisfying the associated minimum rate requirement, the feasible set of Problem (6.43) is given by:

$$\frac{B_{\text{v}}}{M} \log_2 \left[1 + \eta_m (P_T - P_{\text{plc}})\right] \geq r_m, \tag{6.49}$$

which implies that the PA solution can be obtained for Problem (6.43), if P_{plc} satisfies:

$$P_{\text{plc}} \leq P_T - \frac{2^{M r_m / B_{\text{v}}} - 1}{\eta_m}. \tag{6.50}$$

According to Eq. (6.38), we know that the total throughput R_{plc} of the PLC link is actually a function of P_{plc}. By combining Eq. (6.47) and (6.48), the following function of P_{plc} can be obtained:

$$\Psi' = R_{\text{plc}} - \frac{B_{\text{v}}}{M} \log_2 \left[1 + \eta_m (P_T - P_{\text{plc}})\right]. \tag{6.51}$$

Therefore, the value of P_{plc} is obtained, when we arrive at $\Psi' = 0$, which can be found by the classic bisection method. Hence, the power allocation solution of the TDMA aided PLC-VLC network was found.

Chapter 7

Conclusions and Future Research

In this concluding chapter, we will provide our overall summary and conclusions in Section 7.1. Then several research topics concerning potential future studies will be presented in Section 7.2.

7.1 Summary and Conclusions

In this thesis, we have provided detailed UC-VLC network designs to achieve a high throughput. Table 7.1 summarizes the basic characteristics of all our UC-VLC regimes proposed in this thesis, chapter by chapter. More specifically, we proposed a novel clustering strategy termed as the centre-shifting UC-clustering, where the position information of UEs was taken into account. Based on the proposed UC-clustering, a UC-VLC system can be constructed, for which we proposed a dynamic resource allocation algorithm to maximize the achievable sum-throughput. Furthermore, the MA design was also taken into account. Note that the position information of UEs required by clustering can be acquired by our proposed hybrid positioning. Moreover, to constitute a practical VLC network, the PLC system was invoked as the backbone network of VLC, yielding the PLC-VLC network conceived, where a JPA algorithm was proposed for supporting it.

Chapter No.	**Chapter 2**				**Chapter 3**		**Chapter 4**		**Chapter 5**		**Chapter 6**
Concern	Clustering				Positioning		Resource allocation		Multiple Access		backhauling
Scenario	Multi-AP-multi-UE				Multi-AP-multi-UE		Multi-AP-multi-UE		Multi-AP-multi-UE		Single-AP-multi-UE
Compared Scheme	UFR	FR-2	NC-4	UC Radius	Triangu-lation	Finger-printing	NC	Greedy	TDMA	NOMA	TDMA
Throughput gain (Gbs) @ $\Psi_{\text{FoV}} = 90^o$	15.14	16.05	9.04	5.15	$29.6e-3$	$1.4e-3$	2.14	0.21	5.70	-0.13	-
Throughput gain (Gbs) @ $\lvert\mathcal{K}\rvert = 25$	13.85	14.59	6.88	4.56	-	-	2.496	0.149	5.432	-0.05	0.20
OP improve ratio @ $\Psi_{\text{FoV}} = 90^o$	-	-	-	-	0.7650	0	0.33	0.01	0.23	0.05	-
OP improve ratio @ $\lvert\mathcal{K}\rvert = 25$	-	-	-	-	-	-	0.35	0.02	0.20	0.04	0.50

Table 7.1: Summary of UC-VLC design

Scheme	Criterion	Structure	Cons	Pros
UFR	Section 2.3.1.1	one-to-one	ICI vulnerable	Pre-defined boundaries
FR-τ	Section 2.3.1.1	one-to-one	Low throughput	Pre-defined boundaries
NC-ζ	Section 2.3.1.2	many-to-many	Association-blurry Unbalanced-loading	Pre-defined boundaries
Radius-based UC	Section 2.3.2	many-to-many	Performance relies on initialization	Amorphous boundaries
Centre-dynamic UC	Section 2.4	many-to-many	Complexity	Amorphous boundaries ICI elimination

Table 7.2: Summary of various clustering strategies.

- **Chapter 1:** In Chapter 1, we provided a generic overview of the VLC network. To be specific, in Section 1.1, we reviewed the link-level design of VLC, where the single-user transmission and the multi-user transmission were considered, while the latter was expected to have a better performance due to its capability of ICI-mitigation. In Section 1.2, we described the system-level design of VLC, concerning the network association, MA and resource allocation. Furthermore, in Section 1.3, we discussed the practical considerations of VLC networks, including the indoor positioning and backhaul design. Finally, Section 1.4 highlighted the organization as well as the main contributions of this thesis.

- **Chapter 2 [122]:** In Chapter 2, a novel centre-shifting clustering strategy was proposed in the context of a UC-VLC system. This design philosophy relied on the UEs' location information, hence had the potential of outperforming other conventional clustering strategies, such as UFR, FR-τ and NC-ζ. Furthermore, as the proposed strategy constructed clusters by considering the cluster-centre during each expansion, the resultant clusters were separated by sufficiently high distance, which is an exclusive benefit of the UC-VLC system relying on the proposed strategy, since the ICI can be significantly reduced.

  In Section 2.2, a multi-AP-multi-UE indoor VLC system was modelled, considering both its propagation channel and modulation schemes. Given the fact that the energy of higher-order reflections decreased rapidly, only the LoS and the first reflected rays were considered in our VLC system.

  In this multi-AP-multi-UE VLC system, we studied the family of classic network association strategies, which is categorized into two groups, namely the NC-clustering and the UC-clustering. Table 7.2 summarizes the characteristics of those designs. To be specific, the single-attocell NC-clustering, such as UFR and FR-τ was reviewed in Section 2.3.1.1. By simply considering each attocell as an individual cluster, the association between a given UE and AP is decided by the pre-defined cluster boundaries, without considering the UE's position. It can be observe that based on the single-attocell NC-clustering, the system remain vulnerable to the ICI, since the APs are usually deployed densely. Furthermore, we found

from Fig. 2.12 and 2.13 that even though the FR technique was invoked to manage the ICI, the throughput was still unsatisfactory due to the inefficient UE-AP association. As a further development in multi-user transmission, the concept of merging multiple attocells into a large cluster was advocated, so that multiple APs may support multiple UEs within the same time-slot. Motivated by this concept, the multi-attocell NC-clustering strategy was introduced in Section 2.3.1.2, where the system was divided into several clusters according to the pre-defined boundaries. However, since this design still did not consider the distribution of UEs, the UE-AP association-blurring and unbalanced loading degrade its performance. By contrast, following the UC regime, a simple radius-based UC-clustering strategy was investigated in Section 2.3.2, which can be divided into two steps: UE-AP anchoring and clustering, where the former guaranteed the QoS, while the latter grouped multiple UEs based on a pre-defined radius threshold r. Although the clusters constructed took into account the UEs' distribution, we found that the attainable performance strongly depended on the selection of the starting point.

Hence, Section 2.4 proposed a new clustering strategy based on the concept of UE and solved the remaining design issues of the radius-based UC-clustering. More specifically, the centre of the clusters constructed based on our proposed centre-shifting UC-clustering is not fixed, but it is iteratively adjusted according to the position of the grouped UEs, as shown in Eq. (2.19). The proposed clustering consists of three steps, which are the UE-AP anchoring, UE set formation and AP set formation, where the anchoring process is the same as we described in Section 2.3.2. The detailed UE set formation and AP set formation was provided by Algorithm 1, ensuring that the clusters constructed were separated by a safe distance, which is an explicit benefit of the proposed clustering.

The design guidelines of the centre-shifting UC-clustering relying on the parameters d_u and on the communication environment are summarized as follows:

- The values of d_u specify the size of the clusters constructed, where a larger value of d_u contributes to larger clusters, vice versa.
- As we analysed, the multi-AP-multi-UE structure within each constructed cluster is capable of achieving a significantly increased throughput, assisted by the technique of TPC. However, it is not generally true that a larger cluster, containing more APs and UEs, achieves a higher throughput, since the cost of power consumption has to be considered, as shown in Fig. 2.14.
- Furthermore, the environment-related parameters play an important role in the UC-cluster design. To be specific, Fig. 2.14 investigated the decision concerning d_u, when the transmit power or the number of UE is different. When the distribution of UEs is sparse, increasing d_u is capable of slightly boosting the achievable throughput. By contrast, when the distribution of

Technique	FoV	Reflection	Number of APs	Blocking	Tile size
Triangulation	E	E	E	E	-
Fingerprinting	L	L	L	L	E

Table 7.3: Summary of various effects on the positioning performance of triangulation and fingerprinting in visible light positioning, where E represents "easily affected", while L represents "less affected".

UEs is dense, a larger value of d_u leads to a pronounced throughput reduction, since the transmit power is limited.

Finally, in Section 2.5, we characterized the clustering performance of both the no-clipping-distortion and clipping-distortion scenarios, where the basic system parameters employed for the simulations were listed in Table 2.2.

- **Chapter 3 [121]:** In Chapter 2, the UC-clustering philosophy was considered, assuming that perfect knowledge of the UEs' position is available at the central controller. However, how to obtain accurate UEs' position information remained an open issue in our scenario. Therefore, in Chapter 3, we investigated the visible light positioning and proposed a hybrid indoor positioning based on VLC, which is capable of providing quite an accurate positioning result within the centimeter-range.

  Section 3.2 reviewed the family of classic indoor positioning techniques, including proximity, triangulation and scene analysis. Section 3.3 analysed the feasibility of VLC-aided indoor positioning, where the propagation characteristics of VLC enables the visible light positioning to be a potentially efficient solution. Inspired by this, the visible light positioning aided by triangulation and by fingerprinting were investigated in Section 3.4.1 and Section 3.4.2, respectively, where their performance comparison was provided in Table 7.3. More specifically, we found that the complexity of triangulation-based positioning was relatively low, since the estimated positions can be calculated according to their RSS values, as shown in Eq. (3.12). However, its positioning performance is typically affected by the environmental setups, such as FoV (shown in Figs. 3.6 - 3.8), reflection (shown in Figs. 3.9 - 3.11), number of APs (shown in Figs. 3.12, 3.13) and blocking (shown in Fig. 3.14). By contrast, the positioning performance of fingerprinting is more stable, albeit this is achieved at a cost of increased complexity. Since the fingerprinting technique estimates the position based on the matching process between the RSS vector of Eq. (3.18) and the RSS vector stored in database as shown in Eq. (3.17), the size of the database strongly affects its performance. By observing Figs. 3.15 - 3.17, we found that smaller tiles results in more accuracy positioning results, but again the matching complexity increases correspondingly.

Measurement	Positioning Error
Effects of UE density	Fig. 3.22
Effects of blocking	Figs. 3.23, 3.24, 3.25
Effects of AP density	Figs. 3.26, 3.27, 3.28

Table 7.4: Positioning performance summary of the hybrid positioning technique, considering the basic system parameters listed in Table. 3.1.

In Section 3.4.3, we proposed a novel visible light positioning technique by amalgamating triangulation and fingerprinting, striking a balancing between accuracy and complexity. This consists of four steps, namely the preliminary operations, coarse-positioning, evaluation and re-positioning, as detailed in Section 3.4.3. In Section 3.5, we quantified the performance of the proposed technique in terms of its positioning performance and achievable throughput, where the former is summarized in Table 7.4. Note that the throughput was increased by our UC-VLC system, relying on our UC-clustering strategy, where both the scenarios in the absence/presence of clipping-distortions were considered in Figs. 3.29 and 3.30. We found that the throughput difference between the proposed technique and the perfect positioning is significantly lower than for the triangulation and fingerprinting techniques, regardless of FoV. We concluded that by amalgamating the benefits of both triangulation and of fingerprinting, the proposed technique becomes capable of achieving a much higher positioning accuracy than triangulation at a lower complexity than that of fingerprinting.

- **Chapter 4 [122]:** In Chapter 4, we further investigated the resource allocation problems of the UC-VLC constructed based on the UC-clustering strategy proposed in Chapter 2. Instead of relying on a number of idealized simplifying assumptions, such as operating exactly at the Shannon capacity, the modulation-mode-related throughput was invoked for exploring the superiority of UC-VLC over NC-VLC. Therefore, a dynamic resource allocation scheme was designed for operation in the face of practical considerations, which jointly decided the modulation-mode assignment, power allocation and scheduling.

  Section 4.2 described four main practical considerations in our design, which were the LED impairments, backhaul-rate limitation, adaptive modulation-mode assignment and flexibility of system. However, in this chapter, no transmission loss was assumed in backhaul. Then the objective function based on the achievable sum-throughput was formulated in Section 4.3 under practical constraints. More specifically, the conventional ACO/DCO-OFDM was invoked as the point-to-point transmission scheme, taking into account the clipping-distortion. Within each constructed UC-cluster based on the centre-shifting UC-clustering, TPC was invoked for achieving simultaneous transmission. Upon scrutinizing the problem (4.5), we

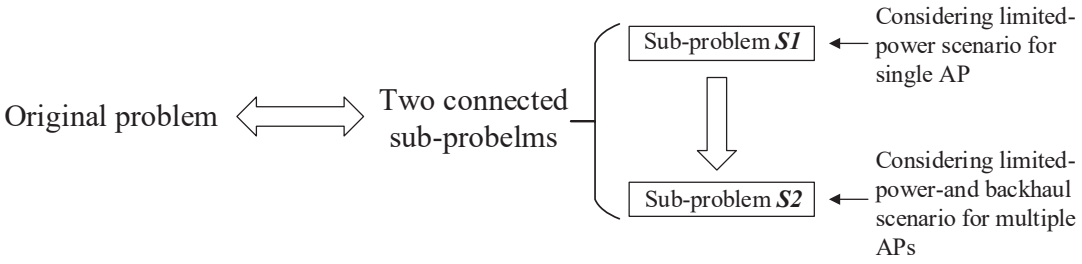

Figure 7.1: A summary of our proposed methodology in Chapter 4.

found that it was a multi-user-dependent maximization problem. To cope with this challenge, we partitioned it into two subproblems and then shown in **Theorem 4.1** that successively solving these two subproblems was equivalent to solving the original problem. To be more specific, Section 4.4.1 studied the first subproblem $\boldsymbol{S1}$, which focussed on the scenario where the power constraint was only applied to a single AP at a time. To solve this, dynamic resource allocation was proposed in Sections 4.4.1.2 and 4.4.1.3, which jointly decided the modulation-mode assignment for the various UEs and the power allocation for the specific AP. Note that the no-transmission modulation-mode was also included in our modulation-mode assignment, leading to the specific scheduling design conceived. The results obtained for $\boldsymbol{S1}$ were further considered in the second subproblem in a multi-AP scenario along with limited power and backhaul. Our proposed algorithm is summarized in Fig. 7.1.

Section 4.5 characterized our UC-VLC system, compared to NC-VLC. We first investigated the effect of positioning errors on UC-VLC, since the UEs' position information used for clustering was based on visible light positioning. Since the proposed UC-clustering relies on the relative distance between UEs, our UC-VLC system was capable of tolerating the positioning errors upto several meters. Then we carried out a comprehensive comparison between the UC-VLC and NC-VLC in terms of its throughput and outage probability. The effects of the value of FoV Ψ_{FoV}, the number of UE $|\mathcal{K}|$ and the backhaul-rate R^{BH} are summarized in Table 7.5, based on our simulation results in Section 4.5. As a benefit of the UC-clustering, the UC-VLC was found to outperform NC-VLC in the various scenarios considered. Furthermore, since the scheduling was dynamically controlled by our proposed algorithm, it achieved a higher throughput and a lower outage probability than the conventional greedy algorithm.

- **Chapter 5 [123]:** A pair of classic link-level transmission schemes, namely ACO-OFDM and DCO-OFDM, were invoked in Chapters 2,3 and 4, where the former

Metrics	Effects	NC-VLC	UC-VLC
TP	Ψ_{FoV}	Obvious drop when $\Psi_{\text{FoV}} > 80^o$	Consistently higher than NC-VLC
	$\|\mathcal{K}\|$	Obvious drop when $\|\mathcal{K}\| > 20$	Nearly stationary
	R^{BH}	-	d_u design can compensate TP-loss
OP	Ψ_{FoV}	Unsatisfactory	Substantially lower than NC-VLC
	$\|\mathcal{K}\|$	Unsatisfactory	Substantially lower than NC-VLC
	R^{BH}	-	Suitable d_u can reduce OP

Table 7.5: A summary of the comparison between NC-VLC and UC-VLC systems according to our simulations based on the parameters in Table 4.1.

is spectrum-inefficient, while the latter is power-inefficient. To improve the overall system-level design, in Chapter 5, the advanced LACO-OFDM transmission scheme was invoked in our UC-VLC system.

The philosophy of the LACO-OFDM transmission scheme was introduced in Section 5.2. Since the transmitted bits were mapped by the modulator to the different subcarrier-related layers, a SIC-based receiver was required to reconstruct them, as shown in Fig. 5.3. However, TPC is incompatible with the SIC-aided demodulation of LACO-OFDM, hence it cannot be directly applied in our previously proposed UC-VLC system. Therefore, a novel system architecture was conceived in this chapter.

More specifically, an overlapped clustering strategy was proposed for our LACO-OFDM aided VLC system in Section 5.3. As shown in Figs. 5.4 - 5.6, by exploring the bidirectional multi-cell connections, a *many-to-many* UE-AP association was conceived, where multiple APs may be associated with more than one UE, while a specific UE may be supported by more than one AP, which we referred to as overlapped clustering. According to our complexity analysis in Section 5.3.2, our proposed clustering is capable of spectacularly reducing the computational complexity, compared to the optimal exhaustive search.

To fully exploit the above-mentioned overlapped association, a sophisticated MA design was proposed in Section 5.4. Thanks to its high capacity, the NOMA technique was invoked in our LACO-OFDM aided VLC system. Recall from Section 5.4.1 that when NOMA was invoked in our overlapped clusters, it was shown to be capable of mitigating the ICI, which is an explicit benefit of the proposed clustering. However, due to the densely deployed APs, purely relying on NOMA may be insufficient, especially when considering all the practical constraints. Therefore, in Section 5.4.2, we explored a hybrid NOMA/OMA scheme, where both FR and TDMA-based scheduling may be dynamically invoked for eliminating the grave ICI. Specifically, the FR technique was supported by a graph-coloring based FRB allocation algorithm, as indicated in Section 5.4.2.1, where the reuse factor of τ was appropriately adjusted for striking a tradeoff between the ICI-elimination and TP-enhancement. The procedure of the proposed TDMA-based scheduling

was detailed in **Algorithm 2**, which had a strong relationship with our resource allocation strategy discussed in Section 5.5.

The LACO-OFDM invoked increased the degree of flexibility. As we indicated in Section 5.5, our objective was to maximize the sum of the modulation-mode-related throughput, relying on allocating different number of transmitted layers to different UEs, where for each active layer different modulation-modes may be assigned. As formulated in (5.26), this maximization problem considered both the rate-related and power-related practical considerations. To solve this problem, a two-tier dynamic resource allocation scheme was proposed, where the 1st-tier focussed on the single-UE modulation-mode assignment, while the 2nd-tier was invoked for arranging the coped power allocation of multiple UEs. Upon conceiving these twinned procedures, the complexity was significantly reduced to polynomial-level from that of the excessive-complexity exhaustive search.

Section 5.6 characterized the proposed LACO-OFDM aided VLC system, where the basic system parameters employed were listed in Table 5.2. More specifically, it can be found from the rate distribution of Figs. 5.13 and 5.14 that our proposed hybrid NOMA/OMA scheme was capable of outperforming both TDMA and NOMA in terms of its outage probability. We found that the higher-throughput modulation-modes tend to be assigned to layers when the proposed hybrid NOMA/OMA scheme was invoked. Then the effects of FR factor, FoV value, association strategy, UE density and load restriction were investigated one-by-one. Based on our numerical results, our design guidelines conceived for our LACO-OFDM aided VLC system are as follows:

- The value of L decides the maximum number of available layers. The higher L, the more subcarriers can be utilized, however the receiver complexity is increased accordingly.
- In a dense UE scenario, we would suggest to invoke the NOMA scheme and the hybrid NOMA/TDMA is recommended for achieving a high sum-throughput as well as low UE outage probability.
- The value of FoV Ψ_{FoV} plays a significantly role in determining the overall performance of the VLC system, since it is related to the RSS and to the strength of ICI. When the FoV is moderate, both the NOMA scheme and the hybrid NOMA/TDMA scheme are suitable, but the latter scheme is capable of achieving a lower UE outage probability than that of the former. By contrast, much more grave ICI is imposed on system, when the FoV is higher than 100^o. In this scenario, the FR aided hybrid NOMA/TDMA scheme would be suggested.
- When the number of supported UEs for each AP is restricted, the FR aided hybrid NOMA/TDMA scheme imposes the lowest throughput loss among all

the MA schemes considered, while keeping the UE outage probability as low as possible.

- **Chapter 6 [124]:** In Chapter 6, we designed and investigated the backhaul network of VLC and conceived a PLC-VLC network, where the ubiquitous power line was invoked for linking the Ethernet and the LED-APs, as shown in Fig. 6.2.

  In Section 6.2, we described the PLC-VLC network conceived, including the channel model of both PLC and of VLC. As PLC constituted a hostile medium, a broadband OFDM modulation scheme was invoked for mitigating its channel impairments, where the frequency response was portrayed in Fig. 6.5. In VLC, our NOMA regime was employed for supporting multi-UE access. To maximize the throughput, the power allocation problem was formulated in Section 6.3 in the face of individual rate requirements. To solve this problem, the power allocated to each subcarrier of OFDM in PLC and to each UE in VLC had to be determined. Section 6.4 analysed the relationship between PLC as well as VLC and proposed the optimal power allocation algorithm for jointly determining the power allocation of both networks.

  In Section 6.5, we characterized the proposed PLC-VLC network and compared it to a TDMA scheme and to other power allocation strategies, i.e. SPA and NGDPA. It can be observed from Figs. 6.14 - 6.17 that our proposed PLC-VLC network was capable of outperforming the network relying on TDMA, SPA or NGDPA, for various UE densities and diverse individual rate requirements. Furthermore, the power allocation was solved by jointly allocating power to both the PLC and VLC networks. As expected, the PLC channel had a substantial influence on the sum-throughput performance, where poor conditions of the PLC channel required more power, hence the power available for the VLC UEs was reduced, leading to an achievable throughput reduction.

7.2 Future Work

In this section, we briefly discuss a number of future research ideas.

7.2.1 Neural Network Based Visible Light Positioning

In Chapter 3, we proposed a VLC-aided indoor positioning technique by combining the triangulation and fingerprinting based techniques, where the fingerprint database was built during an off-line stage. However, indoor environments often change over time, which leads to the undesired situation that the reference data in the database deviates from the reality during the on-line stage [146, 147]. Therefore, the resultant positioning

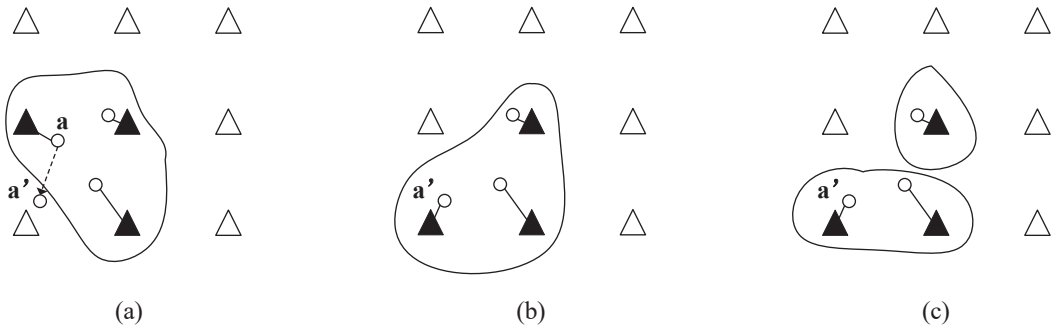

Figure 7.2: A proposal for the breathing clusters design, where APs and UEs are represented by triangles and circles, respectively, while the solid triangles denote the anchoring AP. (a) Cluster at previous time-slot; (b) Potential clustering scheme 1 when UE $\boldsymbol{a}$ is moving to $\boldsymbol{a'}$; (c) Potential clustering scheme 2 when UE $\boldsymbol{a}$ is moving to $\boldsymbol{a'}$.

performance is inevitably affected. To address this issue, employing machine learning based off-line training may be useful to develop more robust positioning schemes, relying for example on the Extreme Learning Machine (ELM), which is capable of providing a good generalization performance at an extremely rapid learning speed [148].

7.2.2 Handover Strategy Design Considering UEs' Movement

In the UC-VLC network constructed, the cluster formation was based on static UE distribution. However, when the UE movements are considered, the clustering strategy, associating with a sophisticated handover scheme has to be designed [149]. Due to the attractive characteristics of UC-clustering, we may combine the clustering design and handover in a moving pedestrian scenario, where the handover is not carried out at the AP-level, it may rather be realized at the cluster-level. More specifically, as shown in Fig. 7.2(a), a UC-cluster based on a 3-AP-3-UE scenario is constructed. When UE $\boldsymbol{a}$ moves from its previous location to the current location, as indicated at $\boldsymbol{a'}$, the previous cluster may evolve to a new 3-AP-3-UE cluster, as shown in Fig. 7.2(b). Alternatively, it may be split into two clusters, as seen in Fig. 7.2(c). This may lead to a breathing clustering design [10].

7.2.3 Enhanced NOMA Design in VLC

In Chapter 5 and 6, the benefits of the ubiquitous NOMA scheme were considered in the context of our VLC and PLC-VLC network, when supporting multi-user transmission. As studied in [150, 151], the performance gain of NOMA over the conventional MA schemes can be further improved by pairing UEs whose channel conditions are more

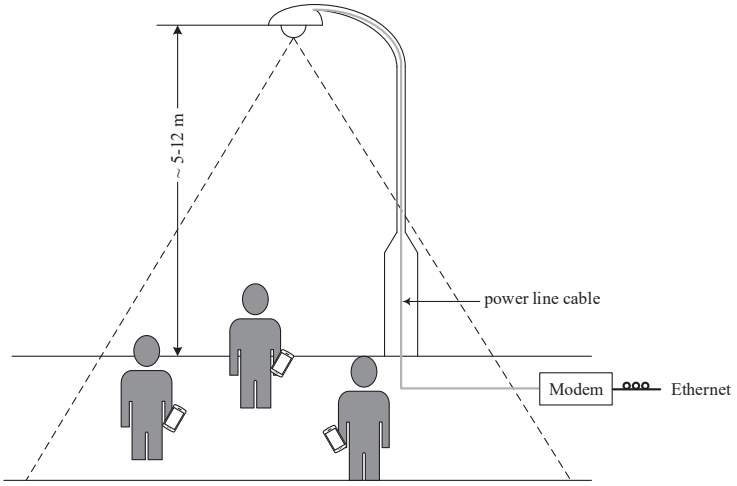

Figure 7.3: An outdoor scenario for PLC-VLC networks, where the elevation of street light fixture is normally around 5 to 12 meters [2].

distinctive. However, in VLC, the channel gain of a UE has a direct relationship with the distance between it and the AP, as shown in Eq. (2.1). Hence the symmetrically distributed UEs may have similar channel conditions, which may degrade the NOMA performance. To circumvent this problem, the performance of the NOMA-VLC system can be further improved by appropriately tuning the transmission angles of the APs and the FoVs of the PDs [55]. These two degrees of freedom may enhance the channel gain differences among UEs, which is critical for enhancing the NOMA performance.

7.2.4 Adaptive Resource Allocation for Outdoor PLC-VLC network

The research of VLC networks reported in this thesis was focussed in indoor scenarios, which are rather different from the outdoor scenarios. For example, as seen in Fig. 7.3, the distance between APs and UEs in outdoor scenarios is normally larger than that in indoor scenarios [2]. In contrast to the indoor VLC channel which is static and stable, the outdoor VLC channel is attenuated by inhomogeneities in the temperature and pressure of the atmosphere, which is further contaminated by ambient noise [152]. Therefore, an adapative resource allocation may become an efficient strategy for the outdoor VLC scenario. To expound further, in the scenario portaryed in Fig. 7.3, the modulation-modes as well as subcarrier allocation may be adaptively controlled in support of multiple VLC UEs, according to their communication conditions. Furthermore, upon employing PLC to feed the VLC network, the subcarrier allocation may be harmonized with that of the PLC OFDM scheme [153].

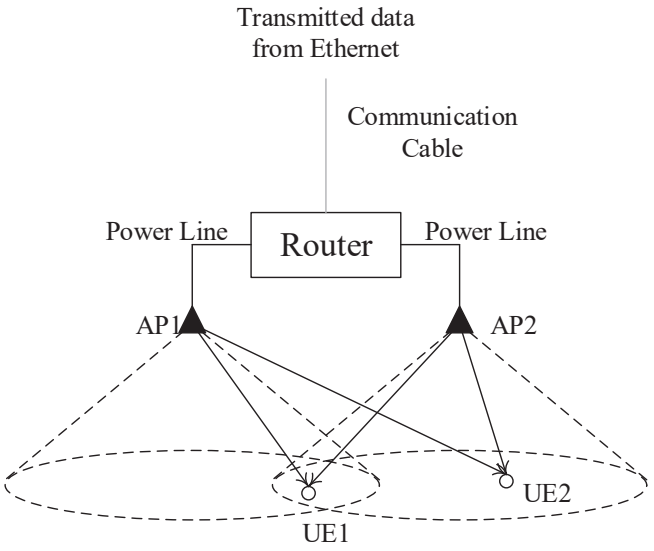

Figure 7.4: A proposal for the cooperative PLC-VLC network.

7.2.5 Cooperative MIMO Design in PLC-VLC Network

In Chapter 6, the PLC-VLC network conceived was only included a single LED-AP to serve multiple UEs. However, the indoor VLC network inherently relies on a multi-transmitter scenario, where a room may have many lighting fixtures interconnected by PLC. Therefore, the cooperation amongst APs constitutes a promising research area [103]. More specifically, with the support of the underlying PLC backbone networking, coordinated transmission of several APs can be realized by designing an interference-aware MIMO matrix, as shown in Fig. 7.4. Hence, multiple UEs can be supported simultaneously without ICI impairment, which may be expected to significantly improve the QoS in indoor networks.

7.2.6 Smart Resource Allocation for Multi-UE VLC Systems

The next-generation wireless networks are expected to have radically new applications [154]. Machine learning has been viewed as one of the most promising artificial intelligence tools [155], which may be invoked for adaptively learn the associated network feature and to make intelligent decisions, so that the diverse requirements of multiple UEs can be satisfied. As a smooth transition from the dynamic programming framework we utilized in Chapters 4 and 5, reinforcement learning relying on dynamic iterative learning constitutes a powerful technique of allocating resource in unknown network

conditions [156]. For example, it may be utilized to predict the location information of mobile UEs so to make decisions concerning both clustering or handover.

Bibliography

[1] M. Zimmermann and K. Dostert. A multipath model for the powerline channel. *IEEE Trans. Commun.*, 50(4):553–559, Apr. 2002.

[2] B. Guzman, V. Jimenez, M. Aguayo-torres, H. Haas, and L. Hanzo. Downlink performance of optical OFDM in outdoor visible light communication. *IEEE Access*, 2018. (early access).

[3] H. Marshoud, S. Muhaidat, P. C. Sofotasios, S. Hussain, M. A. Imran, and B. F. Sharif. Optical non-orthogonal multiple access for visible light communication. *IEEE Wireless Commun.*, pages 82–88, Apr. 2018.

[4] L. Hanzo, H. Haas, S. Imre, D. O'Brien, M. Rupp, and L. Gyongyosi. Wireless myths, realities, and future: From 3G/4G to optical and quantum wireless. *Proc. IEEE*, 100:1853–1888, May 2012.

[5] S. Hranilovic, L. Lampe, and S. Hosur. Visible light communications: The road to standardization and commercialization (part 1). *IEEE Commun. Mag.*, 51(12):24–25, December 2013.

[6] T. Komine and M. Nakagawa. Fundamental analysis for visible-light communication system using LED lights. *IEEE Trans. Consum. Electron.*, 50(1):100–107, Feb. 2004.

[7] V. Chandrasekhar, J. G. Andrews, and A. Gatherer. Femtocell networks: A survey. *IEEE Commun. Mag.*, 46(9):59–67, Sep. 2008.

[8] D. Karunatilaka, F. Zafar, V. Kalavally, and R. Parthiban. LED based indoor visible light communications: State of the art. *IEEE Commun. Surveys Tuts.*, 17(3):1649–1678, Third quarter 2015.

[9] H. Haas, L. Yin, Y. Wang, and C. Chen. What is LiFi? *J. Lightw. Technol.*, 34(6):1533–1544, Mar. 2016.

[10] Rong Zhang, Jiaheng Wang, Zhaocheng Wang, Zhengyuan Xu, Chunming Zhao, and L. Hanzo. Visible light communications in heterogeneous networks: Paving the way for user-centric design. *Wireless Commun.*, 22(2):8–16, April 2015.

[11] J. Armstrong, Y. Sekercioglu, and A. Neild. Visible light positioning: A roaroad for international standardization. *IEEE Commun. Mag.*, 51(12):68–73, Dec. 2013.

[12] F. Yang, J. Gao, and S. Liu. Novel visible light communication approach based on hybrid OOK and ACO-OFDM. *IEEE Photon. Technol. Lett.*, 28(14):1585–1588, July 2016.

[13] J. Luo, L. Fan, and H. Li. Indoor positioning systems based on visible light communication: State of the art. *IEEE Commun. Surveys Tuts.*, 19(4):2871–2893, Fourth Quarter 2017.

[14] G. Ntogari, T. Kamalakis, J. W. Walewski, and T. Sphicopoulos. Combining illumination dimming based on pulse-width-modulation with visible-light communications based on discrete multitone. *IEEE J. Opt. Commun. Netw.*, 3(1):56–65, January 2011.

[15] J. Armstrong and B Schmidt. Comparison of asymmetrically clipped optical OFDM and DC-biased optical OFDM in AWGN. *IEEE Commun. Lett.*, 12(5):343–345, May 2008.

[16] J. Armstrong and A.J. Lowery. Power efficient optical OFDM. *Electron. Lett.*, 42(6), Mar. 2006.

[17] S.D. Dissanayake and J. Armstrong. Comparison of ACO-OFDM, DCO-OFDM and ADO-OFDM in IM/DD systems. *J. Lightw. Technol.*, 31(7):1063–1072, April 2013.

[18] B. Ranjha and M. Kavehrad. Hybrid asymmetrically clipped OFDM-based IM/DD optical wireless system. *IEEE J. Opt. Commun. Netw.*, 6(4):387–396, April 2014.

[19] Q. Wang, C. Qian, X. Guo, Z. Wang, D G. Gunningham, and H. White. Layered ACO-OFDM for intensity-modulated direct-detection optical wireless transmission. *Optics Express*, 23(9), May 2015.

[20] Q. Wang, Z. Wang, X. Guo, and L. Dai. Improved receiver design for layered ACO-OFDM in optical wireless communications. *IEEE Photon. Technol. Lett.*, 28(3):319–322, Feb. 2016.

[21] X. Zhang, Q. Wang, R. Zhang, S. Chen, and L. Hanzo. Performance analysis of layered ACO-OFDM. *IEEE Access*, 5:18366–18381, Aug. 2017.

[22] R. Bai, Z. Wang, R. Jiang, and J. Cheng. Interleaved DFT-spread layered/enhanced ACO-OFDM for intensity-modulated direct-detection systems. *J. Lightw. Technol.*, 36(20):4713–4722, Oct. 2018.

[23] T. Wang, H. Li, and X. Huang. Interference cancellation for layered asymmetrically clipped optical OFDM with application to optical receiver design. *J. Lightw. Technol.*, 36(11):2100–2113, Jun. 2018.

[24] X. Zhang, Z. Babar, R. Zhang, S. Chen, and L. Hanzo. Multi-class coded layered asymmetrically clipped optical OFDM. *IEEE Trans. Commun.*, 2018. (early access).

[25] K. Cui, J. Quan, and Z. Xu. Performance of indoor optical femtocell by visible light communication. *Opt. Commun.*, 298/299:59–66, Jul. 2013.

[26] H. Ma, L. Lampe, and S. Hranilovic. Coordinated broadcasting for multiuser indoor visible light communication systems. *IEEE Trans. Commun.*, 63(9):3313–3324, Sep. 2015.

[27] B. Li, J. Wang, R. Zhang, H. Shen, C. Zhao, and L. Hanzo. Multiuser MISO transceiver design for indoor downlink visible light communication under per-LED optical power constraints. *IEEE Photon. J.*, 7(4), August 2015.

[28] Q. Wang, Z. Wang, and L. Dai. Multiuser MIMO-OFDM for visible light communications. *IEEE Photon. J.*, 7(6), Dec. 2015.

[29] H. Shen, Y. Deng, W. Xu, and C. Zhao. Rate-maximized zero-forcing beamforming for VLC multiuser MISO downlinks. *IEEE Photon. J.*, 8(1), Feb. 2016.

[30] K. Cai and M. Jiang. SM/SPPM aided multiuser precoded visible light communication systems. *IEEE Photon. J.*, 8(2), Apr. 2016.

[31] Z. Sun, H. Yu, Z. Tian, and Y. Zhu. Linear precoding for MU-MISO VLC systems with noisy channel state information. *IEEE Commun. Lett.*, 22(4):732–735, Apr. 2018.

[32] H. Haas. High-speed wireless networking using visible light. *SPIE Newsroom*, Apr. 2013.

[33] R. C. Kizilirmak, O. Narmanlioglu, and M. Uysal. Centralized light access network (C-LiAN): A novel paradigm for next generation indoor VLC networks. *IEEE Access*, 5:19703–19710, Oct. 2017.

[34] M. Kamel, W. Hamouda, and A. Youssef. Performance analysis of multiple association in ultra-dense networks. *IEEE Trans. Commun.*, 65(9):3818–3831, Sep. 2017.

[35] Y. Chen, Y. Chang, Y. Tseng, and W. Chen. A framework for simultaneous message broadcasting using CDMA-based visible light communications. *IEEE Sensors Journal*, 15(12):6819–, Dec. 2015.

[36] Z. Chen, D. A. Basnayaka, and H. Haas. Space division multiple access for optical attocell network using angle diversity transmitters. *J. Lightw. Technol.*, 35(11):2118–2131, Jun. 2017.

[37] R. Zhang, H. Claussen, H. Haas, and L. Hanzo. Energy efficient visible light communications relying on amourphous cells. *IEEE J. Sel. Areas Commun.*, 34(4):894–906, April 2016.

[38] X. Li, R. Zhang, J. Wang, Z. Xu, and L. Hanzo. Users first: User-centric cluster formation for interference-mitigation in visible-light networks. *IEEE Trans. Wireless Commun.*, 15(1):39–53, Jan. 2016.

[39] X. Li, Y. Huo, R. Zhang, and L. Hanzo. User-centric visible light communciations for energy-efficient scalable video streaming. *IEEE Trans. Green Commun. Netw.*, 1(1):59–73, Mar. 2017.

[40] R. Zhang, Y. Cui, H. Claussen, H. Haas, and L. Hanzo. Anticipatory association for indoor visible light communications: Light, follow me! *IEEE Trans. Wireless Commun.*, 17(4):2499–2510, Apr. 2018.

[41] S. S. Bawazir, P. C. Sofotasios, S. Muhaidat, Y. Al-hammadi, and G. K. Karagiannidis. Multiple access for visible light communications: Research challenges and future trends. *IEEE Access*, 6:26167–26174, Jun. 2018.

[42] Y. Saito, Y. Kishiyama, A. Benjebbour, T. Nakamura, A. Li, and K. Higuchi. Non-orthogonal multiple access (NOMA) for cellular future radio access. *IEEE 77th Vehicular Technology Conference (VTC Spring)*, 2013.

[43] Y. Wang, N. Chi, Y. Wang, L. Tao, and J. Shi. Network architecture of a high-speed visible light communication local area network. *IEEE Photon. Technol. Lett.*, 27(2):197–200, Jan. 2015.

[44] M. Kashef, M. Abdallah, and K. Qaraqe. Power allocation for downlink multi-user SC-FDMA visible light communication systems. *in 49th Annu. Conf. Inf. Sci. Syst. (CISS)*, pages 1–5, Mar. 2015.

[45] J. Lian and M. Brandt-Pearce. Multiuser MIMO indoor visible light communication system using spatial multiplexing. *J. Lightw. Technol.*, 35(23):5024–5033, Dec. 2017.

[46] M. F. Guerra-Medina, O. Gonzalez, B. Rojas-Guillama, J. A. Martin-Gonzalez, F. Delgado, and J. Rabadan. Ethernet-OCDMA system for multi-user visible light communications. *Electron. Lett.*, 48(4), Feb. 2012.

[47] S. Chen and C. Chow. Color-shift keying and code-division multiple-access transmission for RGB-LED visible light communications using mobile phone camara. *IEEE Photon. J.*, 6(6), Dec. 2014.

[48] M. Z. Farooqui and P. Saengudomlert. Transmit power reduction through subcarrier selection for MC-CDMA-based indoor optical wireless communications with IM/DD. *EURASIP J. Wireless Commun. Netw.*, 138(1):1–14, 2013.

[49] M. H. Shoreh, A. Fallahpour, and J. A. Salehi. Design concepts and performance analysis of multicarrier CDMA for indoor visible light communications. *J. Opt. Commun. Netw.*, 7(6):554–562, Jun. 2015.

[50] S. Yang and L. Hanzo. Fifty years of MIMO detection: The road to large-scale MIMOs. *IEEE Commun. Surveys Tuts.*, 17(4):1941–1988, Fourth quarter 2015.

[51] L. Yin, X. Wu, and H. Haas. SDMA grouping in coordinated multi-point VLC systems. *in Proc. Summer Topicals Meeting Ser.*, pages 169–170, Jul. 2015.

[52] O. Gonzalez, M. F. Guerra-Medina, I. R. Martin, F. Delgado, and R. P. Jimenez. Adaptive WHTS-assisted SDMA-OFDM scheme for fair resource allocation in multi-user visible light communications. *J. Opt. Commun. Netw.*, 8(6):427–440, Jun. 2016.

[53] NTT DOCOMO. Requirements, candidate solutions & technology roaroad for LTE rel-12 onward. *3GPP RWS-120010*, Jun. 2012.

[54] Z. Ding, Z. Yang, P. Fan, and H.V. Poor. On the performance of non-orthogonal multiple access in 5G systems with randomly deployed users. *IEEE Signal Process. Lett.*, 21(12):1501–1505, December 2014.

[55] H. Marshoud, V. M. Kapinas, G. K. Karagiannidis, and S. Muhaidat. Non-orthogonal multiple access for visible light communications. *IEEE Photon. Technol. Lett.*, 28(1):51–54, Jan. 2016.

[56] H. Marshoud, P. Sofotasios, S. Muhaidat, G. Karagiannidis, and B. Sharif. On the performance of visible light communication systems with non-orthogonal multiple access. *IEEE Trans. Wireless Commun.*, 16(10):6350–6363, Oct. 2017.

[57] L. Yin, W. Popoola, X. Wu, and H. Haas. Performance evaluation of non-orthogonal multiple access in visible light communication. *IEEE Trans. Commun.*, 64(12):5162–5175, December 2016.

[58] X. Zhang, Q. Gao, C. Gong, and Z. Xu. User grouping and power allocation for NOMA visible light communication multi-cell networks. *IEEE Commun. Lett.*, 21(4):777–780, April 2017.

[59] C. Chen, W. Zhong, H. Yang, and P. Du. On the performance of MIMO-NOMA-based visible light communication systems. *IEEE Photon. Technol. Lett.*, 30(4):307–310, Feb. 2018.

[60] Z. Yang, W. Xu, and Y. Li. Fair non-orthogonal multiple access for visible light communication downlinks. *IEEE Wireless Commun. Lett.*, 6(1):66–69, February 2017.

[61] Y. Fu, Y. Hong, L. Chen, and C. Sung. Enhanced power allocation for sum rate maximization in OFDM-NOMA VLC systems. *IEEE Photon. Technol. Lett.*, 30(13):1218–1221, Jul. 2018.

[62] X. Zhao, H. Chen, and J. Sun. On physical-layer security in multiuser visible light communication systems with non-orthogonal multiple access. *IEEE Access*, 6:34004–34017, Jul. 2018.

[63] R. Mitra and V. Bhatia. Precoded chebyshev-NLMS-based pre-distorter for non-linear LED compensation in NOMA-VLC. *IEEE Trans. Commun.*, 65(11):4845–4856, Nov. 2017.

[64] W. Chu, J. Dang, Z. Zhang, and L. Wu. Effect of clipping on the achievable rate of non-orthogonal multiple access with DCO-OFDM. *In the Preceeding of International Conference on Wireless Communications and Signal Processing (WCSP)*, 2017.

[65] B. Lin, W. Ye, X. Tang, and Z. Ghassemlooy. Experimental demonstration of bidirectional NOMA-OFDMA visible light communications. *Optics Express*, 25(4):4348–4355, Feb. 2017.

[66] K. Ali, H. Elsawy, A. Chaaban, and M. Alouini. Non-orthonogonal multiple access for large-scale 5G networks: Interference aware design. *IEEE Access*, 5:21204–21216, September 2017.

[67] L. Wei, H. Zhang, and B. Yu. Optimal bit-and-power allocation algorithm for VLC-OFDM system. *Electron. Lett.*, 52(12):1036–1037, Jun. 2016.

[68] L. Wu, Z. Zhang, J. Dang, and H. Liu. Adaptive modulation sscheme for visible light communications. *J. Lightw. Technol.*, 33(1):117–125, Jan. 2015.

[69] X. Huang, S. Chen, Z. Wang, J. Shi, Y. Wang, J. Xiao, and N. Chi. 2.0-Gb/s visible lignt link based on adaptive bit allocation OFDM of a single phosphorrescent white LED. *IEEE Photon. J.*, 7(5), Oct. 2015.

[70] R. C. Kizilirmak, O. Narmanlioglu, and M. Uysal. Relay-assisted OFDM-based visible light communications. *IEEE Trans. Commun.*, 63(10):3765–3778, Oct. 2015.

[71] C. Gong, S. Li, Q. Gao, and Z. Xu. Power and rate optimization for visible light communication system with liglight constraints. *IEEE Trans. Signal Processing*, 63(16):4245–4256, Aug. 2015.

[72] F. Jin, X. Li, R. Zhang, C. Dong, and L. Hanzo. Resource allocation under delay-guarantee constraints for visible-light communication. *IEEE Access*, 4:7301–7312, Nov. 2016.

[73] Y. Tao, X. Liang, J. Wang, and C. Zhao. Scheduling for indoor visible light communication based on graph theory. *Optics Express*, 23(3):2737–2752, Jan. 2015.

[74] K. Zhou, C. Gong, and Z. Xu. Color planning and intercell interference coordination for multicolor visible light communication networks. *J. Lightw. Technol.*, 35(22):4980–4993, Nov. 2017.

[75] R. Jiang, Q. Wang, H. Haas, and Z. Wang. Joint user association and power allocation for cell-free visible light communication networks. *IEEE J. Sel. Areas Commun.*, 36(1):136–148, Jan. 2018.

[76] D. Bykhovsky and S. Arnon. Multiple access resource allocation in visible light communication systems. *J. Lightw. Technol.*, 32(8):1594–1600, Mar. 2014.

[77] R. Jiang, Z. Wang, Q. Wang, and L. Dai. Multi-user sum-rate optimization for visible light communications with lighting constraints. *J. Lightw. Technol.*, 34(16):3943–3952, Aug. 2016.

[78] K. Park, Y. Ko, and M. Alouini. On the power and offset allocation for rate adaptation of spatial multiplexing in optical wireless MIMO channels. *IEEE Trans. Commun.*, 61(4):1535–1543, Apr. 2013.

[79] H. Yang, C. Chen, and W. Zhong. Cognitive multi-cell visible light communication with hybrid undunder/overlay resource allocation. *IEEE Photon. Technol. Lett.*, 30(12):1135–1138, Jun. 2018.

[80] M. F. Keskin, A. D. Sezer, and S. Gezici. Localization via visible light systems. *Proc. IEEE*, 106(6):1063–1088, Jun, 2018.

[81] Y. Zhuang, L. Hua, L. Qi, J. Yang, P. Cao, Y. Cao, Y. Wu, J. Thompson, and H. Haas. A survey of positioning systems using visible LED lights. *IEEE Commun. Surveys Tuts.*, 20(3):1963–1988, Third Quarter 2018.

[82] C. Yang and H. Shao. Wifi-based indoor positioning. *IEEE Wireless Commun.*, 53(3):150–157, Mar. 2015.

[83] Y. Zhuang, Y. Li, L. Qi, H. Lan, J. Yang, and N. El-sheimy. A two-filter integration of MMSE sensors and WiFi fingerprinting for indoor positioning. *IEEE Sens. J.*, 16(13):5125–5126, May 2016.

[84] J. Hu, D. Liu, Z. Yan, and H. Liu. Experimental analysis on weight K-nearest neighbor indoor fingerprint positioning. *IEEE Internet Things*, 2018. (early access).

[85] S. Zhou and J. K. Pollard. Position measurement using bluetooth. *IEEE Trans. Consum. Electron.*, 52(2):555–558, May 2006.

[86] R. Faragher and R. Harle. Location fingerprinting with bluetooth low energy beacons. *IEEE J. Sel. Areas Commun.*, 33(11):2418–2428, May 2015.

[87] G. Blasio, A. Quesada-Arencibia, C. Garcia, J. Carlos, R. Rodriguez, and R. Moreno-Diaz. A protocol-channel-based indoor positioning performance study for bluetooth low energy. *IEEE Access*, 6:33440–33450, May 2018.

[88] A. Errington, B. Daku, and A. Prugger. Initial position estimation using RFID tags: A least-squares approach. *IEEE Trans. Instrum. Meas.*, 59(11):2863–2869, Apr. 2010.

[89] S. Saab and Z. Nakad. A standalone RFID indoor positioning system using passive tags. *IEEE Trans. Ind. Electron.*, 58(5):1961–1970, Jul. 2011.

[90] C. Huang, L. Lee, C. Ho, L. Wu, and Z. Lai. Real-time RFID indoor positioning system based on kalman-filter drift removal and heron-bilateration location estimation. *IEEE Trans. Instrum. Meas.*, 64(3):728–739, Sep. 2015.

[91] R. Zhang. Localisation, communication and networking with VLC: Challenges and opportunities. 2017.

[92] M. Kashef, M. Abdallah, and N. Al-Dhahir. Transmit power optimization for a hybrid PLC/VLC/RF communication system. *IEEE Trans. Green Commun. Netw.*, 2(1):234–245, Mar. 2018.

[93] J. Rufo, J. Rabadan, F. Delgado, C. Quintana, and R. Perez-Jimenez. Experimental evaluation of video transmission through LED illumination devices. *IEEE Trans. Consum. Electron.*, 56(3):1411–1416, Sep. 2010.

[94] A. Gupta and R. K. Jha. A survey of 5G network: Architecture and emerging technologies. *IEEE Access*, 3:1206–1232, Aug. 2015.

[95] F. Jin, R. Zhang, and L. Hanzo. Resource allocation under delay-guarantee constraints for heterogeneous visible-light and RF femtocell. *IEEE Trans. Wireless Commun.*, 14(2):1020–1034, Feb. 2015.

[96] H. Tam, H. Tuan, D. Ngo, T. Duong, and H. V. Poor. Joint load balancing and interference management for small-cell heterogeneous networks with limited backhaul capacity. *IEEE Trans. Wireless Commun.*, 16(2):872–884, Feb. 2017.

[97] M. Kashef, M. Abdallah, N. Al-Dhahir, and K. Qaraqe. On the impact of PLC bacbackhaul in multi-user hybrid VLC/RF communication systems. *IEEE Global Communications Conference (GLOBECOM)*, pages 1–6, Dec. 2016.

[98] T. Komine and M. Nakagawa. Integrated system of white LED visible-light communication and power-line communication. *IEEE Trans. Consum. Electron.*, 49(1):71–79, Jan. 2003.

[99] M. Zimmermann and K. Dostert. An analysis of the broadband noise scenario in powerline networks. *in Int. Symposium on Power Line Communications and Its Applications (ISPLC)*, pages 131–138, 2000.

[100] T. Komine, S. Haruyama, and M. Nakagawa. Performance evaluation of narrowband OFDM on integrated system of power line communication and visible light wireless communication. *International Symposium Wireless Pervasive Computing*, Jan. 2006.

[101] K. Pujapanda. LiFi integrated to power-line for smart illumination communication. *in IEEE International Conference on Communication Systems and Network Technologies*, pages 875–878, 2013.

[102] P. Amirshahi and M. Kavehrad. Broadband access over medium and low voltage ppower-line and use of white light emitting diodes for indoor communications. *in IEEE Consumer Communications and Networking Conference (CCNC)*, 2:897–901, 2006.

[103] H. Ma, L. Lampe, and S. Hranilovic. Integration of indoor visible light and power line communication systems. *in IEEE 17th International Symposium on Power Line Communications and Its Applications*, pages 291–296, 2013.

[104] H. Ma, L. Lampe, and S. Hranilovic. Hybrid visible light and power line communication for indoor multiuser downlink. *IEEE J. Opt. Commun. Netw.*, 9(8):635–647, Aug. 2017.

[105] J. Song, W. Ding, F. Yang, H. Yang, B. Yu, and H. Zhang. In indoor broadband broadcasting system based on PLC and VLC. *IEEE Trans. Broadcast.*, 61(2):299–308, Jun. 2015.

[106] M. Mossaad, S. Hranilovic, and L. Lampe. Amplify-and-forward integration of power line and visible light communications. *in IEEE Global SIP*, pages 1322–1326, 2015.

[107] M. Kavehrad, Z. Hajjarian, and A. Enteshari. Energy-efficient broadband data communications using white LEDs on aircraft powerlines. *in Integrated Communications, Navigation and Surveillance Conference*, pages 1–8, 2008.

[108] W. Ding, F. Yang, H. Yang, J. Wang, X. Wang, X. Zhang, and J. Song. A hybrid power line and visible light communication system for indoor hospital applications. *ELSEVIER Computers in Industry*, 68:170–178, Feb. 2015.

[109] X. Ma, J. Gao, F. Yang, W. Ding, H. Yang, and J. Song. Integrated power line and visible light communication system compatible with multi-service transmission. *IET Communications*, 11(1):104–111, 2017.

[110] A. Ndjiongue, T. Shongwe, H. Ferreira, N. Ngatched, and A. Vinck. Cascaded PLC-VLC channel using OFDM and CSK techniques. *in IEEE Clobal Communications Conference (GLOBECOM)*, pages 1–6, 2015.

[111] M. Kashef, A. Torky, M. Abdallah, N. Al-Dhahir, and K. Qaraqe. On the achievable rate of a hybrid PLC/VLC/RF communication system. *in IEEE Clobal Communications Conference (GLOBECOM)*, pages 1–6, 2015.

[112] W. Gu, M. Aminikashani, P. Deng, and M. Kavehrad. Impact of multipath reflections on the performance of indoor visible light positioning systems. *J. Lightw. Technol.*, 34(10):2578–2587, May 2016.

[113] K. Gligoric, M. Ajmani, D. Vukobratovic, and S. Sinanovic. Visible light communications-based indoor positioning via compressed sensing. *IEEE Commun. Lett.*, 22(7):1410–1413, Jul. 2018.

[114] W. Xu, J. Wang, H. Shen, H. Zhang, and X. You. Indoor positioning for multiphotodiode device using visible-light communications. *IEEE Photon. J.*, 8(1), Feb. 2015.

[115] F. Alam, M. Chew, T. Wenge, and G. Gupta. An accurate visible light positioning system using regenerated fingerprint database based on calibrated propagation model. *IEEE Trans. Instrum. Meas.*, 2018. (early access).

[116] S. H. Cha. Comprehensive survey on distance/similarity measures between probability density functions. *Int. J. Math. Models Methods Appl. Sci.*, 1(4):300–307, 2007.

[117] B. Lin, Z. Ghassemlooy, C. Lin, X. Tang, Y. Li, and S. Zhang. An indoor visible light positioning system based on optical camera communications. *IEEE Photon. Technol. Lett.*, 29(7):579–582, Apr. 2017.

[118] Z. Wang, Q. Wang, W. Huang, and Z. Xu. *Visible light communications: Modulation and signal processing.* Wiley-IEEE Press, 2018.

[119] M. Rahman, M. Haque, and K. Kim. Indoor positioning by LED visible light communication and image sensors. *Int. J. Elect. Comput. Eng.*, 1(2):161–170, 2011.

[120] J. Fang, Z. Yang, S. Long, Z. Wu, X. Zhao, F. Liang, Z. Jiang, and Z. Chen. High-speed indoor navigation system based on visible light and mobile phone. *IEEE Photon. J.*, 9(2), Apr. 2017.

[121] S. Feng, X. Li, R. Zhang, M. Jiang, and L. Hanzo. Hybrid positioning aided amorphous-cell assisted user-centric visible light downlink techniques. *IEEE Access*, 4:2705–2713, Jun. 2016.

[122] S. Feng, R. Zhang, X. Li, Q. Wang, and L. Hanzo. Dynamic thrthrough maximization for the user-centric visible light downlink in the face of practical considerations. *IEEE Trans. Wireless Commun.*, 17(8):5001–5015, Aug. 2018.

[123] S. Feng, R. Zhang, W. Xu, and L. Hanzo. Multiple access design for ultra-dense VLC networks: Orthogonal v.s. non-orthogonal. *IEEE Trans. Commun.*, 2018. (accepted).

[124] S. Feng, T. Bai, and L. Hanzo. Joint power allocation for the multi-user NOMA-downlink in a power-line-fed VLC network. *IEEE Trans. Veh. Technol.*, 2018. (under review).

[125] P H. Pathak, X. Feng, P. Hu, and P. Mohapatra. Visible light communication, networking, and sensing: A survey, potential and challenges. *IEEE Commun. Surveys Tuts.*, 17(4):2047–2077, 4th Quarter 2015.

[126] J. B. Carruthers and J. M. Kahn. Multiple-subcarrier modulation for nondirected wireless infrared communication. *IEEE J. Sel. Areas Commun.*, 14:538–546, 1996.

[127] O. Gonzalez, R. Perez-Jimenez, S. Rodriguez, J. Rabadan, and A. Ayala. OFDM over indoor wireless optical channel. *IEEE Proc. Optoelectronics*, 152:199–204, 2005.

[128] J. Armstrong. OFDM for optical communications. *J. Lightw. Technol.*, 27(3):189–204, Feb. 2009.

[129] S. Dimitrov, S. Sinanovic, and H. Haas. Clipping noise in OFDM-based optical wireless communication systems. *IEEE Trans. Commun.*, 60(4):1072–1081, April 2012.

[130] S. Dimitrov and H. Haas. *Principles of LED light communications.* Cambridge university press, 2015.

[131] H. Liu, H. Darabi, P. Banerjee, and J. Liu. Survey of wireless indoor positioning techniques and systems. *IEEE Trans. Syst., Man, Sybern. C, Appl. Rev.*, 37(6):1067–1080, Nov. 2007.

[132] T. Do and M. Yoo. An in-depth survey of visible light communication based positioning systems. *Sensors*, 16(5):678, May 2016.

[133] S. Sen, J. Lee, K. Kim, and P Congdon. Avoiding multipath to revive inbusystemsWiFi localization. *in Proc. 11th Annu. Int. Conf. MobiSys*, pages 249–262, 2013.

[134] L. Li, P. Hu, C. Peng, G. Shen, and F. Zhao. Epsilon: A visible light based positioning system. *in Proc. 11th USENIX Symp. NSDI*, pages 331–343, 2014.

[135] X. Li, R. Zhang, and L. Hanzo. Optimization of visible-light optical wireless systems: Network-centric versus user-centric designs. *IEEE Commun. Surveys Tuts.*, 20(3):1878–1904, Mar. 2018.

[136] T. Nguyen, A. Yadav, W. Ajib, and C. Assi. Centralized and distributed energy efficiency designs in wireless backhaul HetNets. *IEEE Trans. Wireless Commun.*, 16(7):4711–4726, Jul. 2017.

[137] Y. Zhang and K. B. Letaief. Multiuser adaptive subcarrier-and-bit allocation with adaptive cell selection for OFDM systems. *IEEE Trans. Wireless Commun.*, 3(5):1566–1575, September 2004.

[138] Z. Shen, J. Andrews, and B. Evans. adaptive resource allocation in multiuser OFDM systems with proportional rate constraints. *IEEE Trans. Wireless Commun.*, 4(6):2726–2737, November 2005.

[139] X. Li, C. Li, and Y. Jin. Dynamic resource allocation for transmit power minimization in OFDM-based NOMA systems. *IEEE Commun. Lett.*, 20(12):2558–2561, December 2016.

[140] K. Cho and D. Yoon. On the general BER expression of one- and two-dimensional amplitude modulations. *IEEE Trans. Commun.*, 50(7):1074–1080, July 2002.

[141] J. M. Kahn and J. R. Barry. Wireless infrared communications. *Proc. IEEE*, 85(2):198–265, Feb 1997.

[142] S.E. Schaeffer. Graph clustering. *Computer Science Review*, pages 27–64, 2007.

[143] D.P. Bersekas. *Dynamic Programming and Optimal Control*, volume I. Athena Scientific, 4th edition, 2017.

[144] T. Esmailian, F.. Kschischang, and P. Gulak. In-building power lines as high-speed communication channels: Channel characterization and a test channel ensemble. *Int. J. Commun. Syst.*, 16:381–400, May 2003.

[145] M. Zimmermann and K. Dostert. Analysis and modmodel of impulsive noise in broad-band powerline communications. *IEEE Trans. Electromagn. Compat.*, 44(1):249–258, Feb. 2002.

[146] Z. Xiao, H. Wen, A. Markham, and N. Trigoni. Robust indoor positioning with lifelong learning. *IEEE J. Sel. Areas Commun.*, 33(11):2287–2301, Nov. 2015.

[147] H. Zou, B. Huang, X. Lu, H. Jiang, and L. Xie. A robust indoor positioning system based on the procrustes analysis and weweight extreme learning machine. *IEEE Trans. Wireless Commun.*, 15(2):1252–1266, Feb. 2016.

[148] X. Lu, H. Zou, H. Zhou, L. Xie, and G. Huang. Robust extreme learning machine with its application to indoor positioning. *IEEE Trans. Cybern.*, 46(1):194–205, Jan. 2016.

[149] M. A. Dastgheib, H. Beyranvand, J. A. Salehi, and M. Maier. Mobility-aware resource allocation in VLC networks using T-step look-ahead policy. *J. Lightw. Technol.*, 36(23):5358–5370, Dec. 2018.

[150] Z. Ding, M. Peng, and H. V. Poor. Cooperative non-orthogonal multiple access in 5G systems. *IEEE Commun. Lett.*, 19(8):1462–1465, Aug. 2015.

[151] Z. Ding, P. Fan, and H. V. Poor. Impact of user pairing on 5G nonorthogonal multiple-access downlink transmissions. *IEEE Trans. Veh. Technol.*, 65(8):6010–6023, Aug. 2016.

[152] Y. Zhu, Z. Sun, J. Zhang, and Y. Zhang. A fast blind detection algorithm for outdoor visible light communications. *IEEE Photon. J.*, 7(6), Dec. 2015.

[153] Y. Zhu, Z. Sun, J. Zhang, Y. Zhang, and J. Zhang. Training rreceiver for repetition-coded MISO outdoor visible light communciations. *IEEE Trans. Veh. Technol.*, 66(1):529–540, Jan. 2017.

[154] C. Jiang, H. Zhang, Y. Ren, Z. Han, K. Chen, and L. Hanzo. Machine learning paradigms for next-generation wireless networks. *IEEE Wireless Commun.*, pages 98–105, Apr. 2017.

[155] J. Wang, C. Jiang, H. Zhang, X. Zhang, V. Leung, and L. Hanzo. Learning-aided network association for hybrid indoor LiFi-WiFi systems. *IEEE Trans. Veh. Technol.*, 67(4):3561–3574, Apr. 2018.

[156] L. Xiao, Y. Li, C. Dai, H. Dai, and H. V. Poor. Reinforcement learning-based NOMA power allocation in the presence of smart jamming. *IEEE Trans. Veh. Technol.*, 67(4):3377–3389, Apr. 2018.

Glossary

AC	Alternating Current
ACO-OFDM	Asymmetrically Clipped Optical OFDM
ACO/DCO-OFDM	ACO-OFDM and DCO-OFDM
ADO-OFDM	Asymmetrically Clipped DC biased OFDM
AF	Amplify-and-Forward
AOA	Angle of Arrival
AP	Access Point
AWGN	Additive White Gaussian Noise
BER	Bit Error Rate
BPA	Bit and Power Allocation
BPF	Bandpass Filter
BPSK	Binary Phase Shift Keying
BS	Base Station
CDF	Cumulative Distribution Function
CDMA	Code Division Multiple Access
CoMP	Coordinated Multi-Point
CSI	Channel State Information
CSK	Color Shift Keying
DC	Direct Current
DCO-OFDM	DC-biased Optical OFDM
DF	Decode-and-Forward
DMT	Discrete Multi-Tone
EC	Effective Capacity
ELM	Extreme Learning Machine
FDMA	Frequency Division Multiple Access
FFT	Fast-Fourier-Transform
FoV	Field-of-View
FPA	Fixed Power Allocation

FR	Frequency Reuse
FRB	Frequency Resource Block
GRPA	Gain Ratio Power Allocation
GPS	Global Positioning System
HACO-OFDM	Hybrid ACO-OFDM
ICI	Inter-Cell Interference
IDFTS-L/e-ACO	Interleaved Discrete-Fourier-Transform-Spread L/e-ACO-OFDM
IFFT	Inverse Fast Fourier Transform
ILI	Inter-Layer Interference
IM/DD	Intensity Modulation / Direct Detection
IPS	Indoor Positioning System
ISI	Inter-Symbol Interference
JPA	Joint Power Allocation
KKT	Karush-Kuhn-Tucker
kNN	k-nearest-neighbor
LACO-OFDM	Layered ACO-OFDM
LAN	Local Area Network
LED	Light Emitting Diode
LED-AP	LED based AP
LoS	Line-of-Sight
MA	Multiple Access
MA-DMT	Multiple Access Discrete Multi-Tone
MC	Multi-Carrier
MIMO	Multiple-Input-Multiple-Output
MISO	Multiple-Input-Single-Output
ML	Maximum Likelihood
MMSE	Minimum Mean-Squared Error
M-QAM	Multi-level Quadrature Amplitude Modulation
MUI	Multi-User Interference
NC	Network-Centric
NGDPA	Normalized Gain Difference Power Allocation
NLoS	Non-Line-of-Sight
NOMA	Non-Orthogonal Multiple Access
OCDMA	Optical Code Division Multiple Access
OCC	Optical Camera Communications
O/E	Optical-to-Electronic
OFDM	Orthogonal Frequency Division Multiplexing
OFDMA	Orthogonal Frequency Division Multiple Access
OMA	Orthogonal Multiple Access

O-NOMA	Optical-NOMA
OOC	Orthogonal Optical Code
OOK	On-Off Keying
OP	Outage Probability
OW	Optical Wireless
PAM-DMT	Pulse-Amplitude-Modulated Discrete Multitone
PAPR	Peak-to-Average Power Ratio
PD	Photo Diode
PLC	Power Line Communications
PPM	Pulse Position Modulation
PSK	Phase Shift Keying
PWM	Pulse Width Modulation
QoS	Quality-of-Service
QPSK	Quadrature Phase Shift Keying
RC	Reference Channel
RF	Radio Frequency
RFID	Radio Frequency Identification
RGB	Red-Green-Blue
RSS	Received Signal Strength
SC	Single-Carrier
SDMA	Space Division Multiple Access
SIC	Successive Interference Cancellation
SINR	Signal-to-Interference-plus-Noise Ratio
SM	Spatial Modulation
SNR	Signal-to-Noise ratio
SO-OFDM	Spatial-optical OFDM
SPA	Static Power Allocation
SPPM	Spatial Pulse Position Modulation
TDMA	Time Division Multiple Access
TDOA	Time Difference of Arrival
TOA	Time of Arrival
TPC	Transmit Pre-Coding
UC	User-Centric
UE	User Equipment
UFR	Unity Frequency Reuse
VLC	Visible Light Communication
VT	Vectorized Transmission
WKNN	Weighted k-Nearest Neighbor
ZF	Zero Forcing